UiT
THE ARCTIC UNIVERSITY OF NORWAY

FACULTY OF SCIENCE AND TECHNOLOGY

Department of Geology

Modeling of seismic amplitude anomalies associated with CO_2 underground storage

—

Janita Louise Nordahl

EOM-3901 Master's Thesis in Energy, Climate and Environment
June 2015

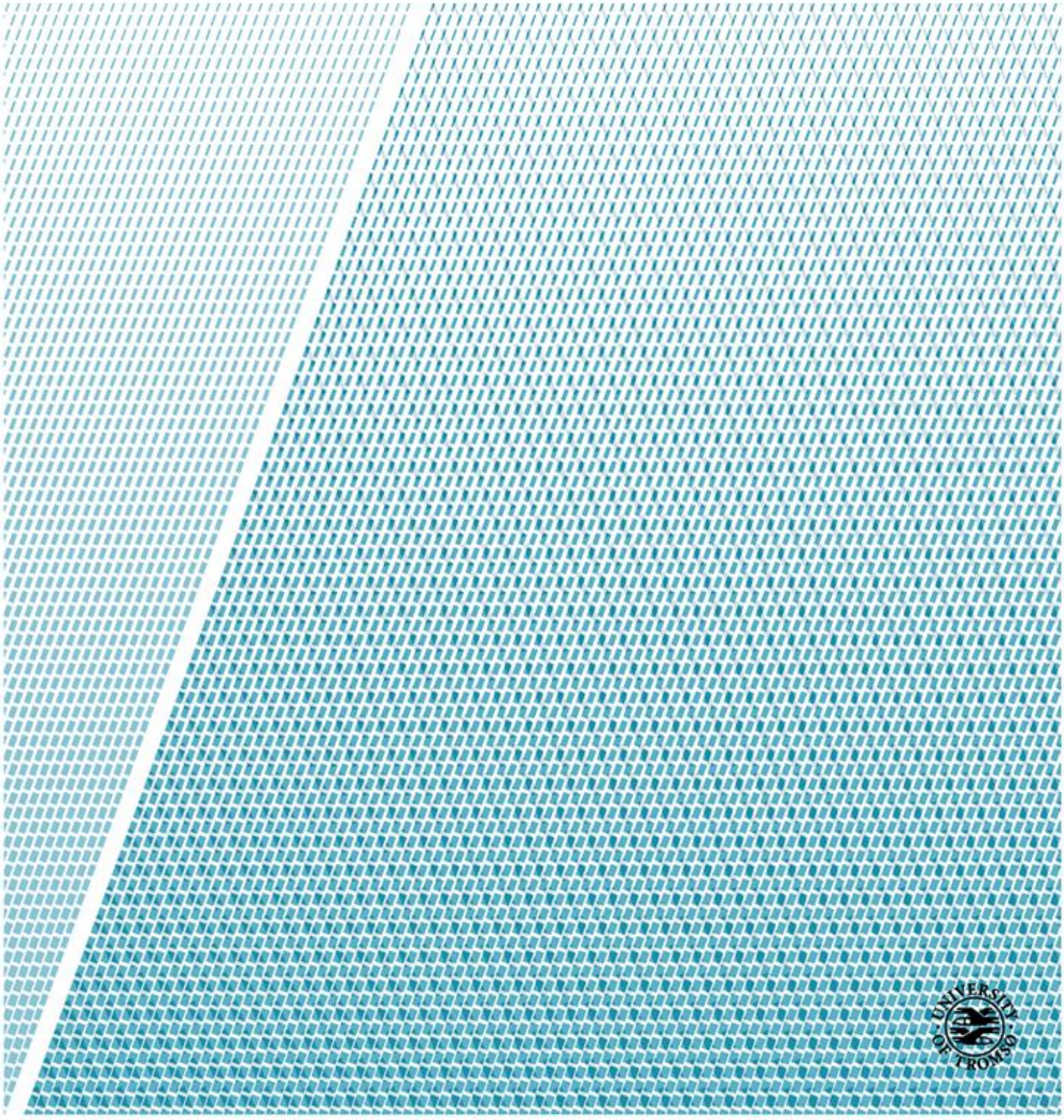

Abstract

Higher amounts of CO_2 in the atmosphere has contributed to finding techniques to mitigate the emissions of CO_2. One of those techniques is Carbon Capture and Storage (CCS). CO_2 can be stored in subsurface reservoirs over time.

Monitoring and modeling of reservoirs is important to avoid leakage and to predict how the CO_2 could migrate. Modeling is also useful when the seismic interpreter has problems, then seismic from modeling with known parameters can be useful.

The first place in the world to inject CO_2 was in the Sleipner field in the Norwegian North Sea. The injection found place in 1996 in the Sleipner East field into the Utsira formation. The reservoir is estimated to have a vertical thickness about 200 m at the injection point, and the estimated caprock for the CO_2 is about 100 m thick. This thesis shows modeling of the seismic response from different synthetic models associated with CO_2 underground storage. The parameters is based on data from the Sleipner field to get a realistic view of the result.

Incident angle, input frequency, CO_2 saturation and geometry of the models are all important parameters affecting the seismic result. Modeling with various incident angles and input frequencies has been done. It showed that higher frequencies gives the best resolution as expected, and that smaller incident angle makes it easier to distinguish interfaces. A frequency of 70 Hz and an incident angle of 20°, made it possible to detect both interfaces of a layer with vertical thickness of 1 m.

Several models with varying vertical and horizontal thicknesses of the plume have been made. The results shows that an incident angle of 20° with 60 Hz and realistic migration options turned on (aperture range and traveltime range) will not create any vertical reflections. Horizontal plumes with an incident angle of 20° using 30 Hz and 60 Hz, is visible with no interference for vertical thickness equal and greater than 40 m and 20 m, respectively. Tuning thickness occurred with a vertical thickness of 20 m and 10 m for respectively 30 Hz and 60 Hz. A stronger reflection in the area the plume is located is visible for vertical thicknesses equal to and greater than 3 m when using both 30 Hz and 60 Hz.

Acknowledgement

Da var tiden endelig kommet for å levere inn masteroppgaven, og 5 år ved Universitetet i Tromsø er over. Jeg har fått muligheten til å lære mye spennende, og ikke minst fått mange gode venner. Først og fremst vil jeg takke min veileder Stefan Bünz. Du har vært viktig i den siste tiden for å få ting på plass. Tusen takk for hjelpen!

Ellers vil jeg gjerne nevne og takke Isabelle Lecomte i NORSAR for mye god hjelp og spørsmål med tanke på SeisRoX og teorien bak. Du har virkelig hjulpet meg i mange frustrerte stunder. Tusen takk!

Ellers skylder jeg mine kjære søstre og svigerbror en stor takk for retting av skrivefeil. Sist men ikke minst vil jeg takke min fantastiske kjæreste, Fredrik for all støtten. Uten deg hadde jeg nok gått på veggen av frustrasjon den siste tiden, takk for at du har oppmuntret og støttet meg.

Janita Nordahl

Juni 2015

1 Contents

1 Introduction 1

1.1 What is CCS? 1

1.2 Why CCS? 3

1.3 Storing of CO_2 5

1.3.1 Reservoir properties for storing CO_2 7

1.3.2 Trapping mechanisms 7

1.3.3 Time-lapse seismic monitoring 8

2 Basic Geophysics 11

2.1 Acoustic impedance and reflection coefficient 11

2.2 Snell's law 11

2.3 Seismic amplitude effects 12

2.3.1 Attenuation of seismic energy 12

2.3.2 AVO/AVA-analysis 14

2.4 Vertical and horizontal resolution 15

2.5 Seismic response of gas 18

2.6 Migration 19

2.6.1 Post-Stack time migration 19

2.6.2 Pre-stack Depth Migration (PSDM) 19

3 Theories of rock physics 21

3.1 Elastic properties 21

3.2 Effects on the elastic properties 24

4 Seismic modeling 25

4.1 SimPLI PSDM modeling algorithm applied in SeisRoX 25

4.1.1 Resolution in SeisRoX 29

5 The Sleipner field in the Norwegian North Sea 31

5.1 Geology of the area 31

5.1.1 Seismic amplitude anomalies observed in the area 34

5.2 CO_2 injection at the Sleipner East field 36

5.2.1 Seismic monitoring of the reservoir 37

6 Data and methods 39

6.1 Properties from Sleipner used in the modeling 39

6.1.1 Elastic parameters used in the modeling 41
6.2 NORSAR 2D and NORSAR 3D 44
6.3 SeisRoX 44
6.3.1 Background model 45
6.3.2 Reservoir model 47
6.3.3 Survey 52
6.3.4 Target area (Simulated PSDM Parameters) 53
6.3.5 Wavelet 54
6.4 Survey and PSDM parameters used in the modeling 56
7 Results 57
7.1 Change in acoustic velocities 57
7.1.1 The seismic images 57
7.1.2 The Point-Spread Function and the PSDM filter 59
7.1.3 Dip and azimuth of illumination vectors 60
7.2 Change in wavelet (frequency) 61
7.2.1 The seismic images and the reflectivity 61
7.2.2 The Point-Spread Function 68
7.2.3 Dip and azimuth of illumination vectors 69
7.3 Change of incident angle 70
7.3.1 The seismic image and the reflectivity 70
7.3.2 The Point-Spread Function 75
7.3.3 Dip and azimuth of the illuminated vectors 76
7.4 When is the plume not visible on the seismic? 77
7.4.1 The seismic image and Point-Spread Function with 30 Hz 78
7.4.2 The seismic image and Point-Spread Function with 60 Hz 87
7.4.3 Dip and azimuth of illumination vectors 96
8 Discussion 97
8.1 Change in acoustic velocities 97
8.1.1 Reflectivity coefficient 97
8.2 Change in wavelet (frequency) 101
8.2.1 Sampling 101
8.2.2 Resolution 102
8.2.3 The seismic result compared to seismic data from Sleipner 107
8.3 Change of incident angle 108

8.3.1 Reflection coefficient 108
8.3.2 Resolution 109
8.3.3 Dip and azimuth of illumination vectors 111
8.4 When is the plume not visible on the seismic? 112
8.4.1 Resolution 112
8.4.2 Plot of illumination vectors compared to depth 117
8.4.3 Could we avoid diffractions? 117
9 Summary and conclusion 119
References 121
Appendix A ..... - 124 -
Appendix B ..... - 137 -
Appendix C ..... - 145 -

1 Introduction

Carbon capture and storage (CCS) subsurface is one technique to help reduce the amount of CO_2 emissions to the atmosphere. Use of fossil fuels for power generations will increase the amount of CO_2 emissions, but capture of CO_2 in the produced natural gas will help mitigate the emissions. When the CO_2 is captured and stored in subsurface reservoirs it is important to monitor the behavior of the CO_2 plume. Monitoring of subsurface seismic amplitudes is important to avoid leakage of CO_2 into the sea and atmosphere and to monitor how the plume will develop over time. The most common technique is time-lapse seismic analysis and this technique is based on 4D seismic, meaning acquisition of the same survey and parameters over a period of time.

The primary objective for this paper is to get a better understanding of seismic amplitude anomalies associated with subsurface storage of CO_2 over time. Several models with varying size of the plume and different saturation of CO_2 will be created. Some of these models will be used in modeling with varying source frequency and incident angle, and other to estimate when the plume cannot be detected on seismic data. The models are hypothetical, but the whole background model is based on data from the CO_2 injection site called Sleipner in the North Sea of Norway, in order to get a realistic setting of the modeling.

Seismic modeling is important in the seismic data acquisition process to give the best possible results considering what the main target is. If the seismic interpreter has problems interpreting the real data, synthetic seismic with known properties can be used for comparison. With modeling, it is possible to test different survey parameters, like spacing of the shots/receivers, frequencies and different offsets. All these parameters will play a vital role in the resulting seismic.

1.1 What is CCS?

CCS stands for CO_2 capture and storage, and according to (IPCC, 2005) the definition is as follows:

> *"Carbon dioxide (CO_2) capture and storage (CCS) is a process consisting of the separation of CO_2 from industrial and energy-related sources, transport to a storage location and long-term isolation from the atmosphere"*

The most common way to store the CO_2 is in geological formations subsurface or onshore. This can be done in depleted oil and gas fields, saline aquifers and unminable coal beds. Other ways to store CO_2 is ocean storage and industrial storage (Figure 1.1) (IPCC, 2005).

The principal of ocean storage is direct release of the CO_2 into the ocean, but this is not considered a good storage options over longer periods (or good for the environment at the

seafloor). Another method is industrial storing, where the CO_2 goes through chemical reactions forming carbonates.

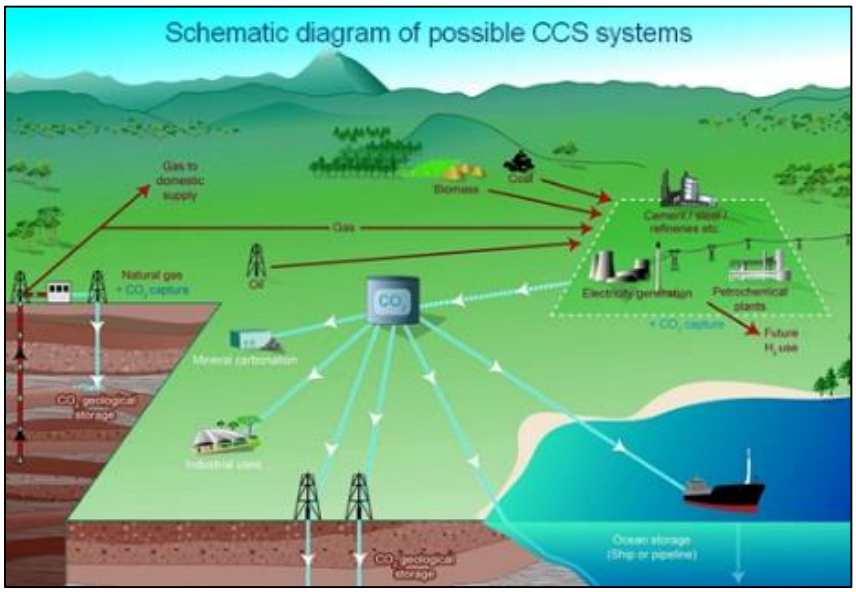

Figure 1.1 Possible CCS systems. From: (IPCC, 2005).

CO_2 can be used in EOR (Enhanced Oil Recovery), and in enhanced coal bed methane recovery (Figure 1.2), and this will be both economical for the producing company and help mitigate the CO_2 release. As mentioned is geological formation the most common way of storing CO2, and this thesis will build on that.

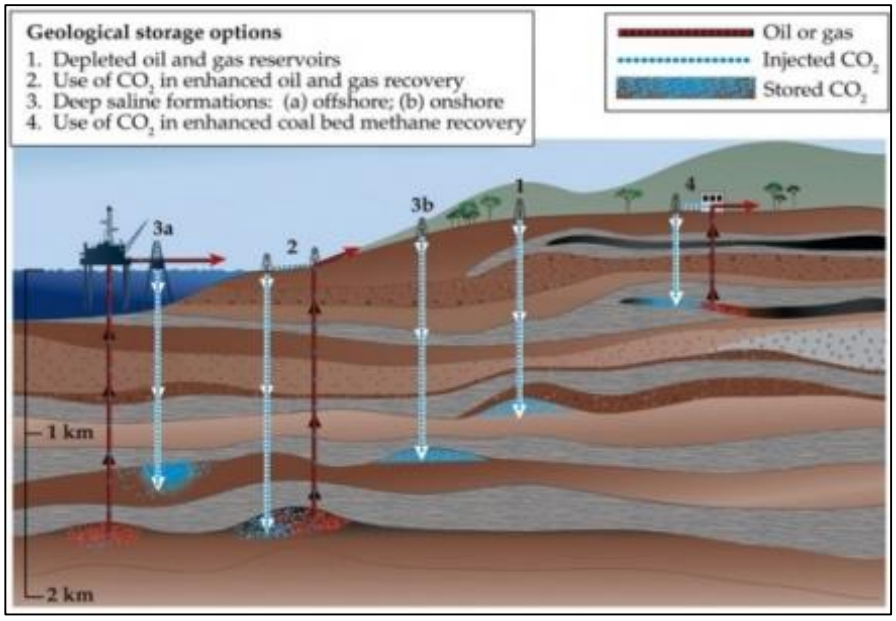

Figure 1.2 Geological storage options of CO_2 like depleted oil and gas fields and saline formations. From: (IPCC, 2005).

1.2 Why CCS?

In the earlier days, people did not know much about the effect greenhouse gases have on the climate. Greenhouse gases was released without thinking about the future consequence, but after a while, a link was found between the amount of greenhouse gases in the atmosphere and the global surface temperature. Figure 1.3 illustrate the concept of the greenhouse effect where the Earth's atmosphere is acting as a greenhouse. Solar radiation consist of short waved UV-light penetrating into the Earth's atmosphere, then the Earth absorb some of the heat before long waved infrared-light is reflected back. Greenhouse gases in the atmosphere reflect some of IR-light back to the Earth's surface, and the temperature on the surface rises. The greenhouse gas CO_2 is the major topic of this thesis, but it is important to mention other gases as well. These other gases is Nitrous oxide (N_2O), Methane (CH_4), Hydrofluorocarbons (HFC_S), Perfluorcarbons (PFC_S) and Sulfur hexafluoride (SF_6). Overall these gases in the atmosphere have increased with 70 % from 1970 to 2004 (IPCC, 2007).

The concentration of CO_2 in the atmosphere has varied over many years. To take an example the concentration has varied from 180 parts per million by volume (ppmv) to 280 ppmv (Bruant et al., 2002). The climate at the actual time can be an explanation for this variation because oceans is a huge carbon sink. After the industrial revolution, the amount of CO_2 increased rapidly to an amount of 370 ppmv (Bruant et al., 2002) due to increase of fossil fuels for power generation, and fossil fuels is a huge emitter of CO_2.

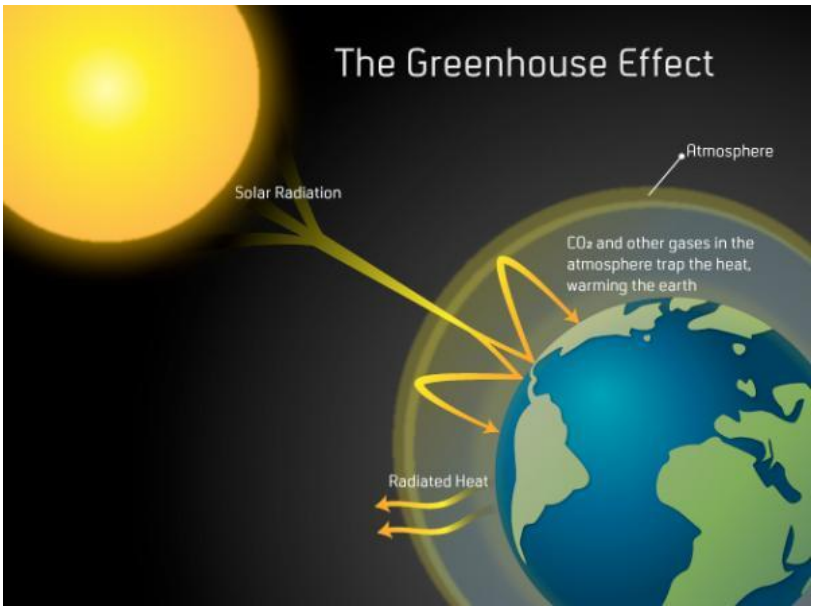

Figure 1.3 The Greenhouse Effect. Solar radiation (shortwave) goes through the Earth's atmosphere and reflected as radiated heat (longwave). Some of the reflected heat are trapped in the atmosphere by greenhouse gases like CO_2. From: (thehigherlearning.com, 2014).

Because of the high increase of CO_2 and global warming, the European Union has a goal of limiting the increase of global temperature by 2 degrees within 2050 (2DS). To accomplish this they have a goal of reducing the emissions of greenhouse gases by 20 %, compared to the level of CO_2 in 1990 (Böhringer et al., 2009). One of the way to do this is by capturing and storing CO_2 in geological reservoirs subsurface both onshore and offshore.

Recently the Norwegian government has set a new goal to decrease the emission of greenhouse gases by 40% compared to the level in 1990 within 2030. This is Norway's part of EU's goal of reducing the temperature by 2 degrees.

Other methods to mitigate the CO_2 emissions are: Fuel switching, Nuclear energy, Renewable energy, increase in efficiency in buildings, transport and electricity generation (Bünz et al., 2014, CMI, 2011).

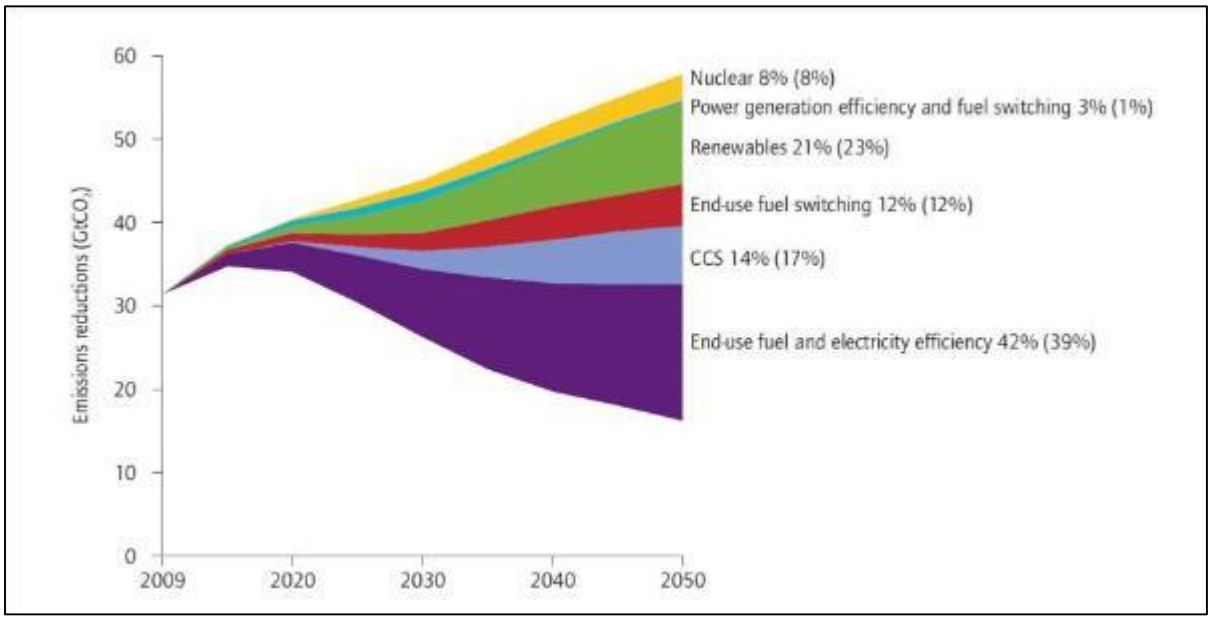

Figure 1.4 Emissions reductions of CO_2 in the future. CCS stands for 14 % (2DS) compared to 17% if the temperature reduction is 6 degrees. From: (OECD/IEA, 2013).

Figure 1.4 illustrate the mitigation options of CO_2 release. These are the numbers they are aiming for, and as you can see, CCS stands for 14 % of the cumulative emissions reductions within 2050 (OECD/IEA, 2013). Due to this, it states that CCS is very important in the future, and hence the monitoring of CO_2 by time-lapse seismic data and seismic modeling is important to get this done in a safe environmental way.

1.3 Storing of CO_2

All over the world there are natural accumulations of CO_2. *"Natural sources of CO_2 include mantle degassing, metamorphism or dissolution of carbonates, oxidation or bacterial degradation of organic matter, an thermal maturation of hydrocarbons"* (Shipton et al., 2004). These natural analogs of CO_2 accumulation are important when deciding a new possible storage site. One can look at the properties and geological structures from the natural reservoirs, and compare these with the observed fluid migration. This will help decrease the possible risk.

The most beneficial way to store CO_2 is in supercritical state (Figure 1.5), and as you can see on Figure 1.5 the volume of CO_2 decreases enormously when going from gas phase to supercritical phase. If we have a thermal gradient of 30 degrees per kilometer downwards and we have a pressure gradient of 10,5 MPa per kilometer. Calculating with a CO_2 density of 1,2 kg/m^3 (standard pressure and temperature) implies that below a depth of 800 m the CO_2 behaves as a supercritical fluid (Bruant et al., 2002, Halland et al., 2011). CO_2 in a supercritical phase has the behavior of a gas phase and the volume of a liquid phase (Halland et al., 2011).

The density of the CO_2 will be smaller than the density of the surrounding reservoir water at shallow depth, less than 5 km (Pruess, 2008). Due to this the molecules of CO_2 will float up in the reservoir (buoyancy effect). The direction of the migration depends on the pressure and permeability. A change in capillary pressure will affect the CO_2 at a much earlier stadium than other fluids. Therefore only a small increase in pressure can make the CO_2 breakthrough the caprock (the capillary pressure is exceeded) (Figure 1.6) (Pearce, 2006).

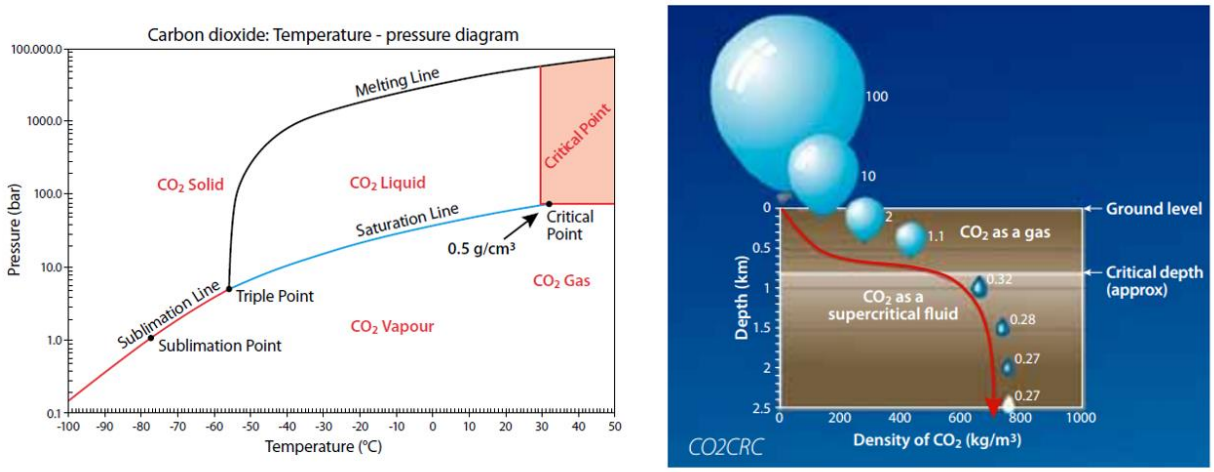

Figure 1.5 Left: CO_2 Temperature – pressure diagram. From: (Halland et al., 2011). Right: CO_2 Depth – density diagram. From: (Halland et al., 2011).

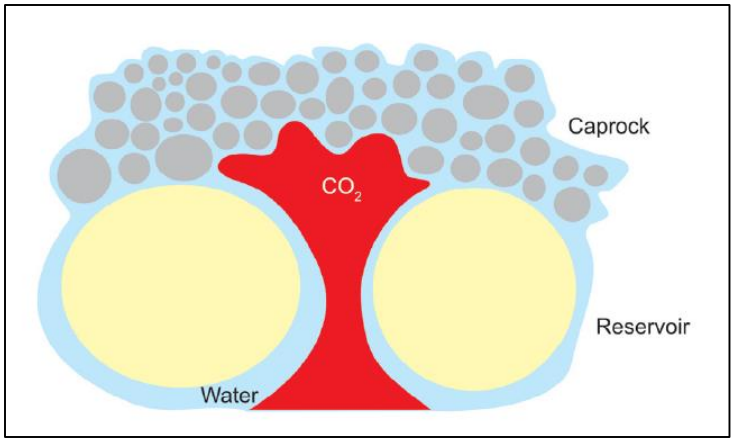

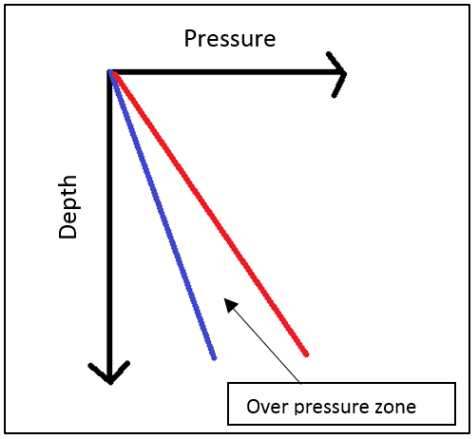

Figure 1.6 Left: CO_2 migration if the capillary pressure is exceeded. From: (Hermanrud et al., 2009). Right: Hydrostatic gradient (blue) and lithostatic gradient (red).

If a leakage occurs from the reservoir, and the CO_2 starts seeping up to the seafloor, the CO_2 molecules will react with H_2O (water) molecules and form carbonic acid. The acid dissolves and the ions of hydrogen decreases the PH-value, and the ocean water gets more acidic (Bünz et al., 2014). This can have a huge impact on plants and animal life at the seafloor. Leakage from a reservoir offshore is therefore not preferable. The same situation will occur in the reservoir, known as solubility trapping (See Chapter 1.3.2).

Microbial organisms convert the CO_2 into CH_4 (methane). This will give an increase in pressure since the compressibility factor for CO_2 is half the size of the compressibility factor for CH_4 (Pruess, 2008). The consequence of increasing pressure is higher risk of leakage. If the CO_2 has escaped from the reservoir and is migrating, it can be self-enhancing. If the reservoir water gets in contact with the migrating CO_2, the water will become acidic. This will decrease the PH value and cause dissolution of minerals, and the migration pathways for the CO_2 become greater since the permeability increases (Pruess, 2008).

The hydrostatic pressure is important to mention, and is defined as the pressure created by the water column above while the lithostatic is pressure created by the weight of the water column and the sediments above. Rapid sedimentation may cause overpressure since the water occupying the pores of the rock does not have time to escape. If the pressure is higher than the capillary entry pressure of the caprock, fluids will break through the caprock and start migrating towards a lower pressure zone. When sedimentation in a normal rate, the pore pressure is always in equilibrium with the hydrostatic pressure, and the water has time to escape.

1.3.1 Reservoir properties for storing CO_2

Deep saline aquifers are probably the best way of storing CO_2 (Halland et al., 2011). The definition of a saline aquifer are a reservoir rock with high porosity and permeability (Bentham and Kirby, 2005). The connection between the grains is important, if the pores are closed or open. Open pores will give higher permeability, and decrease the risk of fracturing of the reservoir rock due to overpressure. The high porosity indicates more empty space between the grains and hence more space for storing CO_2. The permeability allows the stored fluid to migrate within the reservoir rock. When storing in a rock with low permeability the pressure does not have time to stabilize, and this can lead to an overpressure zone close to the injection well (Holloway, 2005).

1.3.2 Trapping mechanisms

Trapping is important to reduce the risk of leakage, and one can have different mechanisms for trapping of CO_2. An effective seal is a required for all different trapping mechanisms. To be an effective seal the rock needs to have low permeability, and the best example is the shale.

The most common trapping is the structural and stratigraphic trapping. The geometry of structural trapping is formed after deposition, and includes structures like anticlines and faults. Stratigraphic trapping geometry is related to the change in lithology, like pinch-out traps and reefs. Residual trapping is another form off trapping, and this phase occurs not long after injection. The definition of this mechanism is as follows; Small droplets of CO_2 are left behind when the CO_2 migrates inside the reservoir.

Over time, the physical and chemical properties of the reservoir play an important part of the storage security (IPCC, 2005). It occurs solubility trapping and mineral trapping. CO_2 dissolves in water and the water with dissolved CO_2 is denser than the water without CO_2. Due to this, the water with CO_2 sinks down to the bottom of the reservoir, decreasing the possibility of leakage (solubility trapping). After a longer period, the water with dissolved CO_2 will react with minerals in the reservoir rock and create carbonate minerals (mineral trapping). This is the most secure trapping mechanisms to store CO_2, but it takes a very long period of time to reach this state (Figure 1.7). Section from (Halland et al., 2011, Selley, 1998).

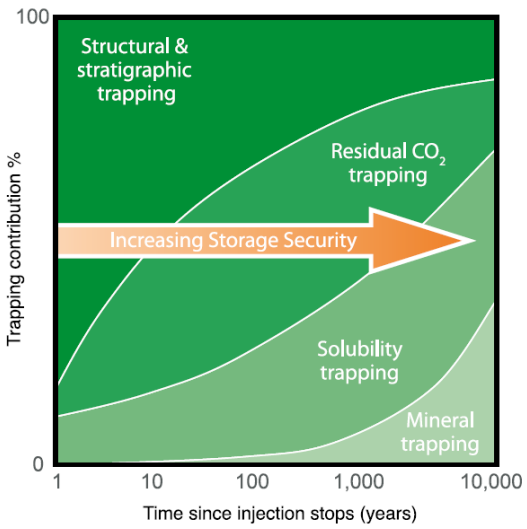

Figure 1.7 Storage security. Increasing from left to right with increasing time period. From: (IPCC, 2005)

1.3.3 Time-lapse seismic monitoring

Monitoring of reservoirs is important to follow the development of fluid migration during production or injection. During production it is beneficial to see where the rest of the hydrocarbons have migrated, to achieve higher recovery numbers. During injection of CO_2, it is important to see how the plume develops and migrates, to help prevent a possible leakage.

It exists several different methods used in time-lapse seismic monitoring, like amplitude changes and AVO/AVA-analysis (Chapter 2.3.2)(Mikkelsen, 2009). Other methods available for monitoring of reservoirs can be seen in Figure 1.8.

During **amplitude-based seismic monitoring,** is the task to detect differences in seismic anomalies in the new seismic acquisition compared to earlier. This is known as time-lapse seismic data (known as 4D data), and it is the most efficient method in use. Repeated acquisition of seismic data with the same survey parameters is required to get 4D data. Seismic is based on TWT (two-way-traveltime), and many parameters can influence this time. During production the porosity may change and also the hydrocarbon saturation, and these are parameters affecting the acoustic velocity. During injection of CO_2 the texture of the reservoir may change due to reaction between the CO_2 and surrounding minerals. This will lead to different porosity, and influence the acoustic velocity. The increase of CO_2 saturation will also influence the velocity since the density of CO_2 is lower compared to the surrounding reservoir water. All these things will affect the TWT, and it is not an easy task to exactly determine what is changing the TWT. Chapter 3.1 will inform that the Gassmann equation could be used to calculate the acoustic velocity due to different saturation of fluids. The physics are well developed, but if we do not know the fluid type we run into bigger problems. In this case, seismic modeling is useful. By using modeling with known parameters and fluid types, we can easily compare the results from the modeling to the real data. Section from: (Dvorkin et al., 2014).

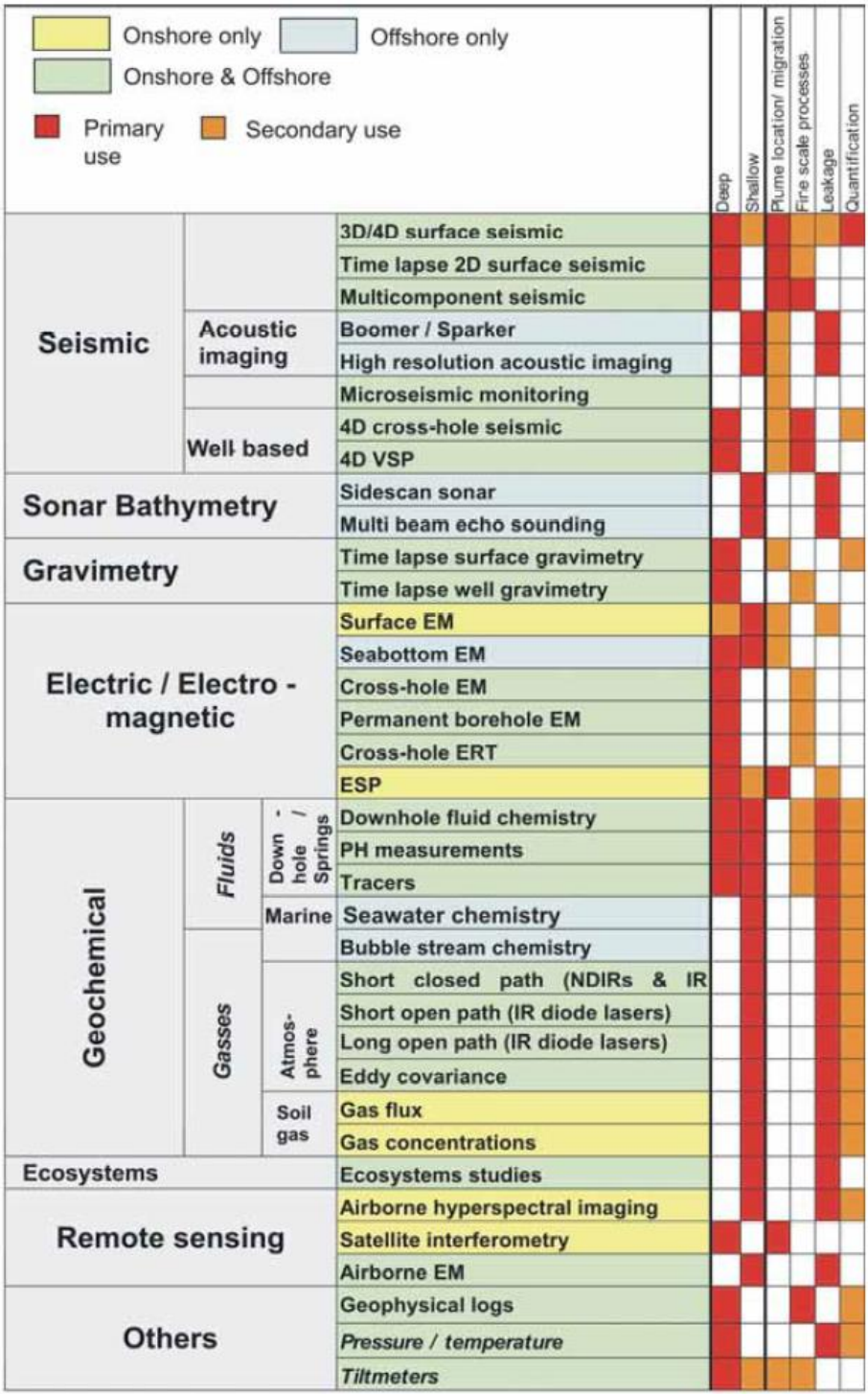

Figure 1.8 Overview of possible ways to monitor CO_2 storage (Chadwick et al., 2008).

2 Basic Geophysics

The following chapter will describe the basics within geophysics like impedance, Snell's law and resolution.

2.1 Acoustic impedance and reflection coefficient

Seismic is the signals reflected from the subsurface layers of the Earth. These reflections help us understand the geological history, and play an important role in the oil and gas industry. The reasons for these reflections are contrasts in the acoustic impedance between the layers. The acoustic impedance Z is a product of the density and the traveling velocity of the material in the subsurface (Dvorkin et al., 2014):

$$Z = \rho \cdot V \qquad \textit{Equation 2.1}$$

Where ρ is defined as the density and V is the P-velocity or the S-velocity.

The reflection coefficient of normal incidence, R is defined by the following equation from (Dvorkin et al., 2014):

$$R = \frac{(Z_2 - Z_1)}{(Z_2 + Z_1)} = \frac{(\rho_2 V_2 - \rho_1 V_1)}{(\rho_2 V_2 + \rho_1 V_1)} \qquad \textit{Equation 2.2}$$

Where Z_1 is the acoustic impedance in layer number 1, and Z_2 is the acoustic impedance in layer 2. The reflection coefficient can both be negative and positive. If the coefficient is positive, it is an indication of Z_1<Z_2, and opposite, if Z_1>$Z_2$the coefficient would be negative. A positive coefficient means that most of the energy is reflected, and a negative coefficient implies that most of the energy is transmitted into layer 2. This equation can be applied both for the S-velocities and the P-velocities.

2.2 Snell's law

Snell's law will provide information how the ray will behave at an interface and is defined by the following equation from (Andreassen, 2009):

$$\frac{sin\theta_i}{V_1} = \frac{sin\theta_t}{V_2} = \frac{sin\theta_r}{V_1} \qquad \textit{Equation 2.3}$$

Where V_1 and V_2 are the seismic travelling velocities in layer 1 and layer 2. θ_i is the angle of incidence, θ_t is the angle of the transmitted ray and θ_r is the angle of the reflected ray.

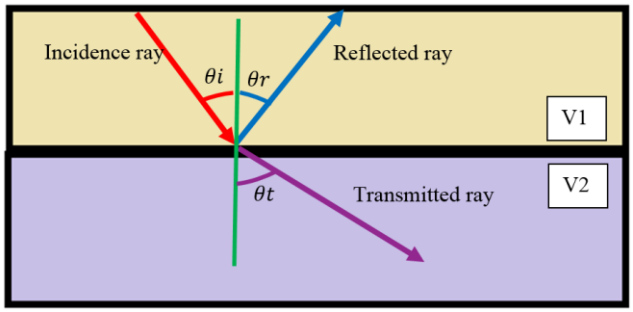

Figure 2.1 Visualization of Snell's law.

Figure 2.1 shows the visualization of the Snell's law. In this case, the velocity V_2 is larger than velocity V_1, and hence the transmitted angle is larger than the incident angle. In the opposite way, that velocity V_1 is larger than velocity V_2, then the transmitted angle would bend toward the green line, and the angle is now smaller than the incident angle. The most common event is that V_2>V_1, since the velocity tends to increase downwards in the subsurface due to compaction of the sediments (Andreassen, 2009).

A normal incident P-wave will not produce any S-waves only the transmitted P-wave and the reflected P-wave. In the case where we have a non-zero incident angle the P-wave will in addition reflect and transmit S-waves. S-waves, will also reflect and transmit P-waves.

2.3 Seismic amplitude effects

This subchapter will describe the seismic amplitude effects from attenuation of seismic energy and how the amplitude changes with increasing offset/angle.

2.3.1 Attenuation of seismic energy

The seismic amplitude and energy in the seismic wave will decrease in depth (the frequency will decrease). Different factors can cause this to happen, like geometric spreading, absorption and intrinsic attenuation (Andreassen, 2009).

Geometric spreading is when the radius of the seismic wave sphere increase due to geometric spreading. The seismic amplitude will decrease proportionally with the increasing factor of the radius.

Absorption is when the seismic energy is translated into heat and or non-elastic behavior of the rock. The new amplitude (A) at distance x (from the original point) is expressed by following equation:

$$A = A^0 e^{-\alpha x} \qquad \textit{Equation 2.4}$$

Where $A^0$is the amplitude at the starting point (shot point) and α is recognized as the attenuation coefficient. Q is equal to the quality/dissipation factor, and can be expressed by following equation using the attenuation coefficient:

$$Q = \frac{\pi f}{\alpha V} \qquad \textit{Equation 2.5}$$

Where;

f = frequency
α = attenuation coefficient
V = acoustic velocity

The dissipation factor can be found in tables for different rock types.

Intrinsic attenuation is when the amplitude decrease due to mode conversions (P-wave to S-wave and S-wave to P-wave), reflections, refractions (when the wave runs along the interface) and scattering of energy. These factors will lead to loss of seismic energy, and this will in turn lead to increase in the wavelength. The amplitude will decrease due to the increase in the wavelength. Scattering of energy occurs when the wavelength is larger than the scattering point, and the energy is scattered in all directions. This is also called diffraction of energy. **Diffraction** is a type of noise in the seismic data, and will occur at abrupt interfaces. The most common case is fault planes, and the diffraction can be recognized as a hyperbolic curve. Section from (Andreassen, 2009).

2.3.2 AVO/AVA-analysis

How the amplitude behaves with increasing offset (Amplitude Versus Offset, AVO) and angle (Amplitude Versus Angle, AVA) is useful to know. These analyses can be used when we only know the change in P-velocity. By using a simplified version of the Zoeppritz equations (1919); Aki and Richards (1980), will make it possible to calculate the reflection coefficient for a P-to-P reflectivity with a non-zero incident angle (θ) (Mavko et al., 1998):

$$Rpp\ (\theta)\ \approx\ \frac{1}{2}\left(\frac{\Delta Vp}{Vp}+\frac{\Delta\rho}{\rho}\right)+\left[\frac{1}{2}\frac{\Delta Vp}{Vp}-2\frac{Vs^2}{Vp^2}\left(\frac{\Delta\rho}{\rho}+2\frac{\Delta Vs}{Vs}\right)\right]sin^2\theta+\ \frac{1}{2}\frac{\Delta Vp}{Vp}\ [tan^2\theta-sin^2\theta] \qquad \textit{Equation 2.6}$$

Where:

$$\Delta\rho\ =\ \rho_2-\rho_1 \qquad \rho\ =\ (\rho_2+\rho_1)/2$$

$$\Delta Vp\ =\ V_{p2}-V_{p1} \qquad Vp\ =\ (V_{p2}+V_{p1})/2$$

$$\Delta Vs\ =\ V_{s2}-V_{s1} \qquad Vs\ =\ (V_{s2}+V_{s1})/2$$

This equation can also be expressed as (Mavko et al., 1998):

$$Rpp\ (\theta)\approx\ R_{P0}+\ B\ sin^2\theta\ +\ C[tan^2\theta-sin^2\theta] \qquad \textit{Equation 2.7}$$

Where;

- R_{P0} is equal to equation X, reflection coefficient for P-to-P reflectivity for a normal incident wave.
- B is referred to the AVO gradient (intermediate offsets)
- C is the gradient at far offsets

The constant B in Equation 2.6, known as the AVO gradient is influenced by the S-velocity. So if we are able to extract the reflection coefficient, can the equation be used to determine the S-velocity. Fluid saturation will not affect the S-velocity very much, but an increase in pore pressure will (due to the effect from pressure to porosity). If we are able to calculate the different S-velocity it can help state if there is fluid change of pressure change in the reservoir, and this will be useful in seismic monitoring (Mikkelsen, 2009).

2.4 Vertical and horizontal resolution

The resolution determines the size of the features detected subsurface by the seismic wave. The resolution can be calculated using the wavelength (λ) defined by following equation (Andreassen, 2009):

$$\lambda = \frac{V}{f} \qquad \textit{Equation 2.8}$$

Where V is the average velocity and f is the frequency**. The vertical resolution** is defined as the wavelength (λ) divided by four (Andreassen, 2009):

$$Vertical\ resolution = \frac{\lambda}{4} \qquad \textit{Equation 2.9}$$

The horizontal resolution for unmigrated sections is defined by the diameter of a Fresnel zone. The Fresnel zone can be explained by the area of a wave first hitting a subsurface reflection (Figure 2.2a). The radius of a Fresnel zone is defined by the following equation from (Andreassen, 2009):

$$rf = \frac{V}{2}\sqrt{\frac{t}{f}} \qquad \textit{Equation 2.10}$$

Where; V = average velocity, t = two-way travel time in seconds, f = dominant frequency in hertz. Since this is the radius, we can skip the division by 2 to get the diameter. Therefore, **the horizontal resolution** is:

$$Horizontal\ resolution = V\sqrt{\frac{t}{f}} \qquad \textit{Equation 2.11}$$

The right picture in Figure 2.2 shows the area of Fresnel zone with low and high frequency. Migration will improve the resolution and especially the horizontal resolution. After migration is the radius of the Fresnel zone approximately equal $\frac{\lambda}{4}$ (Figure 2.3)(Brown, 1999), same as the vertical resolution before and after migration. Low frequency waves penetrate deeper subsurface than high frequency waves. High frequency gives better resolution (Right in Figure 2.2), so is useful when looking at features located at shallower depth.

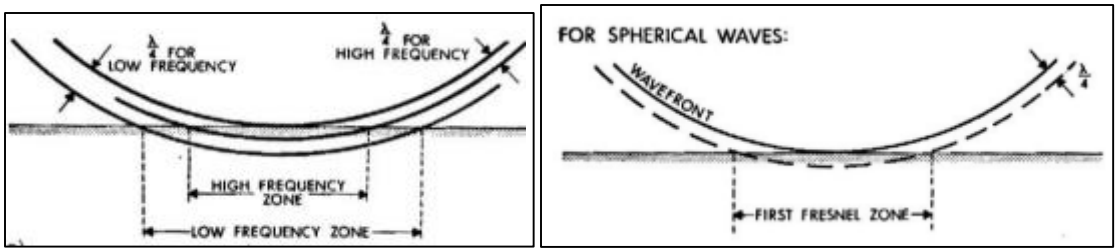

Figure 2.2 Left: First Fresnel zone. Right: High frequency and low frequency. Both from: (Andreassen, 2009)

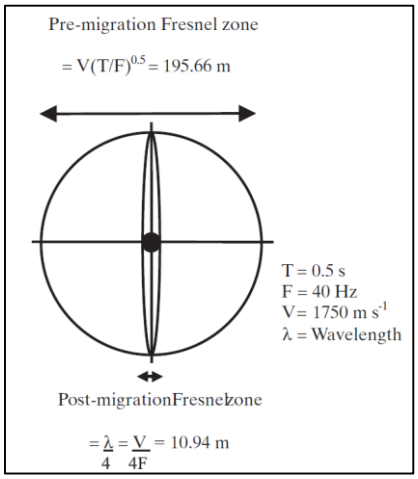

Figure 2.3 Post-migration Fresnel zone, and Pre-migration Fresnel zone. Modified from: (Brown, 1999).

Tuning effect

The left picture in Figure 2.4 illustrate the distance between two acoustic impedance boundaries that will interfere. The term interference can be explained with the following sentences: If the wavelet is longer than the distance from two acoustic impedance boundaries, like the shale-limestone and limestone-shale boundaries in Figure 2.4, the seismic reflections interfere. The interference can both be constructive and destructive (Left in Figure 2.4). The figure shows that a distance of $\frac{\lambda}{2}$ or larger gives no interference while a distance of $\frac{\lambda}{4}$ gives a seismic signal with maximum interference. A part of the wavelength response from the upper and lower interface is overlapping, and improve the seismic signal. This distance of $\frac{\lambda}{4}$ is known as the **tuning thickness or the vertical resolution**. If the distance is smaller than the tuning thickness, the seismic signal still interfere, but the amplitude is not that strong. It is also hard to distinguish the top and bottom interface. If the distance is of thickness $\frac{\lambda}{30}$ or even smaller, the reflection of the two acoustic impedance boundaries does not exist. Section from (Andreassen, 2009).

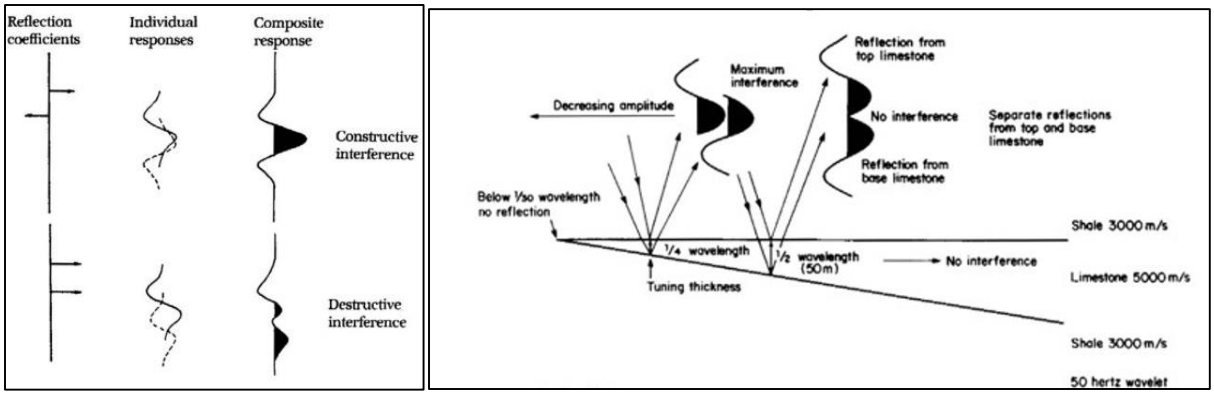

Figure 2.4 Left: Wavelengths effects showing constructive and destructive interference. Left: Interference effects on wedge of two different interfaces with varying thickness. Both picture from: (Andreassen, 2009).

2.5 Seismic response of gas

A gas saturated rock has a lower effective density compared to a water saturated rock. CO_2 in a supercritical phase will have the properties of a gas phase, and it is therefore beneficial to compare the seismic response of gas with the seismic response of CO_2. When a wave propagate into gas filled sediments the acoustic impedance will decrease and create a white trough (Figure 2.5). Opposite, if the acoustic impedance is higher (going from a gas saturated layer to a water saturated layer), the seismic response creates a black peak (Figure 2.5). The bigger the difference is in acoustic impedance between the layers, the bigger the amplitude gets. That is why so-called bright spots on the seismic are often associated with gas accumulations (Figure 2.6 and Figure 2.7) (Andreassen, 2009).

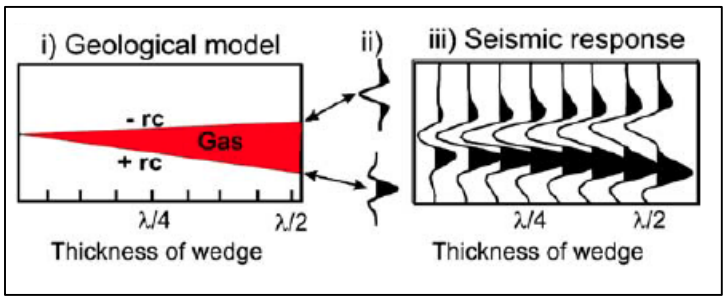

Figure 2.5 Seismic response of gas. From: (Andreassen et al., 2007).

A thick enough gas accumulation will create a flat spot on the seismic under the gas plume (Figure 2.6).

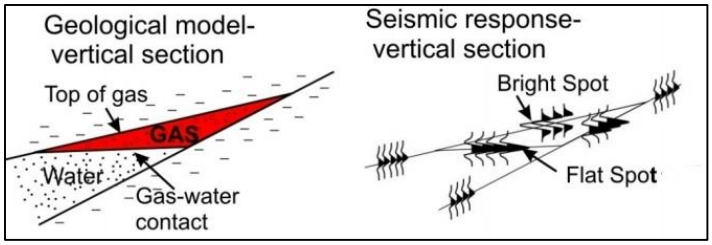

Figure 2.6 Seismic response of gas. Bright spot and flat spot. (Andreassen et al., 2007).

Acoustic masking (Figure 2.7) occurs as the reflection layers are disturbed by the gas. The seismic waves are both scattered (chapter 2.3.1) and absorbed by the gas present, creating a chaotic seismic result.

Velocity pull-down (Figure 2.7) effects occur due to the velocity difference between gas-filled sediments and the surrounding. The gas travels slower through a gas zone, and the two-way travel time for the seismic wave are higher than for the same reflection not located beneath the gas zone. Because of higher travel time, the seismic reflection appears to be deeper than the reality (Andreassen, 2009).

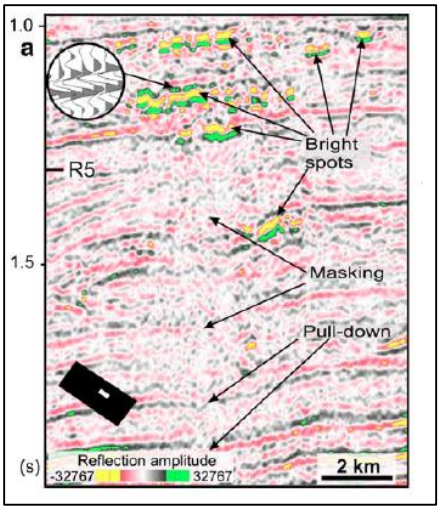

Figure 2.7 Acoustic masking, bright spots and pull-down. (Andreassen et al., 2007)

2.6 Migration

After acquisition of seismic data is completed, the seismic is raw and messy. Several steps are required before we get “clean” seismic, that is possible to interpret and use. One of the steps is called migration.

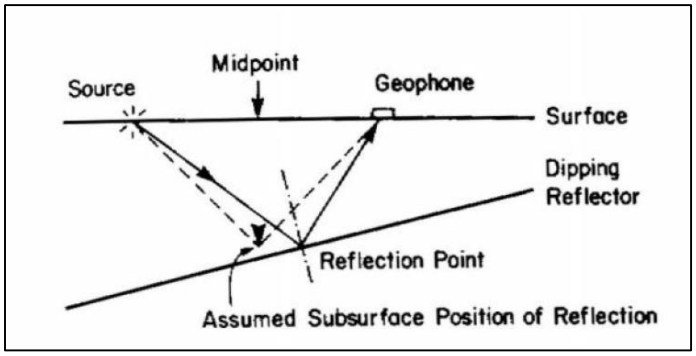

Figure 2.8 Dipping reflector. From: (Andreassen, 2009)

If we have a non-horizontal reflection (Figure 2.8), the signal received at the geophone (in time) are assumed located right below the midpoint, but this is not the case of dipping reflectors. Then we need to migrate the assumed point to the correct location (In depth). This is one reason why we need migration. Migration can be applied before or after the stacking of the seismic, hence pre-stack migration or post-stack migration. Both post-stack time migration and pre-stack depth migration is used during modeling of seismic amplitudes, and methods applying these is described in chapter 4. Section from (Andreassen, 2009, Gelius and Johansen, 2010).

2.6.1 Post-Stack time migration

This is the standard processing technique, and is applied if we have no lateral variations in velocity and if we have layers dipping in the same direction. This is the migration technique represented in the chapter above. To summarize; the post-stack time migration technique will convert a time section of CMP-gathers (Common midpoint) to a depth section with zero-offset to get a more realistic geological model. Section from (Gelius and Johansen, 2010).

2.6.2 Pre-stack Depth Migration (PSDM)

Pre-stack migration on the other hand is useful when the velocity distribution is more complex. Depth migration takes both lateral and vertical changes in velocity into account. PSDM is sensitive to velocities, and needs a good geological model for the overburden. Compared to Post-Stack migration, PSDM takes the overburden parameters into account, the survey geometry is being considered and also the frequency used in the acquisition. Section from (Sheriff and Geldart, 1995, Gelius and Johansen, 2010).

3 Theories of rock physics

This chapter will describe the equations for the elastic properties, the Gassmann equation and provide an insight in how the CO2 affects these parameters.

3.1 Elastic properties

Elastic properties of a rock considered in geophysics are seismic velocities, impedance of both P- and S-waves, Poisson's ratio to porosity, pore fluid and lithology (Dvorkin et al., 2014). In this project paper, I will focus on the P-velocity, S-velocity and pore fluid.

The P-wave velocity (V_p) and the S-wave velocity (V_s) are defined by following equation (Mavko et al., 1998):

$$V_p = \sqrt{\frac{K + \frac{4}{3}\mu}{\rho}} \qquad \textit{Equation 3.1}$$

$$V_s = \sqrt{\frac{\mu}{\rho}} \qquad \textit{Equation 3.2}$$

Where K and μ are defined by the elastic effective parameters; the bulk modulus and the shear modulus, and ρ is the effective density of the rock. Then density can be defined by the following equation (Johansen, 2013):

$$\rho = (1 - \varphi)\,\rho_{matrix} + \varphi\rho_{fluid} \qquad \textit{Equation 3.3}$$

Where ρ is the effective density of the rock, ρ_{matrix} is the density of the matrix, ρ_{fluid} is the density of the fluid, and φ is the porosity of the rock. We can express ρ_{fluid} with following equation (Johansen, 2013):

$$\rho_{fluid} = S_w\rho_w + (1 - S_w)\rho_{CO_2} \qquad \textit{Equation 3.4}$$

Where S_w is the water saturation, and (1-S_w) is the CO_2 saturation (S_{CO_2}).

The dynamic parameters of bulk modulus and shear modulus can be expressed by following equations (Mavko et al., 1998):

$$K = \rho \left(V_p - \frac{4}{3}V_s\right) \qquad \textit{Equation 3.5}$$

$$\mu = \rho {V_s}^2 \qquad \textit{Equation 3.6}$$

The bulk modulus are known as the parameter of the rock to resist volume deformation, and the shear modulus is the resistance to change shape and is defined by the following equations in static condition (f = 0 Hz) (Figure 3.1) (Johansen, 2013):

$$K = \frac{\Delta P}{\Delta V / V} \qquad \textit{Equation 3.7}$$

$$\mu = \frac{P_s}{tan\gamma} \qquad P_s = \frac{F}{A}\text{(Shear stress)} \qquad \textit{Equation 3.8}$$

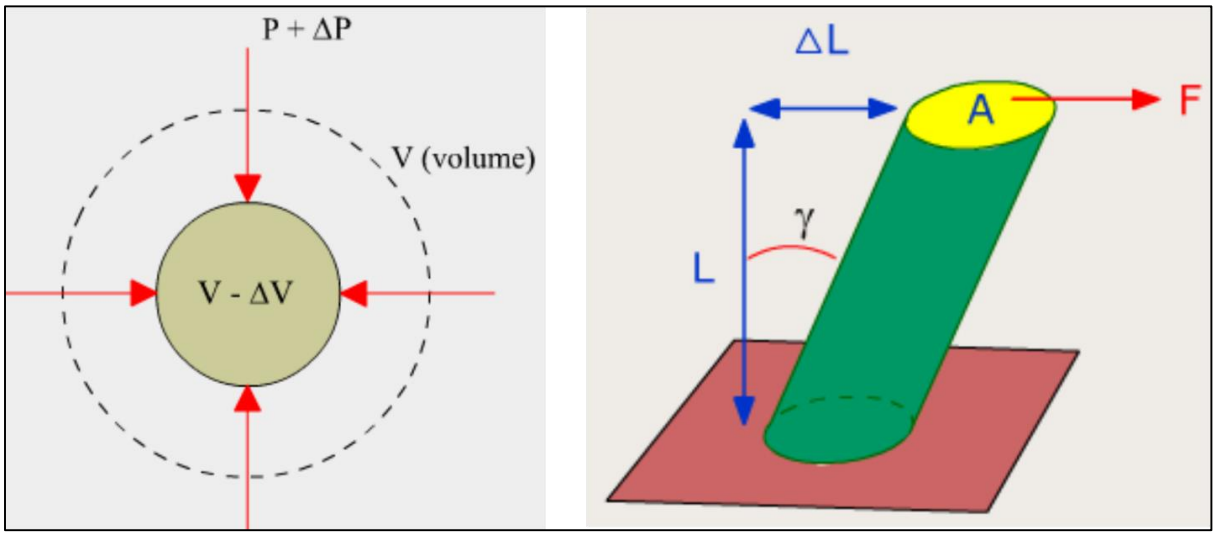

Figure 3.1 Left: Illustration of the static bulk modulus Right: Illustration of the static shear modulus. From (Johansen, 2013, Gelius and Johansen, 2010).

The static equations cannot be used to calculate the acoustic velocities, and more information is needed to be able to do the calculation with the dynamic equations. An equation called Gassmann is used to calculate the effective bulk modulus (K^*) of a rock containing several types of fluids. When knowing the effective bulk modulus it will be easier to calculate the acoustic velocities using the dynamic equations.

The effective bulk modulus can be expressed by the following equation, called the Gassmann Equation (Johansen, 2013):

$$K^* = \frac{Kd\,[-(1+\varphi)+\frac{\varphi Ks}{Kf}]+Ks}{\frac{\varphi Ks}{Kf}-\frac{Kd}{Ks}+(1-\varphi)} \qquad \textit{Equation 3.9}$$

Where; K_d = effective bulk modulus of the dry rock, K_f = effective bulk modulus of the pore fluid, K_s = bulk modulus of the solid/grains, φ = porosity.
The bulk modulus of the pore fluid can be expressed by the following equation (Dvorkin et al., 2014):

$$\frac{1}{K_f} = \frac{S_w}{K_w} + \frac{S_g}{K_g} + \frac{S_l}{K_l} \qquad \textit{Equation 3.10}$$

Where S_w, S_g and S_l is the water saturation, gas saturation and fluid saturation ($S_w + S_g + S_l = 1$). K_w, K_g and K_l are the bulk modulus for the water, the gas (CO_2 in my case) and the fluid available.

The Gassmann equation was formed to help calculate the velocities of a rock influenced by a pore fluid in a static condition (Gelius and Johansen, 2010). Assumptions to filled before using the Gassmann equation are as following from (Mikkelsen, 2009):

- All pores are connected
- All grains have the same physical properties
- The pore fluid is homogenous and fully saturates the pore volume

The effective shear modulus is the same as the shear modulus for a dry rock.

"Since fluids are viscous they have no shear strength (i.e $\mu = 0$*), and pore fluids do generally not affect the overall shear deformation of porous rocks, whenever the pores are connected".* (Gelius and Johansen, 2010).

We can see from these assumptions that the effective shear modulus is equal to the dry rock modulus as the pores are assumed to be connected.

$$\mu^* = \mu_d \qquad \textit{Equation 3.11}$$

When knowing both the effective bulk modulus and shear modulus it is possible to calculate the acoustic velocities using the static equation (Equation 3.5 and Equation 3.6).

3.2 Effects on the elastic properties

Injected CO2 in a supercritical phase will as mentioned have the same properties as a gas phase, and the acoustic velocity will decrease due to lower density than surrounding reservoir water. When injecting CO_2, even small amounts will decrease the velocity with around 30 %. Small bubbles of residual CO_2 will decrease the compressibility of the rock, and the P-velocity will decrease (Arts et al., 2004a). S-waves do not travel in fluid, but in the matrix, so the effect on injected CO_2 will not give noticeable effects on the S-velocity. Pressure will influence the rock porosity and an increase in pore pressure will lead to a decrease in acoustic velocity (Mikkelsen, 2009).

4 Seismic modeling

There are several methods do to seismic modeling like the 1D convolution and PSDM modeling. The normal technique to simulate seismic images used in the oil-industry is the 1D convolution and this method applies post-stack time migration (chapter 2.6.1), and requires no lateral variations in velocity. No lateral variations in velocity is a difficult demand to meet in real life scenarios. The other example mentioned is based on Pre-Stack Depth Migration (chapter 2.6.2) and is useful when both lateral and vertical velocities changes. This method is the one applied in the modeling software, SeisRoX. Compared to older modeling techniques, SeisRoX use a function called SIMPLI 3D PSDM (Simulated Pre-Stack Depth Migration). Using PSDM in the simulator gives a more correct result as the PSDM takes survey geometry, overburden parameters and frequency band into account. The following subchapters will describe the basics of the different migration techniques, and give insight in the SeisRoX modeling algorithm.

4.1 SimPLI PSDM modeling algorithm applied in SeisRoX

This modeling technique uses two different models; the background model and the reservoir model. The **background model** does not need to be very detailed, just a smooth model describing the overburden situation with properties like, P-velocity, S-velocity and density. The **reservoir model** (also called SeisRoX Model) is much more detailed than the background model, and especially around the target area (chapter 6.3.4). This model can also be called the multi-domain model, consisting of domains from the reflectivity, elastic and the geological. It is from this model the reflectivity grid is extracted (Figure 4.4).

This modeling is based on the illumination vectors ($\mathbf{I_{SR}}$) from the background model calculated by ray tracing based techniques (Figure 4.1 and Figure 4.4). From the $\mathbf{I_{SR}}$ we can provide information about the scattering wavenumber vectors, $\mathbf{k_{SR}}$. The $\mathbf{I_{SR}}$ are the result of slowness vectors to the incident wavefield ($\mathbf{P_S}$) and the scattering wavefield ($\mathbf{P_R}$) (Figure 4.1):

$$\mathbf{I_{SR}} = \mathbf{P_S} + \mathbf{P_R} = \frac{\hat{u}\boldsymbol{R} - \hat{u}\boldsymbol{S}}{\boldsymbol{V}} = \frac{\boldsymbol{2cos}(\Theta \boldsymbol{SR}/\boldsymbol{2})}{\boldsymbol{V}} \hat{u}_{SR} \qquad \textit{Equation 4.1}$$

Where $\mathbf{P_S}$ and $\mathbf{P_R}$ are the slowness vectors of the incident and the scattering wavefield as mentioned, and V is the velocity at the point of the incident wave and scattered wave, $\hat{\mathbf{u}}_\mathbf{R}$ and $\hat{\mathbf{u}}_\mathbf{S}$ are unit vectors, $\hat{\mathbf{u}}_\mathbf{SR}$ is the combination of the two unit vectors and $\Theta_{\mathbf{SR}}$ is the opening angle between the incident wave and the scattered wave (Figure 4.1). $\mathbf{I_{SR}}$ will provide information about the subsurface illumination.

If the $\mathbf{l_{SR}}$ is perpendicular to a reflection, this reflection will be illuminated by the survey, and also visible on the resulting seismic image. That is why a range of the $\mathbf{l_{SR}}$ will provide us an image of the azimuth of the visible reflections in the subsurface (Figure 4.2).

The $\mathbf{k_{SR}}$ are parallel to the $\mathbf{l_{SR}}$, and can be found with multiplying the $\mathbf{l_{SR}}$ with the frequency (v):

$$\mathbf{k_{SR}} = v \cdot \mathbf{l_{SR}} = v \cdot (\mathbf{P_S} + \mathbf{P_R}) = \mathbf{k_R} - \mathbf{k_S} = k_R\hat{\mathbf{u}}_\mathbf{R} - k_S\hat{\mathbf{u}}_\mathbf{R} \qquad \textit{Equation 4.2}$$

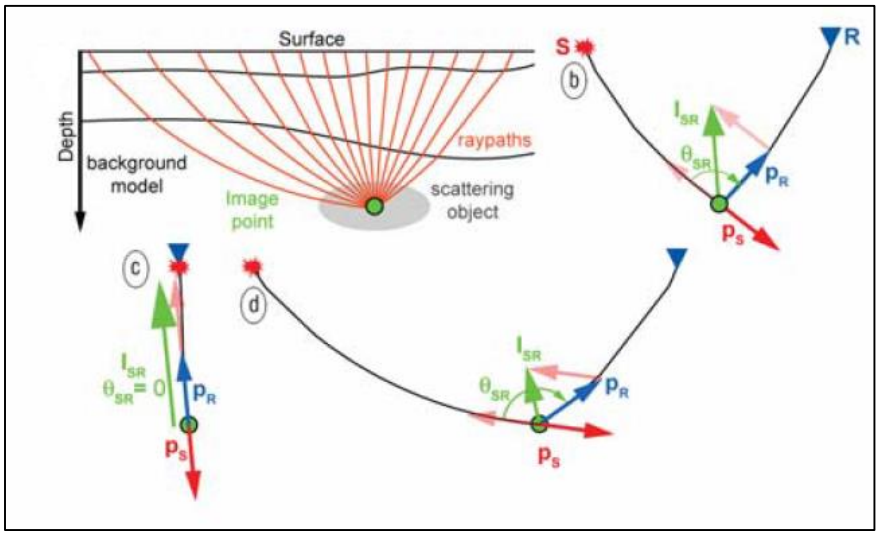

Figure 4.1 Illustration of the Illumination vectors being calculated from the slowness vectors. The distance from the source to the receiver affect the length of the illumination vector. Modified from: (Lecomte, 2008).

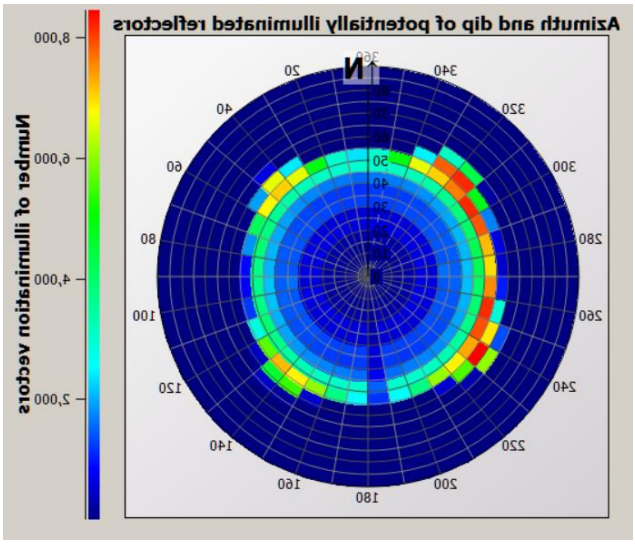

Figure 4.2 Example of the illuminated vectors mapped in the Schmidt diagram showing the angle of dip and azimuth of reflectors visible on the result seismic image. Modified from the SeisRoX manual (NORSAR, 2014a).

The $\mathbf{k_{SR}}$ is very important in calculation of the so-called Point Spread Function (PSF). The $\mathbf{k_{SR}}$ will be calculated for each source-receiver pair for one simple image point (IP). The scattering isochrones (See Appendix B) of the $\mathbf{k_{SR}}$ are constructively interfering at one IP, and destructively interfering elsewhere if everything is correct.

The result is the mapped $\mathbf{k_{SR}}$ vectors in the wavenumber domain for each IP applied with the frequency band. This will give the PSDM filter (earlier called SimPLI filter). This filter is the variation of the mapped vectors at that special IP, but the size of the filter is frequency dependent. The PSF is found by taking the inverse fast Fourier Transform (FFT^{-1}, from wavenumber domain to spatial domain) of the PSDM filter. To summarize this section: Mapping of the $\mathbf{k_{SR}}$ gives the PSDM filter when taking the frequency band into account, and also the PSF when applying FFT-1 (Figure 4.3).

PSDM filter is applied to the reflectivity (extracted from the geological model) (Figure 4.4 and Figure 4.5) in the wavenumber domain to get an image with better resolution, before an FFT^{-1} is applied to get the image in depth domain. The result of this process is the final seismic image. In other words, the seismic image is equal to the reflectivity, but only with a filter.

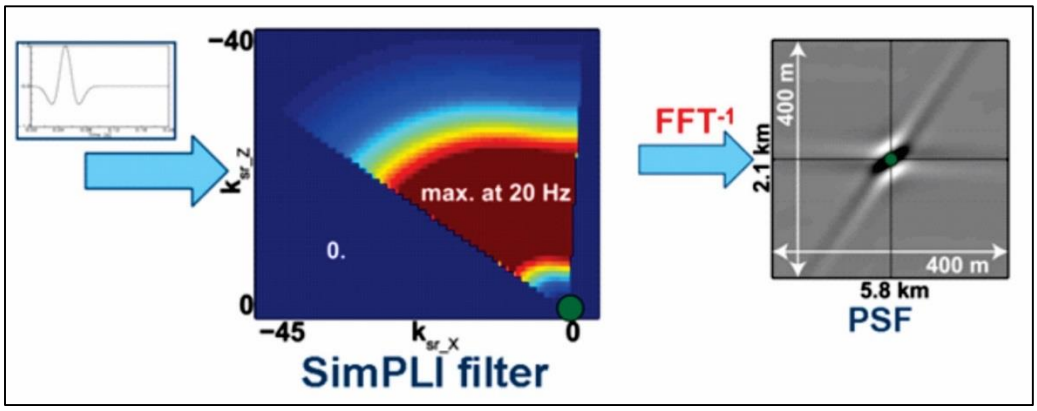

Figure 4.3 The PSDM (SimPLI) filter created from the mapped scattering wavenumber vectors considering a frequency band. The PSF created from an inverse fast Fourier Transform of the PSDM filter. Modified from the SeisRoX manual (NORSAR, 2014a).

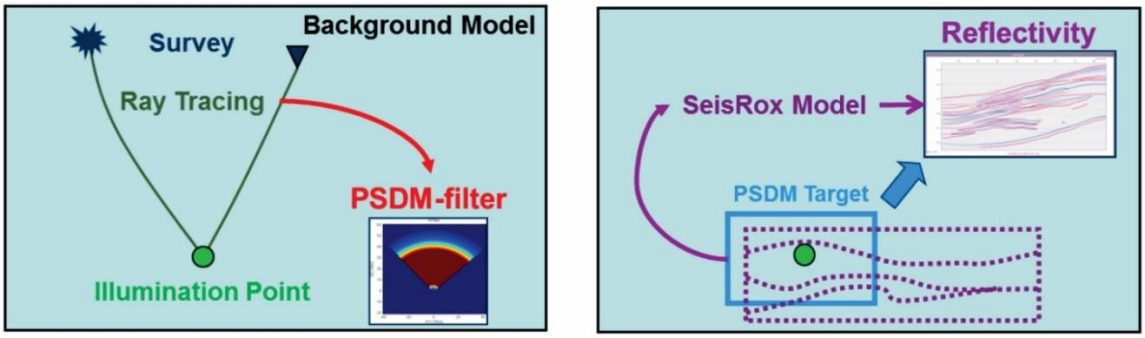

Figure 4.4 Left: The background model is used to create the PSDM filter by using one special IP. Right: The reflectivity is extracted from the reservoir model (SeisRox model) in the target area. Modified from the SeisRoX manual (NORSAR, 2014a).

To summarize the SeisRoX algorithm (Figure 4.4 and Figure 4.5**):**

1. Illumination vectors and scattering wavenumber vectors are calculated by ray based techniques from the background model.
2. Mapping of the scattering wavenumber vectors will provide information of the PSDM filter (old name: SimPLI filter) when applying the frequency band.
3. The PSDM filter will be applied to the reflectivity image obtained from the target area in the reservoir model (also called SeisRoX/multidomain model).
4. The result is the final seismic image after applying the PSDM filter to the reflectivity in the wavenumber domain, before an FFT^{-1} will be applied to get the final image in depth domain.

Chapter from (Lecomte, 2008).

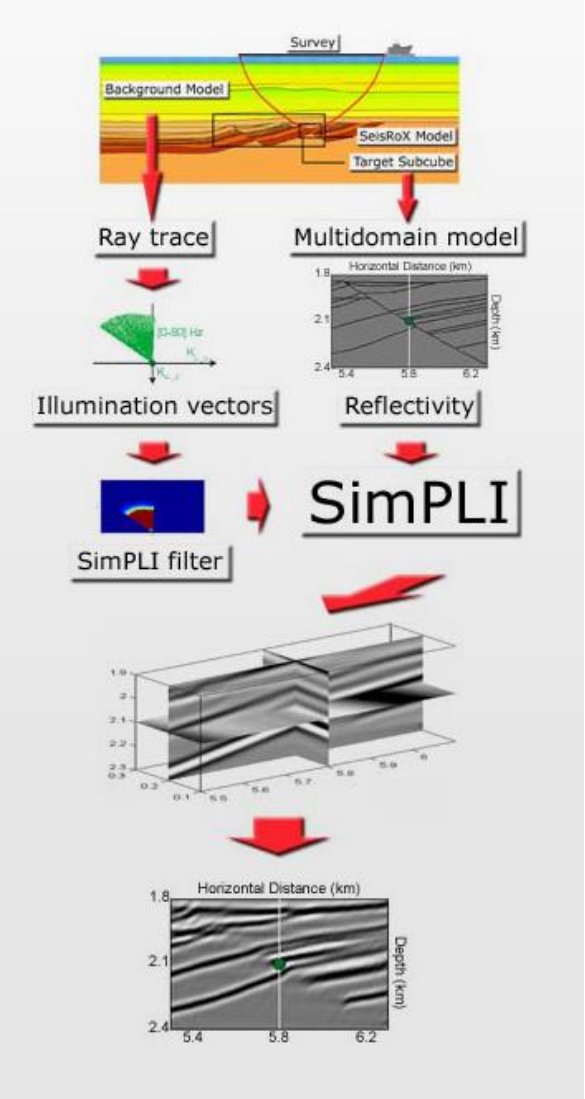

Figure 4.5 The SimPLI workflow. Modified from the NORSAR webpage (NORSAR, 2014b).

4.1.1 Resolution in SeisRoX

The PSF will tell us about the resolution, horizontal and vertical. On Figure 4.6 we can see two different axes, the low resolution (LR) axis, and the high-resolution (HR) axis. The HR axis will give information about what we know as the vertical resolution, and the LR axis information about the horizontal resolution. But as you can see on the image, this is only correct in the left image where we have zero offset survey. That is why these axes are better called cross-reflector resolution (vertical) and lateral resolution (horizontal). Instead of calculating the resolution with the standard formula (Equation 2.9 and Equation 2.11), we get a more correct image of the resolution by looking at the PSF.

The result of PSF is dependent on the size and coverage of the $\mathbf{k_{SR}}$ in the wavenumber domain. The bigger coverage, the better the resolution (vertically and horizontally) in the spatial domain will become. We obtain bigger coverage with a long $\mathbf{k_{SR}}$, and then we also need a small offset between the source and the receiver (Figure 4.1). It is important to mention that the length of $\mathbf{l_{SR}}$ and $\mathbf{k_{SR}}$ is dependent on the opening angle (Θ_{SR}), but the size of the angle is often in relation with the distance of the offset.

The size of the survey, the length of the shot line is very important. If the shot line is to short, we can get aperture effects from the scattering isochrones (Appendix B) since they are interfering best at the middle of the target (illuminated zone). Section from (Lecomte, 2008).

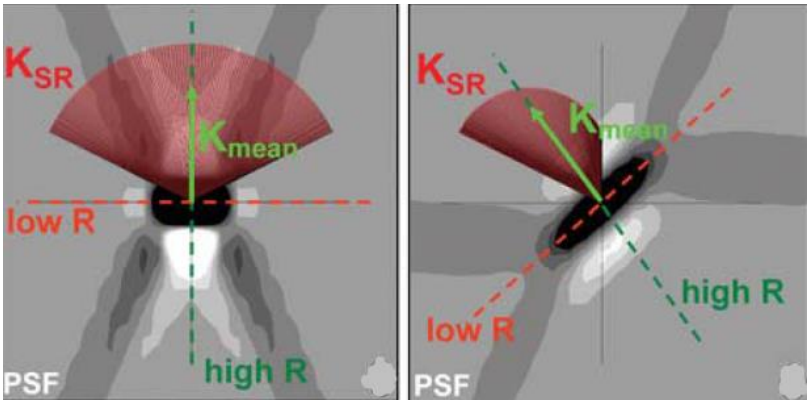

Figure 4.6 The PSF and the mapped $\mathbf{k_{SR}}$ vectors for a zero offset survey (left) and a non-zero offset survey (right). Modified from (Lecomte, 2008).

5 The Sleipner field in the Norwegian North Sea

The following sub chapters will shortly describe the geology of the areas where we find the Sleipner fields (both east and west) and facts about the CO_2-reservoir and the caprock. The first injection of CO_2 found place in 1996 at the Sleipner East field (Arts et al., 2004a), as the first injection plant in the world to help mitigate the CO_2 emissions.

5.1 Geology of the area

The Sleipner filed is located in the Norwegian North Sea (Figure 5.1 and Figure 5.7) and in an area called Sothern Viking Graben (Figure 5.1). The Viking Graben is formed by rifting in the Late Jurassic to Early Cretaceous where the rifting led to rapid sedimentation of shale under an anoxic environment. The result is several known and large hydrocarbon fields, and one of them is Sleipner (Karstens and Berndt, 2015). Figure 5.2 illustrates a geologic time scale, seismic data, and some well logs from the purple star (15/9-11) in Figure 5.1.

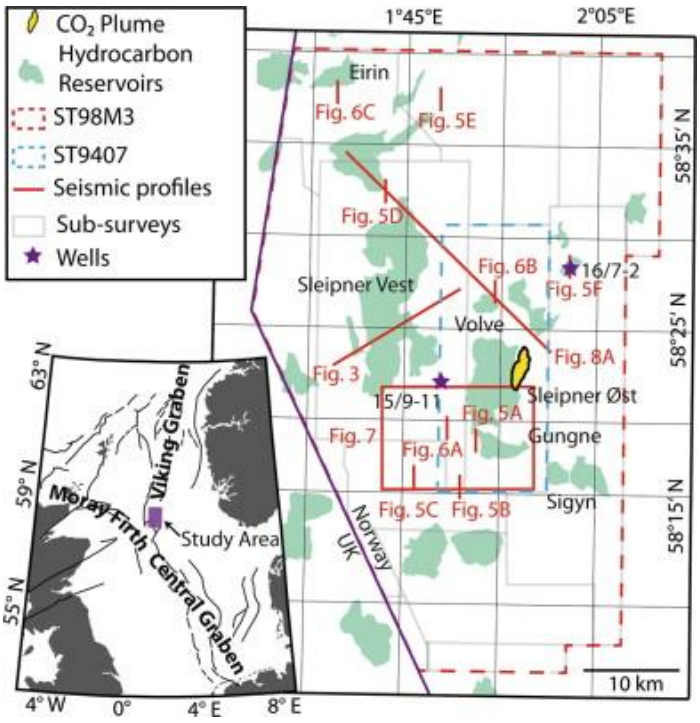

Figure 5.1 The purple box in the picture to the lower left shows the location of the picture to the right. The areas consist of the Sleipner filed among others. The purple star marked with 15/9-11 shows the location of the well in Figure 5.2. The yellow shape illustrates the CO_2 plume in the Sleipner East field. Modified from (Karstens and Berndt, 2015).

The CO_2-injection reservoir is located in the **Utsira formation** in the Sleipner East field, not at the same location as the well in Figure 5.2. The age of the Utsira formation (Figure 5.2 and Figure 5.4) is Mio-Pliocene, and the deposition environment of the Utsira sand (part of the formation) is predicted to be marine with water depths around 100 m (Chadwick et al., 2004b).

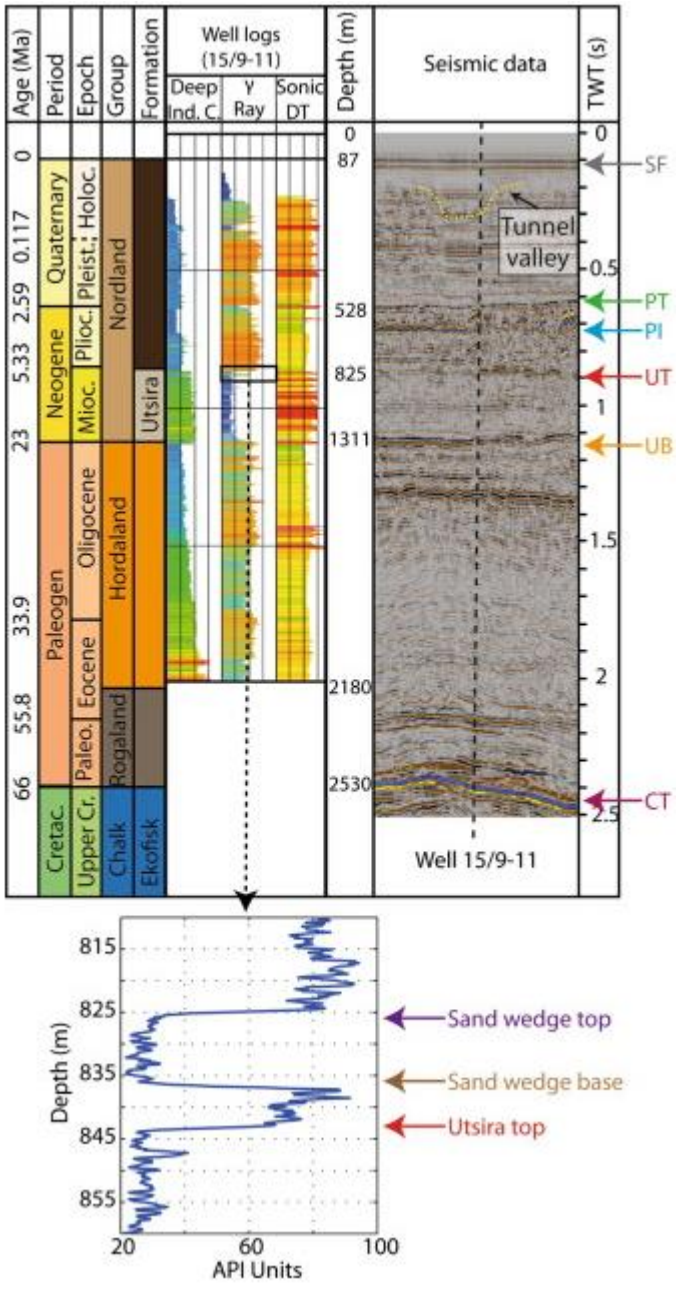

Figure 5.2 The uppermost picture: Geologic time scale, well logs and 2D section of seismic from the area. The lowermost picture: A closer view of the gamma ray response right above the Utsira top showing the presence of the sand wedge. Modified from (Karstens and Berndt, 2015).

The Utsira sand is varying in thickness between 200 and 300 m (Chadwick et al., 2004a), and is about 200 m thick around the injection point and consist of deltaic sand material (Halland et al., 2011). The sand is approximately about 820-1030 m below sea-level (Ghaderi and Landrø, 2009). Due to the marine depositional environment the sand package consist of thin layer of shale in between, ranking from 1-1,5 m thick. About 20 m below the top of the reservoir we find a thicker shale layer, about 5-7 m thick (Figure 5.3) (Arts et al., 2004a). These observations compared to the well log in Figure 5.2 are not exactly the same, and the reason can be the location of the well. From the well logs (Figure 5.2), we observe the Utsira sand to be closer to 300 m thick.

The gamma ray log from Sleipner East at the injection site (Figure 5.3) shows the thin shale layer in the Utsira formation. Gamma ray measures the amount of radioactive material like thorium, uranium and potassium. Shale and source rock material have higher content of these materials than clean sandstone (Rafaelsen, 2013). To be a good storage reservoir the sand must be of high porosity and permeability, and have a huge storage capacity. The Utsira sand fills all this qualifications.

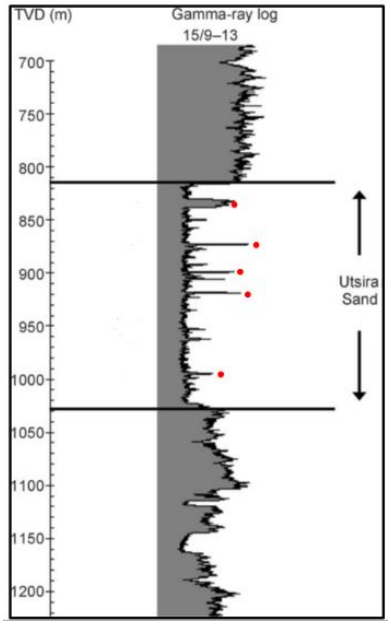

Figure 5.3 Gamma log at the Sleipner injection site. Utsira Sand ranging from 820-1030 m. Red dots shows the outstanding shale layers later used in modeling. Modified from (Ghaderi and Landrø, 2009).

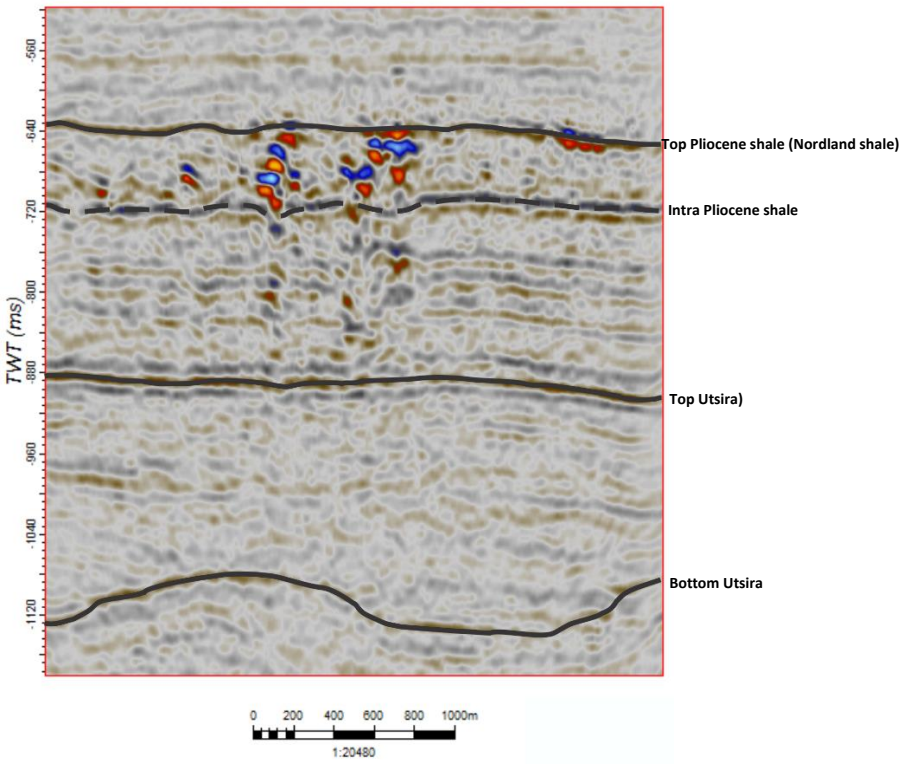

Figure 5.4 Seismic 2D profile from the Sleipner project from east to west. The irregular reflection from the Utsira bottom is interpreted to be mounds formed by the underlying mudstone. Outcrop from a Petrel project.

Figure 5.4 shows that the reflection from Utsira bottom is irregular. The features observed is interpreted to be mounds as a result of the underlying mudstone in the Hordaland group (Figure 5.2) (Karstens and Berndt, 2015).

The formation known as the **caprock** of the CO_2 reservoir is from Pliocene age in the Nordland group, also called the Nordland shale (Figure 5.2 and Figure 5.4). The unit known as the Nordland shale (Pliocene shale) was deposited in a deep marine environment resulting in a low-permeable mudstones with sand in between (Karstens and Berndt, 2015). The unit assumed to be the immediate caprock of the reservoir is about 50-100 m thick, and consist of silty mudstone. The unit above the caprock is coarsening upwards (Chadwick et al., 2004a).

From the well 15/9-11 one can observe a thicker unit (11m) of sand above the Utsira sand, in the Nordland group. It is a 8 m thick package of mudstone between the Utsira sand and the 11m *sand wedge.* Above this sand wedge is the rest of the package known as Nordland shales (Karstens and Berndt, 2015).

5.1.1 Seismic amplitude anomalies observed in the area

Figure 5.5 shows seismic amplitude anomalies as bright spots in the sand wedge, Utsira sand, and the Pliocene shale. Figure 5.6 shows that one can only observe that the Utsira bright spots only occur in the north-east part of the study area, and is not detected above Sleipner East where the injection happens. The bright spots in the Utsira occur close to the top of the formation and is interpreted to be gas accumulations (Karstens and Berndt, 2015). The bright spots in the sand wedge is interpreted to be gas accumulations, same as in the Utsira Sand. In Figure 5.4 and Figure 5.5, one can observe an intra-reservoir shale reflection within the Pliocene shale. Above this reflection, is it seismic anomalies that are chaotic. The same type of anomaly is observed in the Pliocene shale as observed in the sand wedge and the Utsira Sand. Some narrow pipe structures are also visible (Karstens and Berndt, 2015).

Other anomalies observed in Figure 5.6 are type A-anomalies, B-anomalies and C-anomalies. They are recognized respectively as high amplitude vertical reflections, chaotic seismic amplitudes and elongated amplitudes. They are located respectively at TWT (two-way-traveltime) of 50-500 ms, 500-650 ms and the C-anomalies occur at different depths (Karstens and Berndt, 2015).

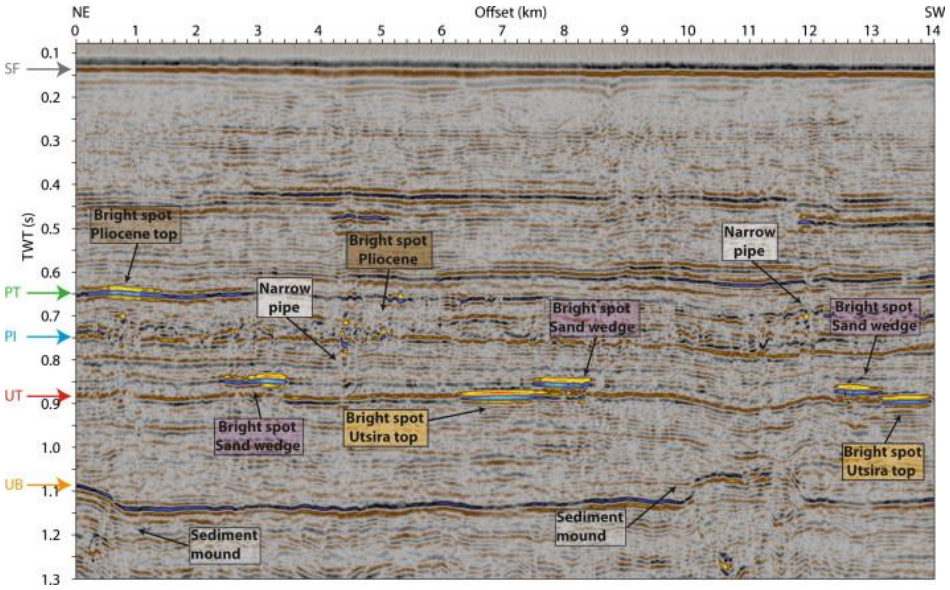

Figure 5.5 2D seismic section announced as the line "Fig. 3" in Figure 5.1 crossing the Sleipner West field. UB = Bottom of Utsira, UT = Top of Utsira, PI = Intra-reservoir shale Pliocene reflection, PT = Top Pliocene shale. The pale purple boxes shows bright spots in the sand wedge, pale yellow boxes shows the bright spots in the Utsira sand, the pale brown boxes show the bright spots in the Pliocene shales (Nordland shales).Features as sediment mounds and pipes are indicated by pale white boxes. From: (Karstens and Berndt, 2015).

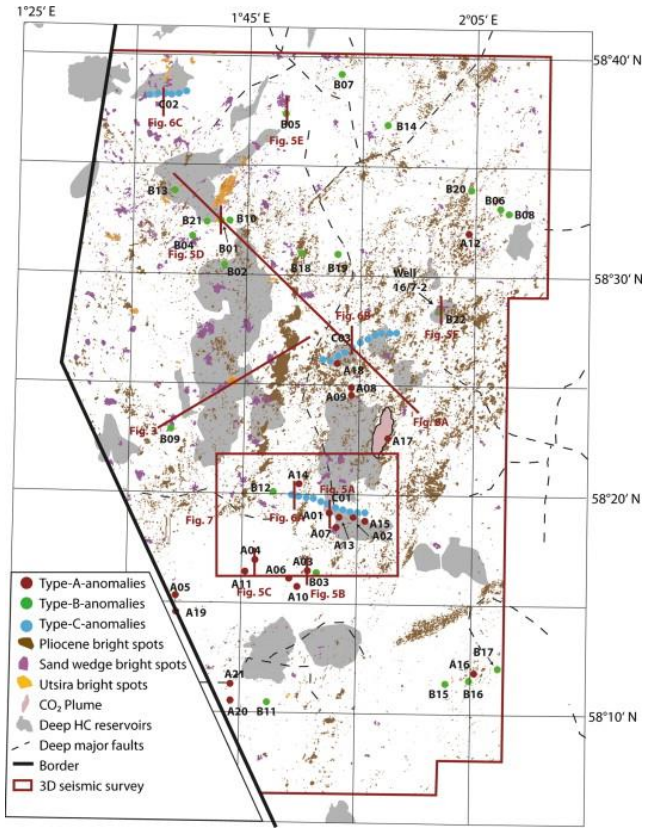

Figure 5.6 The study area showing the location of the A-anomalies (red), B-anomalies (green), C-anomalies (blue), Pliocene bright spots (brown), Sand wedge bright spots (purple), Utsira bright spots (yellow), CO2 plume (light pink), Deep HC reservoir (grey), Deep major faults and 3D seismic surveys used in (Karstens and Berndt, 2015). From: (Karstens and Berndt, 2015).

5.2 CO_2 injection at the Sleipner East field

The Sleipner East field in the North Sea is located 250 km from the coast of Norway (Figure 5.7) (IPCC, 2005). Sleipner East is producing gas/condensate and Sleipner West is producing natural gas, both with Statoil as an operator. The concentrations of CO_2 in the natural gas is too high at the Sleipner West field, so they separate the CO_2 from the gas before the CO_2 is transported by pipeline to the Sleipner East field for injection. Normally they would release the CO_2 into the atmosphere, but in 1991 the Norwegian government implemented tax on the CO_2 emissions. Due to this Statoil and the Sleipner partners started injecting CO_2 both due to economic and environmental reasons in 1996. The water depth at the injections site is about 80 m (Ghaderi and Landrø, 2009) and the injection point is 1010-1013 m below sea level(Arts et al., 2004a). The injection rate is around 1 million tonnes per year and the goal is to store 20 million tonnes (Chadwick et al., 2004a).

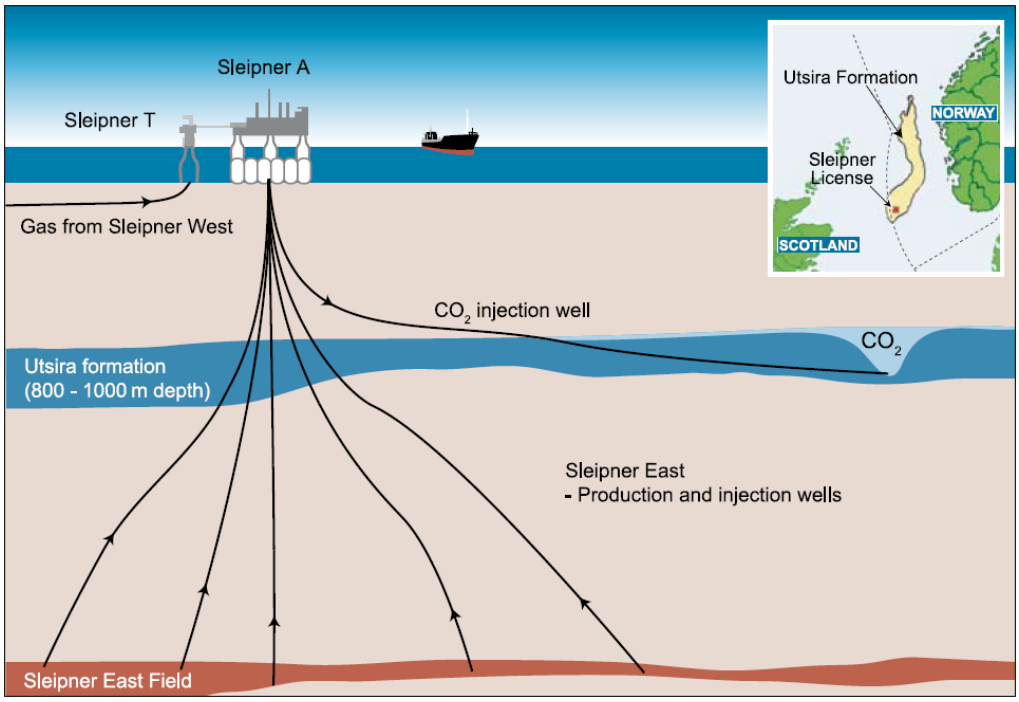

Figure 5.7 The small picture show the location of the Sleipner East field located compared to the Utsira formation and the coast of Norway. The main picture show where the injected formation, Utsira is located. From (IPCC, 2005)

The tuning thickness of a reservoir is important to know. As mentioned on chapter 2.4, a layer with same thickness as the tuning thickness will have constructive interference (Figure 2.4). If the thickness of the plume is thicker than the tuning thickness, the amplitude decreases (Figure 5.8) (Boait et al., 2012). Figure 5.8 is from the Sleipner field where the tuning thickness of a CO_2 plume is about 9 m (Boait et al., 2012). On seismic acquisition before the injection (baseline) in 1994 (Figure 5.9), was it not possible to observe the thin shale layers in the seismic, but after injection of CO_2 they became visible, and this is due to tuning effects from the CO_2 layers between the intra-reservoir shale layers.

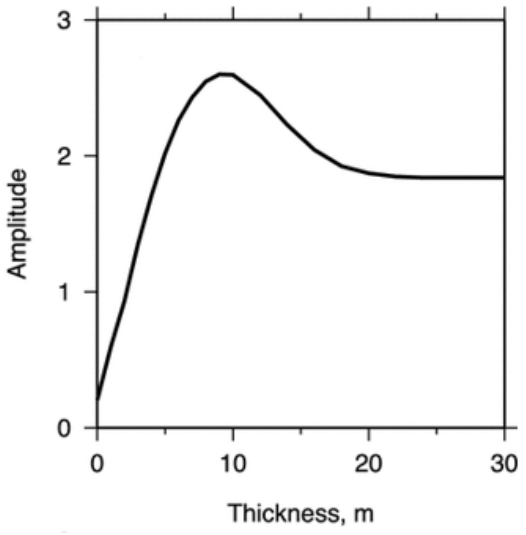

Figure 5.8 Amplitude affected by the thickness of the plume at the Sleipner field. From: (Boait et al., 2012)

5.2.1 Seismic monitoring of the reservoir

Figure 5.9 show the result of time-lapse seismic monitoring at the Sleipner CO_2 field. The pictures are from pre-injection in 1994 up to 2008, 12 years after the first injection. It is important to make a baseline acquisition (1994) of the seismic to have something unaffected to compare with. The plume has developed to be around 200 m high, and has migrated lateral within the reservoir due to the thin shale layers in between. The lowermost picture in Figure 5.9, shows that the plume is elliptical in shape. In 2008 was the maximum horizontal axis about 3 km. Section from (Chadwick and Williams, 2010).

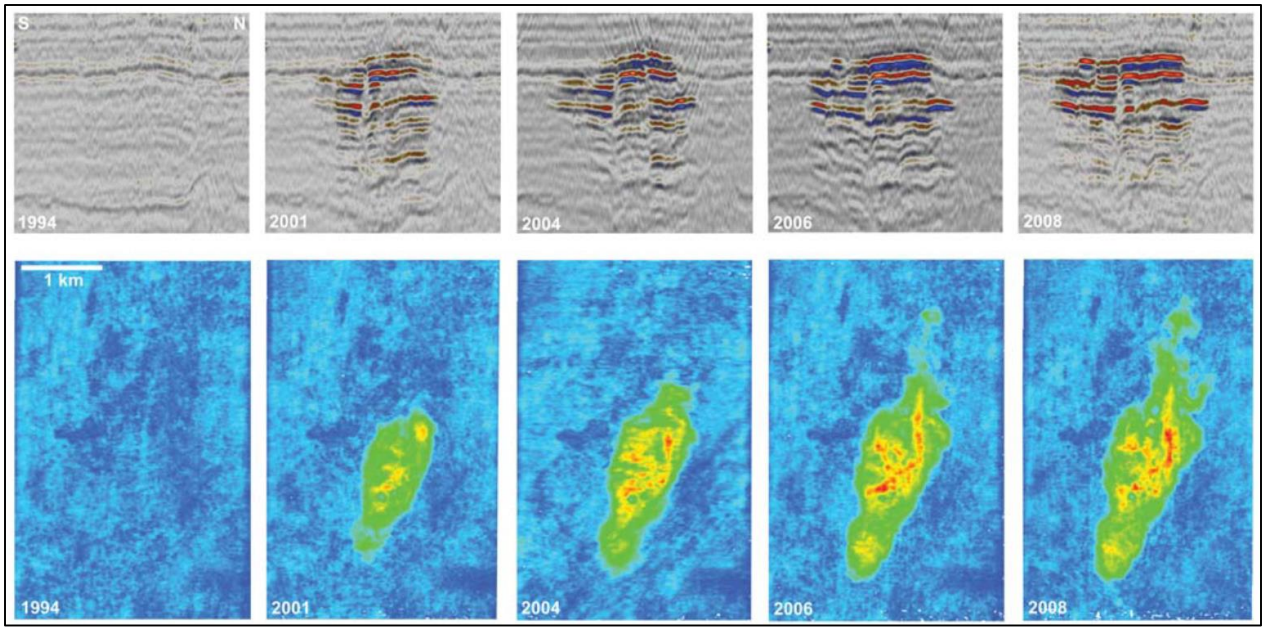

Figure 5.9 Time-lapse amplitudes anomalies from the Utsira reservoir In periods from pre-injection in 1994 to 12 years after the first injection in 2008. Top: Seismic 2D lines in north-south direction. Bottom: Plan view of the amplitude responses of the plume. From: (Chadwick and Williams, 2010).

6 Data and methods

To obtain a modeling project with realistic results, parameters from the Sleipner filed has been used. This can be see in the following sub-chapter. SeisRoX (by NORSAR) was used to simulate the synthetic seismic. Additional softwares like NORSAR 2D and NORSAR 3D were used to create the models.

6.1 Properties from Sleipner used in the modeling

This chapter describes parameters and facts about the caprock and the reservoir used in the calculation of the elastic parameters.

Properties used in the background model:

At the injection site the water depth is about 80 m with a P-velocity of 1480 m/s in the water column (Ghaderi and Landrø, 2009). The P-velocity in the caprock (Pliocene shale) is 2270 m/s, the S-velocity is 850 m/s and the bulk density is 2100 Kg/m^3 (Arts et al., 2004a). These properties are estimated with an uncertainty of 4 %. The acoustic P-velocity in the Utsira sand (with 100% water saturation) is estimated to be 2050 m/s, and the average S-velocity is 643 m/s. The density is in the range of 1960-2080 kg/m^3. The acoustic velocities are only estimates, thus they can vary between 1950-2100 m/s for the P-velocity and 600-680 m/s for the S-velocity (Arts et al., 2004a).

Due to the behavior of the traveling wave in the subsurface, it is important and more realistic to have a linear increasing gradient downwards. Table 6.1 summaries the properties used in the model. Upper unit and lower unit are uncertainties, as they are estimates. They have been calculated with relation of the Pliocene shale (caprock) P-velocity to S-velocity and density.

*Table 6.1 Summary table of the properties used in the **background model.** Depth in meters is below sea-level.*

Layer	P-velocity	S-velocity	Density
Ocean (0-80m)	1480 m/s	0	1000 kg/m^3
Upper unit (80-720m)	2000-2180 m/s	749-816 m/s	1850-2017 kg/m^3
Pliocene Shale (720-820m)	2180-2360 m/s	816-884 m/s	2017-2183 kg/m^3
Utsira Sand (820-1030m)	1950-2100 m/s	600-680 m/s	1960-2080 kg/m^3
Lower unit (1030-2000m)	2200-2500 m/s	824-936 m/s	2035-2313 kg/m^3

Properties used in the reservoir model:

The Utsira sand has high porosity, ranging from 30-42 %, due to weakly cementation. The average value of the porosity is set to be 37 % (Arts et al., 2004a). The bulk modulus and density of CO_2 will vary due to different temperatures. From the article by Ghaderi and Landrø (Ghaderi and Landrø, 2009) we know that the temperature around the injection point will be 37°C, and near the top of the reservoir, the temperature will be around 27°C. Bulk modulus and density of CO_2 at a temperature of 27°C are respectively 0,136 GPa and 800 kg/m3. At a temperature of 37°C the values are 0,064 GPa and 680 GPa. In the modeling properties at 27°C will be used to calculate the acoustic velocities (Appendix A) related to the variation of the CO_2 saturation. All parameters in Table 6.2 are found in the article by Ghaderi and Landrø (Ghaderi and Landrø, 2009), except the shear modulus of dry rock. This value is estimated due to expected results in the calculation (with 100% water saturation). This can contribute to uncertainty in the calculation, but will be discussed in chapter 8.1. Pressure effect on the acoustic velocities at the Sleipner injection site is expected to be small, due to good permeability and no relevant increase in pressure around the injection point (Arts et al., 2004a).

Table 6.2 Summary of constants later used in my reservoir model and calculation of acoustic velocities.

Constants	Value
Porosity (φ)	0,37
Temperature	27 °C
Density of CO_2 (ρ_{CO_2}))	800 kg/m^3
Density of water (ρ_w))	1020 kg/m^3
Density of the matrix (ρ_m)	2650 kg/m^3
Bulk Modulus of CO_2 (K_{CO_2})	0,136 GPa
Bulk Modulus of water (K_w)	2,28 GPa
Bulk Modulus of matrix/solid (K_s)	36,9 GPa
Bulk Modulus of the dry rock (K_d)	2,56 GPa
Shear Modulus of dry rock (μ_d)	0,8569 GPa

6.1.1 Elastic parameters used in the modeling

The reservoir model are not generated with the preferred cycle, by first adding the geological parameters, then use a rock-physics model to calculate the elastic properties, and then calculate the reflectivity using an industry-standard algorithm. The elastic parameters is instead calculated using basic rock physics equations as you can see in Appendix A.

Results of the calculation is listed Table 6.3.

Table 6.3 P-velocity, S-velocity and density for different saturation of CO_2. See Appendix A

Saturation of CO_2	P-Velocity (m/s)	S-Velocity (m/s)	Density (kg/m^3)
0 %	2048	647	2047
10 %	1672	648	2039
20 %	1563	650	2031
30 %	1511	651	2022
40 %	1482	652	2014
50 %	1464	654	2006
60 %	1451	655	1998
70 %	1443	656	1990
80 %	1437	658	1982
90 %	1433	659	1974
100%	1430	660	1966

By comparing the numbers in Table 6.3 with the numbers earlier in this chapter, one can see that the P-velocity and S-velocity with a 100 % water saturation are not the same as first assumed. This is due to uncertainty of the estimated shear modulus of the dry rock during the calculation. Because of this uncertainty, the P-velocity is a bit smaller, and the S-Velocity a bit higher than expected. Instead separate calculations were made to get the velocity for every 10 % increase. The difference is not huge, but can be classified as a small weakness.

Figure 6.1, Figure 6.2 and Figure 6.3 illustrates the variation of the P-velocity, S-velocity and density with different saturations of CO_2.

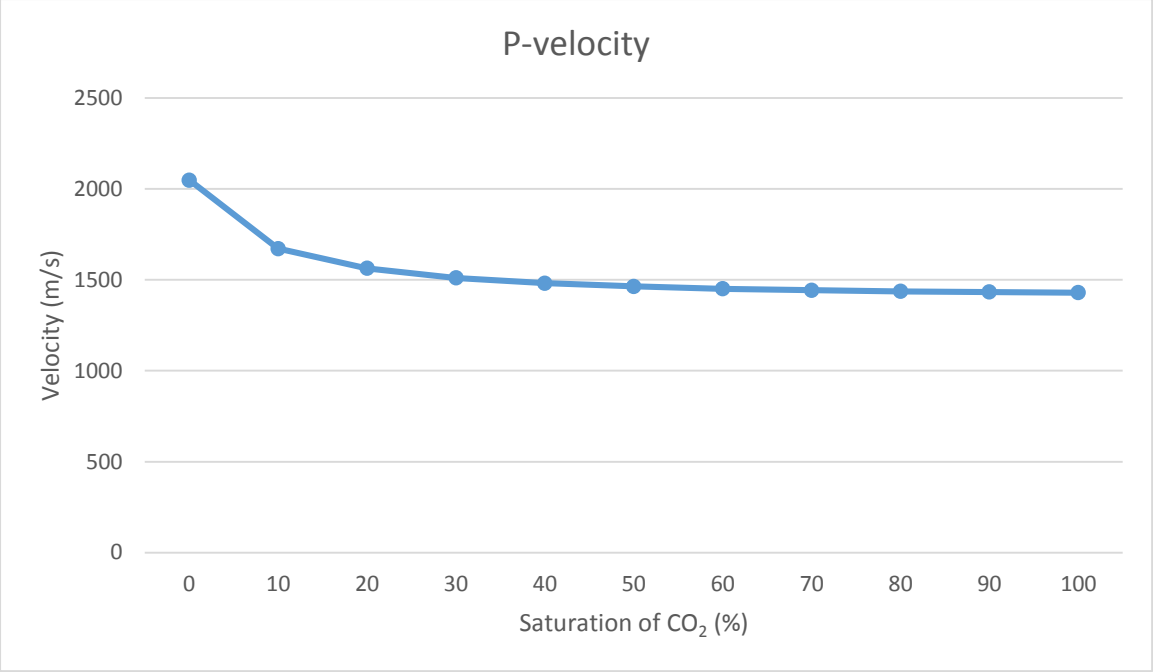

Figure 6.1 Overview of the P-velocity with different CO_2 saturations.

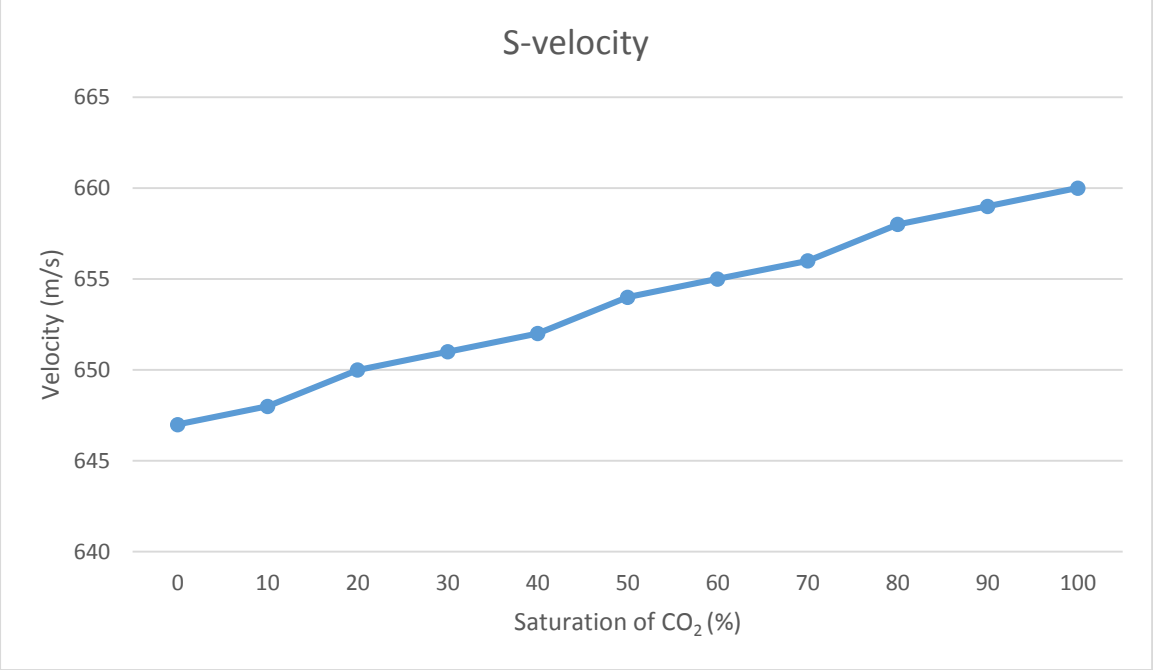

Figure 6.2 Overview of the S-velocity with different CO_2 saturations.

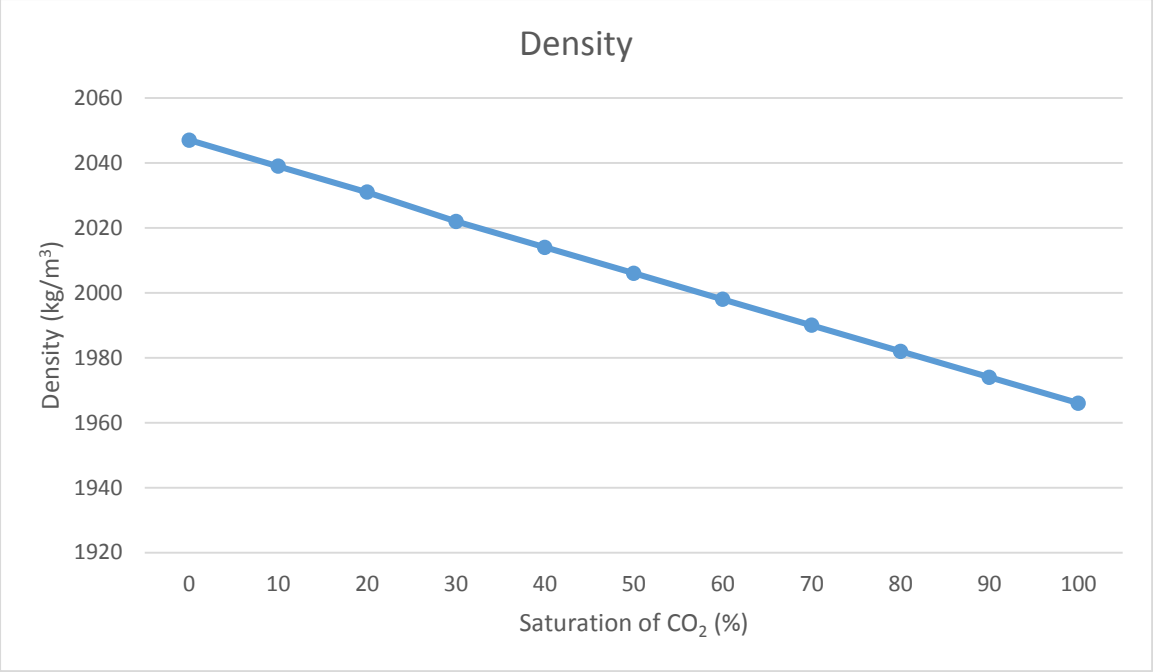

Figure 6.3 Overview of the density with different CO_2 saturations.

6.2 NORSAR 2D and NORSAR 3D

NORSAR 2D and 3D are softwares normally used for seismic ray modeling, but the programs will be used to create the models used in SeisRoX. These softwares are used to get a better understanding of the seismic, and can also be used in teaching to illustrate how the wave propagate with different subsurface models. How to build a model using NORSAR 2D and 3D are shown in Appendix B.

6.3 SeisRoX

SeisRoX is a software used for seismic modeling of geological reservoir models with specific properties, and it easily calculates the seismic response of the reservoir.

SIMPLI 3D PSDM (chapter 4.1) is a technique used when to simulate the seismic response of a target area in the subsurface. This technique requires that the overburden properties are known (Table 6.1), and these properties are used to create the **background model**. According to the background model we also need the **reservoir model** (also called SeisRoX model). More information about these two models can be found in chapter 6.3.1 and 6.3.2.

In SeisRoX one have the possibility to choose a full-field workflow, or a **local-target workflow.** In this thesis, the latter one is used. In the local-target workflow the area of illumination is defined by the target area (Figure 6.4). Only a single PSDM filter and PSF are calculated in this workflow. Due to this, the size of the target area should be as small as possible since all the illuminations plots (green dots in Figure 6.4) use the same PSF and PSDM filter during migration.

All the main information in this chapter and the following subchapters will be found in the SeisRoX manual (NORSAR, 2014a).

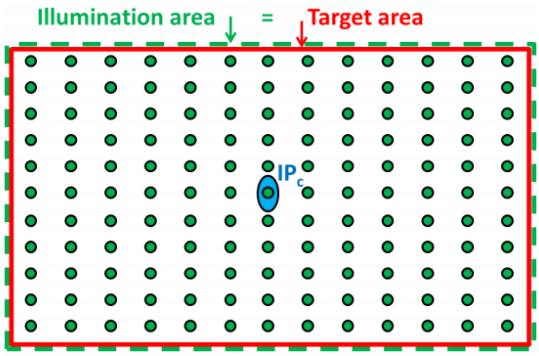

Figure 6.4 Target area used in local-target workflow. The illuminations vectors will be calculated at the blue dot, and the green dots will all be affected by the same PSDM filter/PSF. Modified from the SeisRoX manual (NORSAR, 2014a).

6.3.1 Background model

As mentioned earlier is the background model used to calculate the illumination vectors ($\mathbf{l_{SR}}$) and the scattering wavenumber vectors ($\mathbf{k_{SR}}$) (chapter 4.1). Due to this, the model has a huge influence on the resolution in the PSF.

How to build the background model and how to use NORSAR 2D/3D to make the 3D model ready to use in SeisRoX is illustrated in Appendix B. The same background model is used in all the modeling performed, and the geometry is shown in Figure 6.5. The background model only consists of horizontal horizons. The parameters assigned to the blocks between the horizons are vertical linear functions, except a constant function in the ocean (Table 6.1). In Figure 6.6, Figure 6.7 and Figure 6.8 one can see the background model with assigned P-velocity, S-velocity and density.

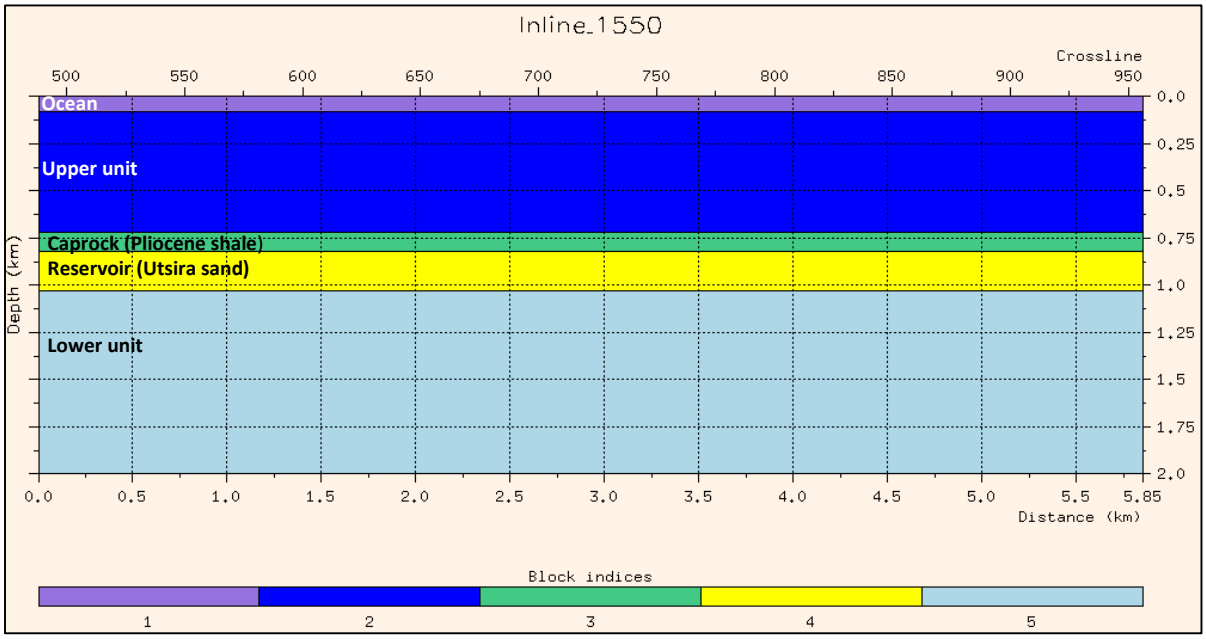

Figure 6.5 The geometry of the background model, blocks without properties.

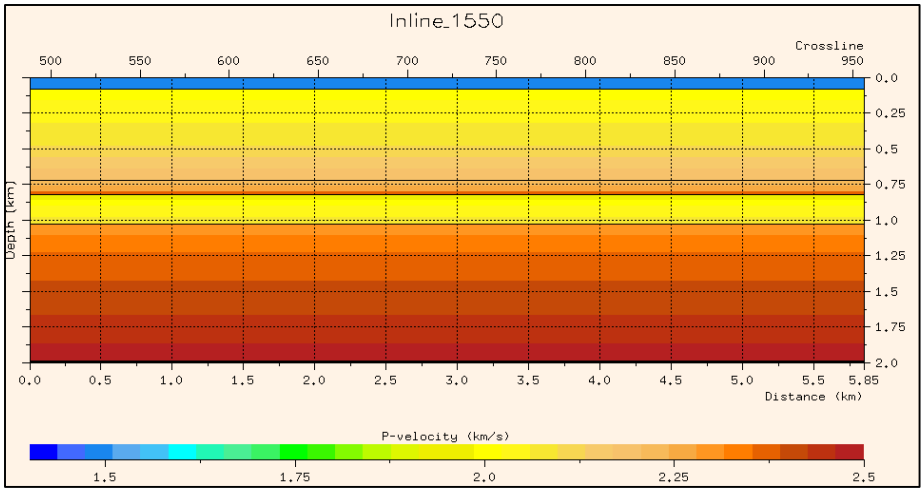

Figure 6.6 The background model with assigned P-velocity.

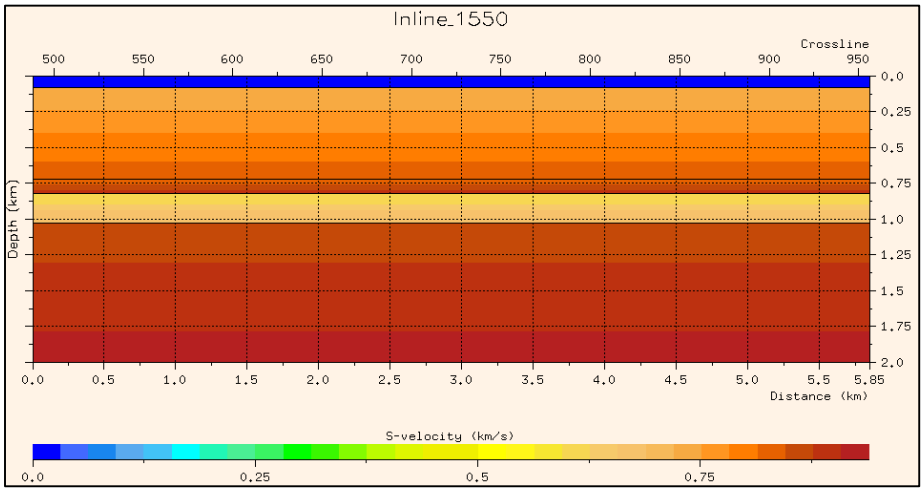

Figure 6.7 The background model with assigned S-velocity.

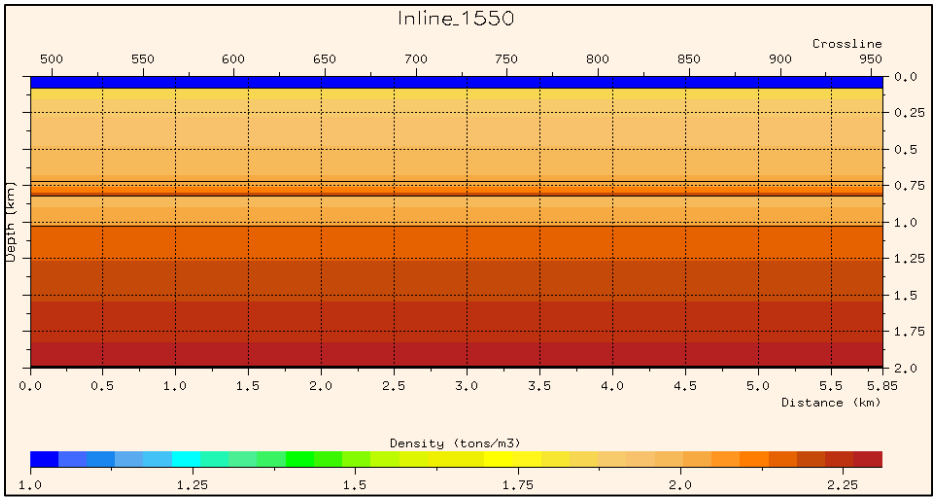

Figure 6.8 The background model with assigned density.

6.3.2 Reservoir model

It is possible to make a rock-physics model if well logs are assessable at the area (not a synthetic case). This rock-physics model can link the geological domain and the elastically domain. Instead, is the elastic parameters calculated using basic equations from rock physics (Appendix A). The reservoir model can be created in SeisRoX or be imported as an Eclipse file from NORSAR or Petrel. As mentioned is NORSAR 2D and 3D used to create the reservoir model and the background model.

6.3.2.1 The reservoir models used in the modeling

This chapter illustrates the geometry (with assigned properties) of the different models used in the modeling. The models are shown in a 2D window in the NORSAR 2D to get the best illustration of the plume.

Reservoir model 1

The reservoir models are equal to the background model plus the plume. The chosen shape of this plume is visualized in Figure 6.9. The deepest point is 1013 m below sea level equal to the plume at Sleipner. The horizontal extension is about 1 km at maximum, and the thickest part of the plume is about 114 m.

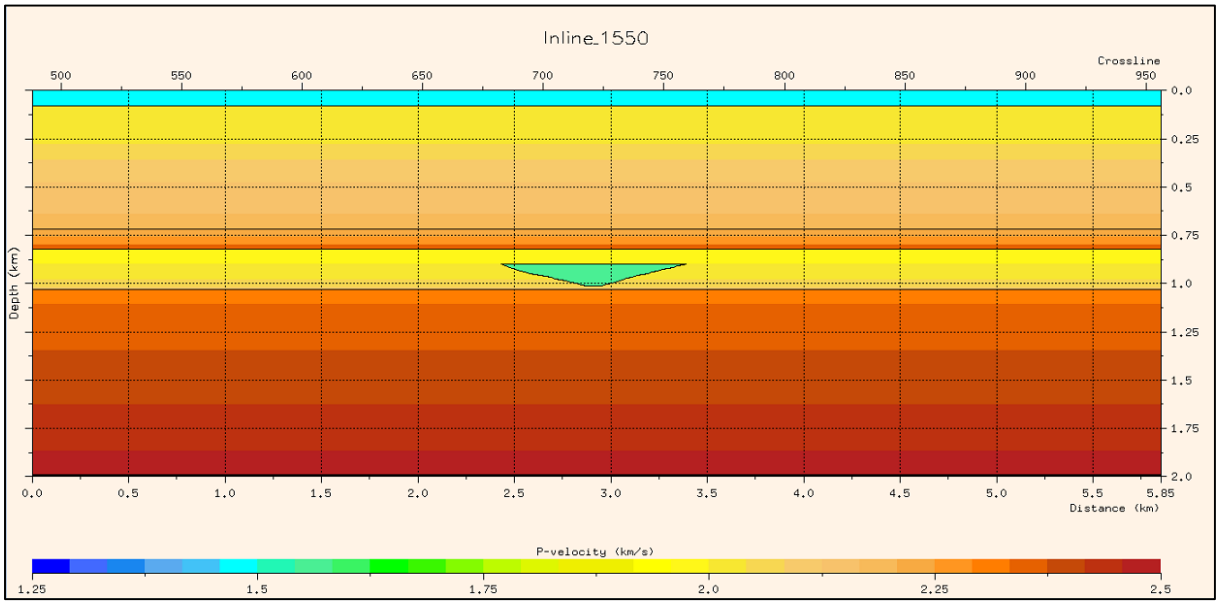

Figure 6.9 Reservoir model 1 is illustrated with P-velocity equal 20 % CO_2 saturation. Maximal horizontal extent of the plume is 1km, and the deepest point is about 1013 m below sea level. The plume is about 114 m thick at maximum.

Reservoir model 2

The plume in this reservoir model is extending from the top of the reservoir to the bottom, with a horizontal extension of about 2 km. The biggest difference with this model compared to the first, is the intra-reservoir shale layers in the Utsira sand (Figure 6.11 and Figure 6.12). These shale layers are added to make the model more realistic to the actual case. As mentioned in chapter 5.1 we know that the Utsira consist of several thin shale layers. These shale layers have the same elastic properties as the Pliocene Shale (caprock) (Arts et al., 2004a). Most of the shale layers are very thin, ranging from 0,5-1 m. In this model, 4 thin shale layers with a thickness of about 1 m is added. The thicker shale unit of about 5-7 m that is located about 20 m below the top reservoir is also applied to the model, with thickness of about 7 m. In Figure 5.3 indicates the red dots, all the shale layers added into this model. Overview of the depth and size of the shale layers can be seen in Table 6.4. The elastic properties (Vp, Vs and density) assigned to the shale layers are the same gradients as used in the caprock. Since the shale layers is located at a deeper point, the parameters will increase, and this is more realistic than having the same values as the caprock (but they use the same parameter gradients).

Table 6.4 Overview of the depths and size of the shale layers within the reservoir and plume.

Shale number	Depth (m bsl)	Thickness (m)	Approximate Vp, Vs and density values
Shale layer 1	840-847	7	2400 m/s, 900 m/s and 2223 kg/m^3
Shale layer 2	873-874	1	2456 m/s, 920 m/s and 2272 kg/m^3
Shale layer 3	901-902	1	2507 m/s, 939 m/s and 2318 kg/m^3
Shale layer 4	918-919	1	2537 m/s, 951 m/s and 2346 kg/m^3
Shale layer 5	992-993	1	2670 m/s, 1001 m/s and 2470 kg/m^3

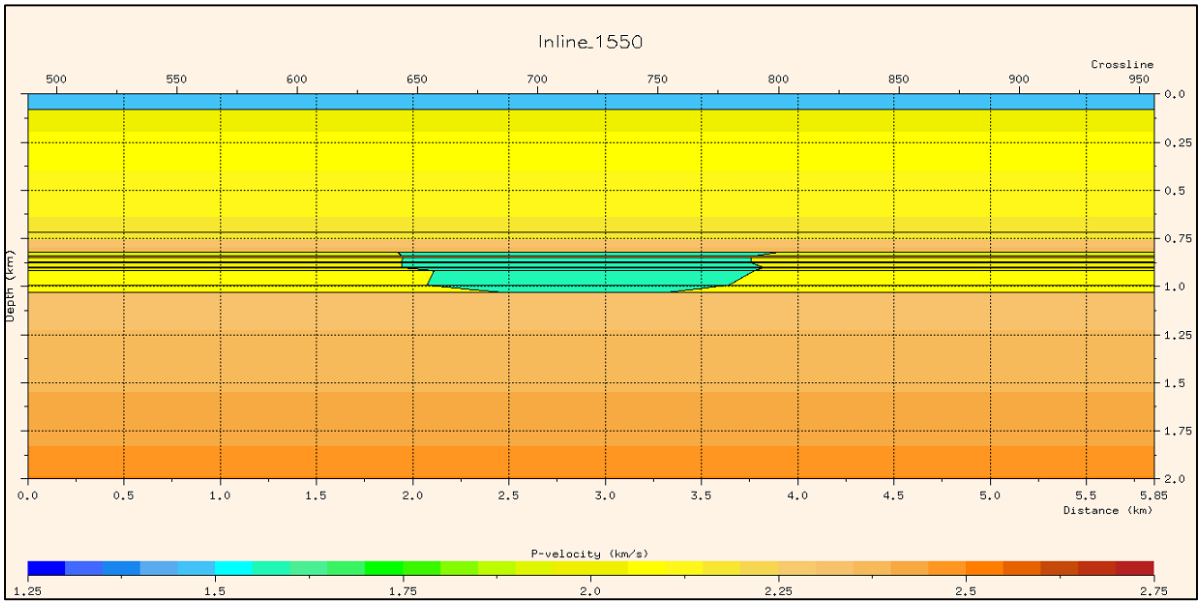

Figure 6.10 Illustrates the complete reservoir model 2 with P-velocity equal 20 % CO_2 saturation.

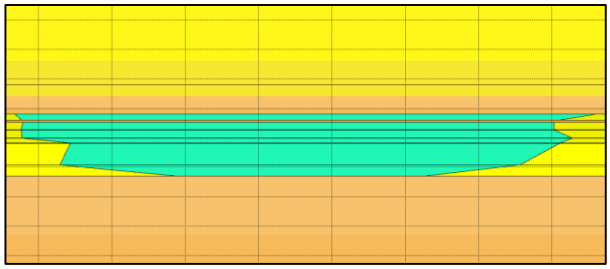

Figure 6.11 Outcrop of reservoir model 2 showing the shape of the plume with thin shale layers.

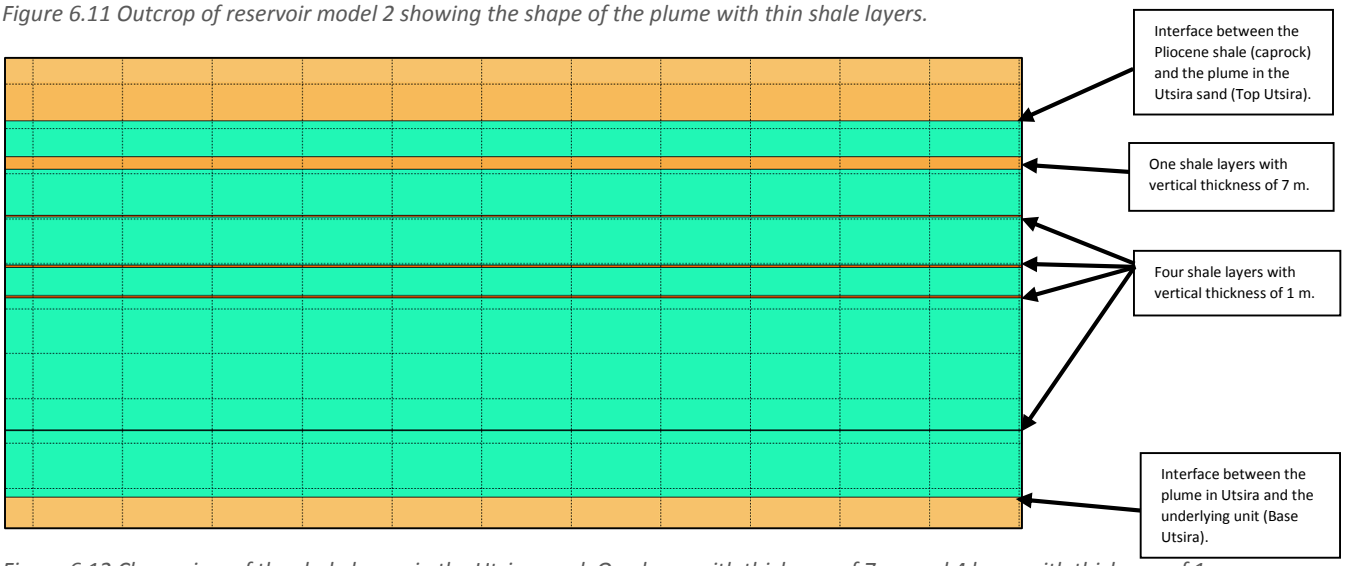

Figure 6.12 Closer view of the shale layers in the Utsira sand. One layer with thickness of 7 m, and 4 layer with thickness of 1 m.

Reservoir model 3

This model consists of a horizontal plume, and as you can see on Figure 6.13 is the shape of the plume wide, and not very thick. The horizontal extent of the plume is about 2 km, and the thickness is 50 m.

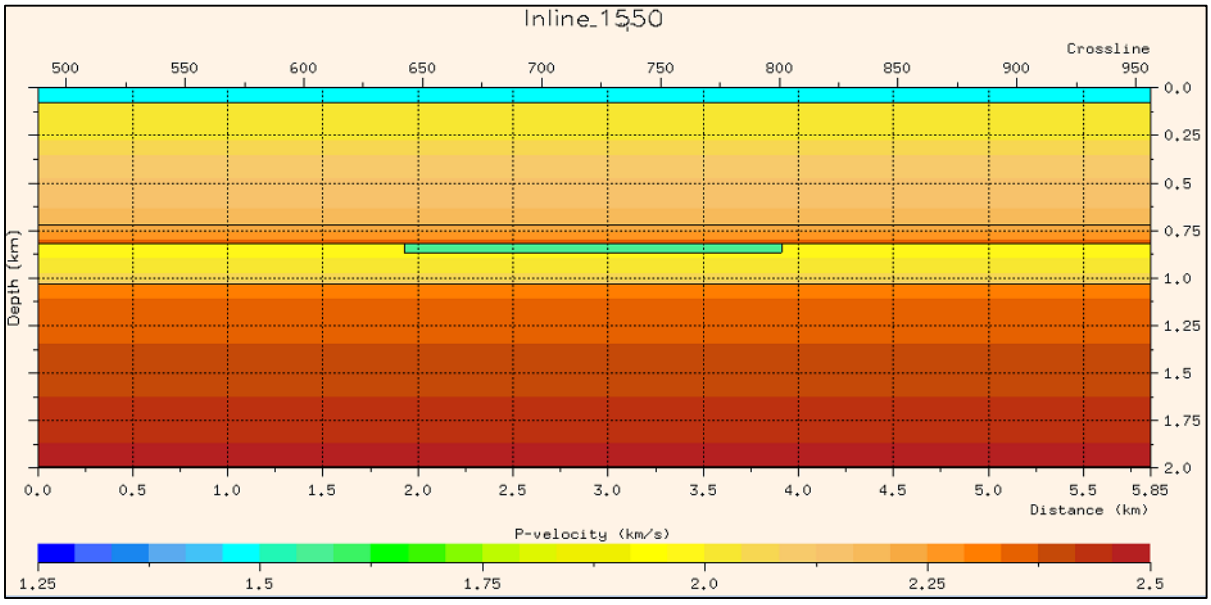

Figure 6.13 Reservoir model illustrated with P-velocity that corresponds to 20 % CO_2 saturation.

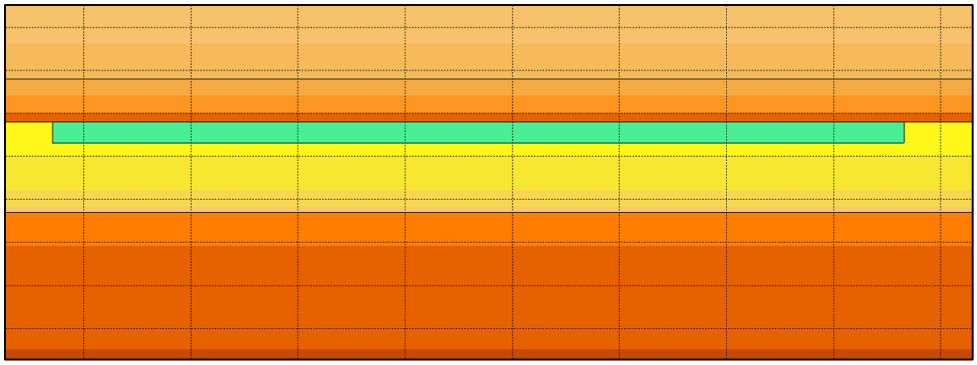

Figure 6.14 Outcrop of the plume in reservoir model 3. Vertical thickness is 50 m. Horizontal extent is about 2 km.

Reservoir model 4-10

The only difference between reservoir model 3 and model 4-10 is the vertical thickness of the plume. Therefore is some of the models illustrated in Appendix C. Overview of the thickness of the models can be seen in Table 6.5.

Table 6.5 Overview of the horizontal and vertical thickness of the horizontal models.

Model	Horizontal thickness	Vertical thickness
Reservoir model 3	2000 m	50 m
Reservoir model 4	2000 m	40 m
Reservoir model 5	2000 m	30 m
Reservoir model 6	2000 m	20 m
Reservoir model 7	2000 m	10 m
Reservoir model 8	2000 m	5 m
Reservoir model 9	2000 m	3 m
Reservoir model 10	2000 m	1 m

Reservoir model 11

The following reservoir models starting with model 11, have been created to show the effect of a vertical plume. The plume stretches from the bottom of the reservoir (TVD 1030m) all the way to the top of the reservoir (TVD 820m), meaning a vertical extent of 210 m. The horizontal thickness of the plume is in this model is 50 m (Figure 6.15).

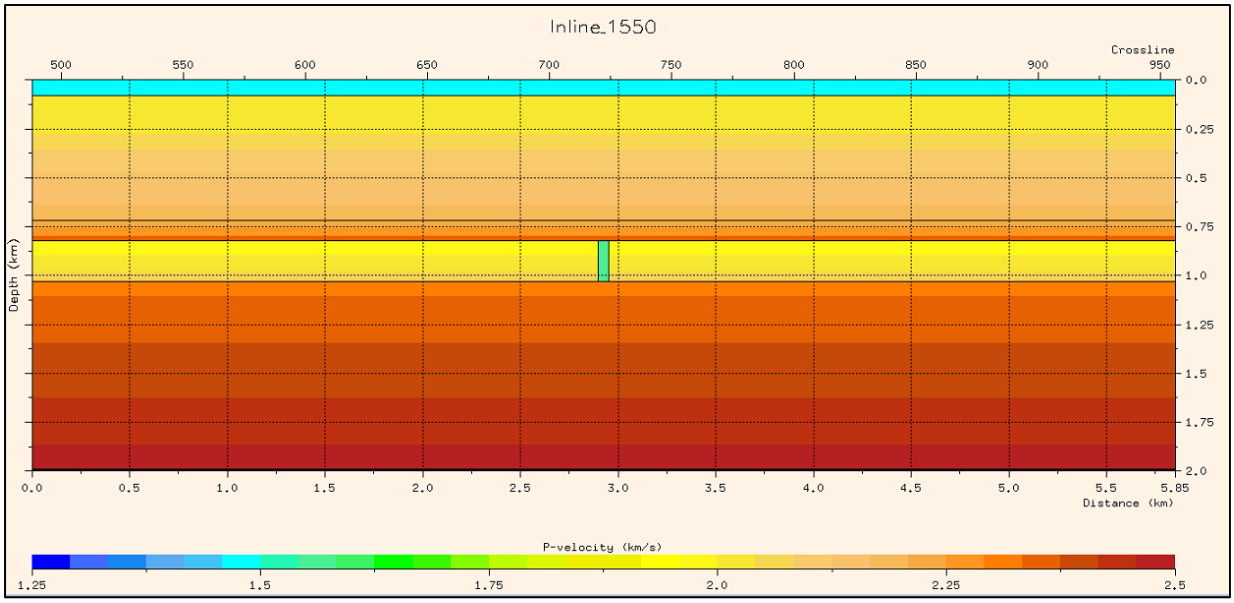

Figure 6.15 Reservoir model 11 showing model with P-velocity equal 20 % CO_2 saturation. The horizontal thickness of the plume is 50 m, and the vertical extent is from bottom Utsira to top Utsira, meaning a vertical extent of 210 m.

Reservoir model 12-18

The only difference between reservoir model 11 and model 12-18 is the horizontal thickness of the plume. Therefore is some of the models illustrated in Appendix C. Overview of the thickness of the models can be seen in Table 6.6.

Table 6.6 Overview of the horizontal and vertical thickness of the vertical models.

Model	Horizontal thickness	Vertical thickness
Reservoir model 11	50 m	210 m
Reservoir model 12	40 m	210 m
Reservoir model 13	30 m	210 m
Reservoir model 14	20 m	210 m
Reservoir model 15	10 m	210 m
Reservoir model 16	5 m	210 m
Reservoir model 17	3 m	210 m
Reservoir model 18	1 m	210 m

6.3.3 Survey

The geometry of the survey is very important for the result seismic image. From chapter 4.1.1, one knows that the angle of incidence influence the length of the illumination vector ($\mathbf{I_{SR}}$), and the length will influence the PSDM filter. The angle of incidence can be related to the distance between the shot and the receiver assigned under the survey parameters. As mentioned earlier, a small angle will create the longest vector, and also gives the highest coverage in the wavenumber domain - again resulting in a better resolution in the PSF.

The marine survey editor can be seen in Figure 6.16. The best location is equal to the center of the target (See chapter 6.3.4). This modeling is using a marine 2D survey with one shot line and one streamer. Since the models is in YZ-plane, the survey must be rotated 90° relative to the X-axis. This is because the inline (the line the models are build on) goes in Y-direction. A single shot line of 6 km is defined, and a receiver line of 3 km. The spacing between the shots and receivers is 12,5 m. The survey parameters used are listed in Table 6.7 in chapter 6.4.

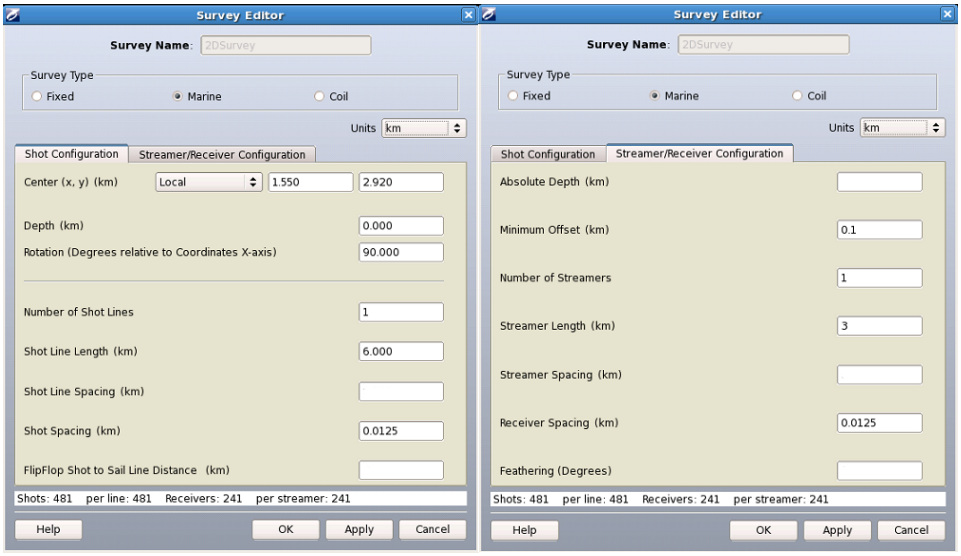

Figure 6.16 Parameters added in the survey. Shot Configuration to the left and Streamer/Receiver Configuration to the right in the picture.

6.3.4 Target area (Simulated PSDM Parameters)

In the target area, one can define the PSDM parameters used in the different workflows. Illustration of the target area-window is shown in Appendix B, Figure B.11. The various parameters are described below:

PSDM Target

In this folder, the center of the target is defined, the size, the sampling of the reflectivity and whether we want a 2D or 3D target. Since the seismic result is best illustrated as 2D, we define a 2D target in the YZ-direction. The size of the target should be as small as possible to avoid mistakes since a single PSF/PSDM filter is used for the whole area. The sampling size is recommended to be 0,01 km in Y-direction and 0,005 km in Z-direction by the SeisRoX manual (NORSAR, 2014a). Smaller sampling gives better resolution and better coverage in the wavenumber domain, but this also increases the workflow run time. It is important to have the correct sampling since it will affect the reflectivity and the PSDM filter. Overall in this modeling is has been used a smaller sampling to avoid a truncated PSDM filter and to get a well gridded reflectivity.

Reflectivity

We have various options defining the reflectivity method, like Zoeppritz-knott (Aki and Richards, 1980) and AVO-R0G (Shuey, 1985). In this modeling will Zoeppritz be used in all the different workflows. It is three different options under the incident angle selection:

1. Zero angle: The incident angle is equal to zero.
2. Average angle: An average of all the incident angles are used.
3. Angle range: The incident angle varies between the angle range, and the angle sampling defines the sub-range. By using an example from the SeisRoX manual (NORSAR, 2014a), an angle range from 0° - 30° and an angle sampling of 10° will decompose the angle range into 4 sub-ranges: (0° - 5°), (5° - 15°), (15° - 25°) and (25° - 35°) providing 4 different seismic images of respectively incident angle of 0°, 10°, 20° and 30°. The $\mathbf{I_{SR}}$ will be calculated for each sub-range, but the reflectivity is only calculated for a single degree. The first sub-range calculates reflectivity for 0°, the second for 10°, and so on. This method is useful if interested in AVA-effects.

Simulated PSDM Method

In this folder one can choose between true amplitude and amplitude effects. In all the workflows preformed in this thesis, true amplitude will be used. If attenuation-effects is interesting, the amplitude effects must be selected. True amplitude is used when it is possible to assume that amplitude corrections is done before modeling. These amplitude corrections include taking geometrical spreading, attenuation etc. into account. When using true amplitude every reflections will be weighted equally, and this is useful when we want faithful amplitude information.

PSDM Filters

Under this folder, the migration options are defined, like the aperture range, travel time range and exclude or include turning waves. The definition of aperture is the distance between the CMP (Common Midpoint) of a source-receiver pair, and the point where the $\mathbf{l_{SR}}$ is calculated. The recommended distance is 0-2 km by the SeisRoX manual (NORSAR, 2014a). The recommended range for travel time is 0-8 sec (NORSAR, 2014a). If the range is too big, $\mathbf{l_{SR}}$ is calculated for very long travel times, and 8 sec are consider the realistic maximum of an acquisition. If diffraction occurs on the result seismic image when using true amplitude, the SeisRoX manual (NORSAR, 2014a) recommend to change these parameters to see if the diffraction disappears. These options will in some cases remove the horizontal part of the filter (Figure 4.3) under migration, and this will make it hard to visualize vertical reflectors. This will be more discussed in chapter 8.

Optional Results

In this folder, one can choose the desired outcome of the workflow, like reflectivity and PSF for instance.

Property Gridding Options

In this folder, one define if we want to interpolate between horizons and extrapolate to boundaries. Interpolation means estimating a value when the nearby values are knows. To extrapolate means stretching one value further in one direction, for example out to the boundaries of the target.

6.3.5 Wavelet

The wavelet applied will have a frequency band attached to the applied frequency. Given for instance; A pulse of 30 Hz will have both higher and lower frequencies. The main frequency is 30 Hz, since this is the frequency with the highest spectrum in the amplitude (Figure 6.17). Figure 6.18 illustrate the wavelets for all different frequencies used.

The wavelet has a huge impact on the result seismic image. As mentioned in chapter 2.4, one knows from basic equations for the resolutions, that a higher frequency gives better resolutions.

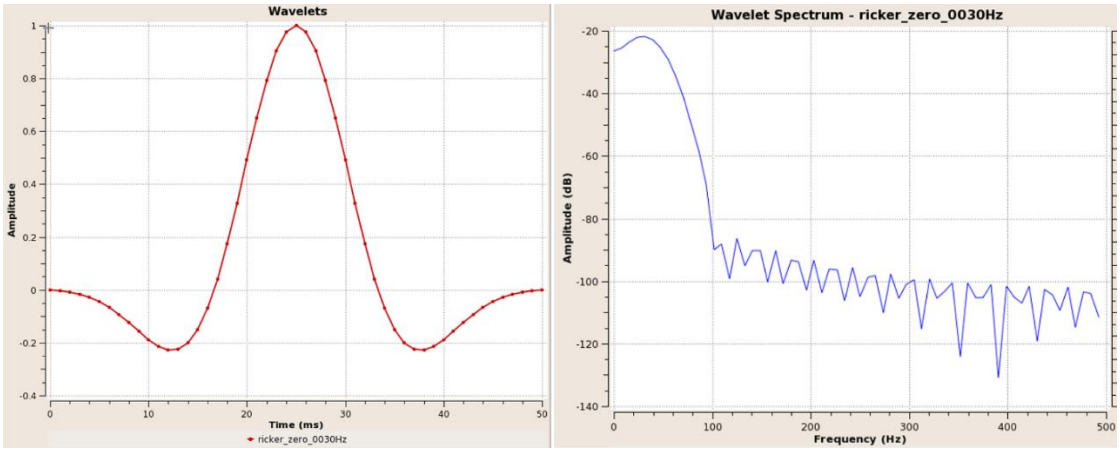

Figure 6.17 Left: Ricker Zero 30 Hz wavelet. Right: Frequency band (spectrum) of Ricker Zero 30 Hz.

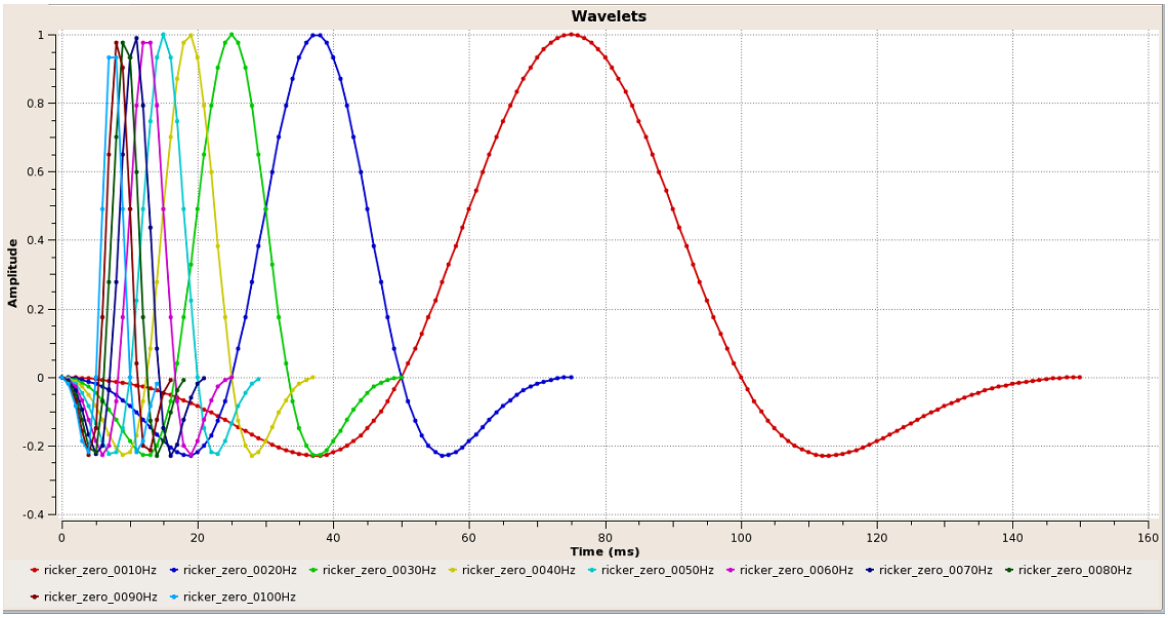

Figure 6.18 Ricker zero wavelets ranging from 10-100 Hz.

6.4 Survey and PSDM parameters used in the modeling

Survey parameters from Table 6.7 is used during all the different workflows.

Table 6.7 Survey Parameters.

Shot Configuration		Streamer/Receiver Configuration	
Center (x,y – local coordinates)	1.55 , 2.92		
Rotation Degrees relative to X-axis	90 °	Minimum Offset (km)	0,1
Number of Shot Lines	1	Number of Streamers	1
Shot Line Length (km)	6	Streamer Length (km)	3
Shot Spacing (km)	0.0125	Receiver Spacing (km)	0.0125

The Simulated PSDM Parameters used during the modeling are listed in Table 6.8. From the table one can see that several parameters: depth, size, sampling and incident angle selection will be defined in each separate workflow.

Table 6.8 SeisRoX Workflow Parameters.

Simulated PSDM Parameters	
PSDM Target	
Center X,Y (km)	1.55 , 2.92
Depth Z (km)	Defined in each separate workflow
Grid type	2D - YZ
Size (km)	Defined in each separate workflow
Sampling (km)	Defined in each separate workflow
Reflectivity	
Reflectivity method	Zoeppritz
Incident angle selection	Defined in each separate workflow
Simulated PSDM Method	
Method	True amplitude
PSDM Filters	
Aperture range (km)	0 - 2
Traveltime range (s)	0 - 8

7 Results

This chapter describes the results from different workflows by using different velocities, frequencies, incident angle and by varying the size of the plume in the reservoir.

7.1 Change in acoustic velocities

The research of how seismic anomalies change based on different saturations of CO_2 is presented in this chapter. In this workflow Reservoir model 1 is used (Figure 6.9), and the standard survey parameters from Table 6.7. Ricker zero 30 Hz is used as the input frequency pulse. The PSDM parameters used are listed in Table 6.8, and the angle range option is used under reflectivity. By using an incident angle of 20° to 20°, and sampling of 10°, will this provide an $\mathbf{I_{SR}}$ range from 15-25°, resulted in a $\mathbf{I_{SR}}$ coverage of 19,72 % of all available. Overview of the PSDM parameters and the frequency assigned to this workflow is listed in Table 7.1

Table 7.1 PSDM Parameters and input frequency used in workflow 7.1.

Depth Z (km)	0.925
Size (km)	1.2 , 0.8
Sampling (km)	0.005 , 0.0025
Incident angle selection	Angle range, 20°-20°
Input frequency	Ricker Zero 30 Hz

7.1.1 The seismic images

Figure 7.1 shows an outcrop of the final seismic images (Figure 7.2) with different CO_2 saturation ranging from 10-100 %. It is important to notice that this amplitude is relative, and not equal to the reflection coefficient due to effects from migration. The reflection coefficient will be further described in chapter 8.1. The reflectivity from the plume with 20 % CO_2 saturation is shown in Figure 7.3. This figure shows that all interfaces from the reservoir model with 20 % CO_2 saturation will be visible, and they will also be visible on the final seismic image. Interfaces were also visible on reflectivity images from other saturations than 20 %, only with a different reflections value. To take a closer look at how the seismic amplitude anomalies changes with different CO_2 saturation, outcrops (Figure 7.1) of the pictures in Figure 7.2 was made. Figure 7.1 shows clearly an increase in amplitude strength as the saturation increases. This is expected because of the decrease in acoustic P-velocity from Table 6.3.

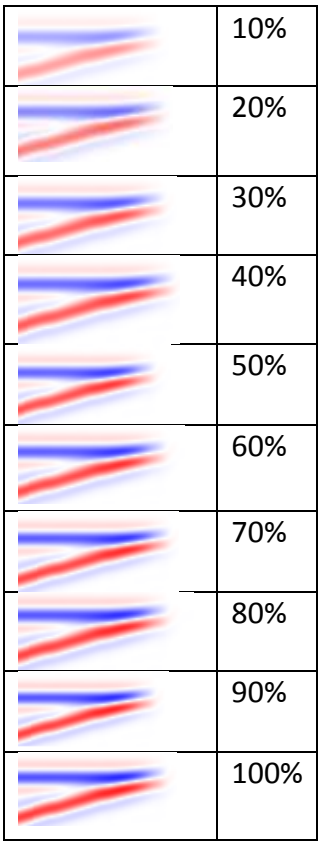

Figure 7.1 Illustration of seismic amplitude anomalies with different CO_2 saturation.

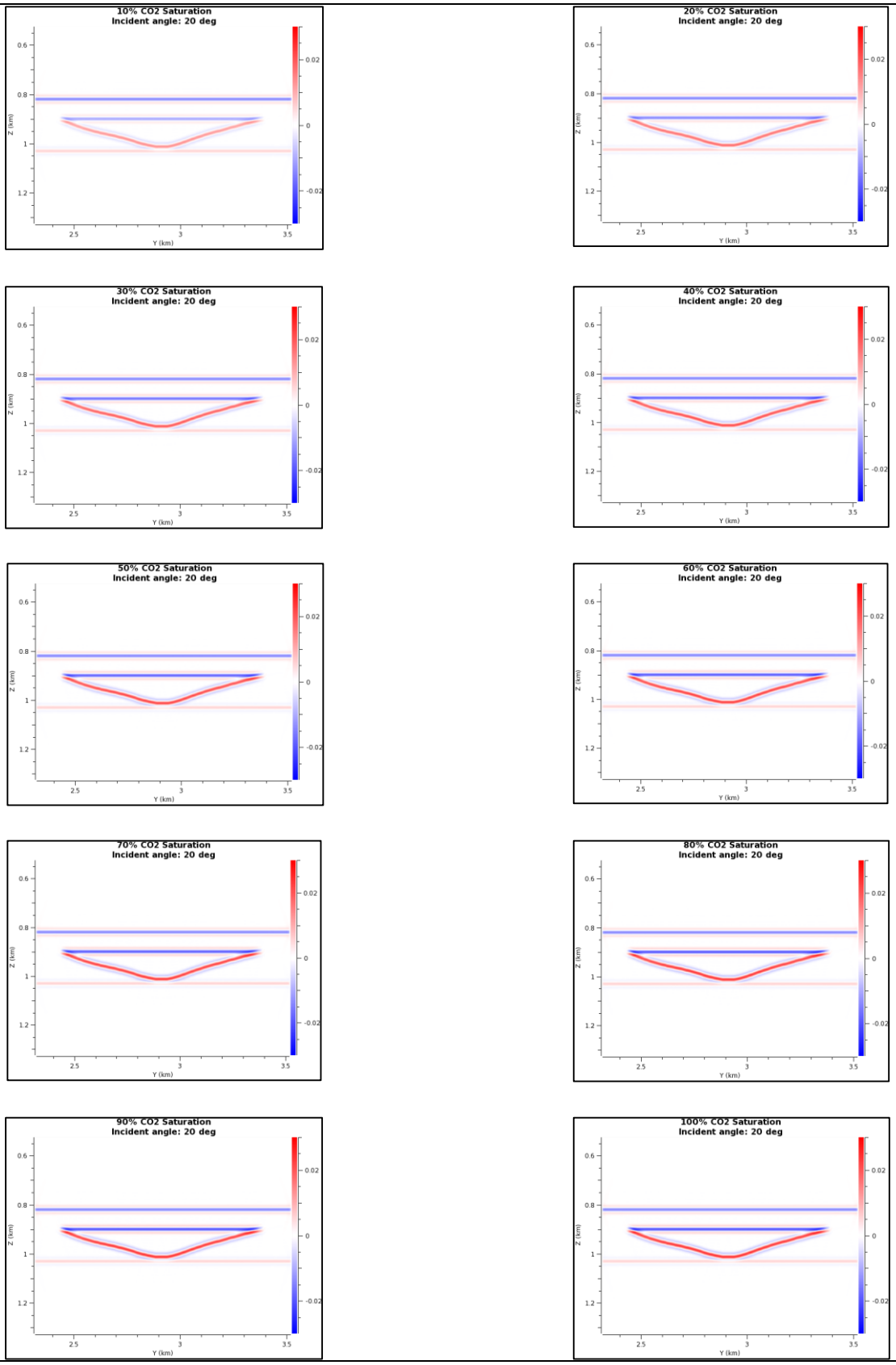

Figure 7.2 Reservoir model 1, Incidence angle of 20°, increasing CO_2 saturation from 10-100%, the scale bar is the same in all figures.

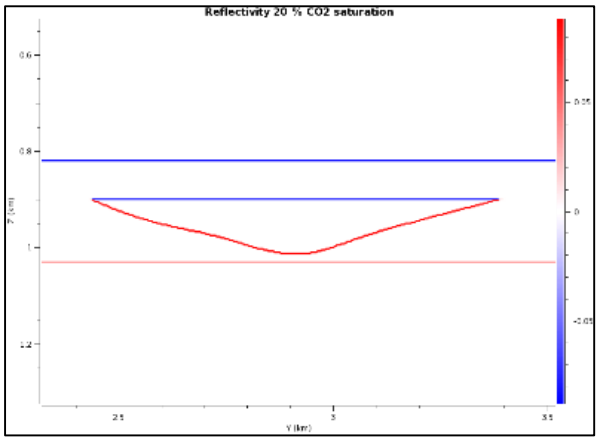

Figure 7.3 Reflectivity from Reservoir model 1 with 20 % CO_2 saturation.

7.1.2 The Point-Spread Function and the PSDM filter

The PSF will provide information about the cross reflector (known as vertical) resolution and the lateral (horizontal) resolution (Chapter 4.1.1). In this modeling the PSF (Figure 7.4) are not "dipping", and the old names of the resolution can be used, vertical and horizontal resolution. The PSF is not dipping since the target is placed right below the survey (zero offset survey). In this workflow it is only variations in the CO_2 saturations, meaning that only the elastic parameters of the velocity and density will change in the reservoir model. Because of this will the PSF be the same with different saturations of CO_2. By looking at the PSF in Figure 7.4, is the vertical resolution about 18 m, and the horizontal resolution is 28 m.

The PSDM filter (Figure 7.4) is the result of the mapped $\mathbf{k_{SR}}$ vectors with the frequency band as a weight factor. The different colors shows the amplitude of the frequency band. The red colors is the frequency with highest amplitude, which in this case is 30 Hz.

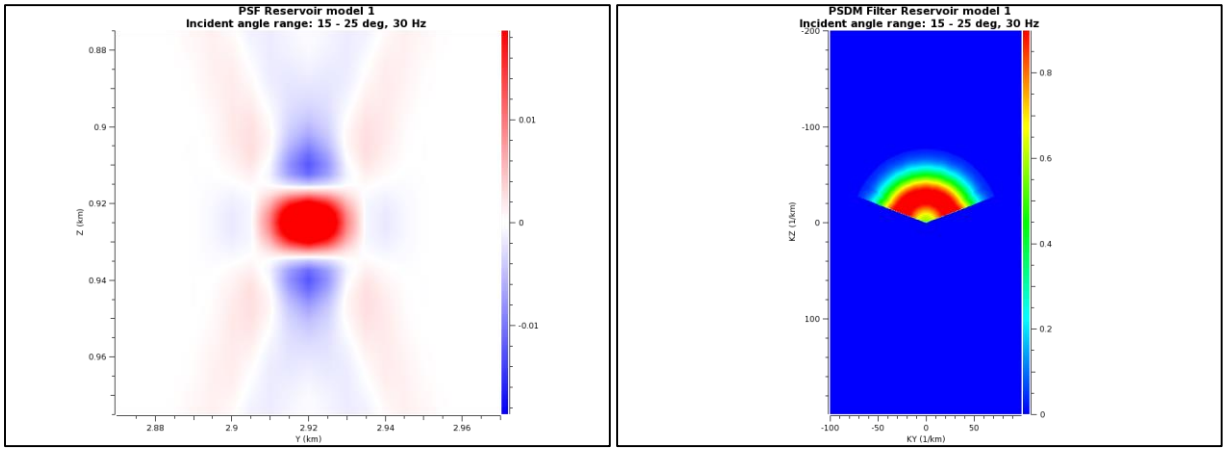

Figure 7.4 Incident angle of 20° with I_{SR} calculated in the angle range of 15-25°. Left: PSF. Right: PSDM filter.

7.1.3 Dip and azimuth of illumination vectors

Figure 7.5 shows the plot of all accessible I_{SR} during this workflow. With an incident angle of 20°, is the coverage in I_{SR} equal to 19,72 % of the total I_{SR} available. Even if the workflow is only using 19,72 % of the I_{SR} to calculate the filter and PSDM, will the I_{SR} plot show 100 % of the I_{SR}. The colors indicate the amount of I_{SR} available at the respectively dip and azimuth. Red color indicates a high amount of I_{SR} collected from that area. On the other hand, blue color indicates a small amount of I_{SR} plotted. The I_{SR}-vectors is plotted in N-S direction, the same directions as the survey. Since the survey is 2D, is it also expected to only have a single line of I_{SR}-vectors plots. This line dominates the figure, but the figure also shows a small amount of vectors of zero degrees dipping towards west. From the figure, we see that that the reflections will be obtained up to a dip of 90°. This information tells us that in the seismic image reflectors in N-S directions with dips from 0-90° will be visible. In this workflow, the I_{SR} coverage is very good at high degrees (50-55° and 60-65°) in both North and South directions (red and yellow).

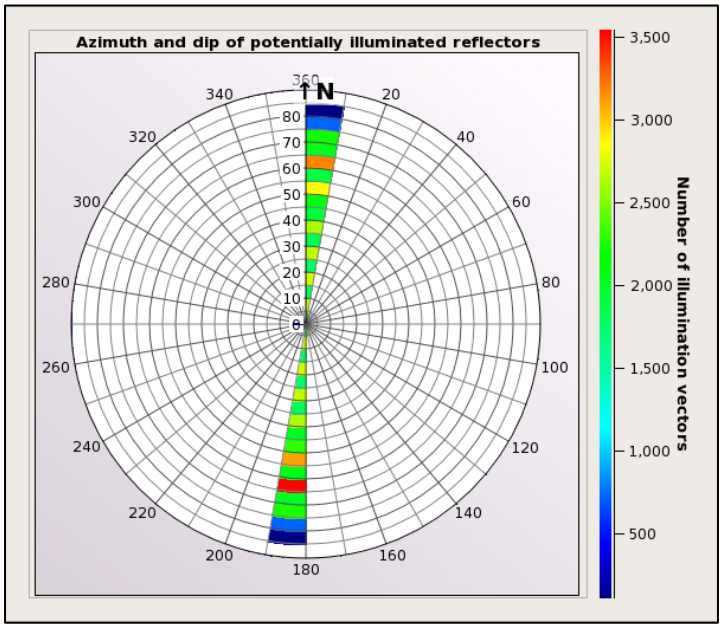

Figure 7.5 Plotted illumination vectors from reservoir model with incident angle of 20°, and I_{SR} from a range from 15-25°. The plot is illustrating 100 % of the available I_{SR}.

7.2 Change in wavelet (frequency)

In this workflow is reservoir model 2 (Figure 6.10) used to model how the seismic react on different frequencies. This model is quite more complex than the first two, since it also contains shale layers inside the reservoir. The plume's elastic parameters with a CO_2 saturation of 20 % is used. This means a P-velocity equal to 1563 m/s, S-velocity equal to 650 m/s and density equal to 2031 kg/m^3. The angle range option is also used in this modeling, with an incident angle of 20°. This gives a sampling range of the $\mathbf{I_{SR}}$ in between 15-25°, and a 19,72% coverage of all the available $\mathbf{I_{SR}}$-vectors (Same as in the previous workflow). Survey parameters and the PSDM parameters are equal to the ones in Table 6.7 and Table 6.8. The size of the target is equal to 2,5 km in Y-direction and 1 km in Z-direction. Smaller sampling is used in this workflow due to bad gridding of the reflectivity image. Summary of the PSDM parameters used that differ from Table 6.8 is listed in Table 7.2.

Table 7.2 PSDM Parameters and input frequencies used in the workflow 7.2.

Depth Z (km)	0.925
Size (km)	2.5 , 1.0
Sampling (km)	0.001 , 0.001
Incident angle selection	Angle range, 20°-20°
Input frequency	Ricker Zero 10-100 Hz

7.2.1 The seismic images and the reflectivity

The result of the final seismic image reflects the effect the input reflectivity has on the final seismic. Figure 7.7 to Figure 7.16, shows how the resolution of the seismic images is getting better by increasing frequency.

In Figure 7.6 is the reflectivity extracted from the reservoir. Only the visible interfaces on the reflectivity image will be visible on the final image, since the final seismic image is the result of the PSDM filter applied to the reflectivity. In this case, is the image of the reflectivity equal with varying frequency. The interface between caprock and the plume will be a negative reflection coefficient (blue colors) because of transition from a higher impedance to a lower impedance layer. The shale layers inside the reservoir and the plume will first be marked with a positive interface (red colors) since we go from a layer with lower impedance to layers with higher impedance. The interface from the thin shale layers back to the plume will then be the opposite, negative reflection coefficient (blue colors).

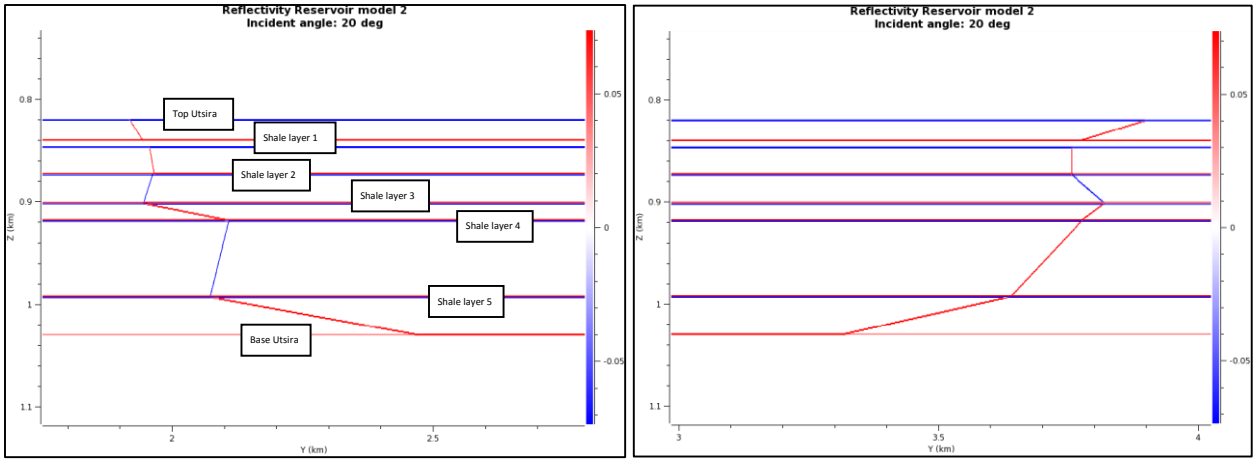

Figure 7.6 Left: Reflectivity from the left side of reservoir model 2. Shale layers in the model is numbered, and top Utsira and base Utsira is illustrated. Right: Reflectivity from the right side of reservoir model 2. One reflection from the CO_2 plume between shale layer 1 and shale layer 2, is close to vertical.

In the seismic result with frequency pulse of 10 Hz (Figure 7.7), one can observe that not all layers from the reflectivity image is visible (Figure 7.6). Figure 7.7 describes the visible layers, like Top Utsira, Base Utsira and a combination of shale layer 3 and 4 (interference).

With a frequency of 20 Hz (Figure 7.8) are the interfaces much clearer, and the shale layers 1, 2 and 5 is visible as a single reflection. Shale layer 3+4 is reflected as a combination. With a frequency of 30 Hz is shale layer 3 and 4 visible, but they are partly interfering. With a frequency of 40 Hz (Figure 7.10), is all shale layers visible as in the reflection image (Figure 7.6).

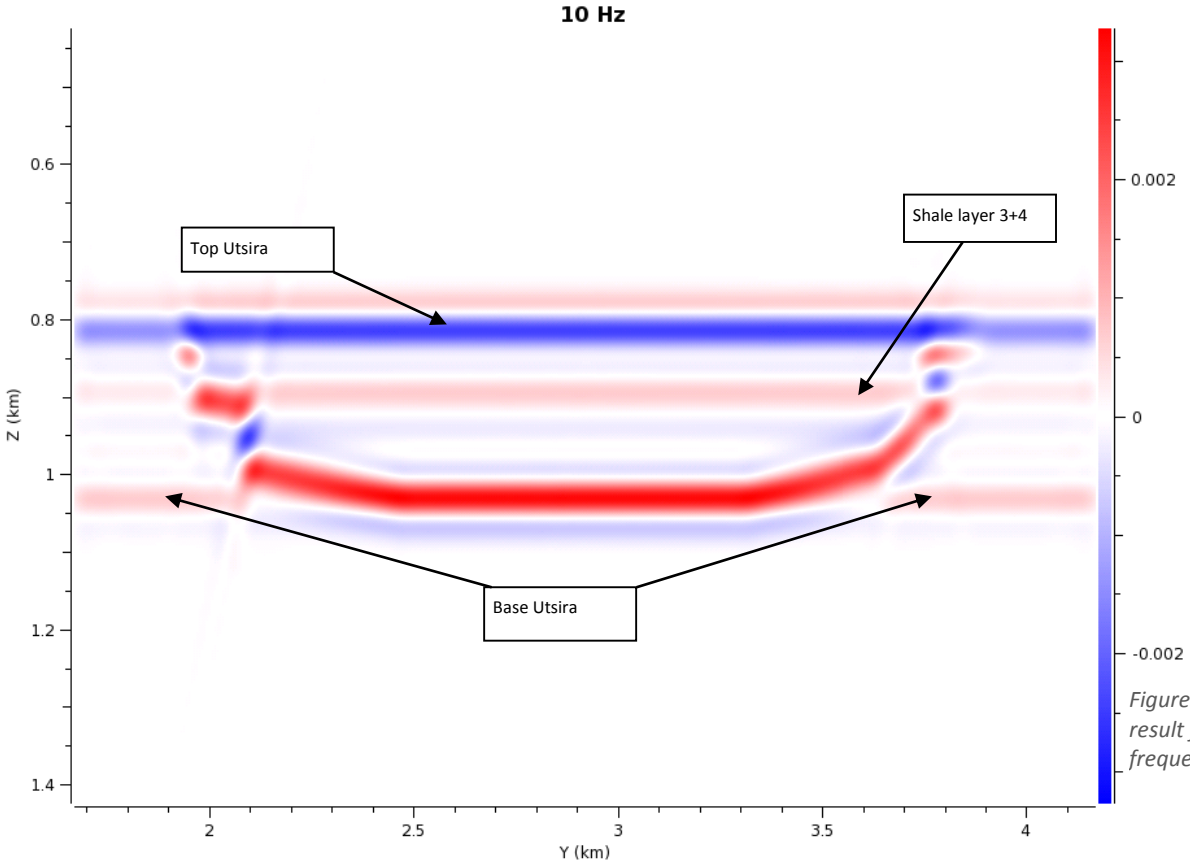

Figure 7.7 Seismic result from input frequency of 10 Hz.

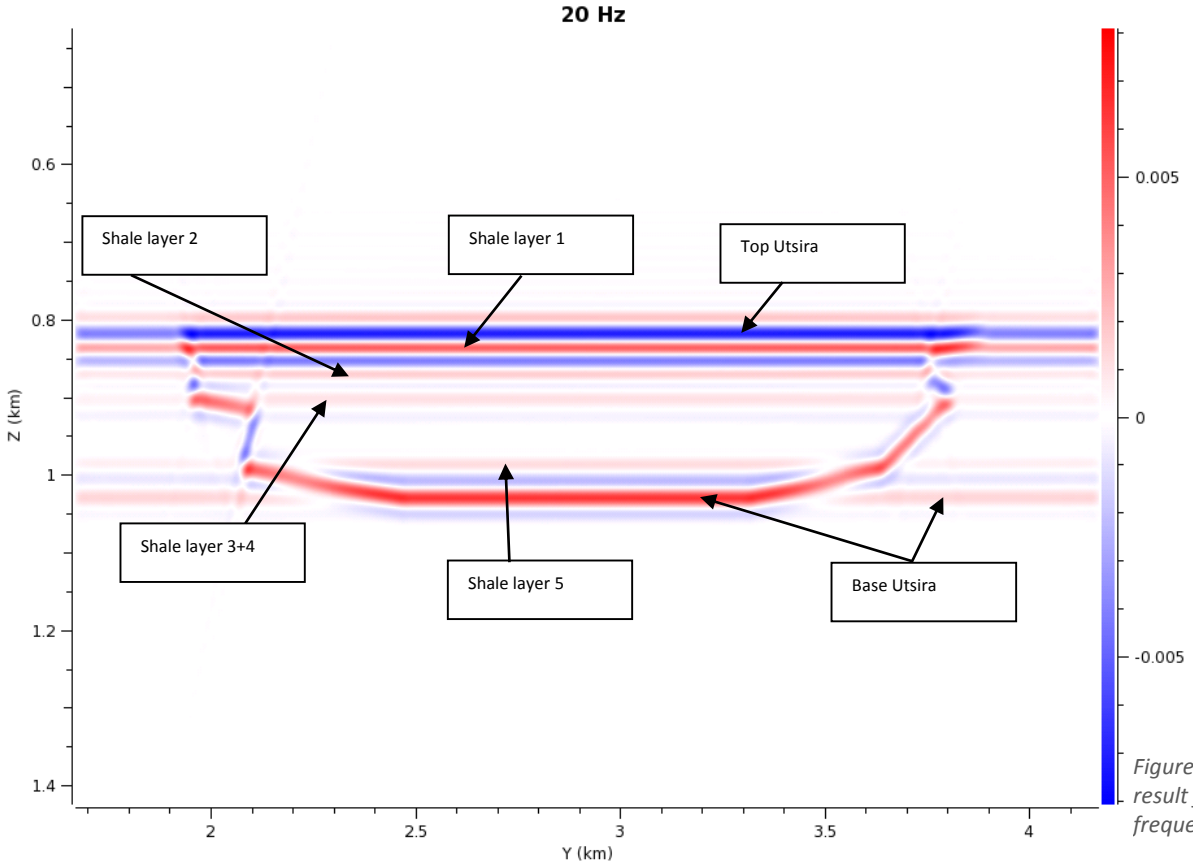

Figure 7.8 Seismic result from input frequency of 20 Hz.

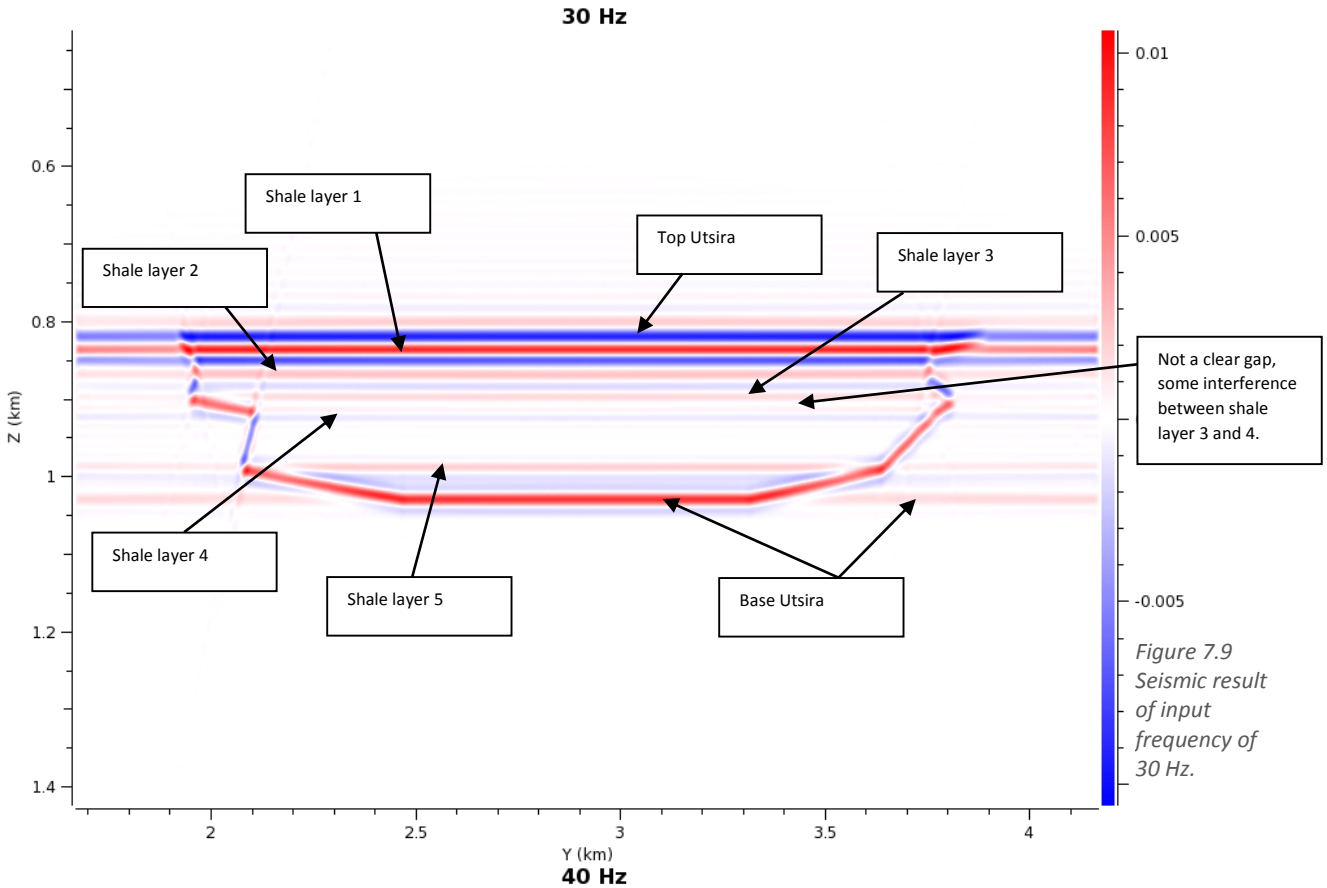

Figure 7.9 Seismic result of input frequency of 30 Hz.

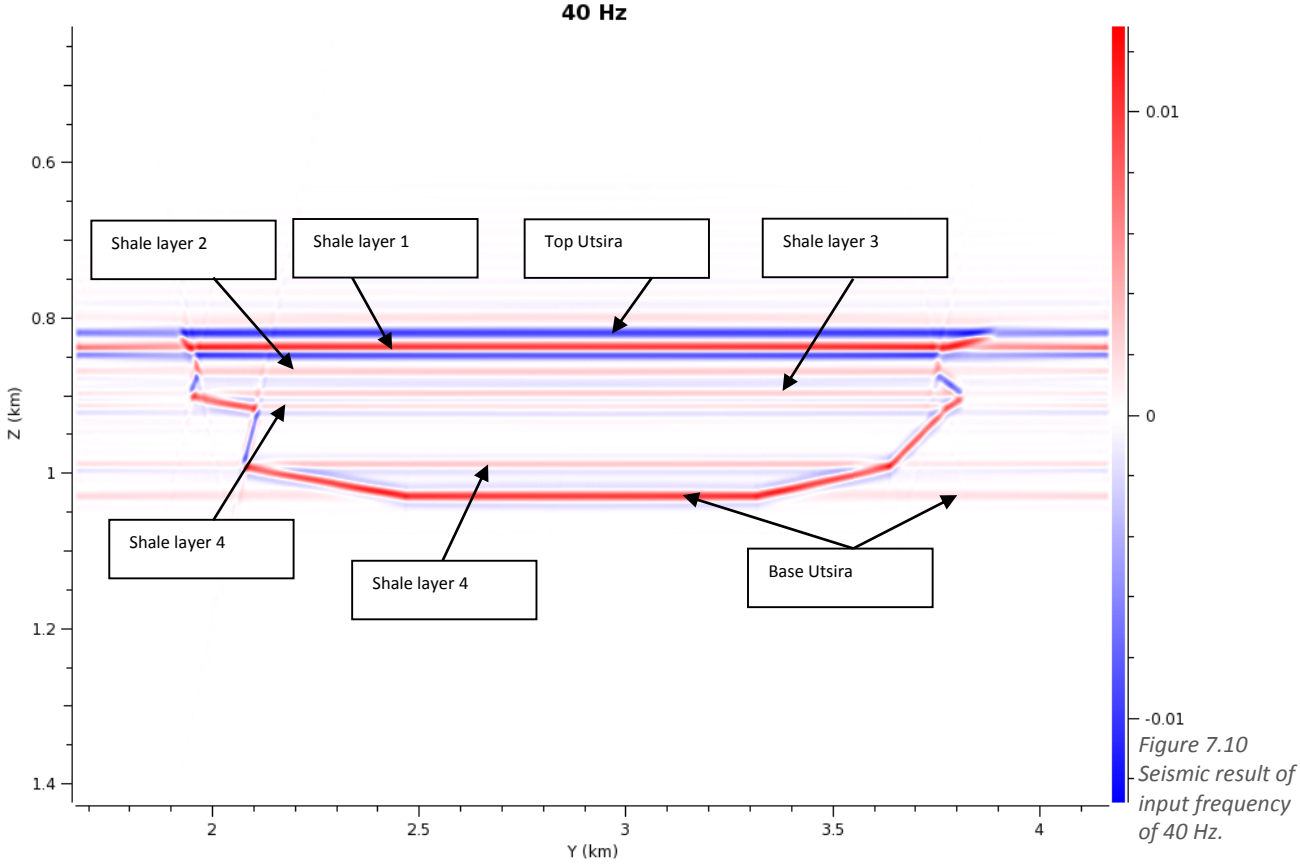

Figure 7.10 Seismic result of input frequency of 40 Hz.

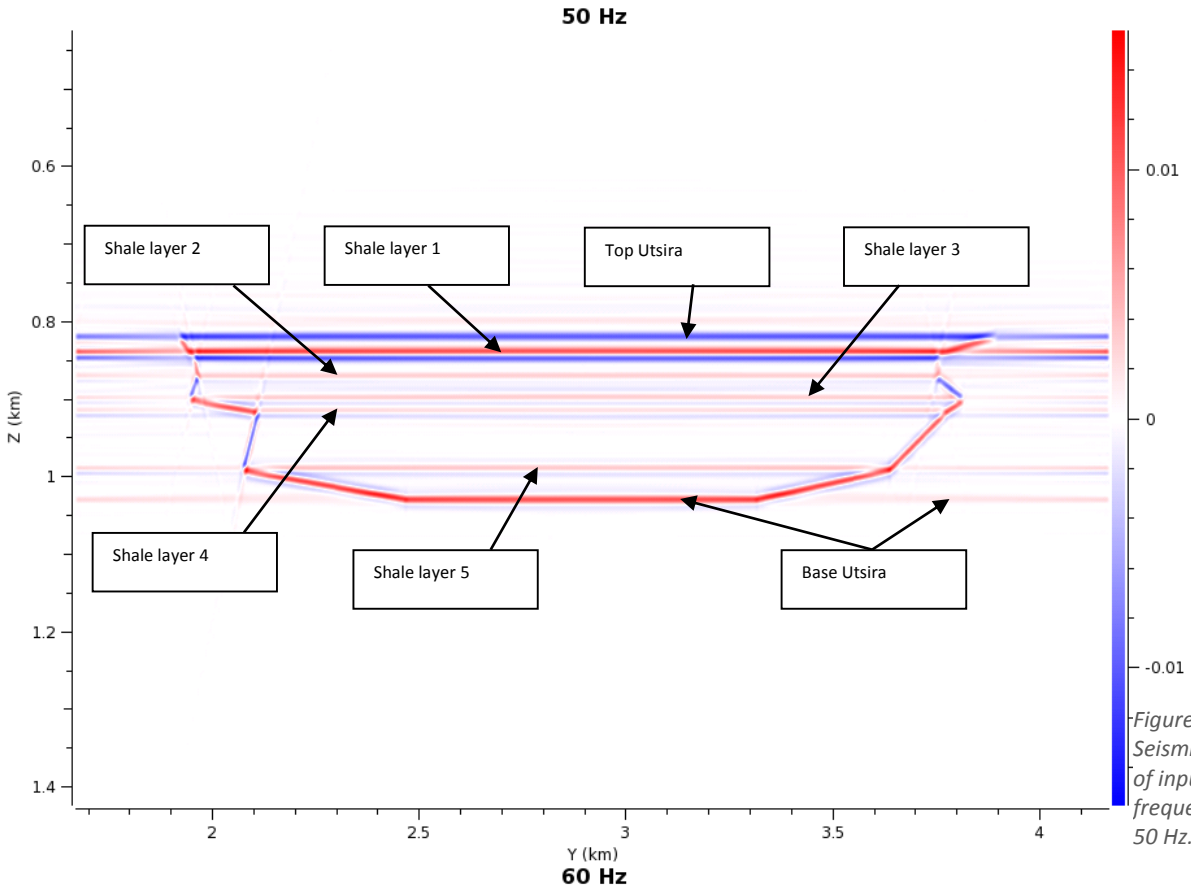

Figure 7.11 Seismic result of input frequency of 50 Hz.

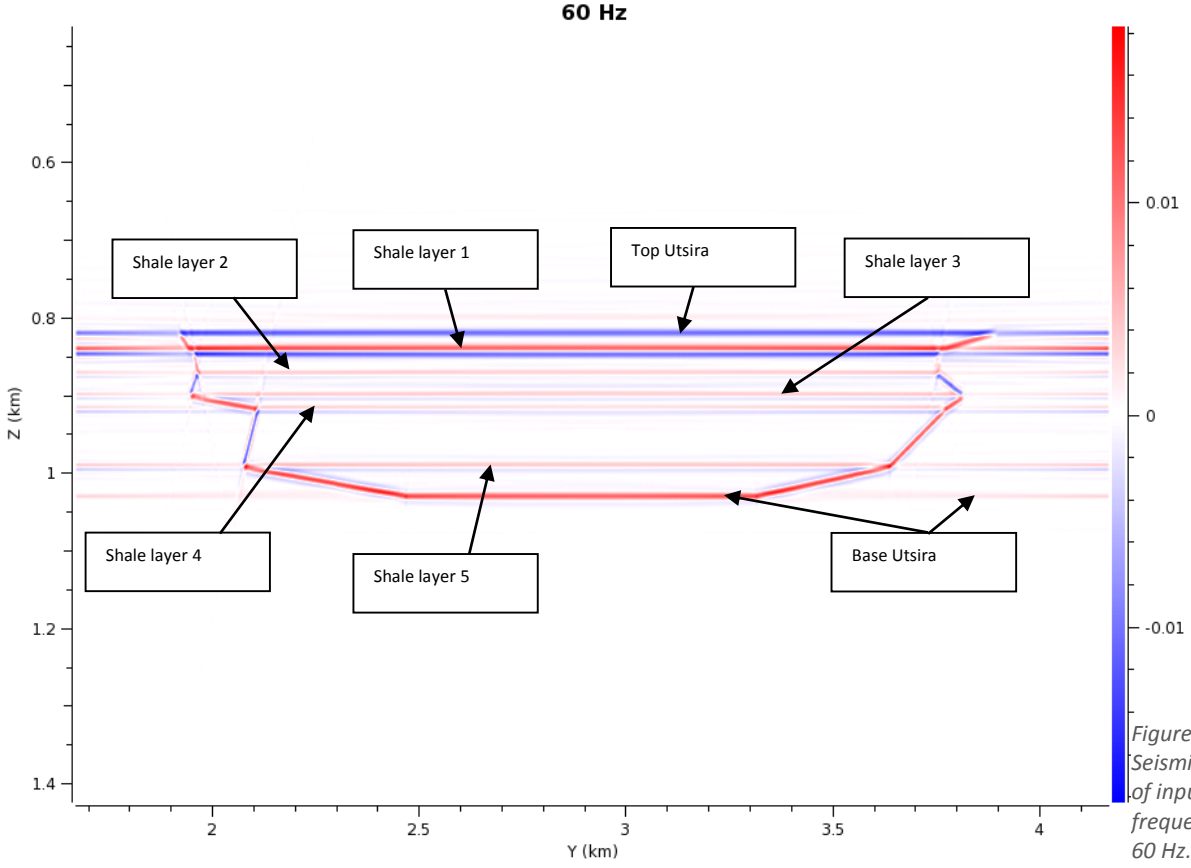

Figure 7.12 Seismic result of input frequency of 60 Hz.

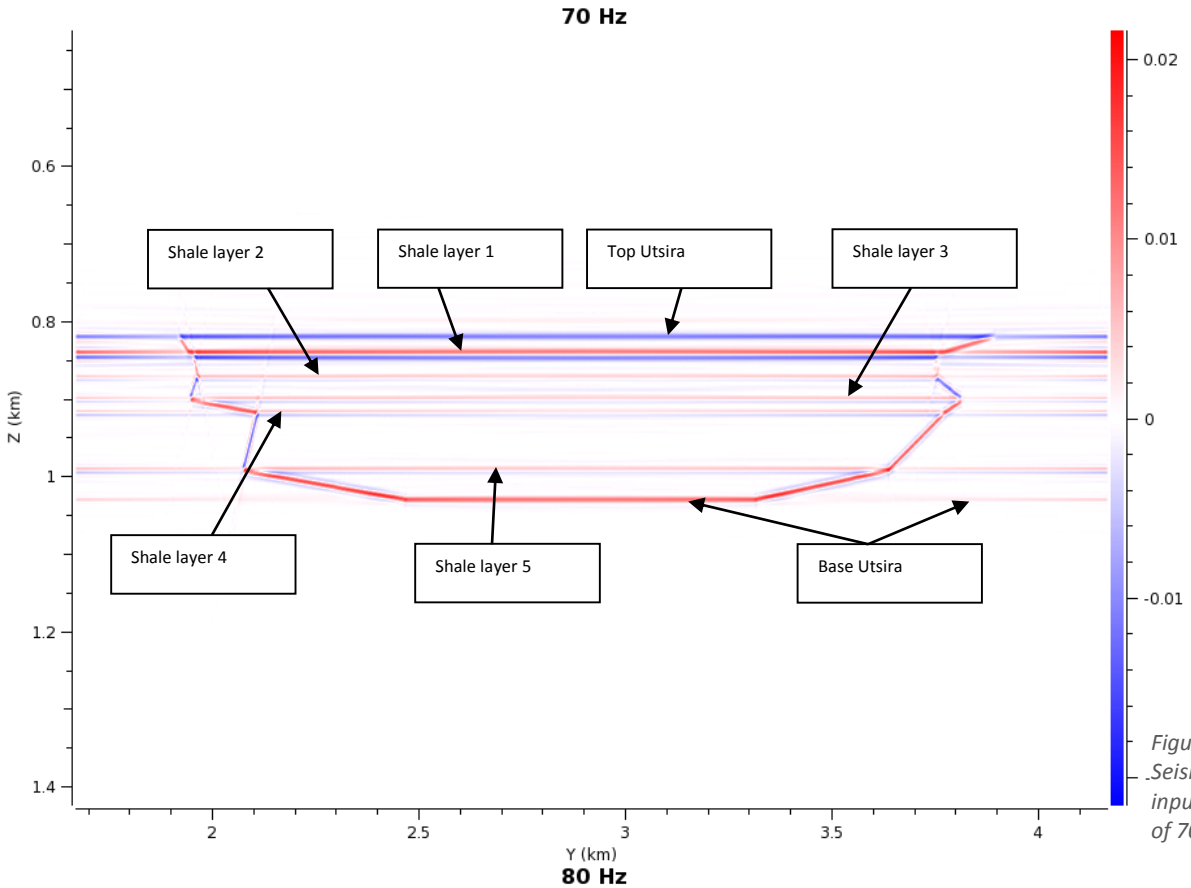

Figure 7.13 Seismic result of input reflectivity of 70 Hz.

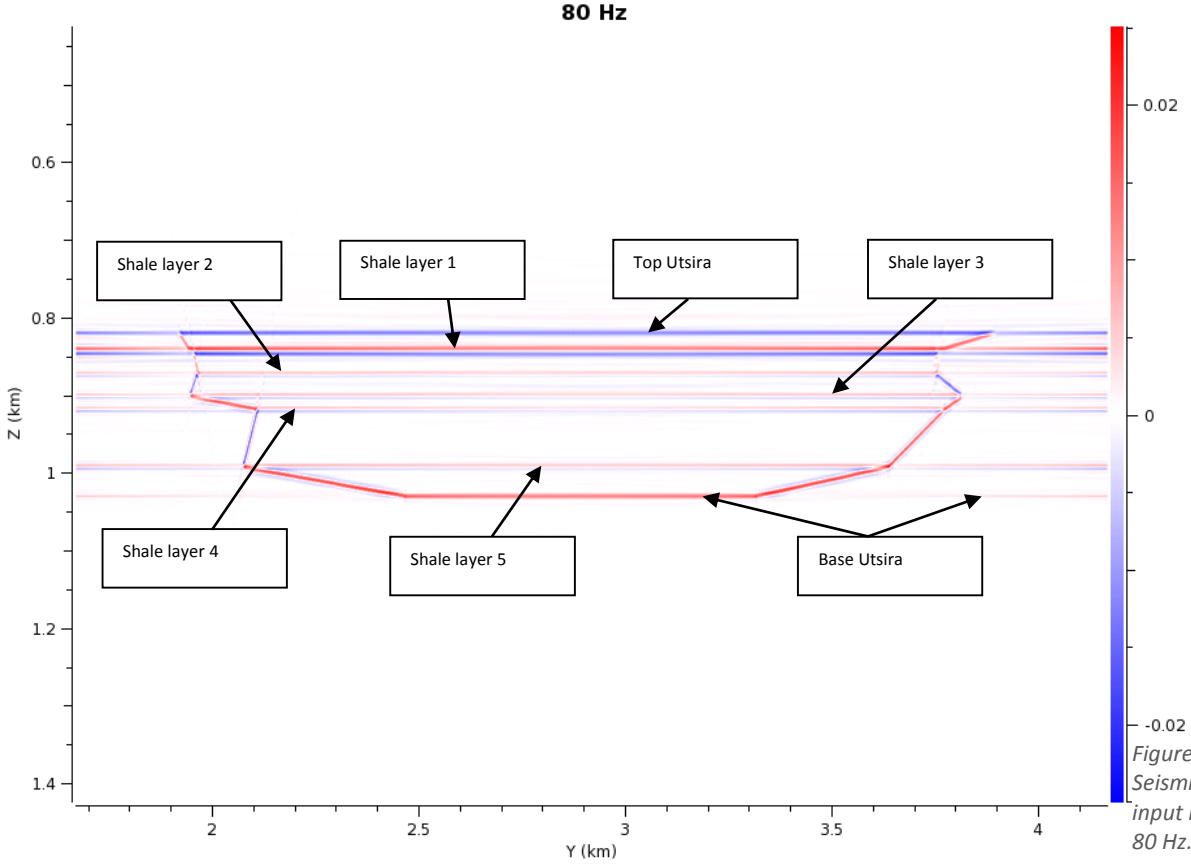

Figure 7.14 Seismic result of input reflectivity of 80 Hz.

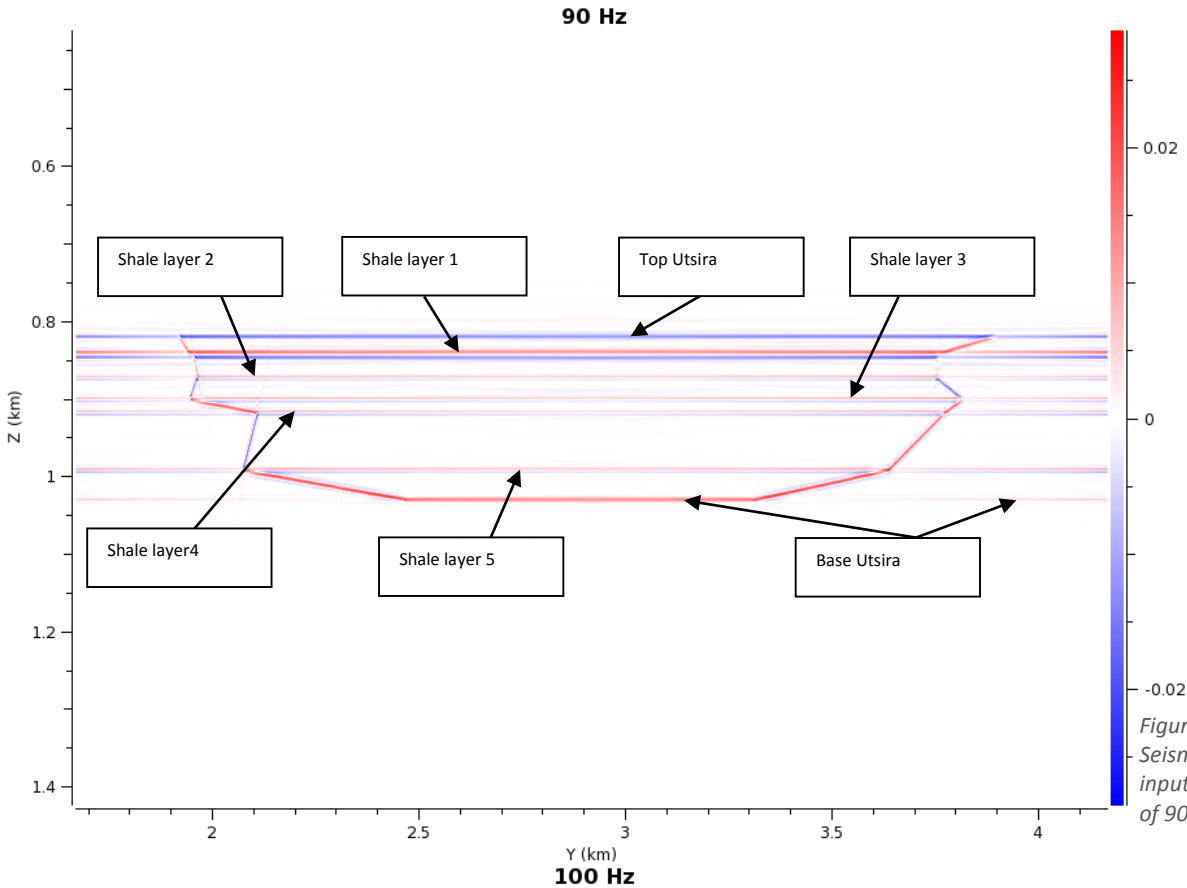

Figure 7.15 Seismic result of input reflectivity of 90 Hz.

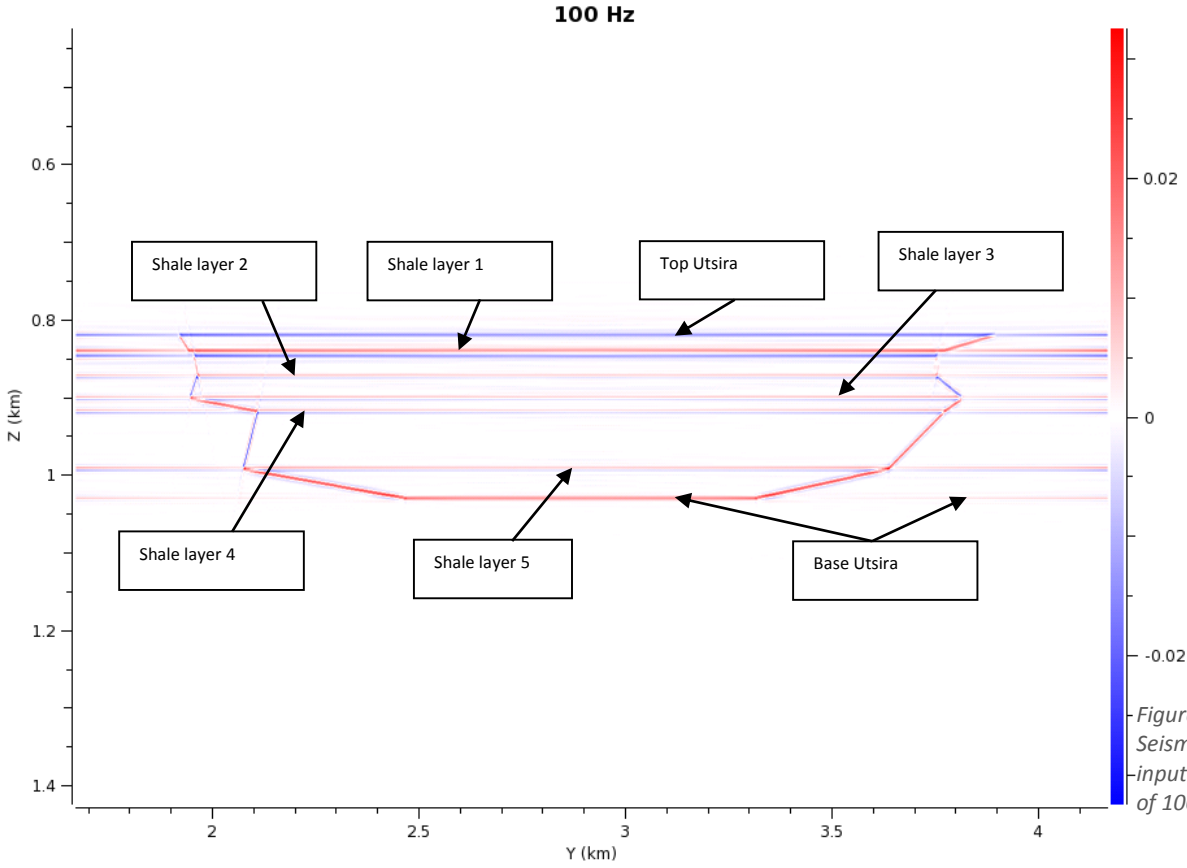

Figure 7.16 Seismic result of input reflectivity of 100 Hz.

7.2.2 The Point-Spread Function

The PSF is frequency dependent and $\mathbf{I_{SR}}$ dependent. How the PSF is varying in respect to different frequency is shown in Figure 7.17. As mentioned earlier, smallest frequency will give the lowest vertical and horizontal resolution, and this is very clear on the PSF for 10 Hz. This PSF is biggest, hence implying lowest resolution.

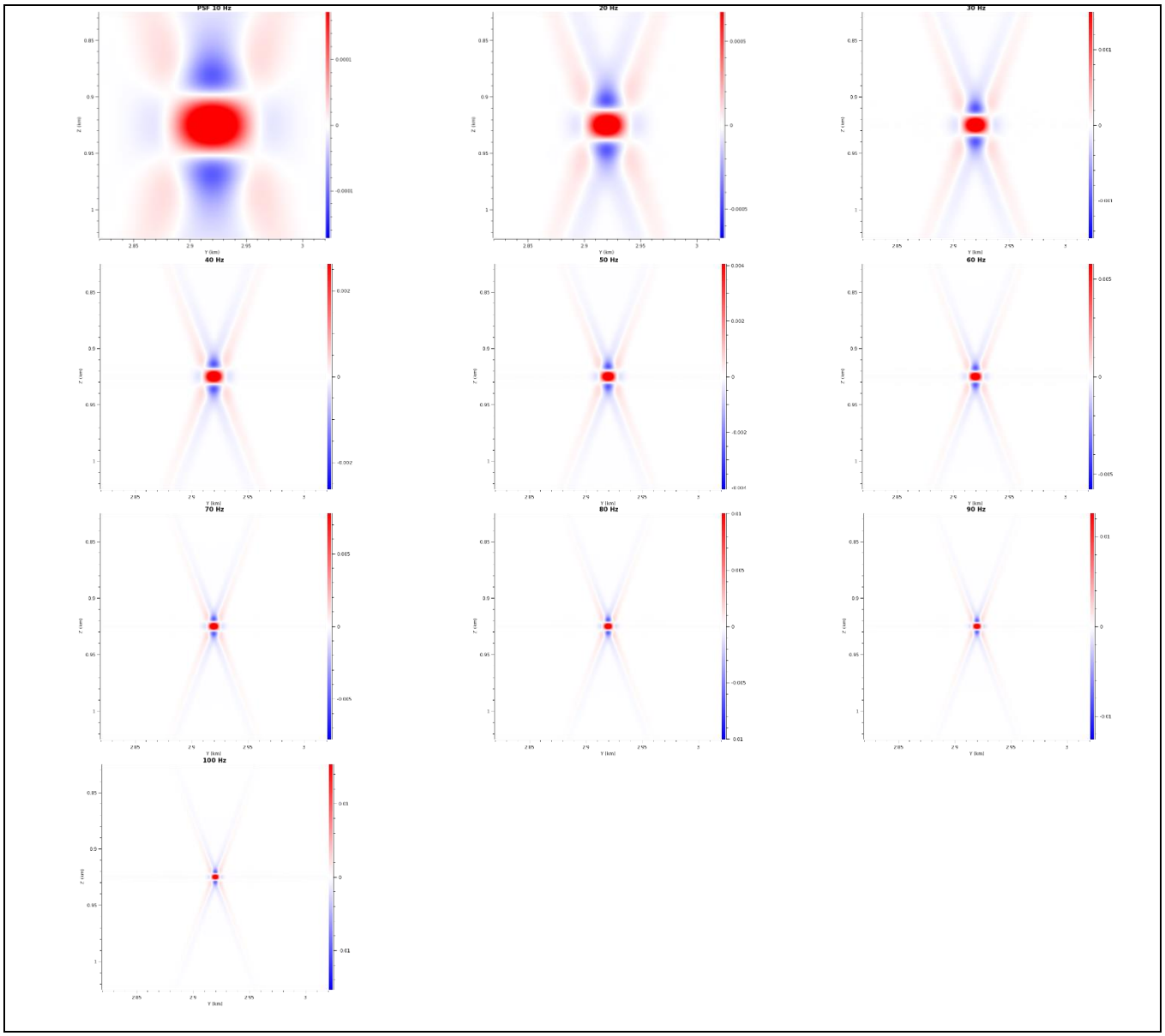

Figure 7.17 The PSF for different frequency input ranging from 10-100 Hz.

The PSFs gives information about the horizontal and vertical resolution listed in Table 7.3

Table 7.3 Overview of the vertical and horizontal resolution extracted from the PSF with different frequency.

Frequency	Vertical resolution	Horizontal resolution
10 Hz	54 m	85 m
20 Hz	26 m	42 m
30 Hz	18 m	28 m
40 Hz	14 m	21 m
50 Hz	10 m	17 m
60 Hz	9 m	14 m
70 Hz	8 m	12 m
80 Hz	7 m	10 m
90 Hz	6 m	9,5 m
100 Hz	5,4 m	8 m

7.2.3 Dip and azimuth of illumination vectors

The plotted $\mathbf{I_{SR}}$ for this workflow is equal to the one in Figure 7.5. This is due to the same survey parameters, same depth of the target area and same background model.

7.3 Change of incident angle

Reservoir model 2 (Figure 6.10) is also used in this workflow with elastic parameters equal to a 20 % CO_2 saturation. This means a P-velocity of 1563 m/s, an S-velocity equal to 650 m/s and density equal to 2031 kg/m^3. In this modeling, ricker zero 30 Hz is used as the input frequency since this is normal to use. The survey parameters and the PSDM parameters are equal to the ones in Table 6.7 and Table 6.8. The size of the target is equal to 2,5 km in Y-direction and 1 km in Z-direction. The angle range is used in incident angle selection under PSDM parameters, and the angles are varying from 0-50°, with a sample window of 10°. This gives an $\mathbf{I_{SR}}$ coverage of 6,17 %, 20,63 %, 19,72%, 15,8%, 13,46 % and 12,22 % for respectively incident angle of 0°, 10°, 20°, 30°, 40° and 50°. In this workflow the sampling in Y-Z-direction is the same as the previous. This is smaller than the standard to get the reflectivity image well gridded. An overview of the various PSDM parameters and frequency used is listed in Table 7.4.

Table 7.4 Overview of the PSDM parameters and frequency used in the workflow 7.3.

Depth Z (km)	0.925
Size (km)	2.5 , 1.0
Sampling (km)	0.001 , 0.001
Incident angle selection	Angle range, 0˚-50°
Input frequency	Ricker Zero 30 Hz

7.3.1 The seismic image and the reflectivity

Figure 7.18 to Figure 7.23 illustrates the final seismic images. It is a clear difference with increasing incident angle. The biggest difference is between 40° and 50°. The image from an angle of 50° is very blurry, and not all reflectors is visible. The reflectivity of incident angle of 40° and 50° (Figure 7.24 and Figure 7.25), illustrates that some reflectors will not be visible on the final seismic image. This is due to overcritical reflectors, meaning that the incident angle is bigger than the critical incident angle. In that case, incident angles of 40° and 50° are not to preferred.

The reflectivity from incident angles between 0° and 30° show all the same interfaces as in the previous workflow (Figure 7.6), only with different reflection values, and the final seismic images will contain all interfaces. With incident angle of 0°, 10° and 20° is all shale layers visible, but with an icident angle of 20°, is a blue reflection not visible between shale layer 3 and 4, and the interfaces are partly interfering. With incident angle of 30° is shale layer 3 and 4 closer. They are interfering and it is not a clear gap inbetween.

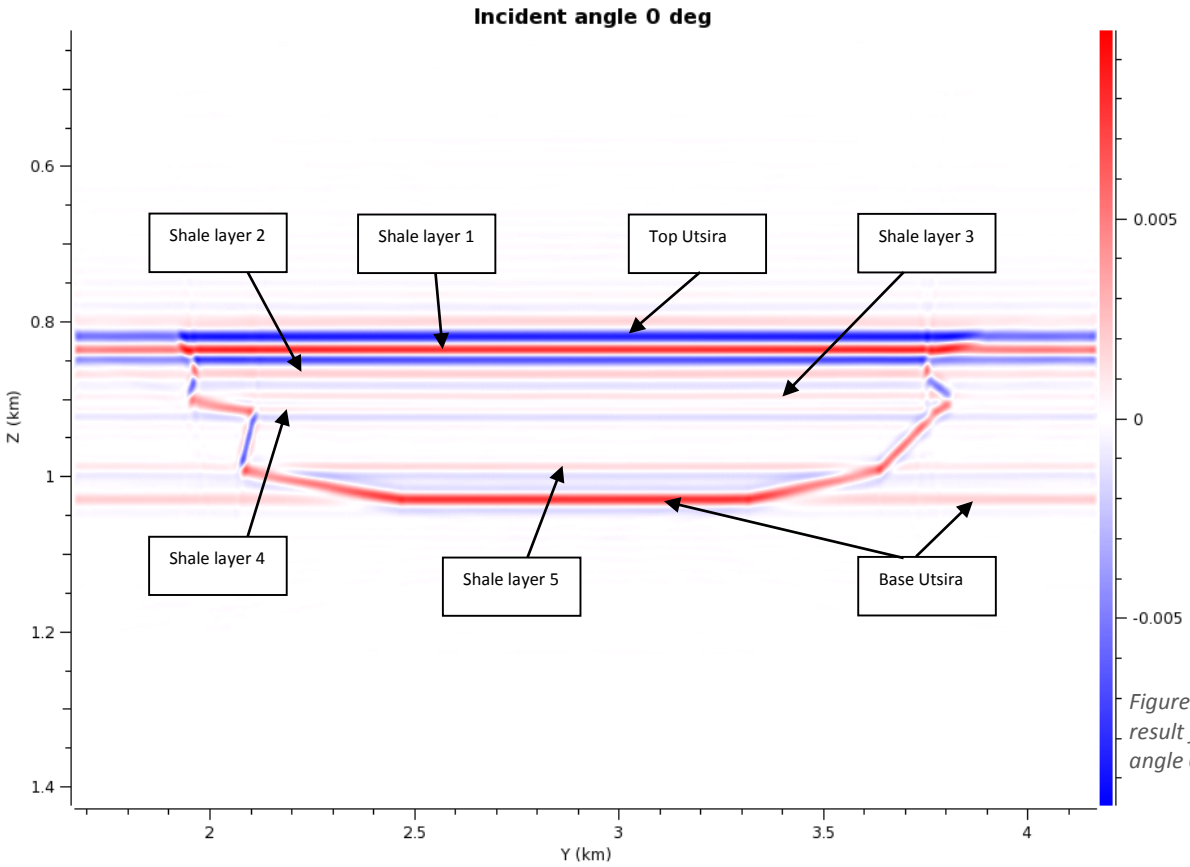

Figure 7.18 Seismic result from incident angle 0°.

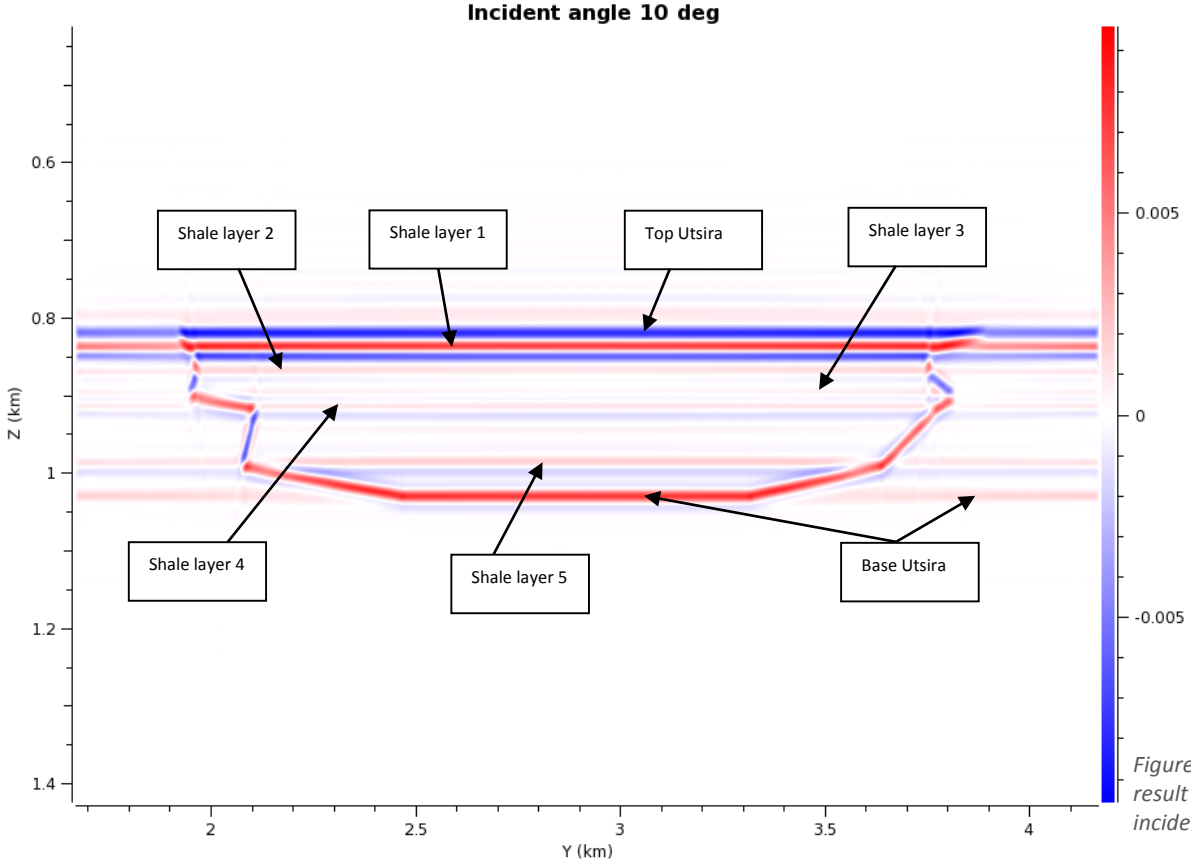

Figure 7.19 Seismic result from incident angle 10°.

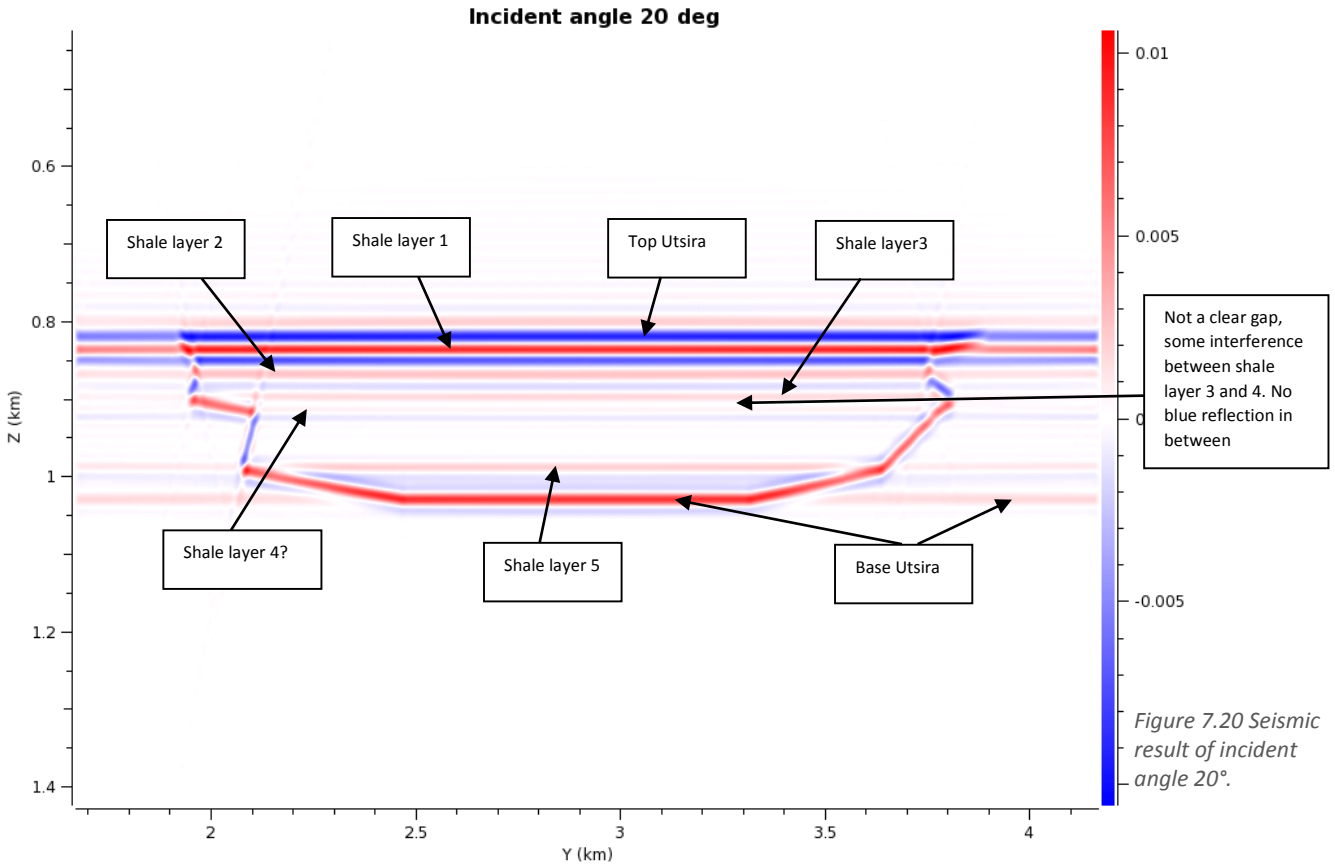

Figure 7.20 Seismic result of incident angle 20°.

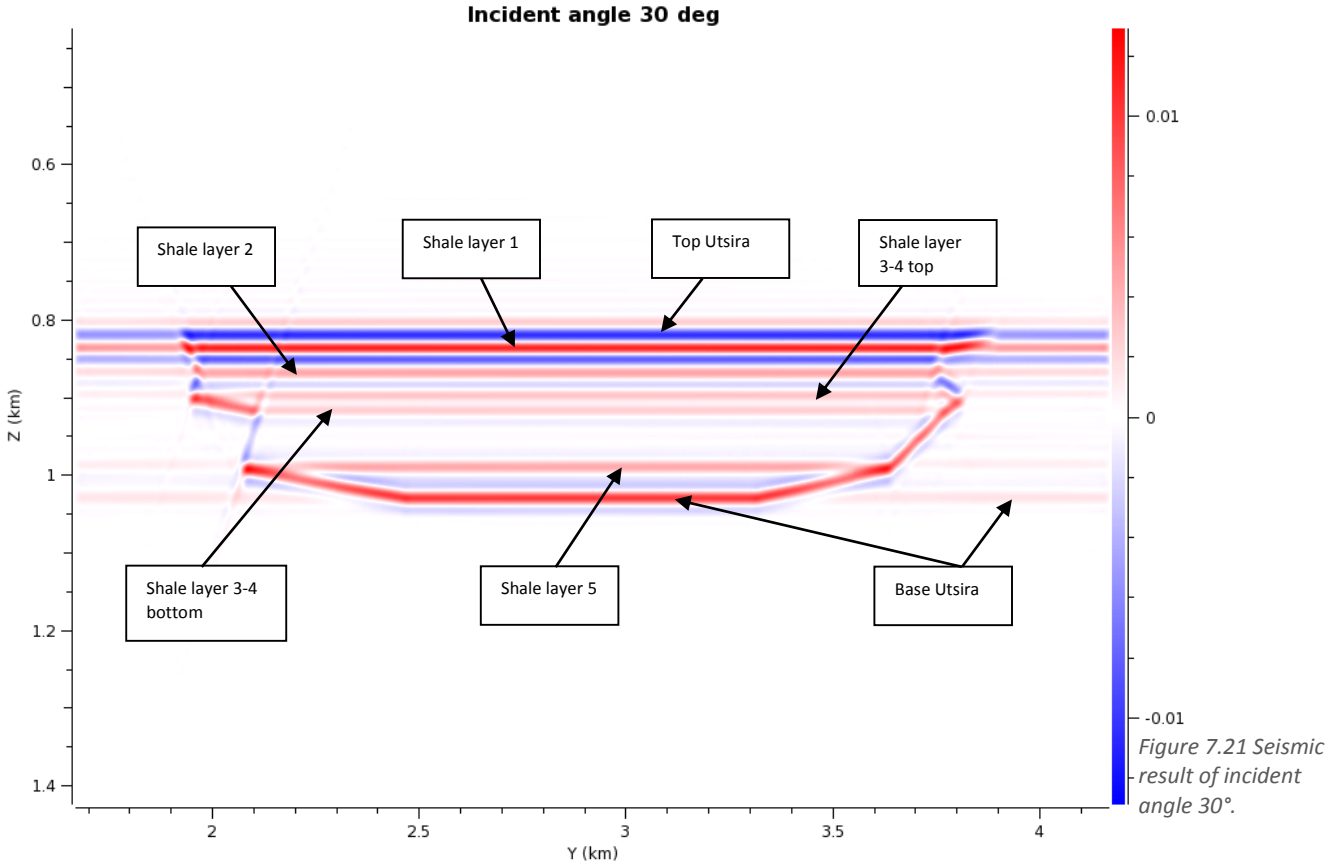

Figure 7.21 Seismic result of incident angle 30°.

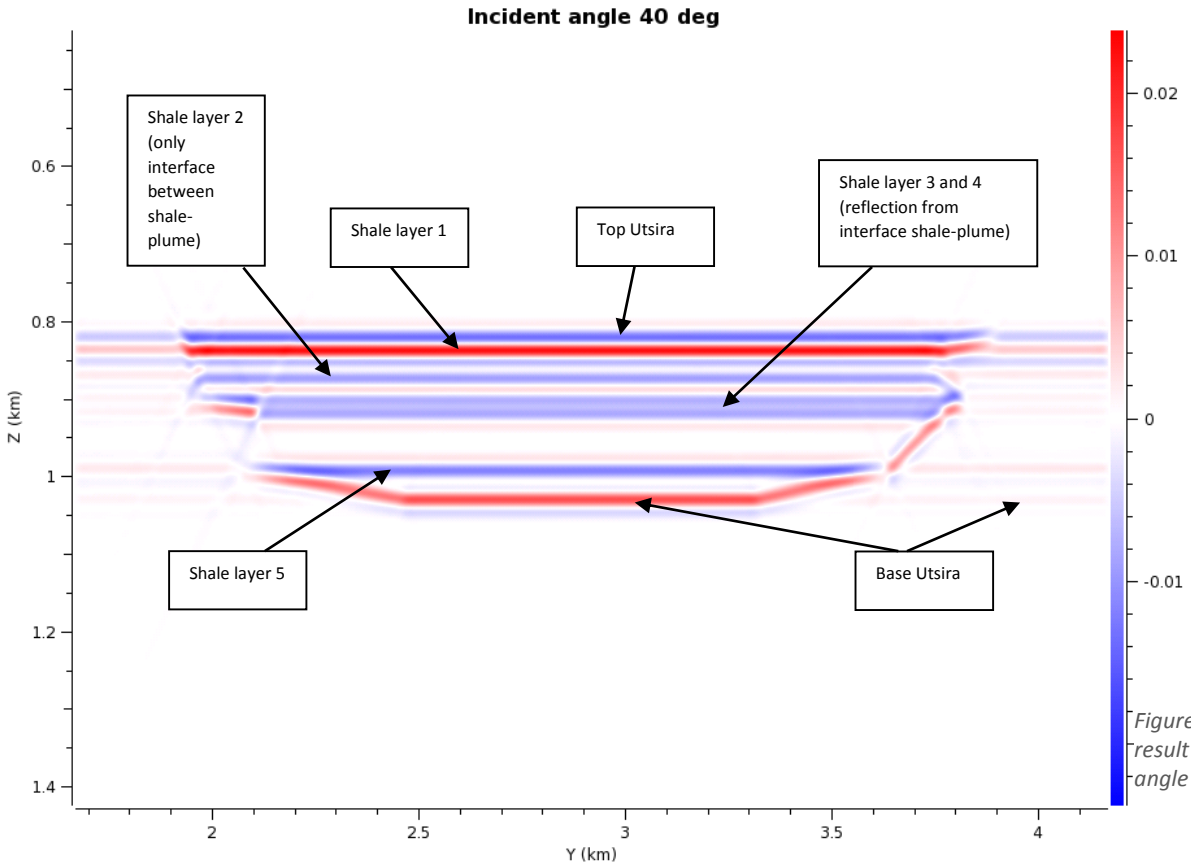

Figure 7.22 Seismic result of incident angle 40°.

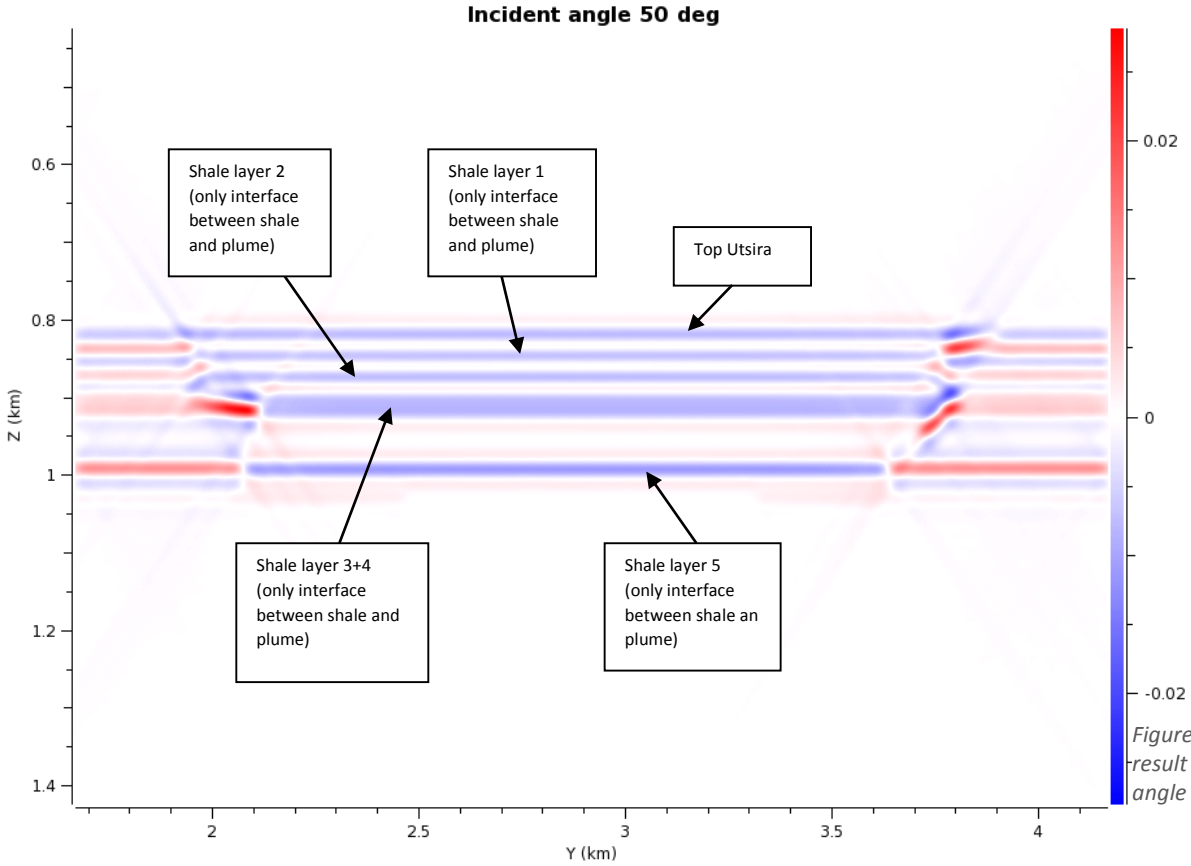

Figure 7.23 Seismic result of incident angle 50°.

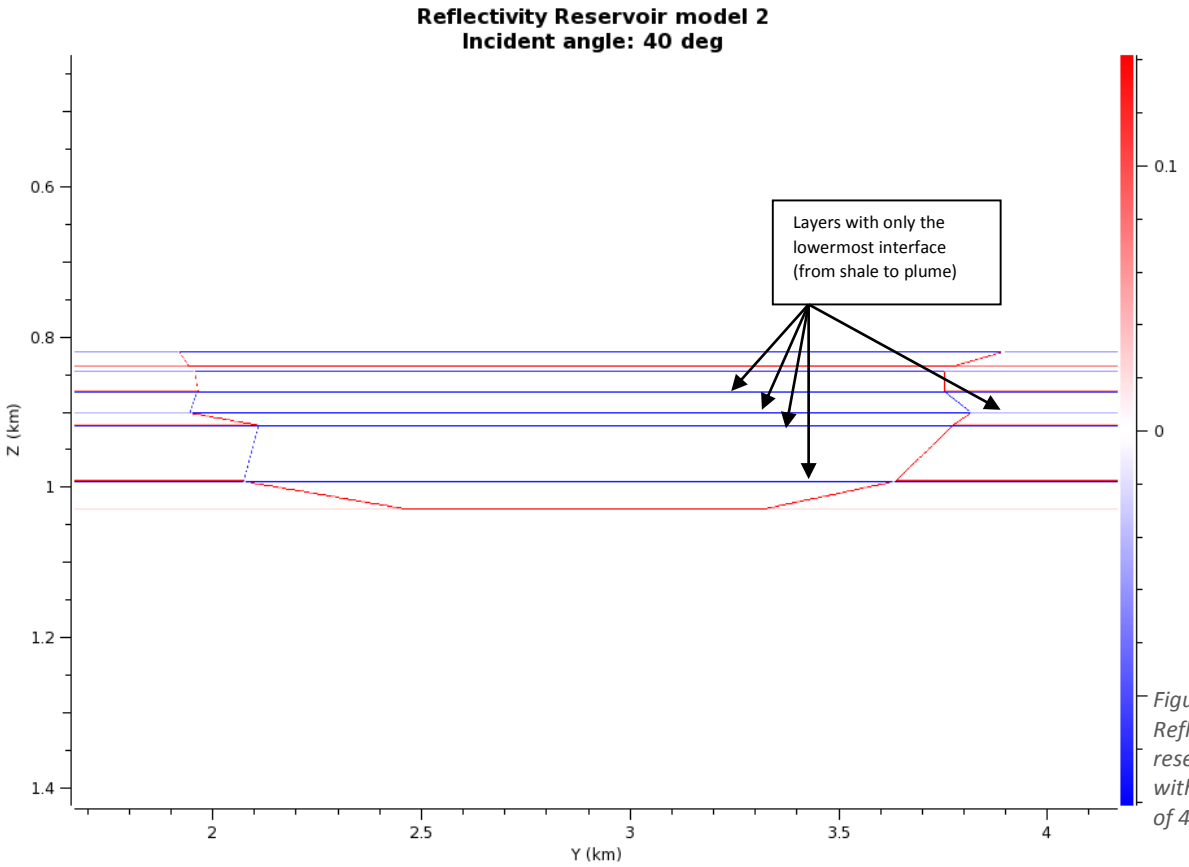

Figure 7.24 Reflectivity from reservoir model 2 with incident angle of 40°

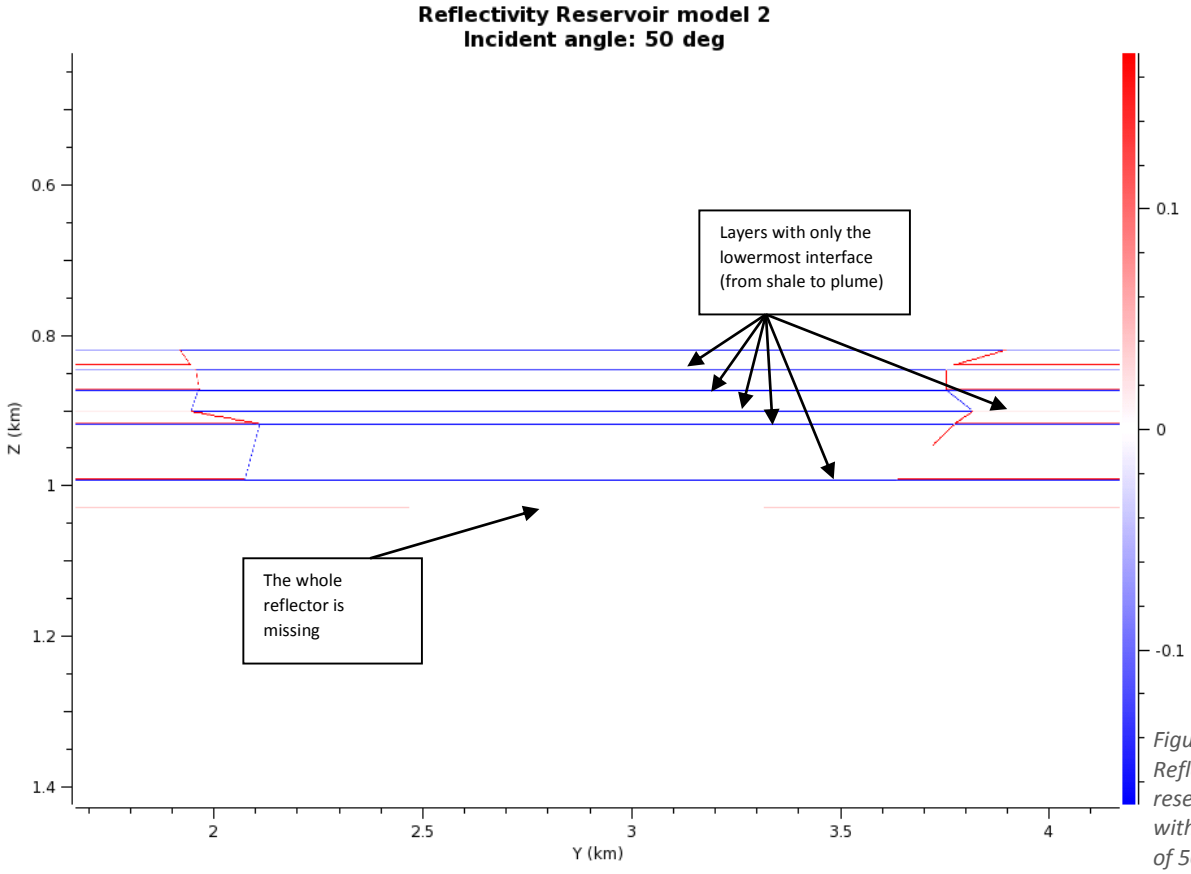

Figure 7.25 Reflectivity from reservoir model 2 with incident angle of 50°.

7.3.2 The Point-Spread Function

Figure 7.26 shows the various PSFs for each incident angle. As expected by looking at the PSDM images, is the best resolution with smaller angles. In addition, the PSF of an incident angle of 50° is distinguished from the others. In this case is the horizontal resolution measured to be about 90,6 m, and the vertical resolution is 18 m. The horizontal and vertical resolution at an incident angle of 0 ° is equal to 21 m and 20 m. The seismic result from 0° (Figure 7.18) and 50° (Figure 7.23) are reflecting the difference between the resolution.

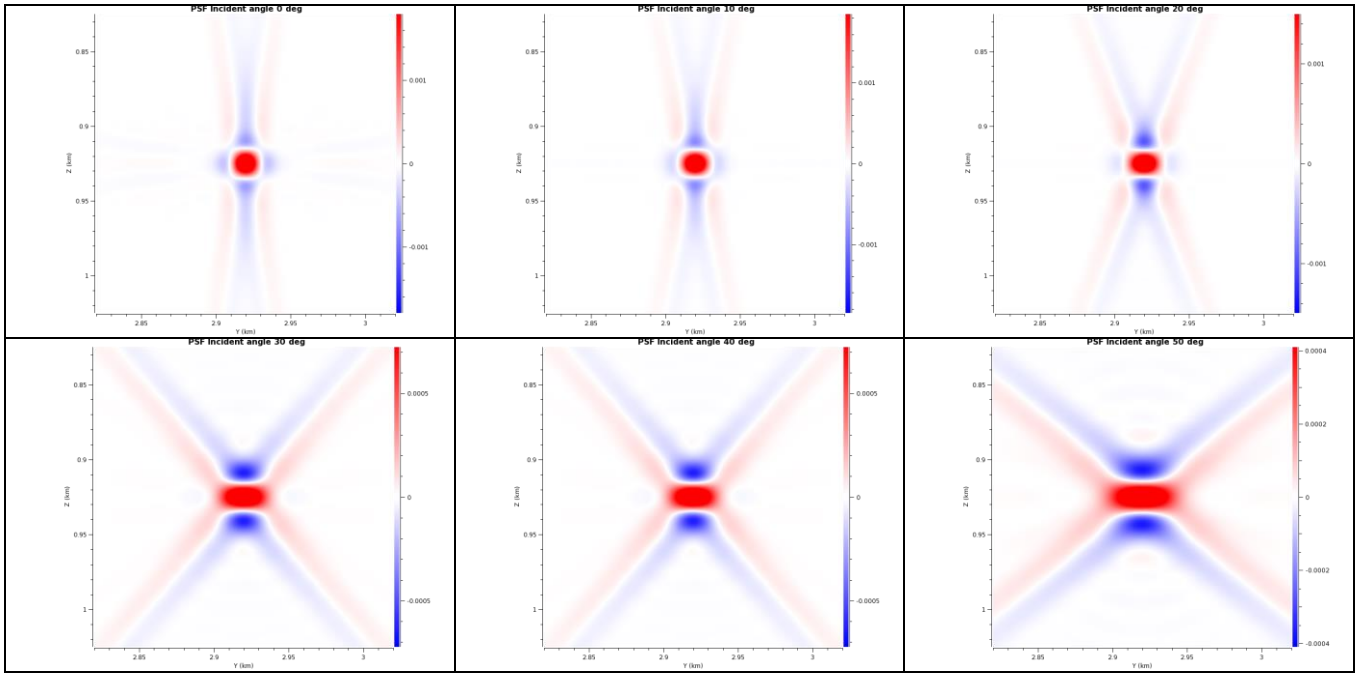

Figure 7.26 Showing PSF for different incident angle. We can clearly see a change in horizontal resolution.

An overview of the vertical and horizontal resolution extracted from the PSFs is illustrated in Table 7.5

Table 7.5 Overview of the horizontal and vertical resolution extracted from the PSFs.

Incident angle	Vertical resolution	Horizontal resolution
0°	20 m	21 m
10°	20 m	24 m
20°	18 m	28 m
30°	18 m	36 m
40°	18 m	50,4 m
50°	18 m	90,6 m

7.3.3 Dip and azimuth of illuminated vectors

The image of the illumination vectors showing dip and azimuth is equal to the one in the two previous workflows (Figure 7.5). The $\mathbf{I_{SR}}$ is dependent on the survey geometry (incident angle), depth of the target and background model. All these parameters is the same in the different workflows. The incident angle is varying in this workflow, but as mentioned earlier, will the $\mathbf{I_{SR}}$ plot always showing 100% of all $\mathbf{I_{SR}}$ available.

7.4 When is the plume not visible on the seismic?

The modeling approach of this workflow is to determine the size of the plume when it is no longer visible on the seismic. The reservoir models with varying vertical and horizontal thickness is used. Elastic parameters to a CO_2 plume with 20 % CO_2 saturation is used. This means the plume has a P-velocity of 1563 m/s, an S-velocity equal to 650 m/s and the density is equal to 2031 kg/m^3. The frequency pulse used is either ricker zero 30 Hz or ricker zero 60 Hz. Survey parameters and PSDM parameters are equal to Table 6.7 and Table 6.8. Angle range with incident angle of 20° is used, giving a $\mathbf{I_{SR}}$ sampling window of 15-25° to be 19,66 %. The size of the target is equal to 2,5 km in Y-direction and 1 km in Z-direction. Compared to the previous workflows is the depth of the target shallower, at 821 m. This is because the PSF and the PSDM filter should be calculated in the area where we find the plume. A sampling of 0,5 m (0,0005km) is used in both Y- and Z-direction. This was necessary to get well gridded reflectivity images since some of the plumes are only 1 m in horizontal or vertical direction. Overview of the new PSDM parameters and the input frequency is listed in Table 7.6.

Reservoir model 3, reservoir model 4, reservoir model 5, reservoir model 6, reservoir model 7, reservoir model 8, reservoir model 9 and reservoir model 10 is used when looking at different vertical thickness. When looking at differences in horizontal thickness, reservoir model 11, reservoir model 12, reservoir model 13, reservoir model 14, reservoir model 15, reservoir model 16, reservoir model 17 and reservoir model 18 is used. All these models are modeled with an input pulse of both ricker zero 30 Hz and 60 Hz.

True amplitude is the reflection method used in this workflow (same as all the previous), and as mentioned in chapter 6.3.4 will this method weight each reflection equally. With true amplitude, we assume attenuation effects have been taken into account prior to the modeling. Due to this, will the result seismic image show reflections weighted equally, but with some diffractions from abrupt interfaces looking like a footprint of the PSF.

Table 7.6 Overview of the PSDM parameters and input frequency used in workflow 7.4

Depth Z (km)	0.821
Size (km)	2.5 , 1.0
Sampling (km)	0.0005 , 0.0005
Incident angle selection	Angle range, 20°-20°
Input frequency	Ricker Zero 30 Hz and 60 Hz

7.4.1 The seismic image and Point-Spread Function with 30 Hz

Figure 7.28 to Figure 7.35 shows the final seismic images with varying vertical thickness of the plume. The horizontal extent is the same for all pictures, about 2 km. In the images from vertical thickness of 50 m, 40 m, 30 m and 20 m(Figure 7.28 - Figure 7.31), it is visible diffractions due to the abrupt interfaces. These diffractions is a footprint of the PSF (Figure 7.27). It is clearly a gap between the top and bottom interface for vertical thickness 50 m and 40 m. With thickness of 30 m and 20 m will the plume be visible, but it is not a clear gap between the top and bottom interface. For vertical thickness of 10 m or thinner, is the reflection from the caprock to the reservoir a bit higher where we expected to see the plume, the interfaces are partly interfering. The result from thickness 3 m and 1 m is almost equal, except that the strength of the reflection is not changing remarkably in the area of the plume with vertical thickness of 1 m.

Figure 7.36 to Figure 7.42 shows the final seismic images with varying horizontal thickness of the plume. The vertical extent is the same for all pictures, meaning a height of the plume about 210 m (same as the reservoir thickness). Vertical reflections is not visible on any of the seismic from the vertical plumes, only diffractions from abrupt interfaces is visible. The diffractions is interfering from horizontal thickness of 10 m or smaller, and the results is equal.

Figure 7.27 shows the PSF for this workflow. From the PSF we get a vertical resolution of 20 m, and a horizontal resolution of 28 m.

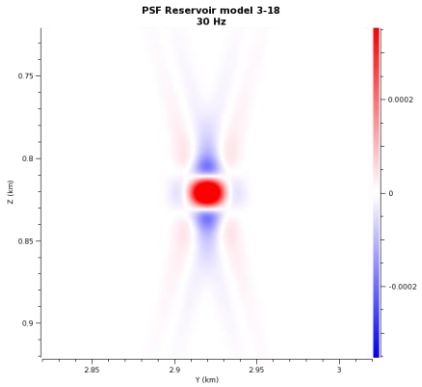

Figure 7.27 PSF reservoir model 3-18 with an input frequency of 30 Hz.

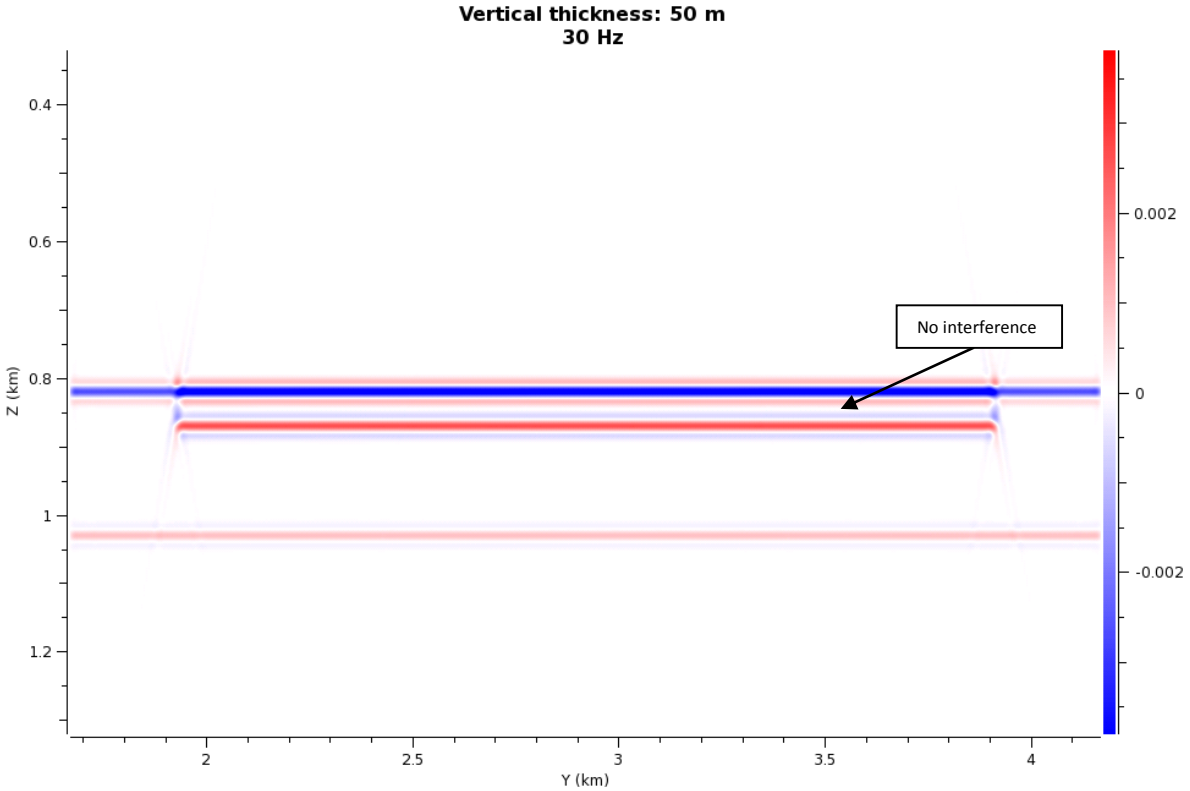

Figure 7.28 Seismic result of a plume with vertical thickness of 50 m, and input frequency of 30 Hz.

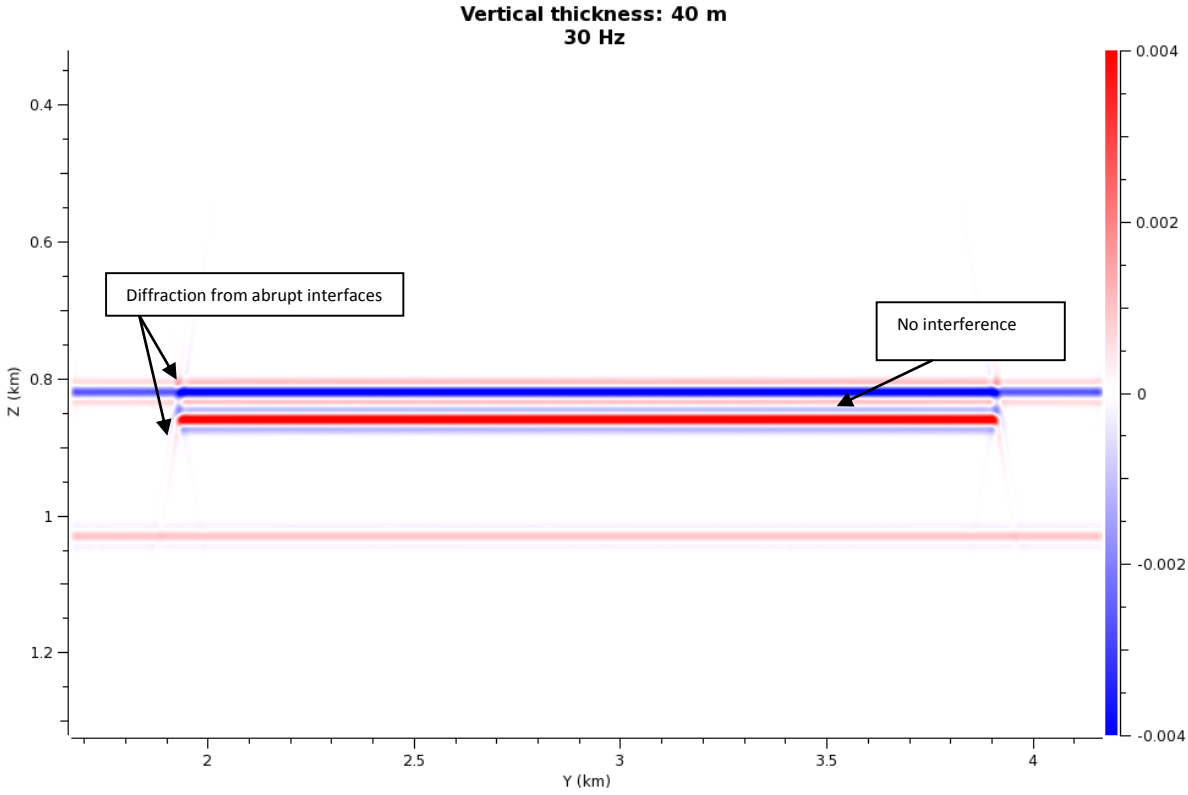

Figure 7.29 Seismic result of a plume with vertical thickness of 40 m, and input frequency of 30 Hz.

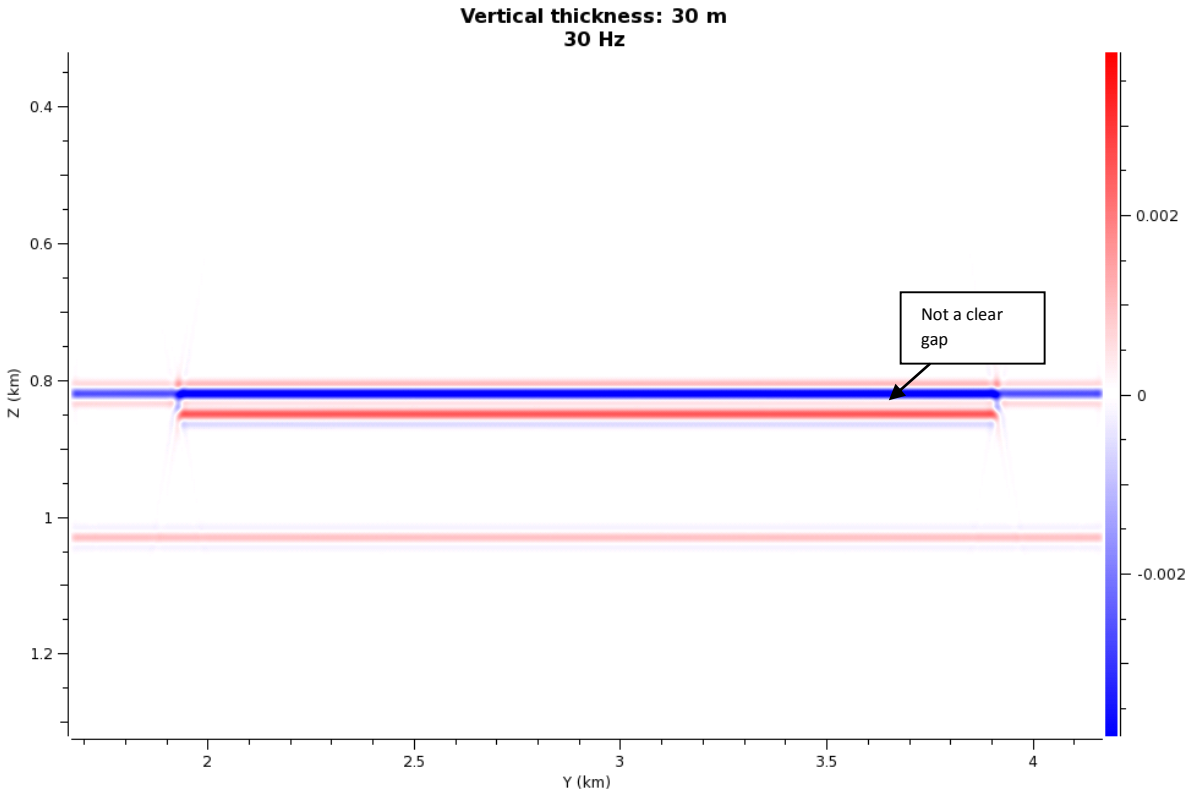

Figure 7.30 Seismic result of a plume with vertical thickness of 30 m, and input frequency of 30 Hz.

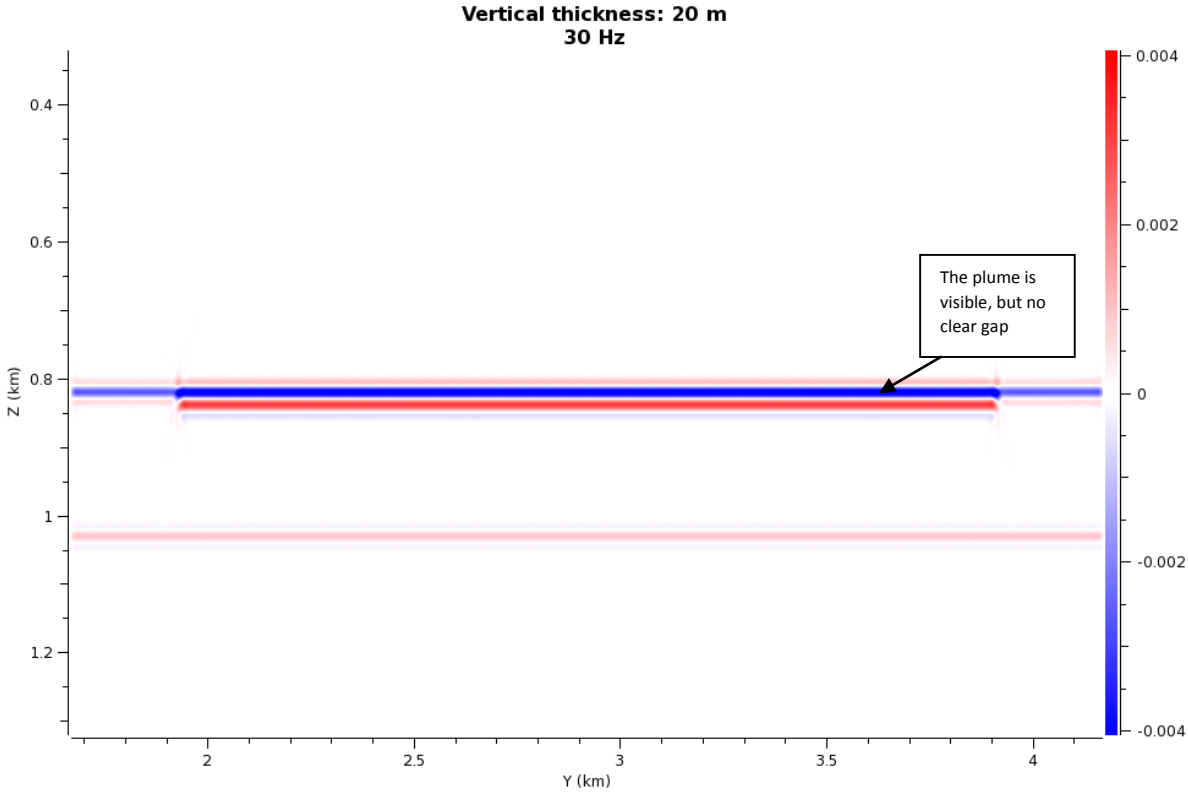

Figure 7.31 Seismic result of a plume with vertical thickness of 20 m, and input frequency of 30 Hz.

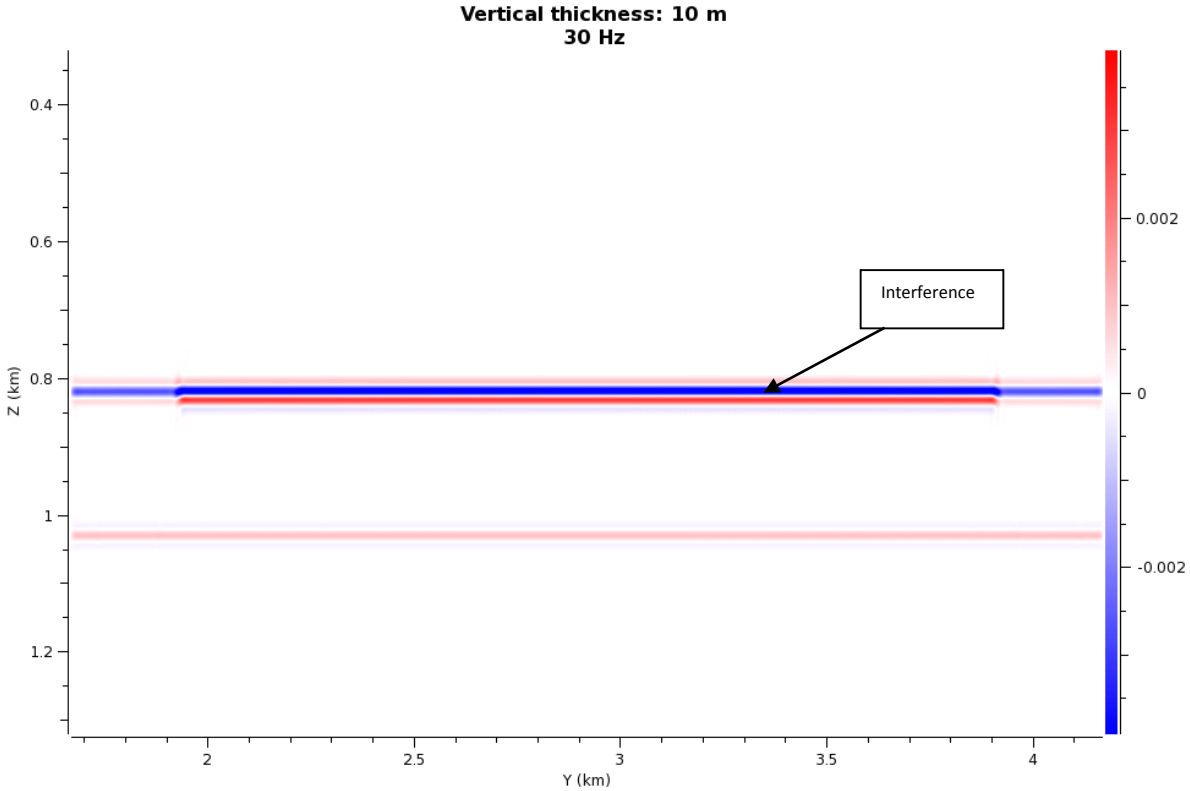

Figure 7.32 Seismic result of a plume with vertical thickness of 10 m, and input frequency of 30 Hz.

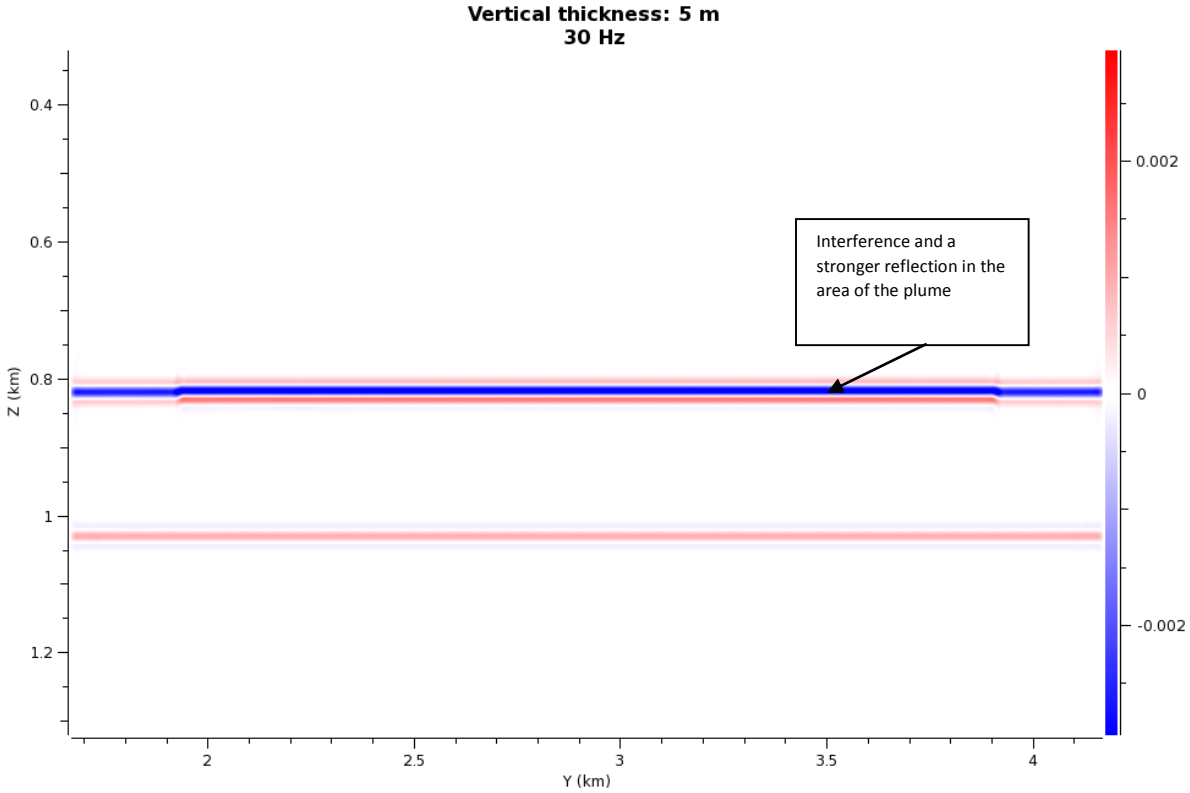

Figure 7.33 Seismic result of a plume with vertical thickness of 5 m, and input frequency of 30 Hz.

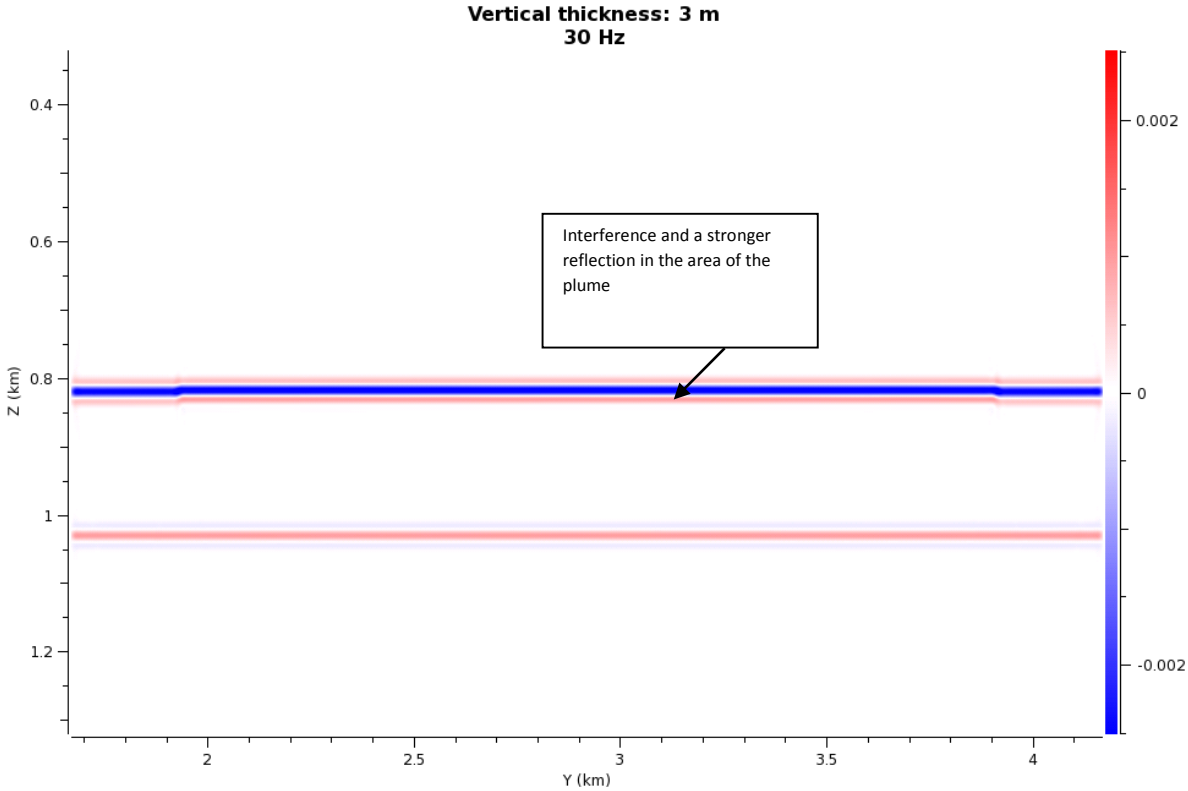

Figure 7.34 Seismic result of a plume with vertical thickness of 3 m, and input frequency of 30 Hz.

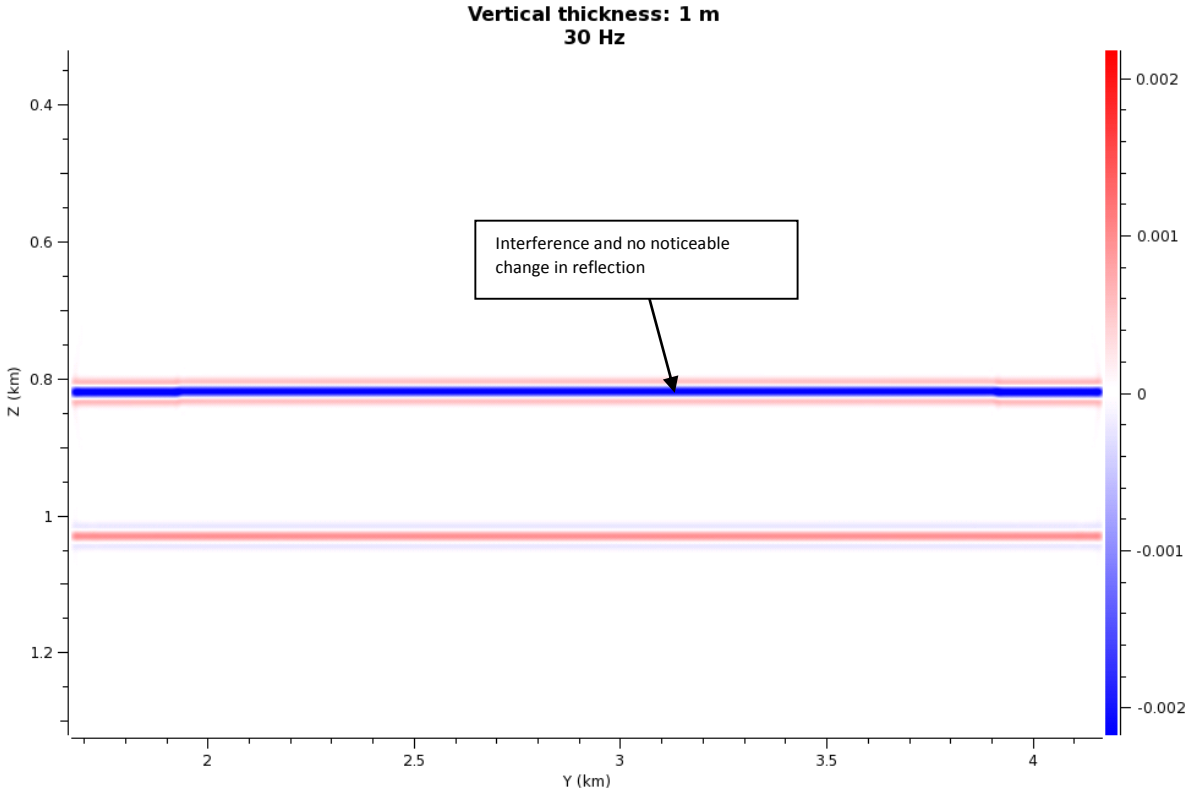

Figure 7.35 Seismic result of a plume with vertical thickness of 1 m, and input frequency of 30 Hz.

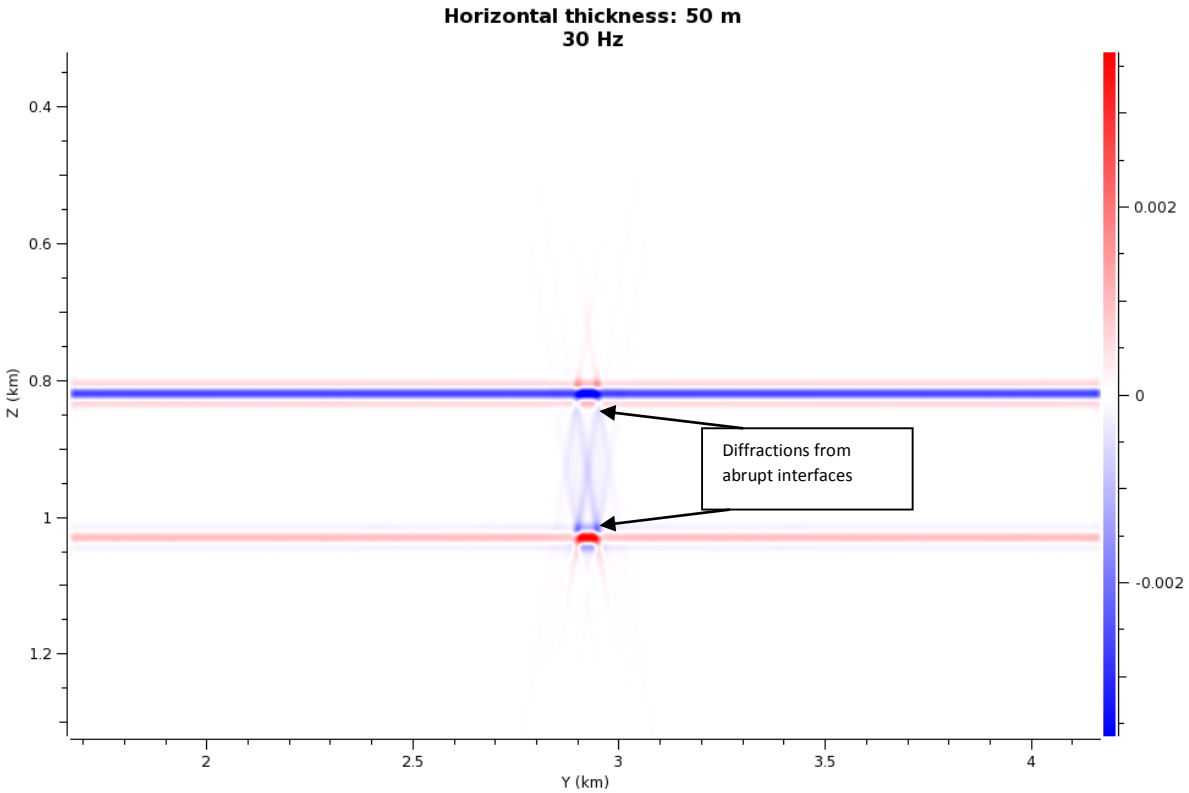

Figure 7.36 Seismic result of a plume with horizontal thickness of 50 m, and input frequency of 30 Hz.

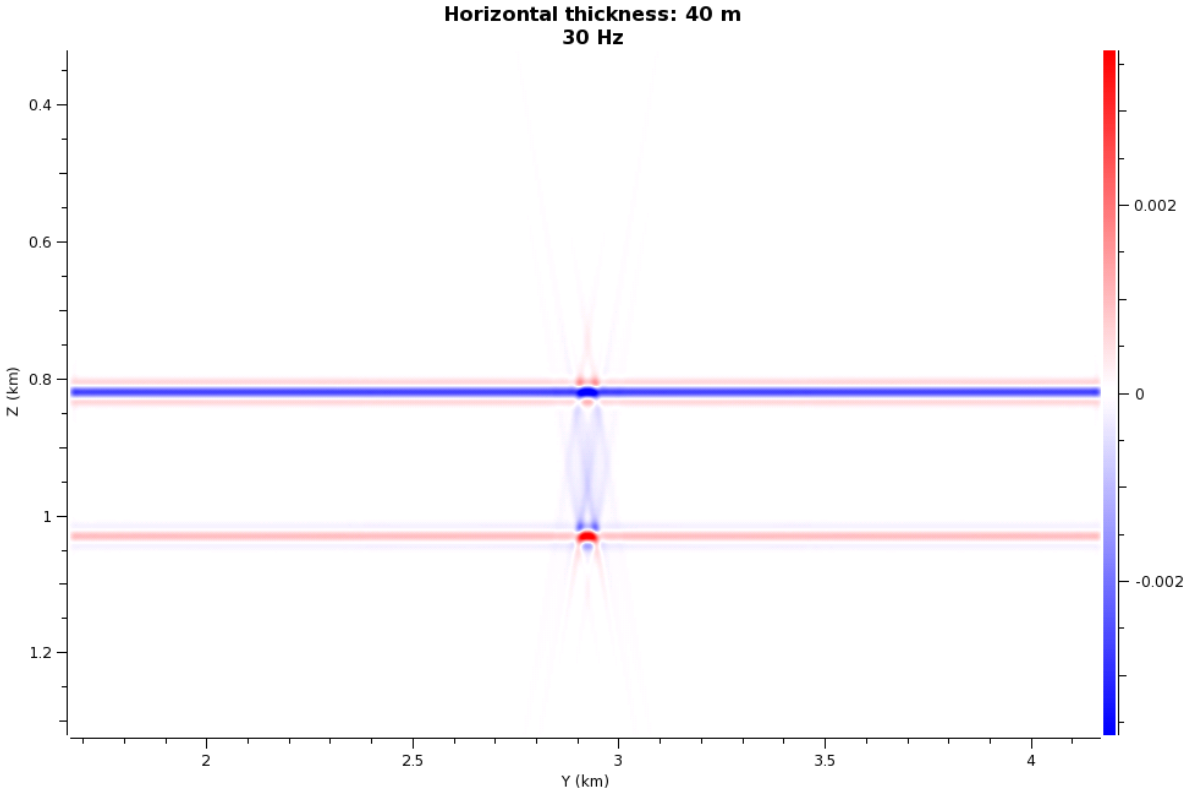

Figure 7.37 Seismic result of a plume with horizontal thickness of 40 m, and input frequency of 30 Hz.

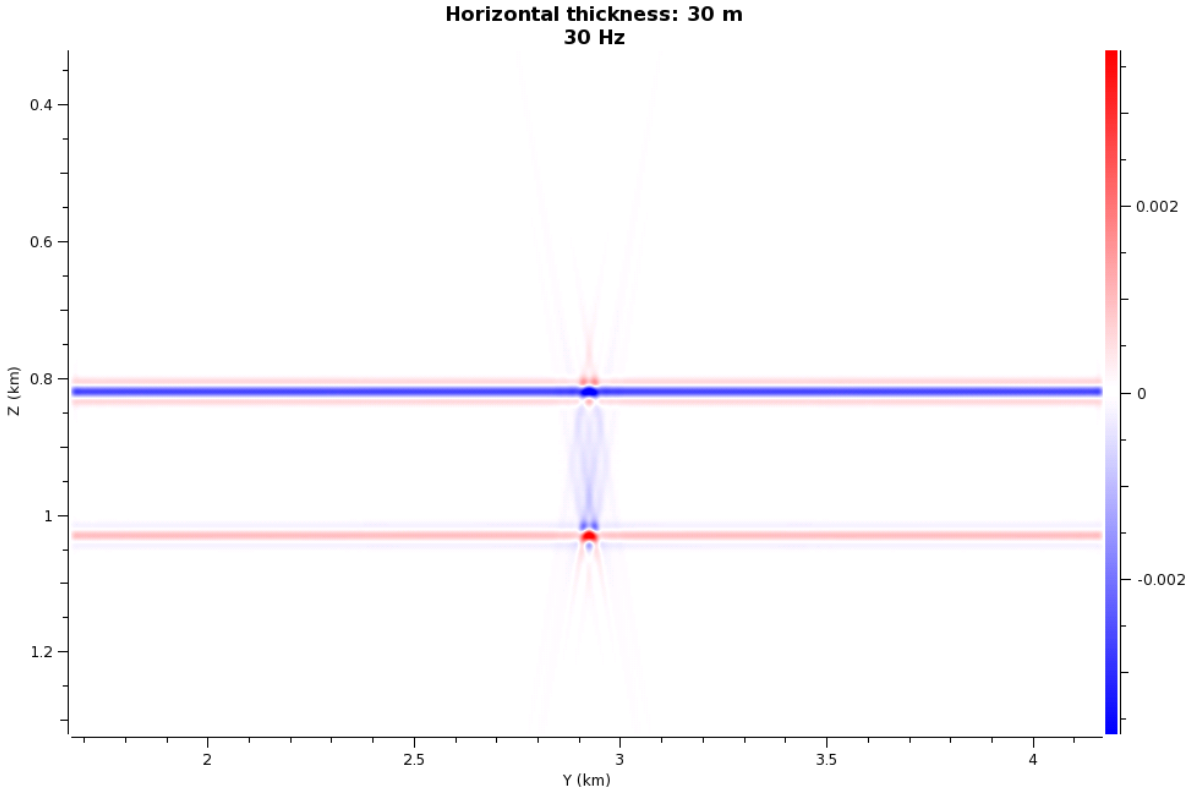

Figure 7.38 Seismic result of a plume with horizontal thickness of 30 m, and input frequency of 30 Hz.

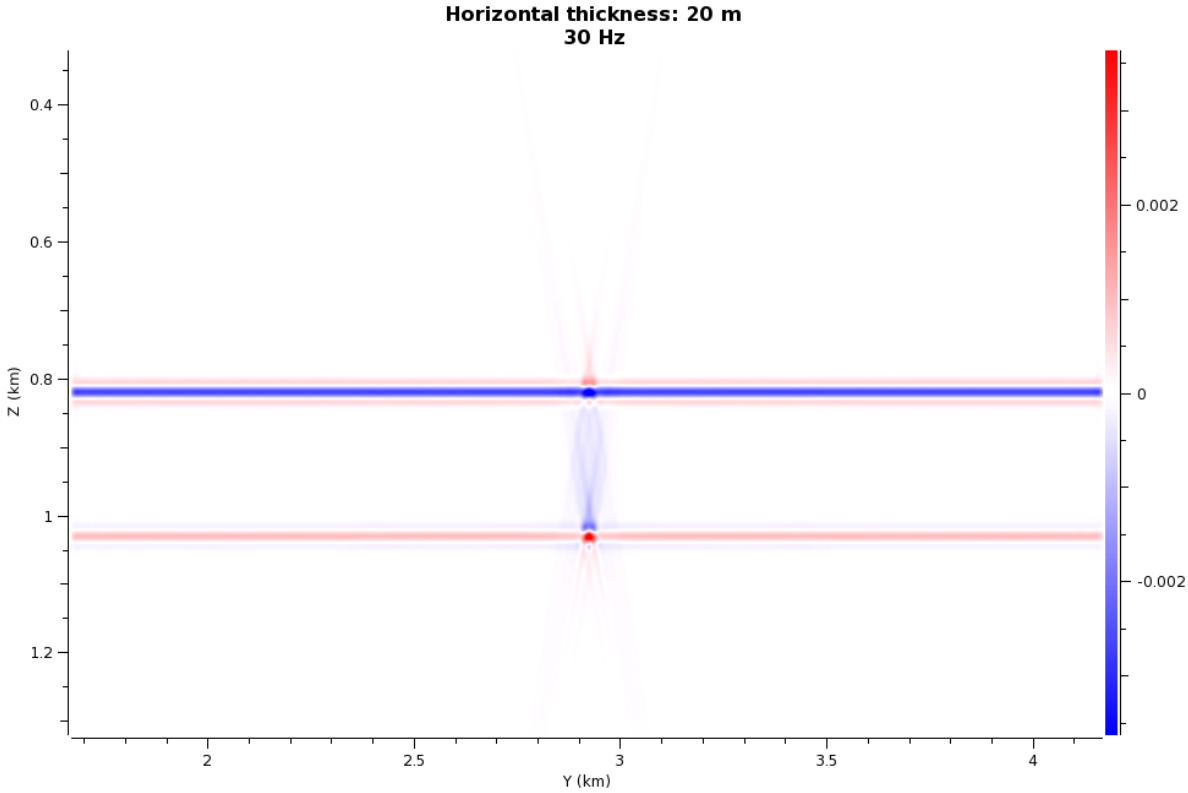

Figure 7.39 Seismic result of a plume with horizontal thickness of 20 m, and input frequency of 30 Hz.

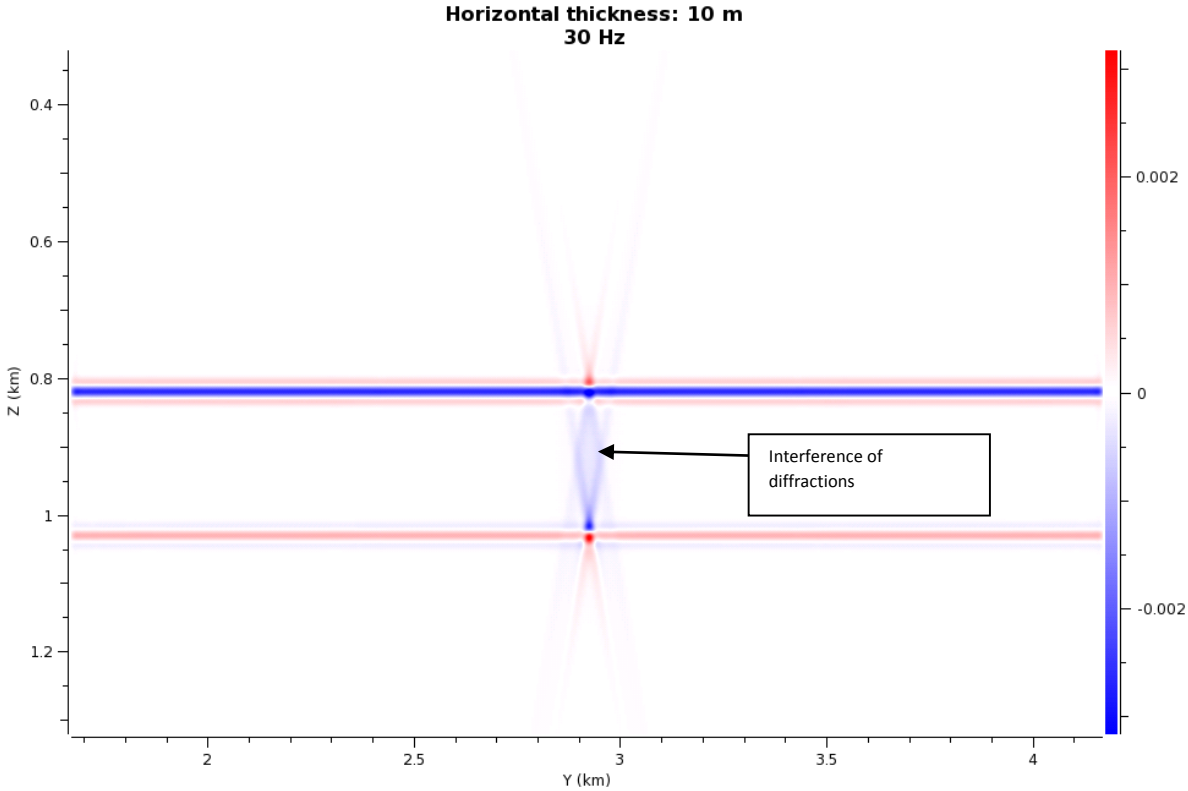

Figure 7.40 Seismic result of a plume with horizontal thickness of 10 m, and input frequency of 30 Hz.

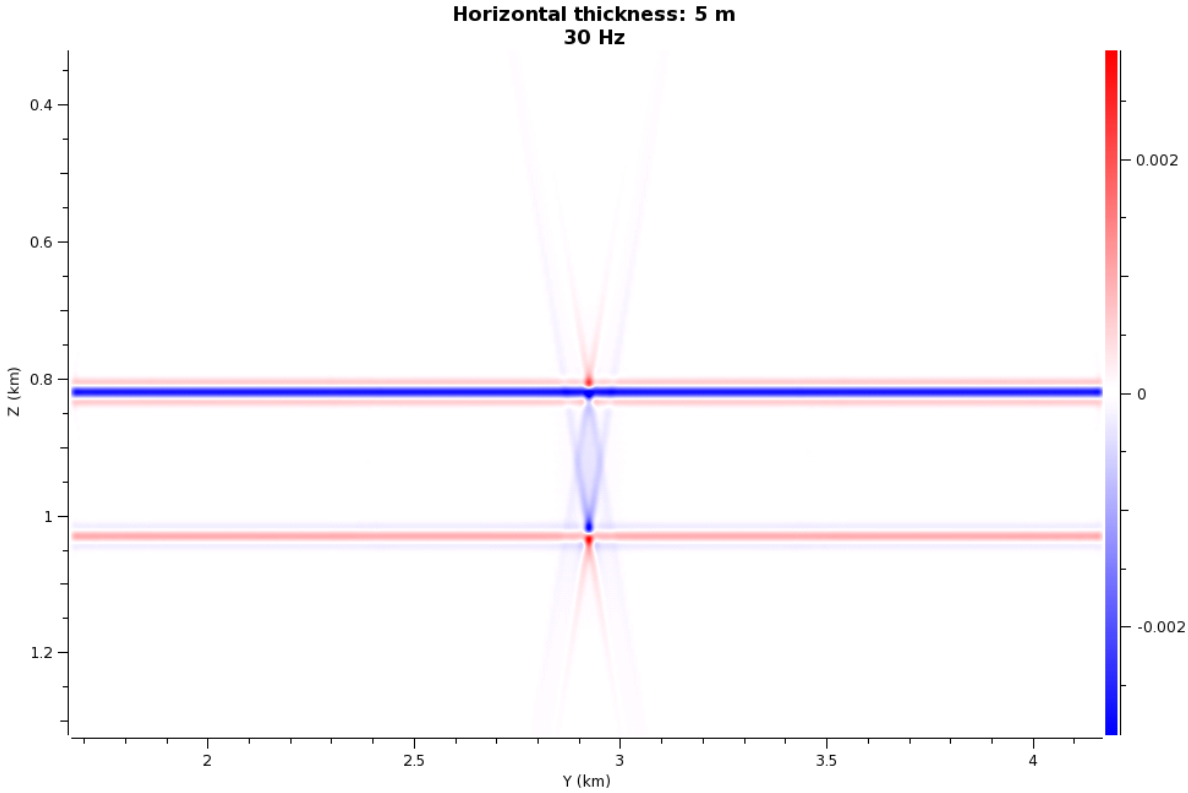

Figure 7.41 Seismic result of a plume with horizontal thickness of 5 m, and input frequency of 30 Hz.

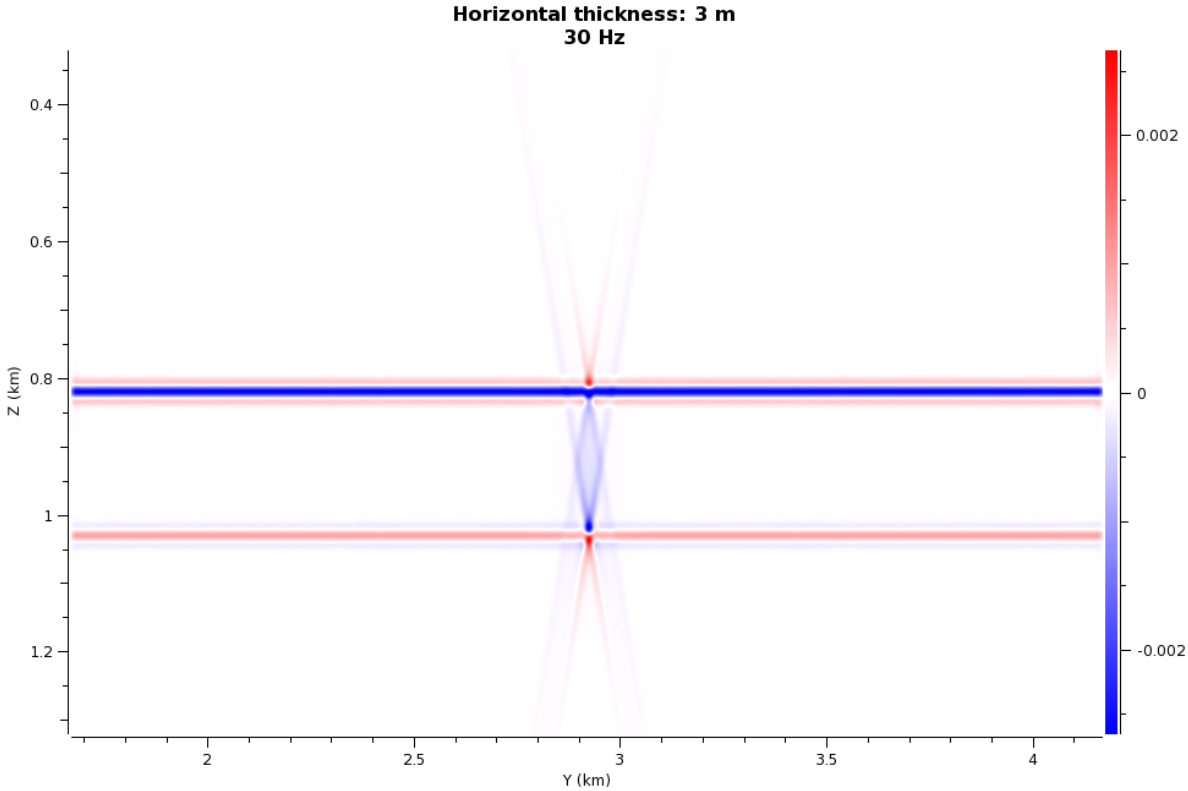

Figure 7.43 Seismic result of a plume with horizontal thickness of 3 m, and input frequency of 30 Hz.

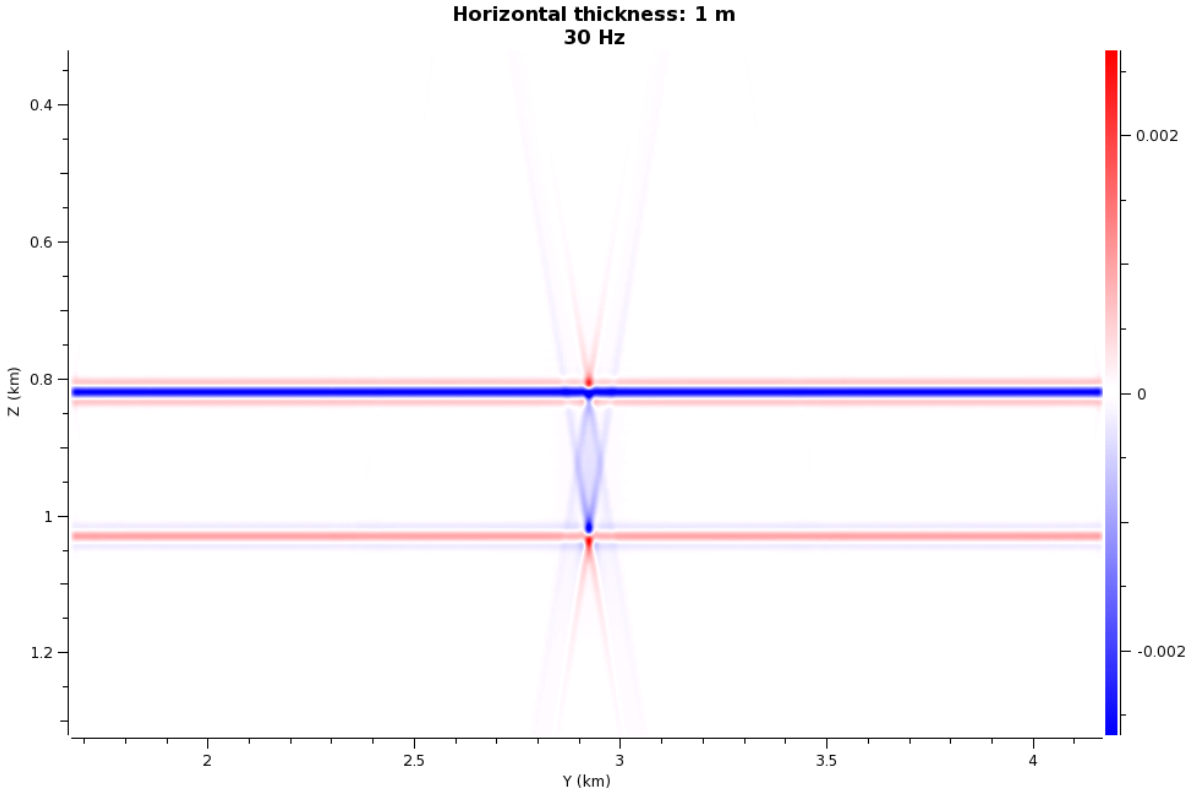

Figure 7.42 Seismic result of a plume with horizontal thickness of 1 m, and input frequency of 30 Hz.

7.4.2 The seismic image and Point-Spread Function with 60 Hz

Figure 7.45 to Figure 7.52 shows the final seismic images with varying vertical thickness of the plume with input frequency of 60 Hz. In the images from vertical thickness of 50 m, 40 m, 30 m, 20 m and 10 m(Figure 7.45 to Figure 7.49), diffractions due to the abrupt interfaces are visible. These diffractions are a footprint of the PSF (Figure 7.44). The top and bottom interface is visible with a gap in between from a vertical thickness of 20 m or thicker. With vertical thickness of 10 m the plume is still visible, but not with a clear gap. For a vertical thickness of 5 m or smaller, there is partly interference between the caprock and the plume. The area the plume is located is a bit higher, and a clear plume with gap in between is not visible. For a vertical thickness of 1 m the reflection strength is not changing remarkably in the area of the plume.

Figure 7.53 to Figure 7.59 shows the final seismic images with varying horizontal thickness of the plume. As for the results with 30 Hz this result is not showing any vertical reflections, only the footprint from the PSF. From thickness 5 m and smaller, the diffraction is interfering, and it is hard to distinguish these results.

Figure 7.44 shows the PSF for this workflow. From the PSF we get a vertical resolution of 10 m, and a horizontal resolution of 14 m.

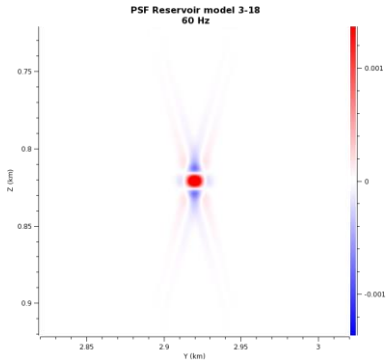

Figure 7.44 PSF for reservoir model 3-18 with an input frequency of 60 Hz.

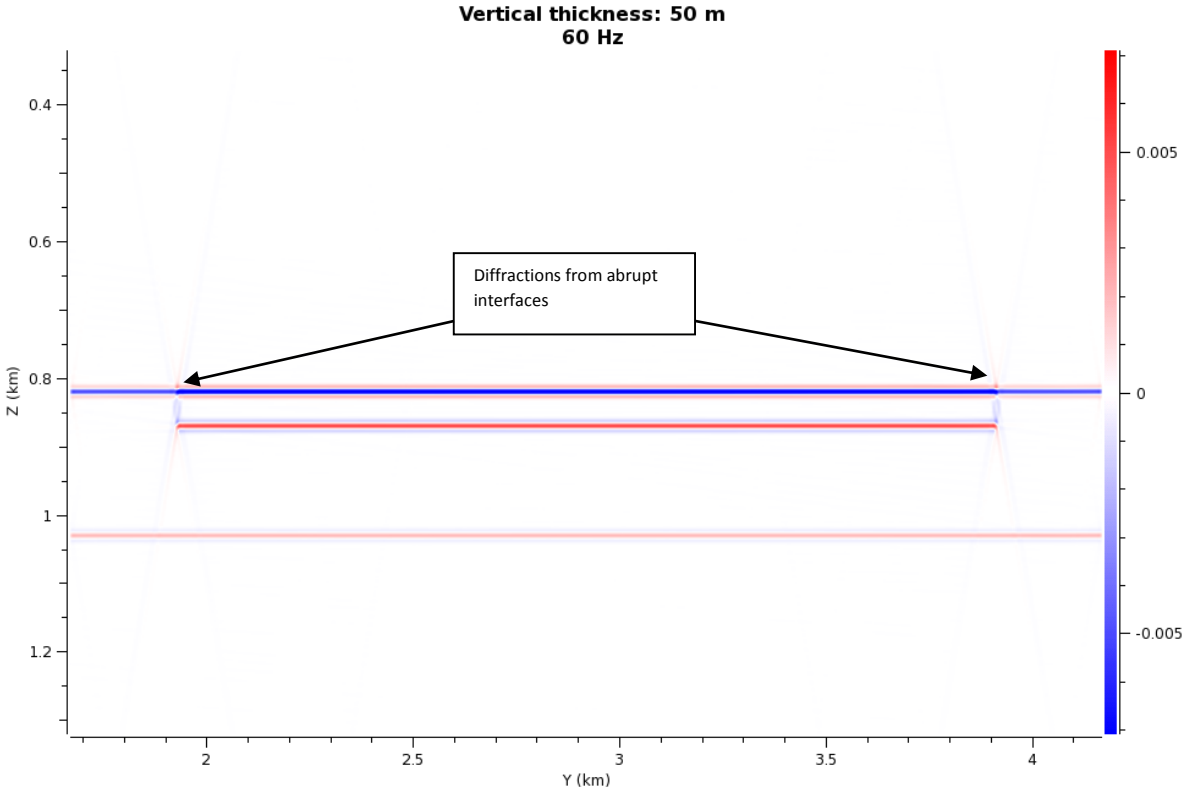

Figure 7.45 Seismic result of a plume with vertical thickness of 50 m, and input frequency of 60 Hz.

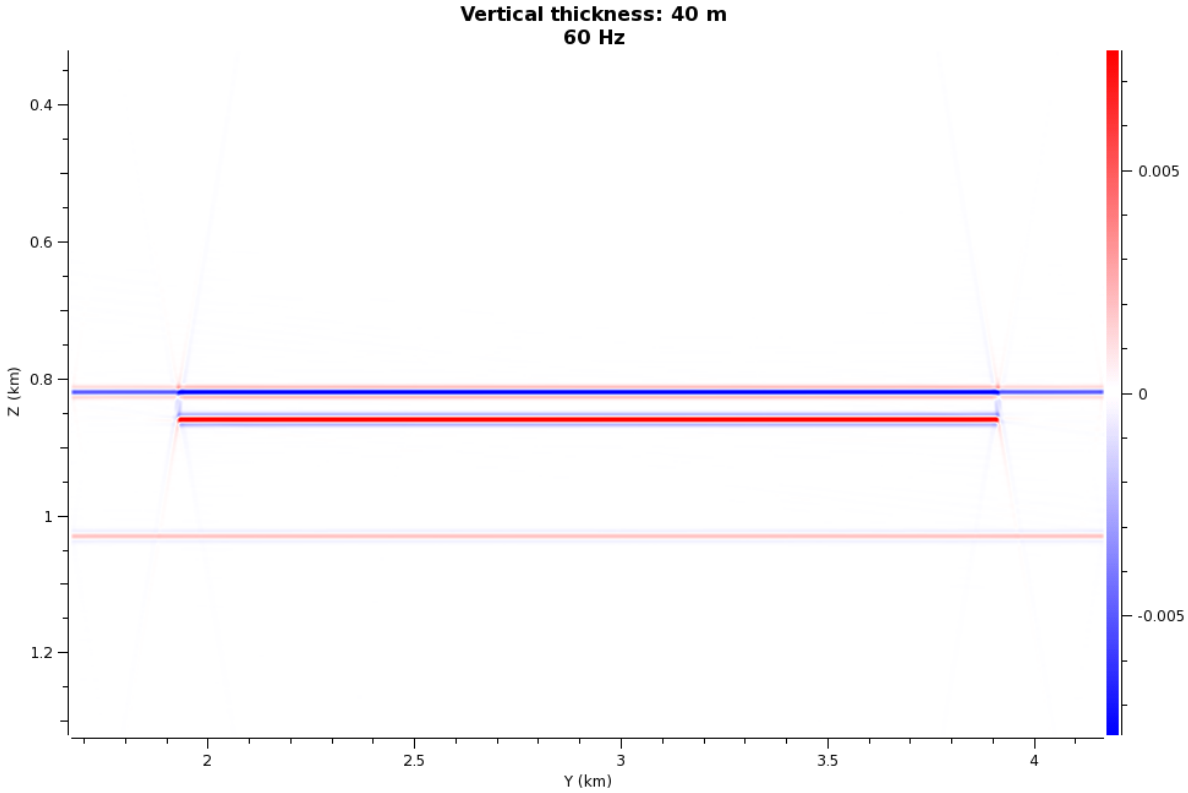

Figure 7.46 Seismic result of a plume with vertical thickness of 40 m, and input frequency of 60 Hz.

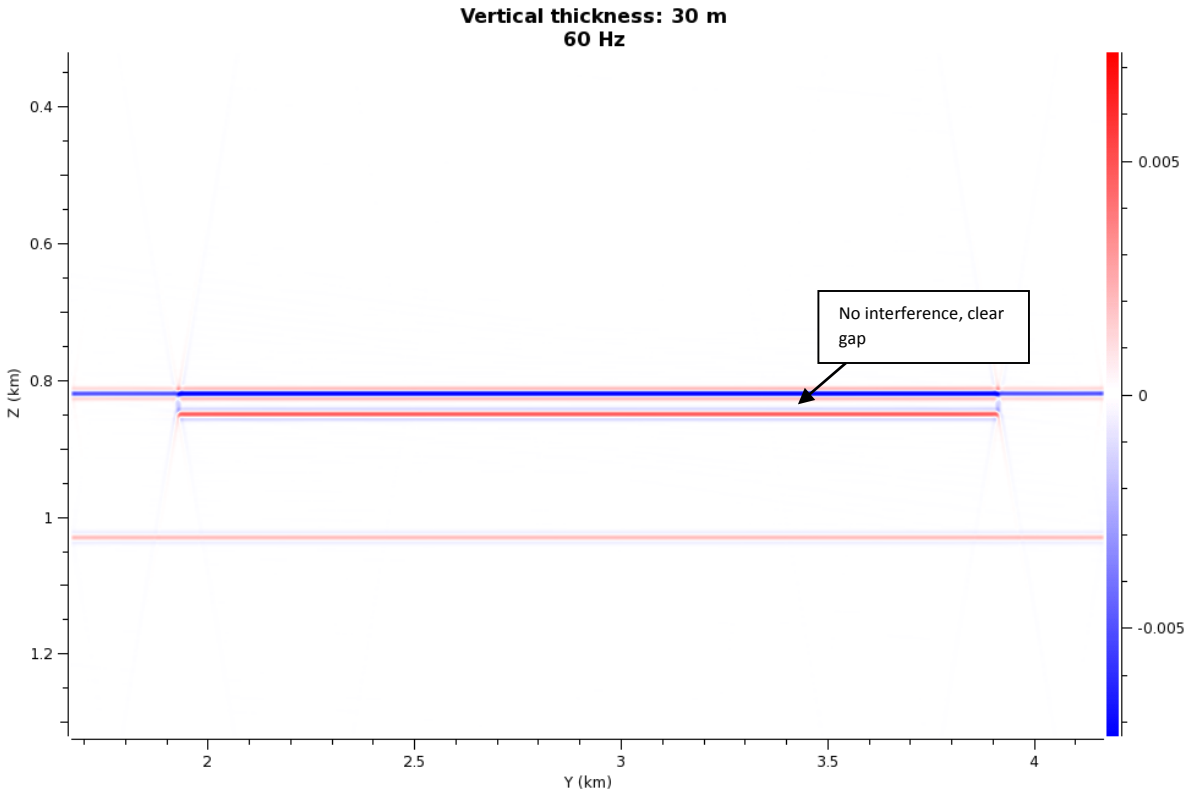

Figure 7.47 Seismic result of a plume with vertical thickness of 30 m, and input frequency of 60 Hz.

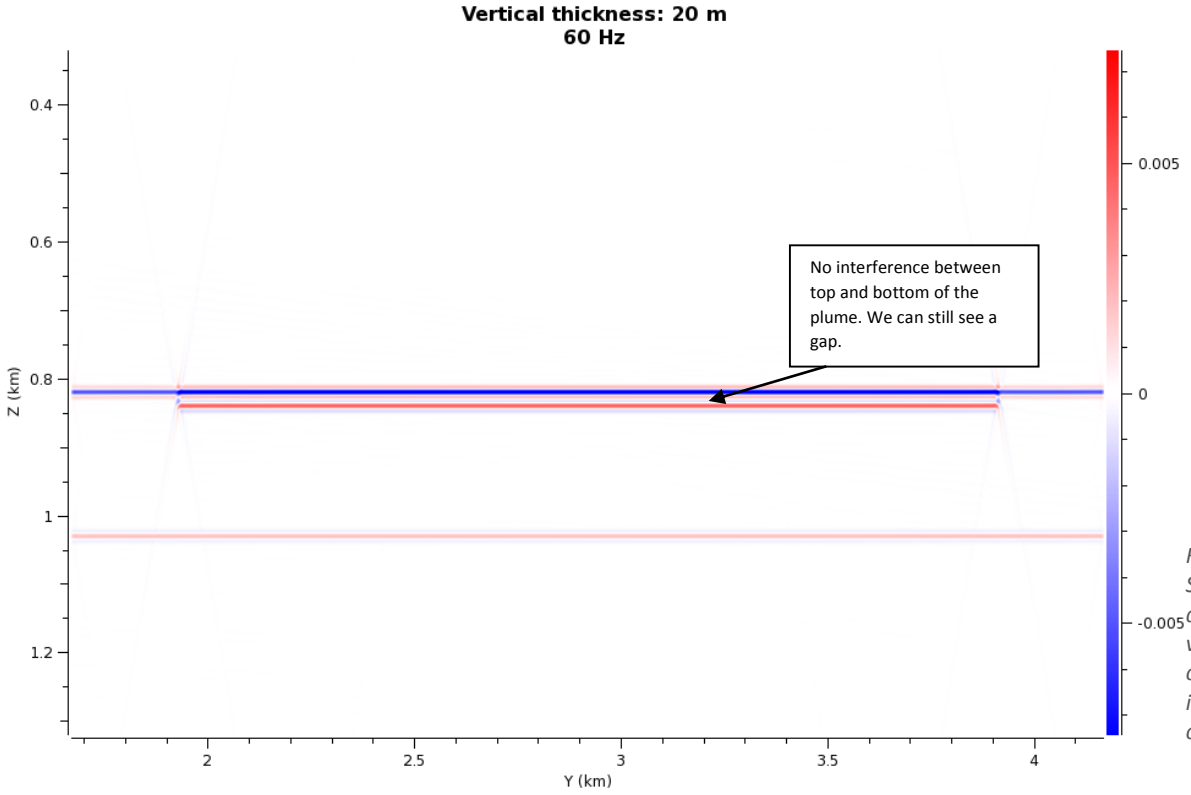

Figure 7.48 Seismic result of a plume with vertical thickness of 20 m, and input frequency of 60 Hz.

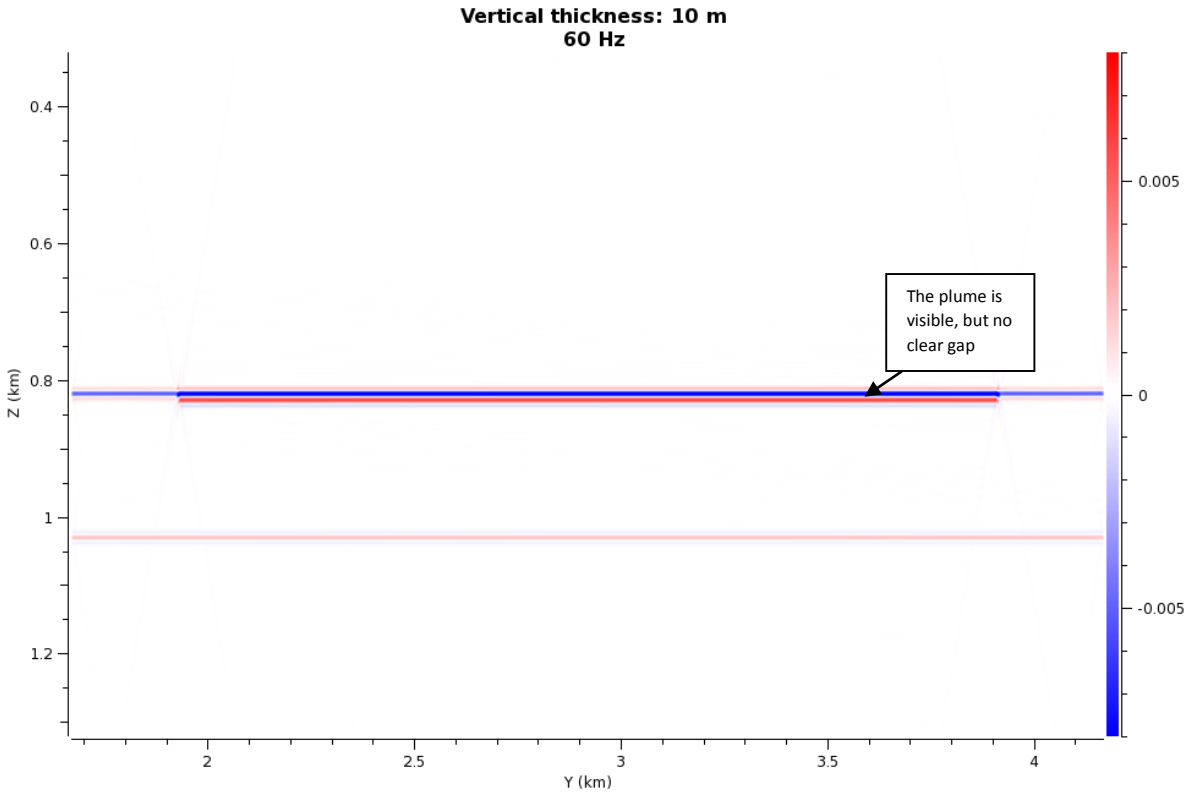

Figure 7.49 Seismic result of a plume with vertical thickness of 10 m, and input frequency of 60 Hz.

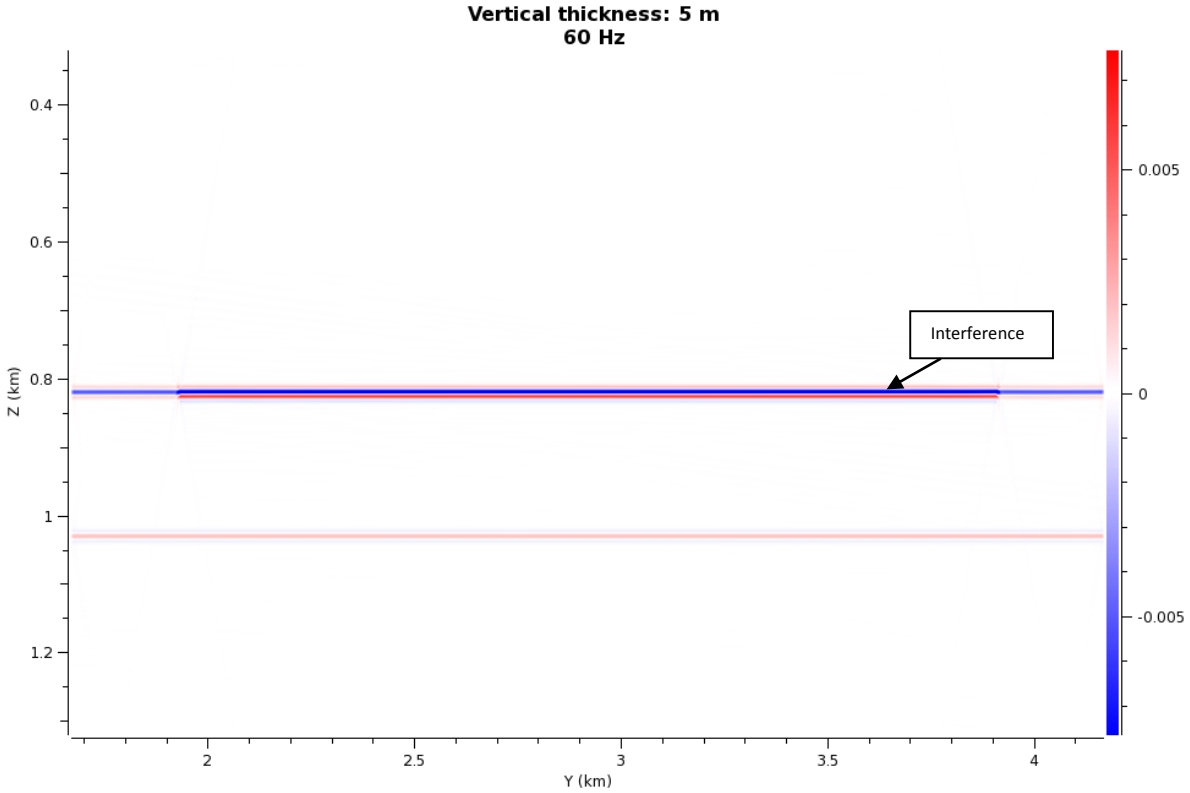

Figure 7.50 Seismic result of a plume with vertical thickness of 5 m, and input frequency of 60 Hz.

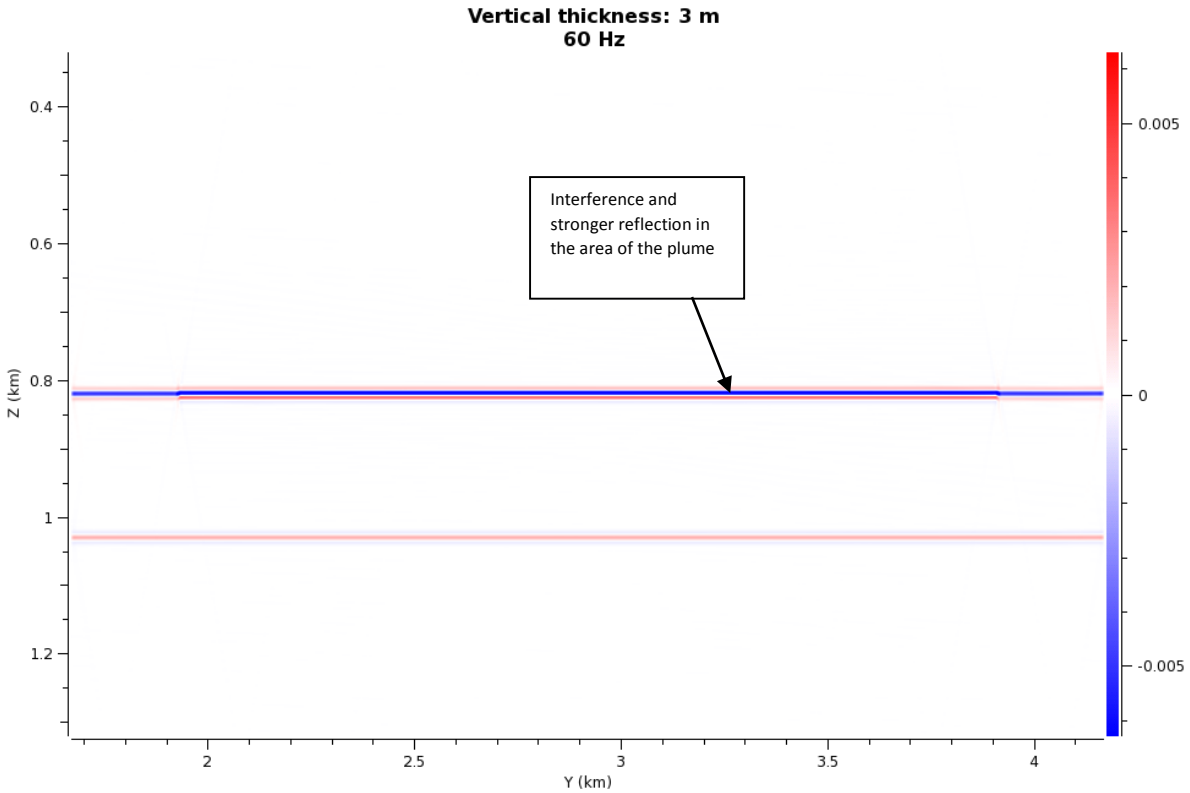

Figure 7.51 Seismic result of a plume with vertical thickness of 3 m, and input frequency of 60 Hz.

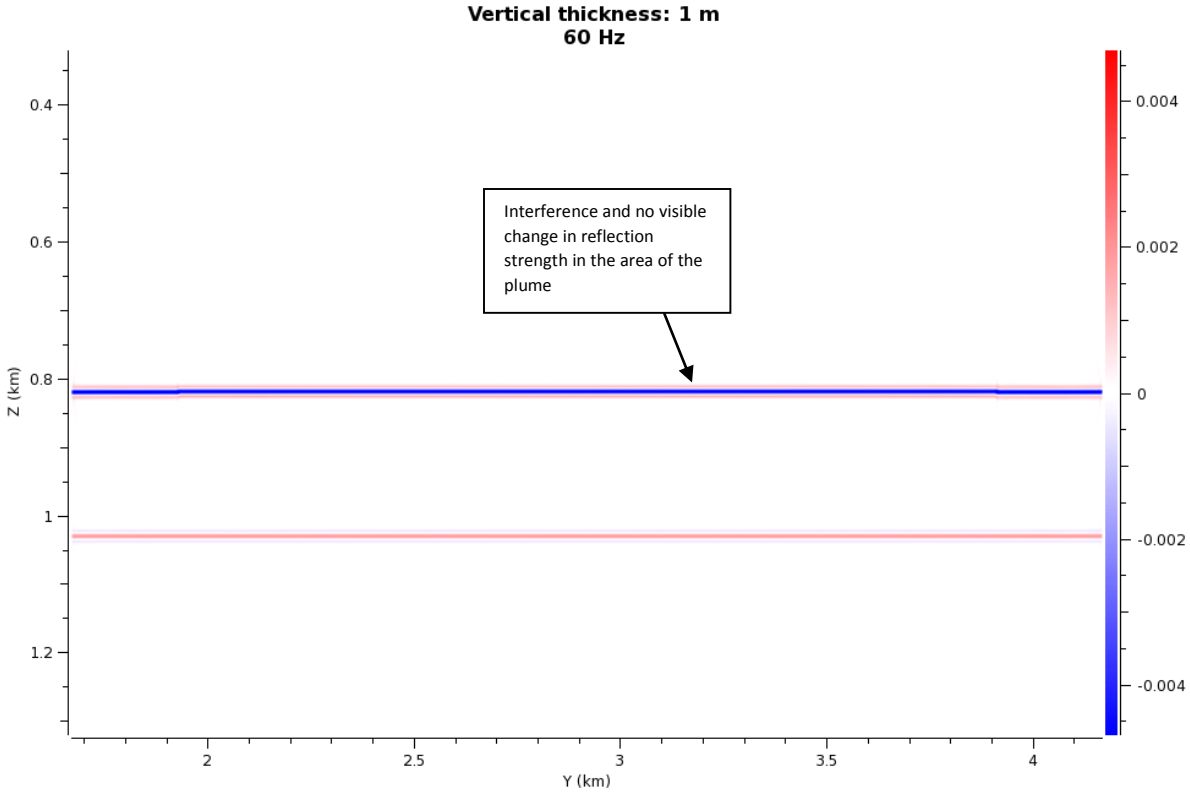

Figure 7.52 Seismic result of a plume with vertical thickness of 1 m, and input frequency of 60 Hz.

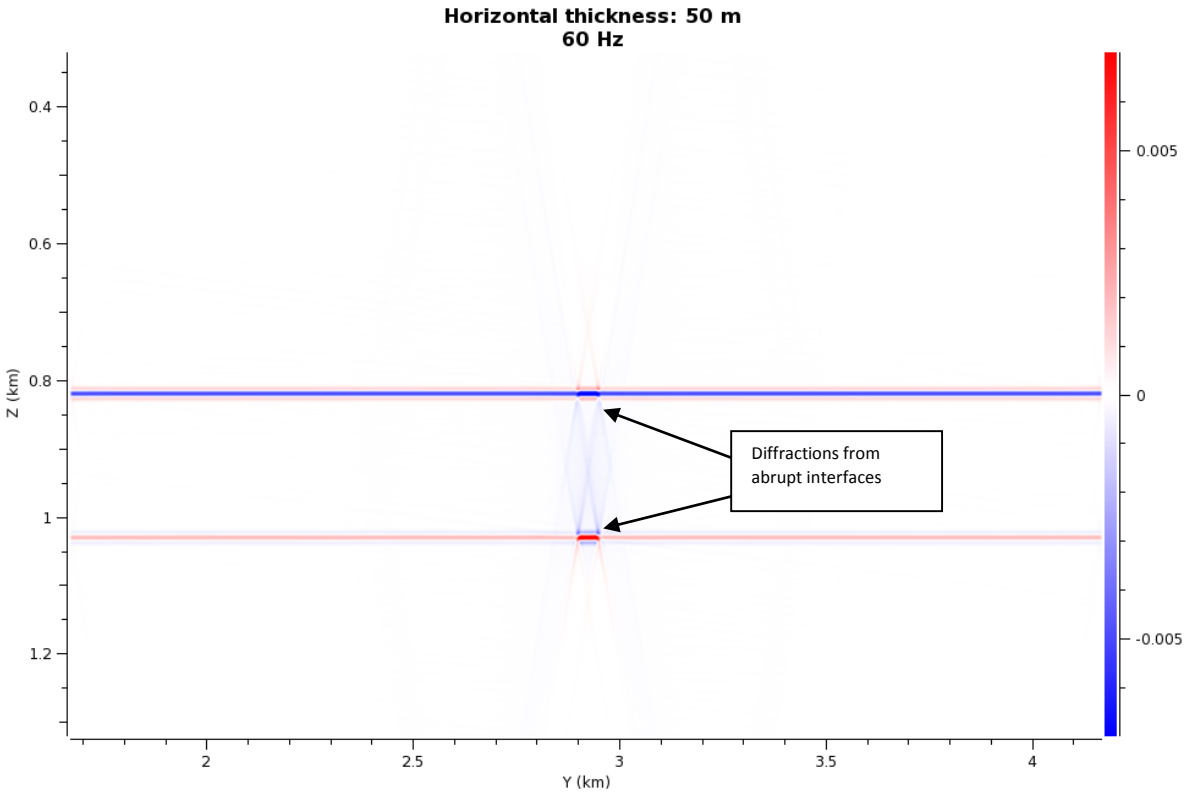

Figure 7.53 Seismic result of a plume with horizontal thickness of 50 m, and input frequency of 60 Hz.

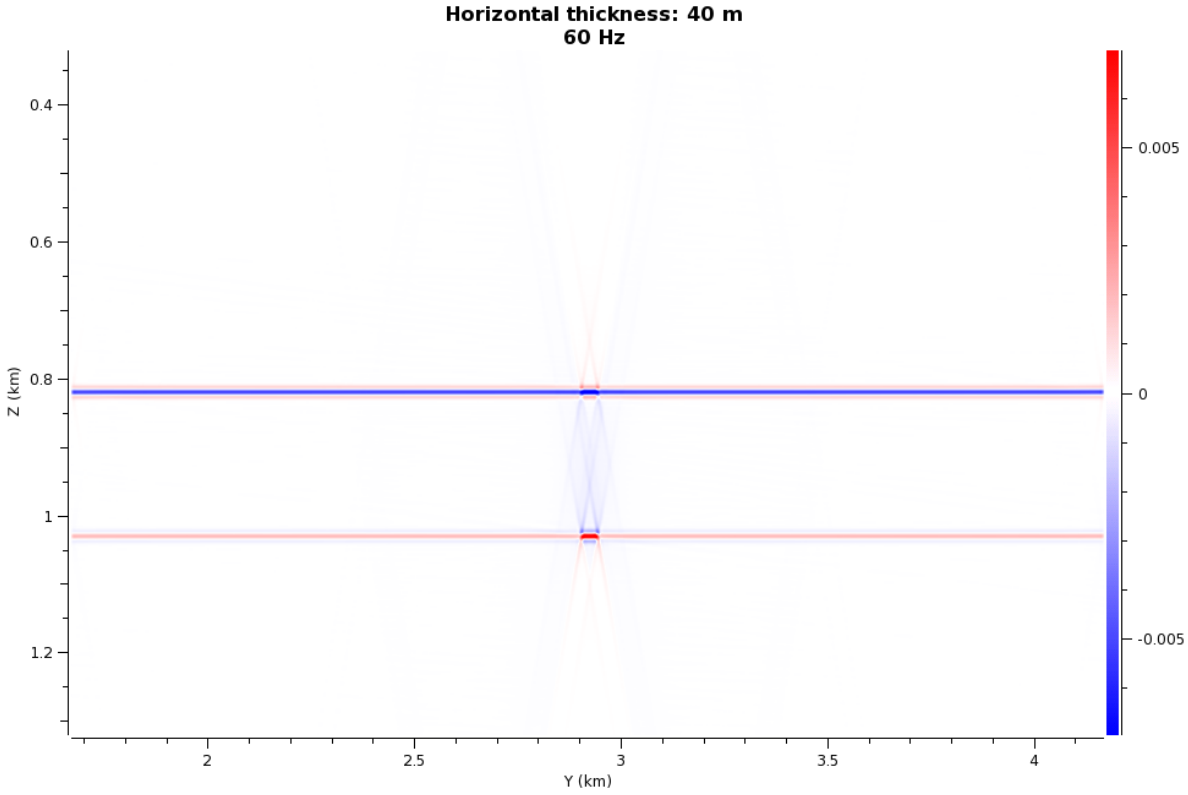

Figure 7.54 Seismic result of a plume with horizontal thickness of 40 m, and input frequency of 60 Hz.

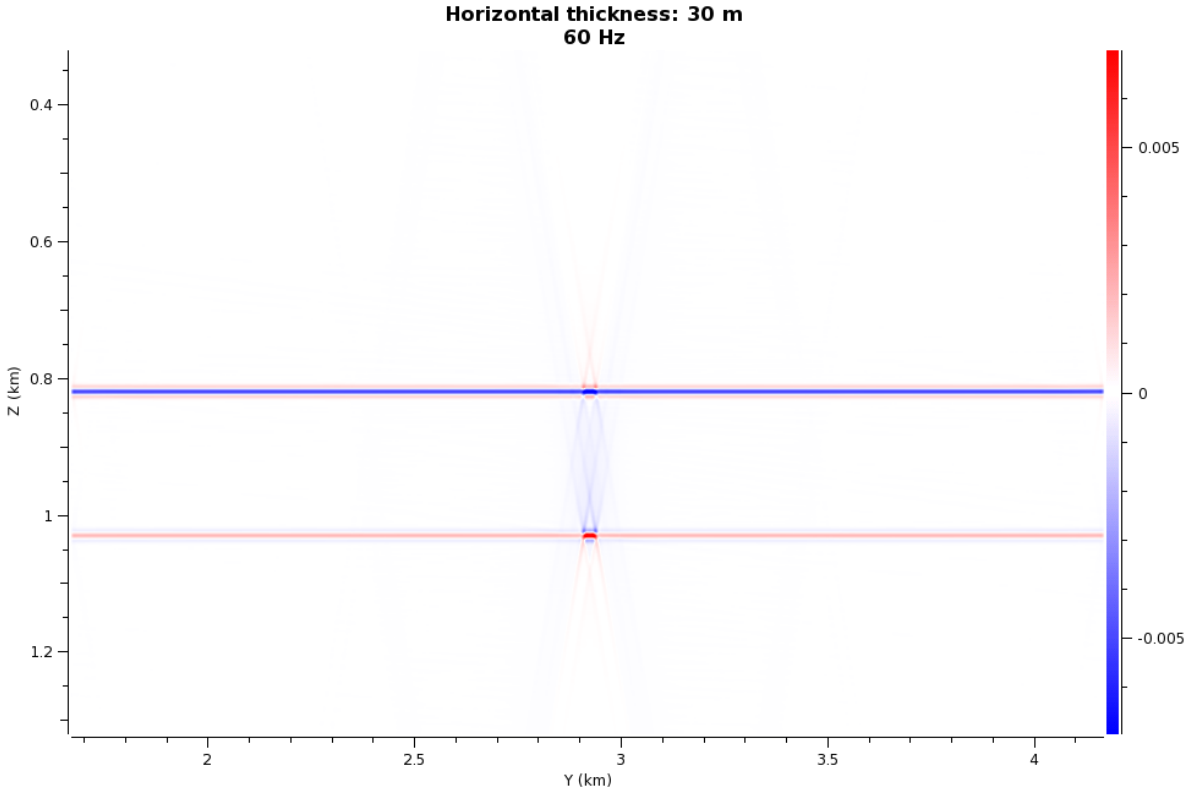

Figure 7.55 Seismic result of a plume with horizontal thickness of 30 m, and input frequency of 60 Hz.

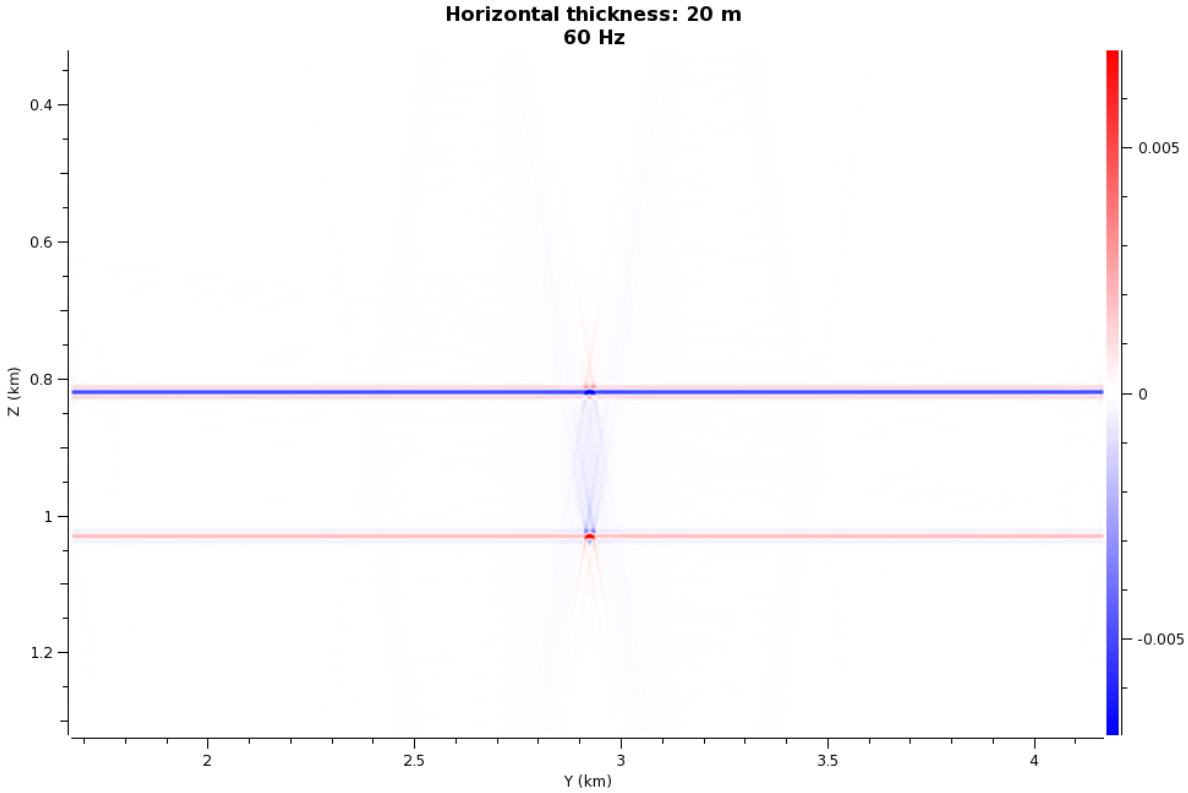

Figure 7.56 Seismic result of a plume with horizontal thickness of 20 m, and input frequency of 60 Hz.

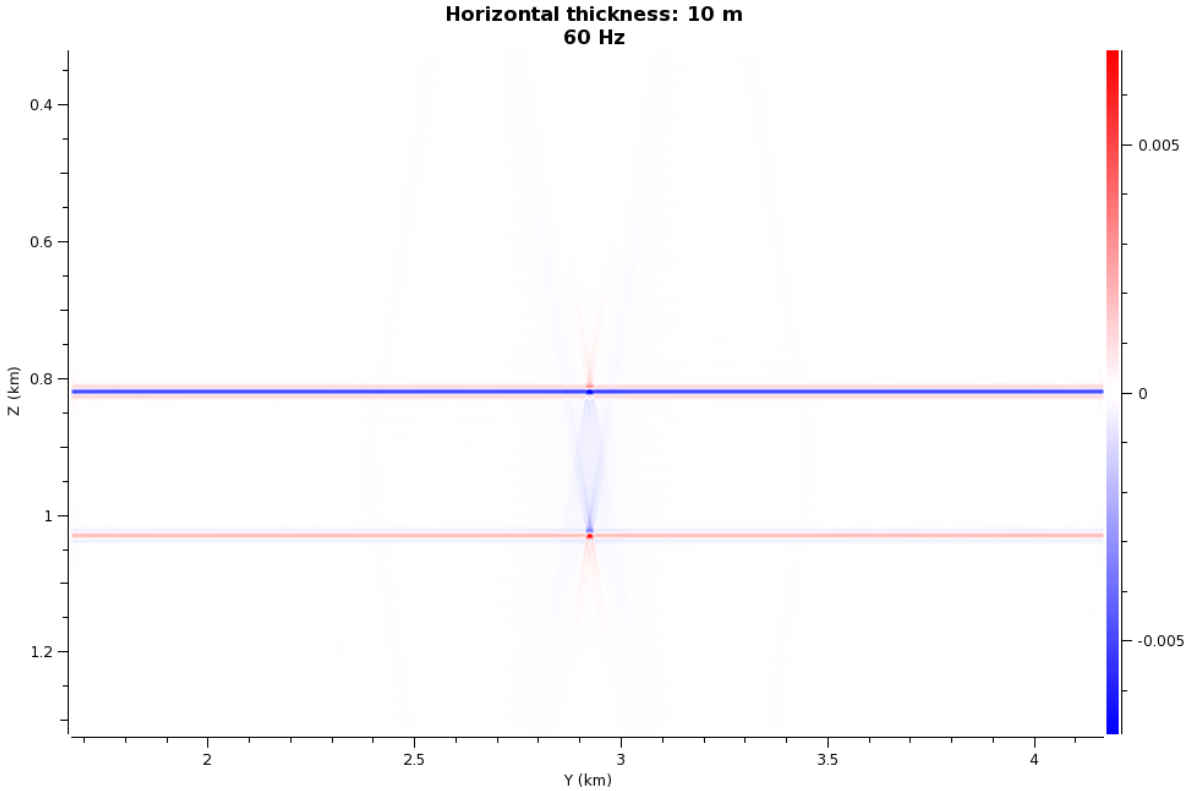

Figure 7.57 Seismic result of a plume with horizontal thickness of 10 m, and input frequency of 60 Hz.

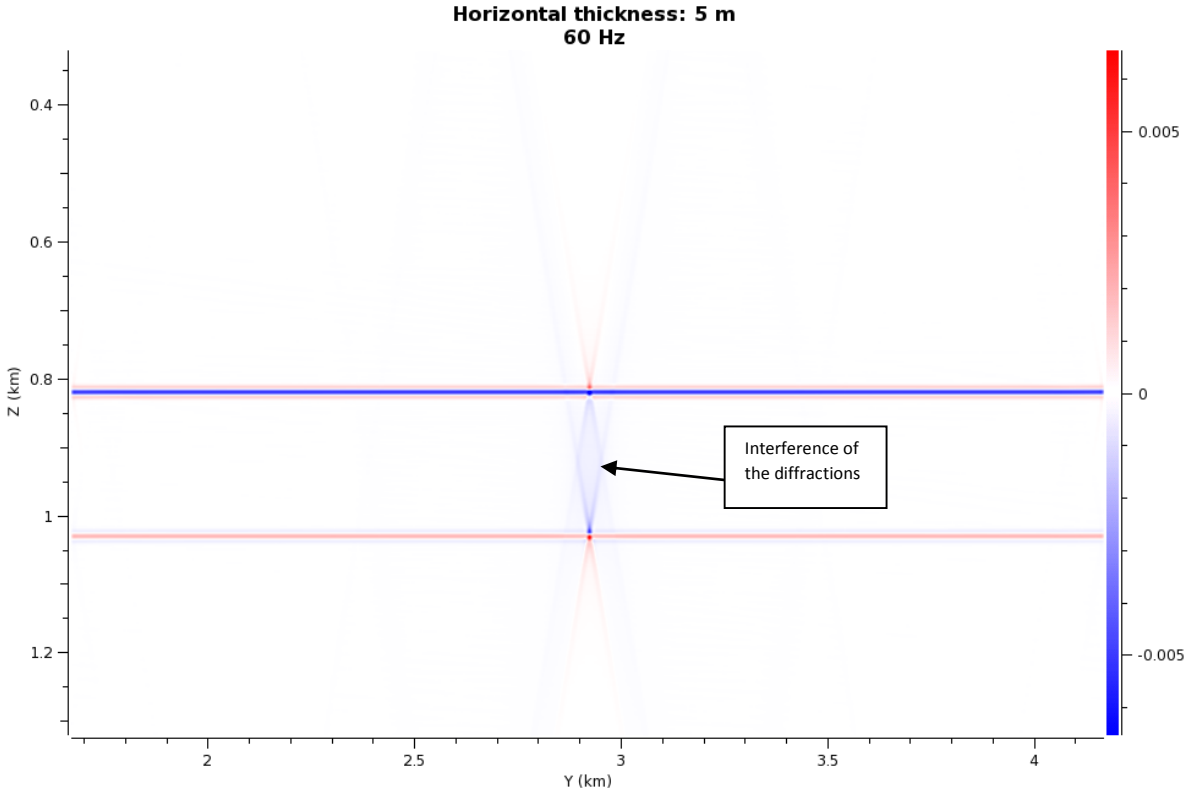

Figure 7.58 Seismic result of a plume with horizontal thickness of 5 m, and input frequency of 60 Hz.

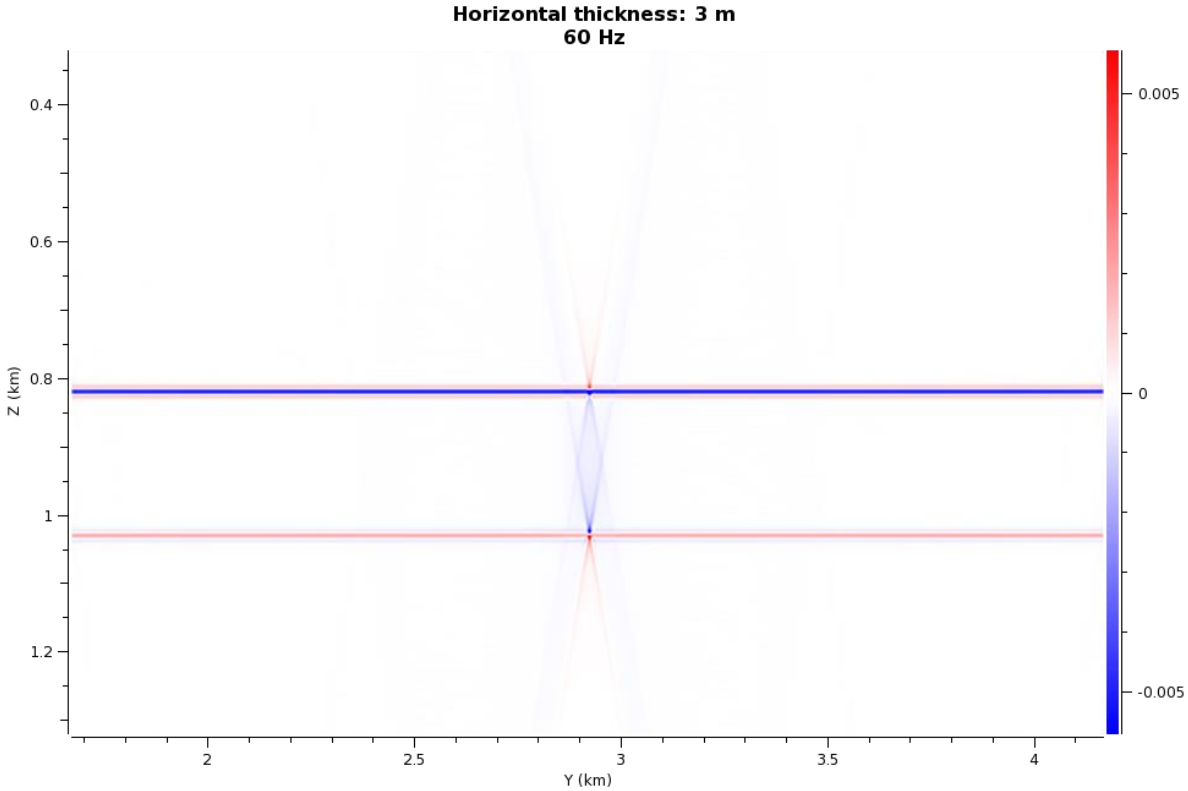

Figure 7.60 Seismic result of a plume with horizontal thickness of 3 m, and input frequency of 60 Hz.

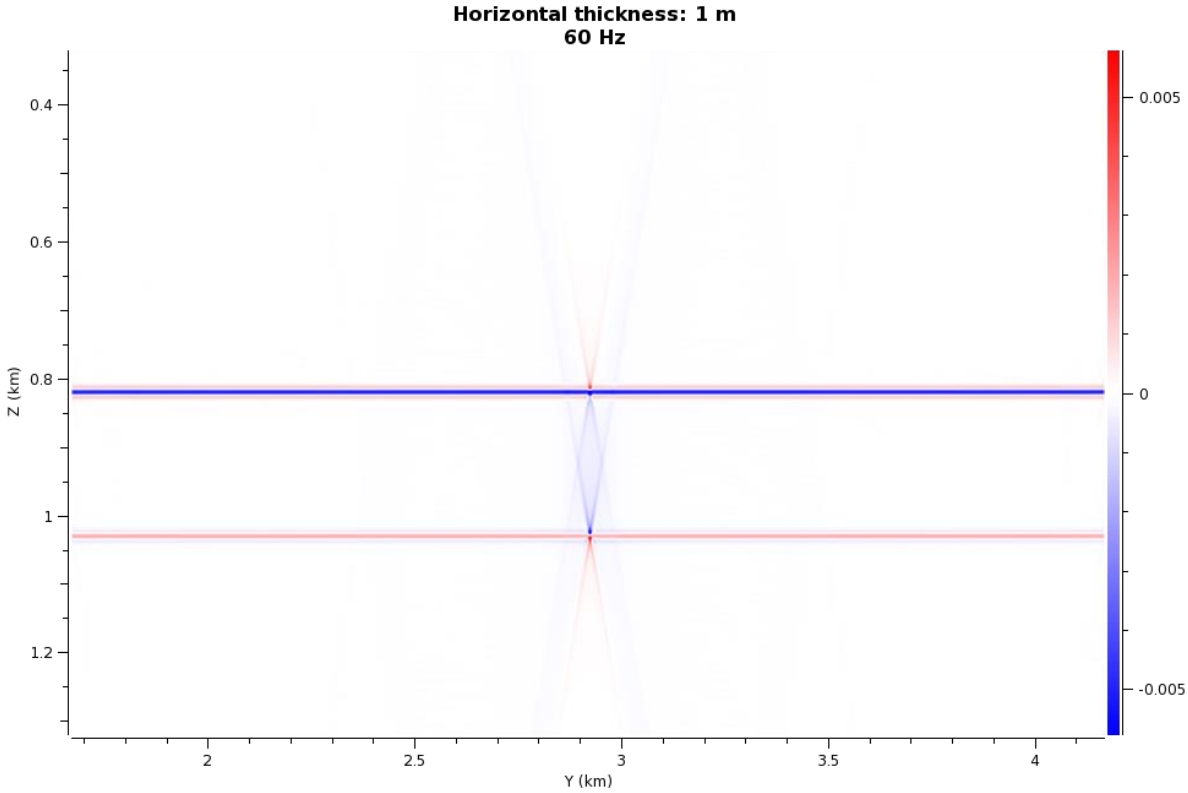

Figure 7.59 Seismic result of a plume with horizontal thickness of 1 m, and input frequency of 60 Hz.

7.4.3 Dip and azimuth of illumination vectors

In Figure 7.61 we can see the $\mathbf{I_{SR}}$ plot for this workflow. The $\mathbf{I_{SR}}$ is plotted in North-South Direction, and is ranging from 0-100°. The highest mapping is around 50-55°, 60-65° and 70-75° in both North and South direction. This mapping is not equal to the previous workflows due to different depth of target.

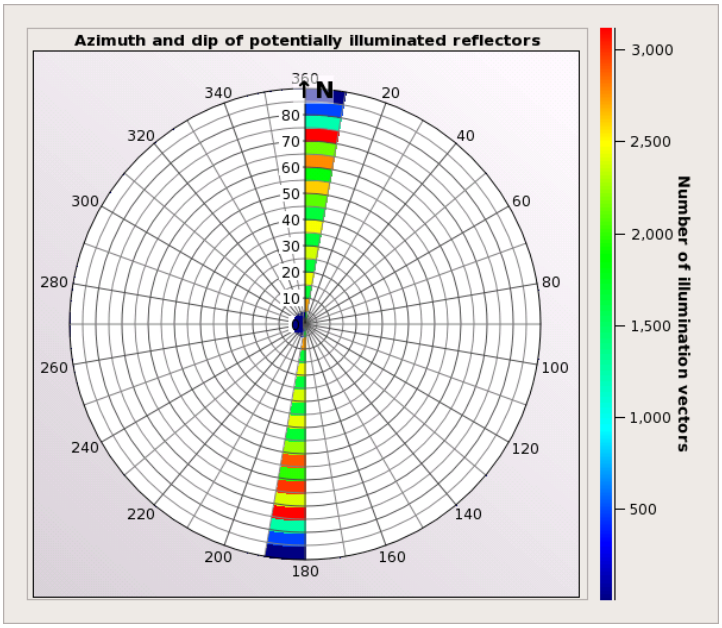

Figure 7.61 Plotted illumination vectors for reservoir model 3-18.

8 Discussion

8.1 Change in acoustic velocities

The task of this workflow was to model a plume with different CO_2 saturations, and see how the seismic amplitude anomalies responds. How the various velocities affected the reflection coefficient will be discussed, and also how the reflection coefficients compare with values from the article by Ghaderi and Landrø (Ghaderi and Landrø, 2009).

8.1.1 Reflectivity coefficient

Figure 8.1 illustrates the reflectivity from reservoir model 1 with the point A, where the reflection coefficient is retrieved from SeisRoX (Table 8.1).

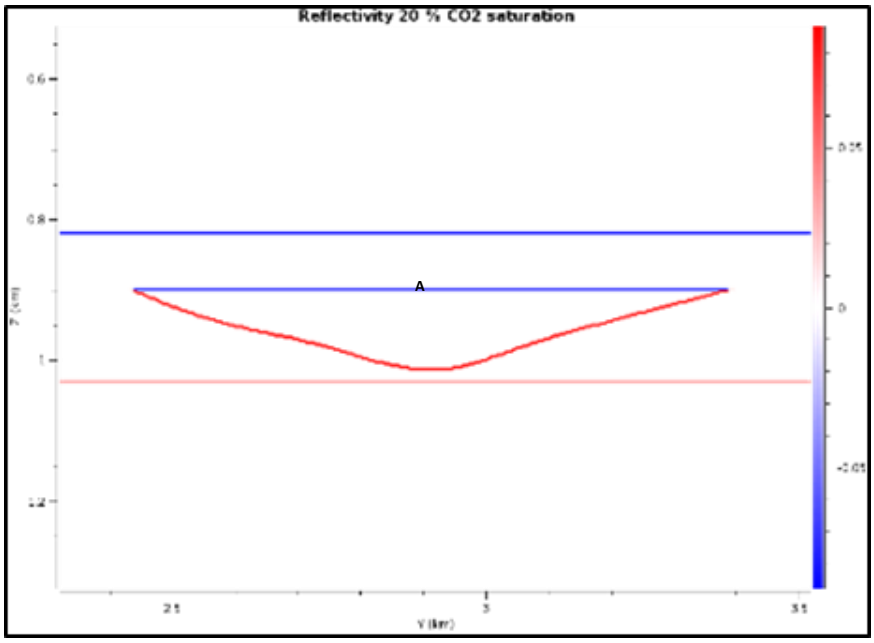

Figure 8.1 Reflectivity from reservoir model 1 with 20 % CO_2 saturation. The reflection coefficients is retrieved from the point we find the capital letter A.

Table 8.1 Reflection coefficients from reservoir model 1 with different CO_2 saturations.

CO_2 saturation	**Reflection coefficient at position A (Figure 8.1)**
10 %	-0,0941
20 %	-0,1321
30 %	-0,1521
40 %	-0,1641
50 %	-0,1724
60 %	-0,1790
70 %	-0,1837
80 %	-0,1879
90 %	-0,1912
100 %	-0,1942

The reflection method used in SeisRoX in this workflow is Zoeppritz-Knott (Aki and Richards, 1980), and this equation is taking the incident angle into account. Equation 2.2 is used to calculate the reflection coefficient with normal incidence angle, and to compare this result with the one obtained from Zoeppritz-Knott in Table 8.1. The acoustic impedance in layer 1 (reservoir rock above the plume) will by using Equation 2.1 be:

$$Z_1 = \rho \cdot V = 2004{,}3\ kg/m^3 \cdot 2005{,}4\ m/s = 4{,}019 \cdot 10^6$$

The acoustic impedance for layer 2 (the plume) with different saturation of CO_2 is listed in Table 8.2

Table 8.2 Acoustic impedance coefficient for layer 2 (the plume). The result is rounded.

CO_2 saturation	**Acoustic impedance calculated using** Equation 2.1
10 %	$Z_2 = \rho \cdot V = 2039\ kg/m^3 \cdot 1672\ m/s \approx 3{,}409 \cdot 10^6$
20 %	$Z_2 = \rho \cdot V = 2031\ kg/m^3 \cdot 1563\ m/s \approx 3{,}174 \cdot 10^6$
30 %	$Z_2 = \rho \cdot V = 2022\ kg/m^3 \cdot 1511\ m/s \approx 3{,}055 \cdot 10^6$
40 %	$Z_2 = \rho \cdot V = 2014\ kg/m^3 \cdot 1482\ m/s \approx 2{,}985 \cdot 10^6$
50 %	$Z_2 = \rho \cdot V = 2006\ kg/m^3 \cdot 1464\ m/s \approx 2{,}937 \cdot 10^6$
60 %	$Z_2 = \rho \cdot V = 1998\ kg/m^3 \cdot 1451\ m/s \approx 2{,}899 \cdot 10^6$
70 %	$Z_2 = \rho \cdot V = 1990\ kg/m^3 \cdot 1443\ m/s \approx 2{,}872 \cdot 10^6$
80 %	$Z_2 = \rho \cdot V = 1982\ kg/m^3 \cdot 1437\ m/s \approx 2{,}848 \cdot 10^6$
90 %	$Z_2 = \rho \cdot V = 1974\ kg/m^3 \cdot 1433\ m/s \approx 2{,}829 \cdot 10^6$
100 %	$Z_2 = \rho \cdot V = 1966\ kg/m^3 \cdot 1430\ m/s \approx 2{,}811 \cdot 10^6$

The result from the calculation by only using P-velocity is listed in Table 8.3. The result is the reflection coefficient of a P-to-P reflection with normal incident angle.

Table 8.3 Reflection coefficient considering normal incident angle and only P-velocity.

CO_2 saturation	**Calculations using** Equation 2.2	**Reflection (R) calculated by normal incidence (only considering Vp)**
10 %	$R = \frac{(Z_2 - Z_1)}{(Z_2 + Z_1)} = \frac{(3{,}409 \cdot 10^6 - 4{,}019 \cdot 10^6)}{(3{,}409 \cdot 10^6 + 4{,}019 \cdot 10^6)}$	-0,0821
20 %	$R = \frac{(Z_2 - Z_1)}{(Z_2 + Z_1)} = \frac{(3{,}174 \cdot 10^6 - 4{,}019 \cdot 10^6)}{(3{,}174 \cdot 10^6 + 4{,}019 \cdot 10^6)}$	-0,1175
30 %	$R = \frac{(Z_2 - Z_1)}{(Z_2 + Z_1)} = \frac{(3{,}055 \cdot 10^6 - 4{,}019 \cdot 10^6)}{(3{,}055 \cdot 10^6 + 4{,}019 \cdot 10^6)}$	-0,1363
40 %	$R = \frac{(Z_2 - Z_1)}{(Z_2 + Z_1)} = \frac{(2{,}985 \cdot 10^6 - 4{,}019 \cdot 10^6)}{(2{,}985 \cdot 10^6 + 4{,}019 \cdot 10^6)}$	-0,1476
50 %	$R = \frac{(Z_2 - Z_1)}{(Z_2 + Z_1)} = \frac{(2{,}937 \cdot 10^6 - 4{,}019 \cdot 10^6)}{(2{,}937 \cdot 10^6 + 4{,}019 \cdot 10^6)}$	-0,1555
60 %	$R = \frac{(Z_2 - Z_1)}{(Z_2 + Z_1)} = \frac{(2{,}899 \cdot 10^6 - 4{,}019 \cdot 10^6)}{(2{,}899 \cdot 10^6 + 4{,}019 \cdot 10^6)}$	-0,1619
70 %	$R = \frac{(Z_2 - Z_1)}{(Z_2 + Z_1)} = \frac{(2{,}872 \cdot 10^6 - 4{,}019 \cdot 10^6)}{(2{,}872 \cdot 10^6 + 4{,}019 \cdot 10^6)}$	-0,1664
80 %	$R = \frac{(Z_2 - Z_1)}{(Z_2 + Z_1)} = \frac{(2{,}848 \cdot 10^6 - 4{,}019 \cdot 10^6)}{(2{,}848 \cdot 10^6 + 4{,}019 \cdot 10^6)}$	-0,1705
90 %	$R = \frac{(Z_2 - Z_1)}{(Z_2 + Z_1)} = \frac{(2{,}829 \cdot 10^6 - 4{,}019 \cdot 10^6)}{(2{,}829 \cdot 10^6 + 4{,}019 \cdot 10^6)}$	-0,1738
100 %	$R = \frac{(Z_2 - Z_1)}{(Z_2 + Z_1)} = \frac{(2{,}811 \cdot 10^6 - 4{,}019 \cdot 10^6)}{(2{,}811 \cdot 10^6 + 4{,}019 \cdot 10^6)}$	-0,1769

By looking at Table 8.1 and Table 8.3 we notice that the reflection coefficient calculated by only using P-velocity and normal incidence angle are weaker at all different saturations. Figure 8.2 illustrated the reflection coefficient for a plume with 50 % CO_2 saturation. This figure shows that the reflection coefficient will increase by increasing angle for this specific interface. This will support the weaker reflections coefficients in Table 8.3 compared to Table 8.1.

Parameters from the article by Ghaderi and Landrø (Ghaderi and Landrø, 2009) are used to calculate the acoustic velocities (Appendix A). By calculating the reflection coefficient with the actual parameters (Table 8.4) from the article (not using the result from calculation in Appendix A), we see that the reflection coefficient will be a bit different (Table 8.5). By comparing Table 8.4 with Table 6.3 we notice that parameters from the calculation in Appendix A are not the same. The P-velocity is a bit smaller, and the S-velocity is a bit higher. The density is almost the same, and is not considered a weakness. The results in Table 6.3 are calculated using the estimated effective shear modulus, and this could be the reason for the different results.

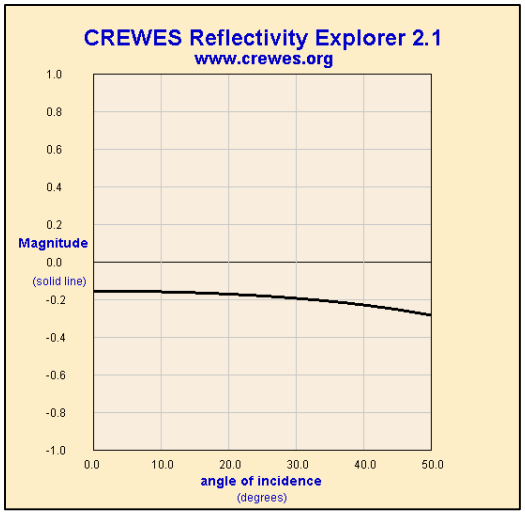

Figure 8.2 Reflection coefficient (Zoeppritz-Knott) for interface reservoir-plume. The values of the plume is equal 50 % CO_2 saturation. From:(CREWES, 2001-2005).

The actual P-velocity (Table 8.4) which is a bit higher than the parameter calculated in Appendix A, could explain the stronger reflection coefficient in Table 8.3 due to higher acoustic impedance contrast.

Table 8.4 Elastic parameters from (Ghaderi and Landrø, 2009).

CO_2 saturation	P-velocity (m/s)	S-velocity (m/s)	Density (kg/m^3)	Acoustic impedance (Vp·ρ)
20 %	1568	645	2030	$Z_2 = 3{,}183 \cdot 10^6$
50 %	1470	649	2006	$Z_2 = 2{,}949 \cdot 10^6$
100 %	1437	656	1965	$Z_2 = 2{,}824 \cdot 10^6$

Table 8.5 Reflection coefficient only considering normal incidence angle, density and P-velocity from Table 8.4.

CO_2 saturation	Calculations using Equation 2.2	Reflection calculated by normal incidence (only considering Vp from Table 8.4)
20 %	$R = \frac{(Z_2 - Z_1)}{(Z_2 + Z_1)} = \frac{(3{,}183 \cdot 10^6 - 4{,}019 \cdot 10^6)}{(3{,}183 \cdot 10^6 + 4{,}019 \cdot 10^6)}$	-0,1161
50 %	$R = \frac{(Z_2 - Z_1)}{(Z_2 + Z_1)} = \frac{(2{,}949 \cdot 10^6 - 4{,}019 \cdot 10^6)}{(2{,}949 \cdot 10^6 + 4{,}019 \cdot 10^6)}$	-0,1536
100 %	$R = \frac{(Z_2 - Z_1)}{(Z_2 + Z_1)} = \frac{(2{,}824 \cdot 10^6 - 4{,}019 \cdot 10^6)}{(2{,}824 \cdot 10^6 + 4{,}019 \cdot 10^6)}$	-0,1746

Overall the reflection coefficient is increasing in strength (more negative) with increasing saturation of CO_2 as expected.

8.2 Change in wavelet (frequency)

The aim for this workflow was to illustrate how the seismic result behaves with different frequencies, and how this affects the resolution. The vertical resolution will be calculated using Equation 2.9, to compare these results with the numbers obtained from the PSF in Table 7.3. The importance of choosing correct sampling will be discussed, and a small discussion about the seismic result obtained in this workflow compared to the seismic from the Sleipner field.

8.2.1 Sampling

In this workflow using reservoir model 2 (Figure 6.10), smaller spatial sampling was used to get the reflectivity well gridded. The PSDM filter will be the same as in the previous workflow, if using the same parameters (depth, frequency and incident angle). This is because the PSDM filter and PSF are not dependent on the reservoir model, only the background model. Figure 7.4 shows the PSDM filter with 30 Hz, if using the same sampling as in the previous workflow (0,005 and 0,0025), and Figure 8.3 shows an outcrop of left side of the reflectivity.

In the figure of the PSDM filter (Figure 7.4) is the area available for coverage in the wavenumber domain is much smaller than in the PSDM filter used in this workflow (left in Figure 8.4).

In this case the PSFM filter was not truncated in any of these workflows. The right picture in Figure 8.4, show how the filter is truncated by using the standard sampling parameters (0,01 and 0,005) from the SeisRoX manual (NORSAR, 2014a). One of the reasons for using small enough sampling was to avoid truncation of the filter, and this was achieved with the sampling used in the previous workflow (0,005 and 0,0025), and the one used in this workflow (0,001 and 0,001). Another reason to choose small enough sampling is to get the reflectivity image well gridded, and the reflectivity with sampling 0,005 and 0,0025 in Figure 8.3 is not well gridded. That is why smaller sampling was used in this workflow, 0,001 and 0,001. By using this sampling all the interfaces in Figure 7.6 are well gridded.

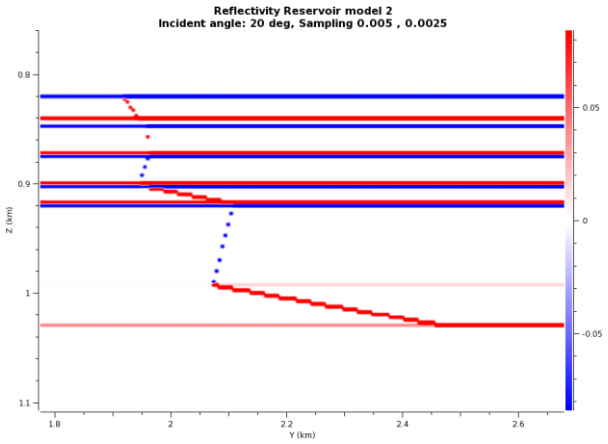

Figure 8.3 Outcrop of the left side of the reflectivity in reservoir model 2 when using sampling 0,005 and 0,0025, 30 Hz.

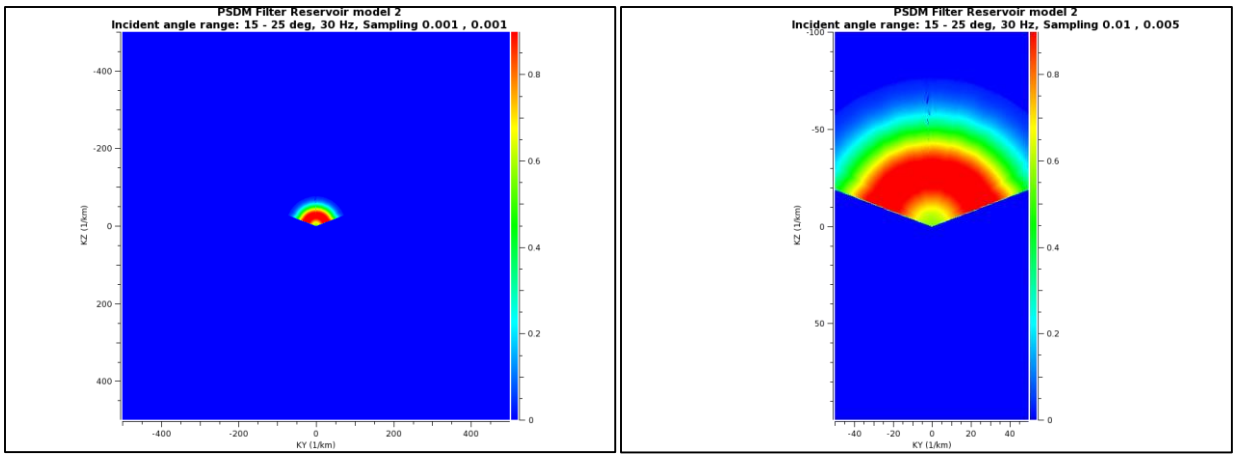

Figure 8.4 Left: PSDM filter with sampling 0,001 and 0,001, Input frequency is 30 Hz. Right: PSDM filter with sampling 0,01 and 0,005, input frequency 30 Hz.

Table 8.6 illustrates horizontal and vertical resolution with different sampling parameters. The table states that the vertical resolution will not be affected by changing the sampling, only the horizontal resolution will. Chapter 2.4 tells that the migrated horizontal resolution would be approximately equal the vertical resolution. Observations from Table 8.6 indicate that this is only valid with small angles, and when the sampling is equal in both directions.

Table 8.6 Vertical and horizontal resolution (from PSF) with different spatial sampling is SeisRoX. Input frequency 30 Hz.

Sampling (Y and Z) (Km) / Incident angle	0°	10°	20°	30°
0,01 and 0,005	V = 19 m H = 30 m	V = 19 m H = 32 m	V = 18 m H = 35 m	V = 18 m H = 40 m
0,001 and 0,001	V = 20 m H = 21 m	V = 20 m H = 24 m	V = 18 m H = 28 m	V = 18 m H = 36 m

8.2.2 Resolution

This chapter will discuss the resolution and thickness of the layer possible to detect using numbers from the PSF, and calculated numbers using parameters from the background model and the equation for vertical resolution (Equation 2.9).

8.2.2.1 Resolution from the PSF

By considering the resolution from PSF (Table 7.3), there is a huge difference in resolution going from 10 Hz to 20 Hz (Vertical resolution 54 m to 26 m), and this reflects itself in the seismic images (Figure 7.7 and Figure 7.8). The vertical distance between the shale layers is ranging from 16-73 m (Table 8.7), and by using a frequency of 10 Hz we would not be able to distinguish interfaces with a smaller distance than 54 m. Figure 7.7 shows that the gap between shale layer 3+4 and base Utsira, and top Utsira is clear.

This is due to higher vertical distance. All other shale layers are vertically closer, and according to the vertical resolution with 10 Hz (54 m) will it not be a clear gap between these layers.

Table 8.8 shows the estimated wavelength by setting the vertical resolution obtained from the PSF equal the equation for vertical resolution (Equation 2.9). The vertical resolution is expected to decrease, hence poorer resolution with increasing angle, but according to Table 8.6 there will not be a huge change in vertical resolution with small angles. Due to this, one can set the vertical resolution obtained from PSF equal Equation 2.9 to estimate the wavelength (Table 8.8). Chapter 2.4 informed that no interference occur for a layer equal to, or greater than half the wavelength. The chapter also informed that constructive interference occurs if a layer is equal to a quarter of the wavelength, and that the reflection for a layer equal and smaller than a thirtieth wavelength would not be visible. The result of the calculations is in Table 8.9.

With a frequency of 40 Hz the vertical resolution from the PSF is equal to 14 m, and this indicates that all separate shale layers will be visible (Figure 7.10) (Table 8.7). Table 8.9 states that there will occur interference for layers with vertical thickness smaller than 28 m, and this implies that the layer between shale layer 4 to 5, and shale layer 5 to base Utsira will be visible with no interference. With a frequency of 30 Hz, and a vertical resolution of 18 m, all shale layers except the gap between shale layer 3 and shale layer 4 would be visible. This reflects itself in the seismic image (Figure 7.9), where there is not a clear gap between shale layer 3 and 4, and the interfaces are partly interfering. Table 8.9 indicates that the smallest frequency able to detect both interfaces of 1 m thick layers is 70 Hz. This is also visible in Figure 7.13. Using a frequency of 70 Hz will also illustrate the result with no interference between the interfaces (Figure 7.14).

Table 8.7 Vertical distance between the shale layers, top Utsira and bottom Utsira.

Layer	Vertical distance between
Top Utsira - Shale layer1	20 m
Shale layer 1 – Shale layer 2	26 m
Shale layer 2 – Shale layer 3	27 m
Shale layer 3 - Shale layer 4	16 m
Shale layer 4 – Shale layer 5	73 m
Shale layer 5 – Base Utsira	37 m

Table 8.8 Estimated wavelength calculated the vertical resolution obtained from the PSF (Table 7.3) and Equation 2.9.

Frequency	Estimated wavelength (λ) using Equation 2.9 and the vertical resolution obtained from the PSF
10 Hz	$\frac{\lambda}{4} = 54\ m \rightarrow \lambda = 4 \cdot 54\ m = 216\ m$
20 Hz	$\frac{\lambda}{4} = 26\ m \rightarrow \lambda = 4 \cdot 25\ m = 100\ m$
30 Hz	$\frac{\lambda}{4} = 18\ m \rightarrow \lambda = 4 \cdot 18\ m = 72\ m$
40 Hz	$\frac{\lambda}{4} = 14\ m \rightarrow \lambda = 4 \cdot 14\ m = 56\ m$
50 Hz	$\frac{\lambda}{4} = 10\ m \rightarrow \lambda = 4 \cdot 10\ m = 40\ m$
60 Hz	$\frac{\lambda}{4} = 9\ m \rightarrow \lambda = 4 \cdot 9\ m = 36\ m$
70 Hz	$\frac{\lambda}{4} = 8\ m \rightarrow \lambda = 4 \cdot 8\ m = 32\ m$
80 Hz	$\frac{\lambda}{4} = 7\ m \rightarrow \lambda = 4 \cdot 7\ m = 28\ m$
90 Hz	$\frac{\lambda}{4} = 6\ m \rightarrow \lambda = 4 \cdot 6\ m = 24\ m$
100 Hz	$\frac{\lambda}{4} = 5{,}4\ m \rightarrow \lambda = 4 \cdot 5{,}4\ m = 21{,}6\ m$

Table 8.9 Vertical thicknesses with no interference, maximum interference and minimum vertical thickness able to detect on the seismic, calculated using the estimated wavelength from the PSF (Table 8.8).

Frequency	Minimum thickness with no interference	Thickness of maximum interference – tuning thickness	Smallest detectable thickness of a layer
10 Hz	108 m	54 m	7,2 m
20 Hz	50 m	25 m	3,3 m
30 Hz	36 m	18 m	2,4 m
40 Hz	28 m	14 m	1,9 m
50 Hz	20 m	10 m	1,3 m
60 Hz	18 m	9 m	1,2 m
70 Hz	16 m	8 m	1,0 m
80 Hz	14 m	7 m	0,9 m
90 Hz	12 m	6 m	0,8 m
100 Hz	10,8 m	5,4 m	0,72 m

8.2.2.2 Calculated resolution

The following table (Table 8.10) is illustrating the wavelength for different frequencies. The vertical resolution is calculated by using Equation 2.9. The result from the calculation is listed in Table 8.11. In this calculation the parameters will be the same as in the background model, at the point the PSF is calculated. This means a P-velocity of 2025 m/s. These results differ from the results in Table 7.3, from the PSF. The vertical resolution is almost the same, only a bit smaller value in the calculation. Due to this, we notice the importance of using the PSF as an indicator of visible layers instead of Equation 2.9. Results from chapter 8.2.1 indicates that the horizontal resolution is only approximately equal $\frac{\lambda}{4}$, when using 0° incident angle and same spatial sampling in both directions. Due to this observation would it not be completely correct to calculate the horizontal resolution using this equation.

Table 8.12 indicates it should be possible to detect both interfaces for a 1 m thick layer using a frequency of 70 Hz, same result as in Table 8.9. Using a frequency of 70 Hz will also make all interfaces visible without interference. Using a frequency of 40 Hz implies that all layers will be visible (Table 8.7), and this is the same as observed in Table 8.9.

Table 8.10 Calculations of the wavelength using Equation 2.10.

Frequency	Calculated wavelength
10 Hz	$\lambda = \frac{V}{f} = \frac{2025\ m/s}{10\ Hz} = 202{,}5\ m$
20 Hz	$\lambda = \frac{V}{f} = \frac{2025\ m/s}{20\ Hz} = 101{,}3\ m$
30 Hz	$\lambda = \frac{V}{f} = \frac{2025\ m/s}{30\ Hz} = 67{,}5\ m$
40 Hz	$\lambda = \frac{V}{f} = \frac{2025\ m/s}{40\ Hz} = 50{,}6\ m$
50 Hz	$\lambda = \frac{V}{f} = \frac{2025\ m/s}{50\ Hz} = 40{,}5\ m$
60 Hz	$\lambda = \frac{V}{f} = \frac{2025\ m/s}{60\ Hz} = 33{,}8\ m$
70 Hz	$\lambda = \frac{V}{f} = \frac{2025\ m/s}{70\ Hz} = 28{,}9\ m$
80 Hz	$\lambda = \frac{V}{f} = \frac{2025\ m/s}{80\ Hz} = 25{,}3\ m$
90 Hz	$\lambda = \frac{V}{f} = \frac{2025\ m/s}{90\ Hz} = 22{,}5\ m$
100 Hz	$\lambda = \frac{V}{f} = \frac{2025\ m/s}{100\ Hz} = 20{,}3\ m$

Table 8.11 Calculation of the vertical resolution.

Frequency	Vertical resolution
10 Hz	$\frac{\lambda}{4} = \frac{202{,}5\ m}{4} = 50{,}6\ m$
20 Hz	$\frac{\lambda}{4} = \frac{101{,}3\ m}{4} = 25{,}3\ m$
30 Hz	$\frac{\lambda}{4} = \frac{67{,}5\ m}{4} = 16{,}9\ m$
40 Hz	$\frac{\lambda}{4} = \frac{50{,}6\ m}{4} = 12{,}7\ m$
50 Hz	$\frac{\lambda}{4} = \frac{40{,}5\ m}{4} = 10{,}1\ m$
60 Hz	$\frac{\lambda}{4} = \frac{33{,}8\ m}{4} = 8{,}5\ m$
70 Hz	$\frac{\lambda}{4} = \frac{28{,}9\ m}{4} = 7{,}2\ m$
80 Hz	$\frac{\lambda}{4} = \frac{25{,}3\ m}{4} = 6{,}3\ m$
90 Hz	$\frac{\lambda}{4} = \frac{22{,}5\ m}{4} = 5{,}6\ m$
100 Hz	$\frac{\lambda}{4} = \frac{20{,}3\ m}{4} = 5{,}0\ m$

Table 8.12 Vertical thicknesses with no interference, maximum interference and minimum vertical thickness able to detect on the seismic, calculated using the estimated wavelength in Table 8.10.

Frequency	Minimum thickness with no interference	Thickness of maximum interference – tuning thickness	Smallest detectable thickness of a layer
10 Hz	101,1 m	50,6 m	6,8 m
20 Hz	50,7 m	25,3 m	3,4 m
30 Hz	33,7 m	16,9 m	2,3 m
40 Hz	25,3 m	12,7 m	1,7 m
50 Hz	20,3 m	10,1 m	1,4 m
60 Hz	16,9 m	8,5 m	1,1 m
70 Hz	14,4 m	7,2 m	1,0 m
80 Hz	12,7 m	6,3	0,9 m
90 Hz	11,3 m	5,6	0,8 m
100 Hz	10,1 m	5,0 m	0,7 m

During all calculation the numbers are rounded, and the differences between Table 8.9 and Table 8.12 could be bigger, but it seems that a frequency of 70 Hz in both cases will detect both interfaces for a layer of vertical thickness of 1 m. It also seems that a frequency of 40 Hz, in both cases will be able to detect all layers between the shale layers.

8.2.3 The seismic result compared to seismic data from Sleipner

Several articles from the Sleipner field informed that the intra-reservoir shale layers was not visible prior to injection. One of these articles is by Arts et al (Arts et al., 2004b). This means, the shale layers is not visible outside the plume in real life (see Figure 5.9). These shale layers were too thin to be visible on seismic before injection, and after injection there is constructive interference between the top and bottom of the thin CO_2 layers (between the shale layers).

Therefore, the question is; why are these shale layers visible outside the plume in the result in Figure 7.7 to Figure 7.16? Only a few numbers of the total shale layers was added to reservoir model 2, so the model is not completely the same as in real life. The shale layers is still visible outside the plume for every input frequency. The explanation could be better resolution in this modeling, or the missing shale layers. The vertical distance between the shale layers is higher since only a few were added, and this makes them easier to detect also with smaller resolution.

8.3 Change of incident angle

The purpose of this workflow was to check how the seismic differ with various incident angles. How the reflection coefficient changes with respect to incident angle will be discussed, and also the calculated vertical resolution compared to the PSF.

8.3.1 Reflection coefficient

It is possible to visualize the reflection coefficient for different interfaces and varying incident angle, this can be done using a website called crewes.org (CREWES, 2001-2005). The reflection coefficient from the interface marked A in Figure 8.5, going from the overlying caprock into the plume will be discussed (blue reflection). The interface going from the plume to shale layer 5 marked with a B in Figure 8.5 will also be discussed (red reflection).

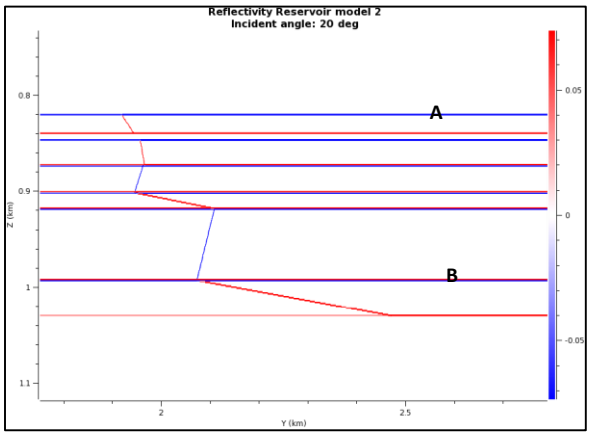

Figure 8.5 Reflectivity of reservoir model 2, incident angle 20°.

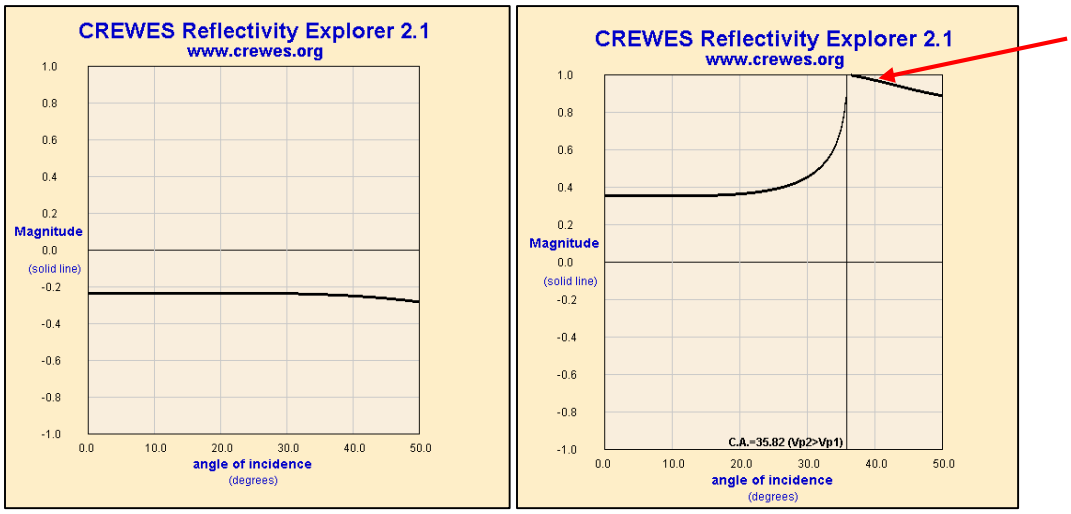

Figure 8.6 Left: Reflection coefficient (Zoeppritz-Knott) from interface A (caprock → plume). Right: Reflection coefficient (Zoeppritz-Knott) from interface B (plume →shale layer 5), the vertical line represents the critical angle. From (CREWES, 2001-2005).

The reflection coefficient will be negative for all incident angles in the left picture in Figure 8.6. Reflection Point A will be visible with for all incident angles, also 40° and 50° (Figure 7.24 and Figure 7.25). Interface B is not observed with incident angle of 40° and 50°, but it will be visible for angles from 0-30 °. After completed the workflow in SeisRoX, a warning message occured; "20.3 % overcritical reflections for incident angle 40° and 30,6 % overcritical reflections for incidence angle of 50°". Due to this warning, the result is not valid, and the reflections from certain interfaces will not occur. SeisRoX is created in the way it rejects overcritical reflections. That is why interface B, and others, will not be visible in Figure 7.24 and Figure 7.25.

The left picture in Figure 8.6, shows a drastic change in the reflection coefficient around 35,82°. The reflection coefficient is suddenly adjusted to a much higher value. This happens at the critical angle, 35,82°, and it is marked with a vertical line in the figure. Angles that are bigger than the critical angle, will not generate any transmitted wave. Due to this, it is expected a higher value in the reflection coefficient (see arrow on Figure 8.6), and especially close to the critical angle. This phenomena is called "wide angle reflection" (Sheriff and Geldart, 1995). The arrow (Figure 8.6) is pointing at the reflection that is expected to be visible in Figure 7.24 and Figure 7.25, but it is not. As mentioned is this because SeisRoX is rejecting overcritical reflections, but just to mention; the geometry and parameters of the survey is very important when it comes to visualizing of reflectors. In this case, if SeisRoX did NOT reject the overcritical reflections, the most reasonable explanation why interface B and some other interfaces is not visible, is due to survey geometry.

8.3.2 Resolution

The vertical resolution from PSF in Table 7.5, is getting better with increasing angle (lower value of the resolution). It is the opposite with horizontal resolution, poorer resolution with increasing angle. The vertical resolution is expected to decrease, hence poorer resolution with increasing angle, but it may not be very clear with small angles. The PSF is directly related to the $\mathbf{I_{SR}}$-vectors. In chapter 4.1 (Figure 4.1), show how the $\mathbf{I_{SR}}$ is shorter with larger incident angles, and this will lead to a shorter PSDM filter, and thus a larger resolution in the PSF. In fact, it seems from the seismic images that the resolution is best with small angles, and a gap between shale layer 3 and 4 is clearer. The number in Table 7.5 may not be correct due to inaccurate reading from the PSF.

By estimating the wavelength (Table 8.13) using the equation for vertical resolution (Equation 2.9) and the result obtained from the PSF (Table 7.5), it is possible also in this case to calculate the thickness with no interference and maximum interference (Table 8.14 and Table 8.15). According to these tables, it should not be possible to observe both interfaces of shale layers of 1 m. It should not be possible to observe any layers without interference, except the layer from shale layer 4 to shale layer 5 for only incident angle of 20-50˚, and shale layer 5 to base Utsira for 0-50˚ (Table 8.7).

Also, in this case, a comparison with the resolution obtained from the PSFs and the calculated resolution has been considered. The PSFs is calculated from the same depth and the same background model as in the previous workflow, so the value used for P-velocity in calculation will be the same.

Due to this, the vertical resolution is the same as for 30 Hz in Table 8.11 where the vertical resolution is 16,9 m. Table 7.5 shows the vertical and horizontal resolution obtained from the PSFs. Here, the vertical and horizontal resolution is 20 m and 21 m provided 0° incident angle. In this case as well, the resolution calculated using Equation 2.9 is of smaller value than the one obtained from the PSF. It will in this case also not be correct to calculate the migrated horizontal resolution.

Considering the numbers of the resolution obtained from the PSF in Table 7.5, suggests that the migrated horizontal resolution is approximately equal to the vertical resolution only with small incident angles. This is supported by results in chapter 8.2.1.

Table 8.13 Estimated wavelength for incident angle of 0-10° and 20-50°.

Incident angle	**Estimated wavelength (λ) using Equation 2.9 and the vertical resolution obtained from the PSF**
0° and 10°	$\frac{\lambda}{4} = 20\ m \rightarrow \lambda = 4 \cdot 20\ m = 80\ m$
20°, 30°, 40° and 50°	$\frac{\lambda}{4} = 18\ m \rightarrow \lambda = 4 \cdot 18\ m = 72\ m$

Table 8.14 Vertical thicknesses with no interference, maximum interference and minimum vertical thickness able to detect on the seismic for incident angle of 0-10°, calculated using the estimated wavelength in Table 8.13.

0° and 10°	
Minimum thickness with no interference	$\frac{\lambda}{2} = \frac{80\ m}{2} = 40\ m$
Maximum interference – tuning thickness	$\frac{\lambda}{4} = \frac{80\ m}{4} = 20\ m$
Minimum thickness of a layer to be visible	$\frac{\lambda}{30} = \frac{80\ m}{30} = 2{,}66\ m$

Table 8.15 Vertical thicknesses with no interference, maximum interference and minimum vertical thickness able to detect on the seismic for incident angle of 20-50°, calculated using the estimated wavelength in Table 8.13.

20°, 30°, 40° and 50°	
Minimum thickness with no interference	$\frac{\lambda}{2} = \frac{72\ m}{2} = 36\ m$
Maximum interference – tuning thickness	$\frac{\lambda}{4} = \frac{72\ m}{4} = 18\ m$
Not possible to detect the layer	$\frac{\lambda}{30} = \frac{72\ m}{30} = 2{,}4\ m$

The diagram from Monk (Monk, 2010) in Figure 8.7 shows how the horizontal resolution (Fresnel dimension) will decrease with increasing offset, as expected. The located depth of the target will play a vital role, as observed in Figure 8.7 the horizontal resolution will be smallest for the deepest located target. Due to this observation and the observation from Table 8.6, it will not be correct to always say that the migrated horizontal resolution will be equal to $\frac{\lambda}{4}$. This supports the assumption that it will not give realistic numbers when calculating the migrated vertical resolution.

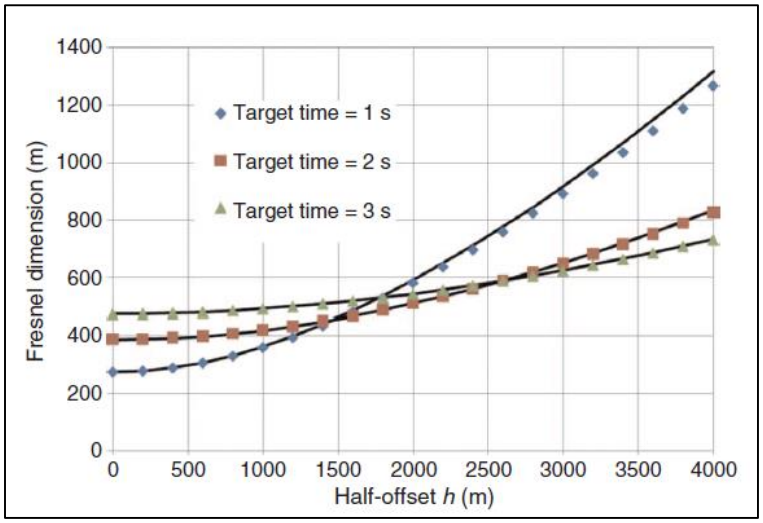

Figure 8.7 Fresnel dimension compared to offset. The model is synthetic and considering a constant velocity field, with 30 Hz. The different lines represent different depth of target. Target with time 1 s is the shallowest one. From: (Monk, 2010).

8.3.3 Dip and azimuth of illumination vectors

The image in workflow 1, Figure 7.5 is equal to the one obtained in this workflow even if this workflow includes angles from 0-50°. The explanation for this is that the $\mathbf{I_{SR}}$ plot always plots 100 % of the available $\mathbf{I_{SR}}$, and is not dependent on the incident angle used.

8.4 When is the plume not visible on the seismic?

The aim of this workflow was to determine when it is not possible to detect the vertical and horizontal plumes on the seismic. Smaller sampling is also used in this workflow. To be able to get the reflectivity image of the thinnest reservoir models well gridded, a sampling of 0,5 m (0,0005 km) is used in both directions.

8.4.1 Resolution

In this workflow, input frequency of 30 Hz and 60 Hz is used. The vertical and horizontal resolution obtained from the PSF for 30 is respectively 20 m and 28 m. For a frequency of 60 Hz the vertical and horizontal resolution will be 10 m and 14 m. These numbers indicate a better resolution with higher frequency as expected. By using the vertical resolution, it is possible to estimate the wavelength of 30 Hz and 60 Hz, the result is listed in Table 8.16. This is done by using Equation 2.9 for vertical resolution.

Table 8.16 Estimated wavelength for input frequency 30 Hz and 60 Hz.

Frequency	**Estimated wavelength (λ) using Equation 2.9 and the vertical resolution obtained from the PSF**
30 Hz	$\frac{\lambda}{4} = 20\ m \rightarrow \lambda = 4 \cdot 20\ m = 80\ m$
60 Hz	$\frac{\lambda}{4} = 10\ m \rightarrow \lambda = 4 \cdot 10\ m = 40\ m$

8.4.1.1 Horizontal plumes

Chapter 2.4 informed that no interference occur for a layer equal to, or greater than half the wavelength. The chapter also informed that constructive interference occurs if a layer is equal to a quarter of the wavelength, and that the reflection for a layer equal and smaller than a thirtieth wavelength would not be visible. In Table 8.17 and Table 8.19 the thicknesses is calculated using the estimated wavelength for 30 Hz and 60 Hz.

30 Hz

Table 8.17 indicates that it should be possible to observe a gap between top and bottom of the plume for vertical thickness 40 m and 50 m. This is possible to observe in (Figure 7.28 and Figure 7.29). For vertical thickness of 30 m the interfaces are partly interfering and the reflection is not that strong. For a vertical thickness of 20 m the plume is visible, and constructive interference occurs, this is known as the tuning thickness.

The reflection is stronger compared to vertical thickness of 30 m. For thicknesses smaller than the tuning thickness, partial interference will occur, and the reflection is weaker.
Table 8.17 states that it should not be possible to observe a layer of thickness smaller than 2,6 m. In Figure 7.34 with a vertical thickness of 3 m a stronger reflection is still visible, but in Figure 7.35 with a vertical thickness of 1 m, there is no noticeable change in the reflection strength. This observation confirms the calculation in Table 8.17. A summary of the conclusion made by comparing observations in the seismic images with results in Table 8.17, is listed in Table 8.18

Table 8.17 Calculations using 30 Hz.

30 Hz	
Minimum thickness with no interference	$\frac{\lambda}{2} = \frac{80\ m}{2} = 40\ m$
Maximum interference – tuning thickness	$\frac{\lambda}{4} = \frac{80\ m}{4} = 20\ m$
Minimum thickness of a layer to be visible	$\frac{\lambda}{30} = \frac{80\ m}{30} = 2{,}6\ m$

Table 8.18 Overview of the observed result for horizontal plumes using 30 Hz.

30 Hz	
Vertical thickness	**Interference?**
50 m	No interference
40 m	No interference
30 m	Partly interfering
20 m	Constructive interference, tuning thickness
10 m	Partly interfering
5 m	Partly interfering
3 m	Partly interfering
1 m	Not possible to detect the layer

60 Hz

The same pattern is observed with frequency of 60 Hz. Table 8.19 indicates that it should be possible to observe reflections from top and bottom of the plume with no interference, for thickness equal and greater than 20 m. For vertical thickness of 10 m the plume is visible, but with constructive interference, and the reflection is stronger. For thickness smaller than 10 m the interfaces are partly interfering, creating a weaker reflection. In this case for 30 Hz, it is not possible to detect a layer of vertical thickness of 1 m. The reflection is not changing noticeable, and this is supported by the calculation in Table 8.19. A summary of the conclusion is listed in Table 8.20.

Table 8.19 Calculations using 60 Hz.

60 Hz	
Minimum thickness with no interference	$\frac{\lambda}{2} = \frac{40\ m}{2} = 20\ m$
Maximum interference – tuning thickness	$\frac{\lambda}{4} = \frac{40\ m}{4} = 10\ m$
Minimum thickness of a layer to be visible	$\frac{\lambda}{30} = \frac{40\ m}{30} = 1{,}3\ m$

Table 8.20 Overview of the observed result for horizontal plumes using 60 Hz.

60 Hz	
Vertical thickness	**Interference?**
50 m	No interference
40 m	No interference
30 m	No interference
20 m	No interference
10 m	Constructively interfering, tuning thickness
5 m	Partly interfering
3 m	Partly interfering
1 m	Not possible to detect the layer

8.4.1.2 Vertical plumes

In the vertical plumes with varying horizontal thickness no vertical reflections could be observed, even the plot of $\mathbf{I_{SR}}$-vectors (Figure 7.61) illustrate that reflections up to 100° would be visible. The $\mathbf{I_{SR}}$ plot is important deciding if the reflector would be visible, but the shape of the PSDM filter will also play a vital role. Traveltime range and aperture range assigned under PSDM parameters (chapter 6.3.4: PSDM filter) is used to get a realistic migration result. These options may sometimes migrate away parts of the filter, and it is often the horizontal parts that are missing. No visible vertical reflections occurred by changing these parameters and also turning them completely off with results from an incident angle of 20°.

With incident angle of 20° for 60 Hz the PSDM filter is smooth and without holes (Figure 8.8). By looking at Figure 8.9 from incident angle of 0°, with and without all PSDM filter options on, holes is observed in both filters. These holes will generate more noise on the final seismic image (Figure 8.10 and Figure 8.11). A difference is observed by comparing the filter from all PSDM filter options on (Left in Figure 8.9) with the filter with all PSDM options turned off (Right in Figure 8.9). In the filter with all PSDM filter options off is some of the $\mathbf{k_{SR}}$ horizontal, the filter is creating a half circle.

These horizontal k_{SR} is indicating that vertical reflections would be visible on the seismic image (Figure 8.11), but as mentioned with a lot of noise due to holes in the filter. This result implies that it is possible to observe vertical reflections but not realistic. The vertical reflections was only visible when the aperture range and traveltime range were completely turned off, and without these or by having a huge sampling range the result would not be realistic. Incident angle of 20°, with all PSDM filters turned on is used to get a realistic result. It is not realistic to have completely incident angle of 0°, and the PSDM filter was also smoother with angle of 20°.

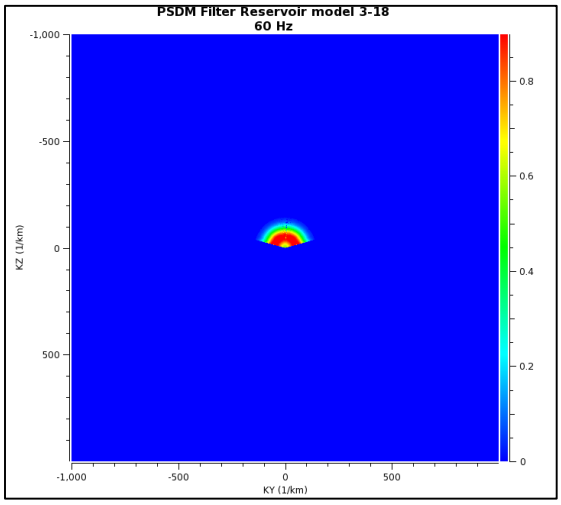

Figure 8.8 PSDM filter reservoir model 3-18 for incident angle of 20°, 60 Hz.

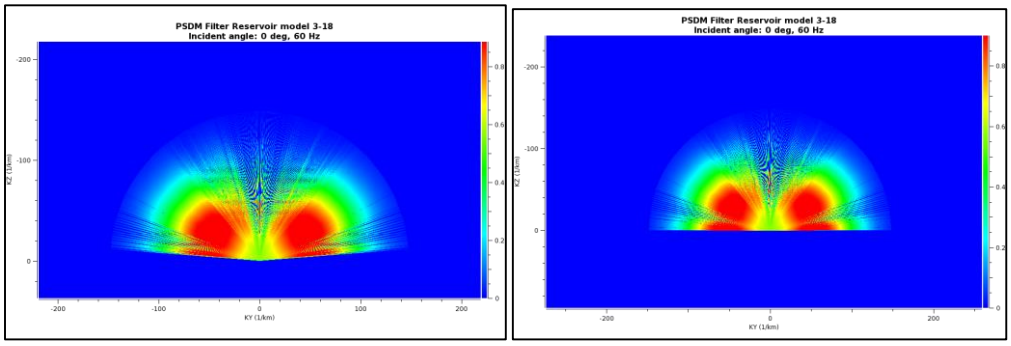

Figure 8.9 Outcrop of the PSDM filter for reservoir model 3-18, incident angle 0° and 60 Hz. Left: All PSDM filter options on. Right: All PSDM filter options off.

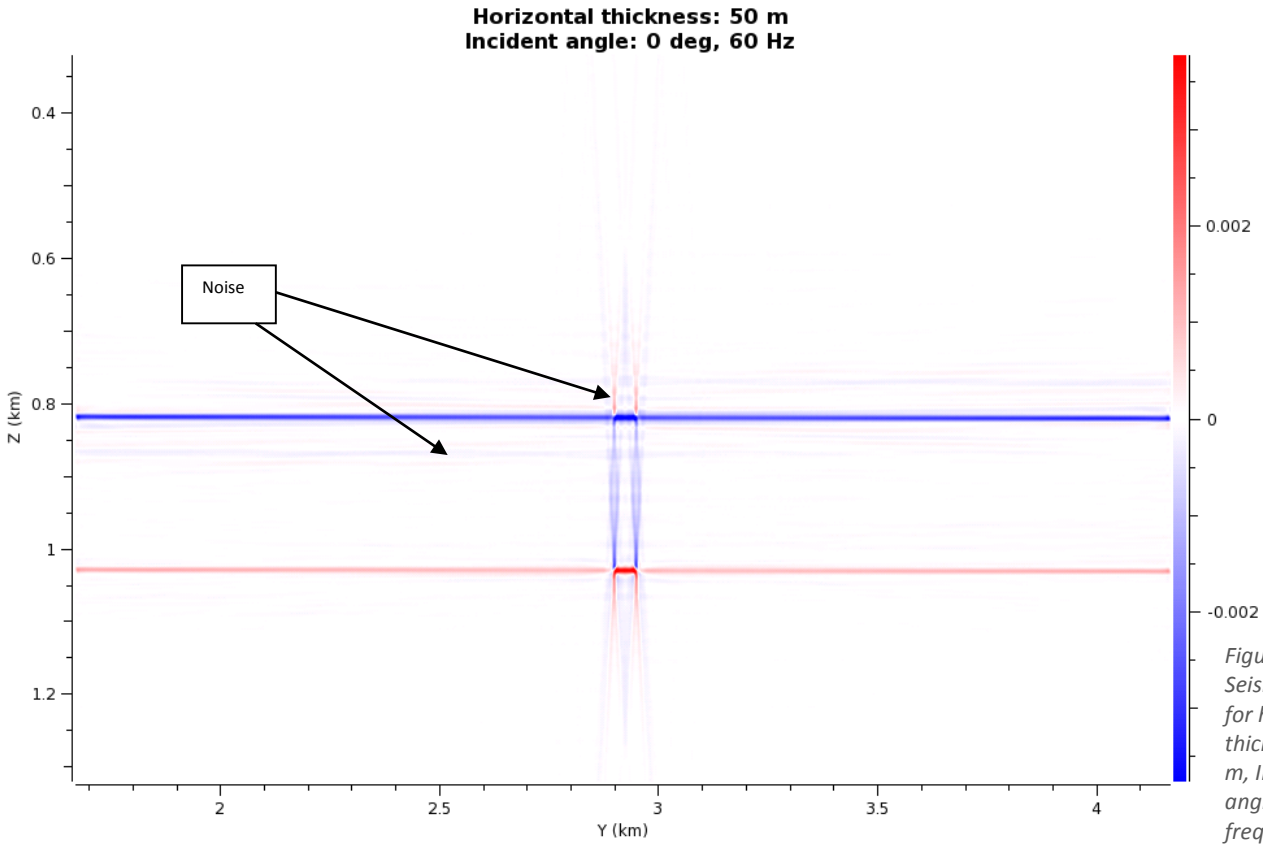

Figure 8.10 Seismic result for horizontal thickness of 50 m, Incident angle 0°, frequency 60 Hz and all PSDM filter options on.

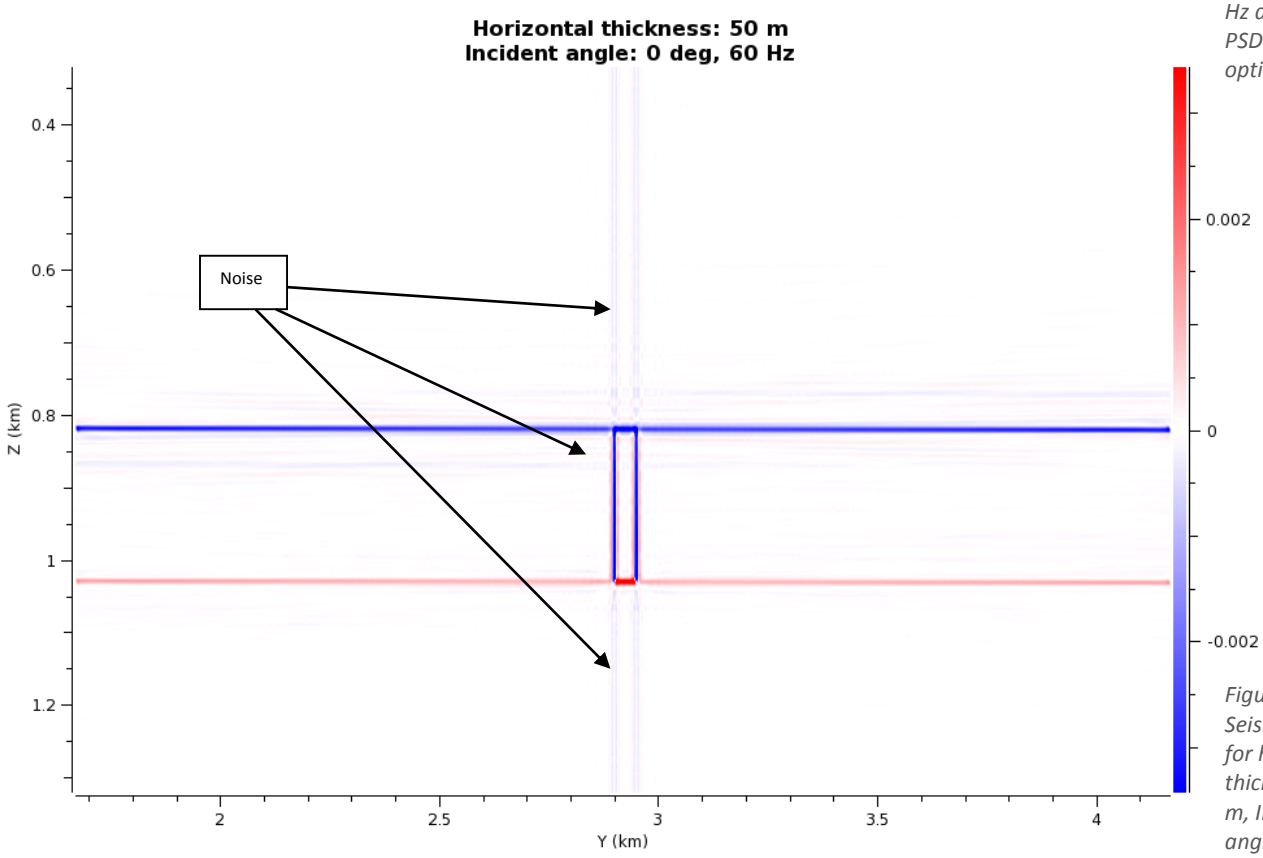

Figure 8.11 Seismic result for horizontal thickness of 50 m, Incident angle 0°, frequency 60 Hz and all PSDM filter options off.

8.4.2 Plot of illumination vectors compared to depth

Comparing the $\mathbf{I_{SR}}$ plot from depth of 925 m (Figure 7.5), with the plot from this workflow (821 m) (Figure 7.61), a higher coverage in angles is observed. The $\mathbf{I_{SR}}$ plot is always considering all available $\mathbf{I_{SR}}$. It is not plotting solely the $\mathbf{I_{SR}}$ used in the angle range. Therefore this can not be the explanation of the difference. The only element that differ, is the depth of the target. Higher center of the target gives better and bigger coverage in $\mathbf{I_{SR}}$, but we know from the previous chapter that the $\mathbf{I_{SR}}$ alone is not enough to get vertical interfaces visible on the seismic.

8.4.3 Could we avoid diffractions?

With true amplitude (chapter 6.3.4) the model is pre-processed to take geometrical spreading and attenuation into account before applying migration. Some diffractions is still visible at abrupt interfaces of the model. These diffractions are the footprint of the PSF, and are some sort of noise. In the SeisRoX manual (NORSAR, 2014a) we can find a suggestion to try a different aperture range and traveltime options to see if the diffractions disappear. In this case, they did not disappear with increasing traveltime range and aperture range that still could be realistic.

9 Summary and conclusion

Modeling various frequencies, incident angles and varying reservoir models has been performed. The modeling has confirmed that input frequency is important to the outcome resolution, and that the reflection strength is depending on the incident angle. Overall, the PSF gives more precise information about the resolution.

- The reflection coefficients value increased due to higher saturation of CO_2 as expected.
- It is important to choose the right sampling to get the reflectivity image well gridded and to avoid truncation of the PSDM filter.
- In this case the spatial sampling is not affecting the vertical resolution in PSF, but the survey parameters, $\mathbf{l_{SR}}$-vectors and frequency are. The sampling is only affecting the horizontal resolution.
- The Fresnel zone used to determine horizontal resolution is approximately equal to $\frac{\lambda}{4}$ after migration; this means that migration improves the horizontal resolution. In this case it is only valid for 0° incident angle, and the same spatial sampling.
- The depth of the target where the PSF is calculated will affect the coverage of the $\mathbf{l_{SR}}$. The $\mathbf{l_{SR}}$ is also affected by the survey parameters and background model.
- A frequency of 40 Hz gives good enough resolution to detect all shale layers in reservoir model 2 when using incident angle of 20°. A frequency of 70 Hz will make it possible to detect both interfaces of a vertical layer of 1 m.
- With a frequency of 30 Hz, and a varying incident angle, it was possible to detect all layers in the reservoir model 2, except between the layer shale layer 3 and 4. Interference occurred in almost all layers. It was not possible to detect the layers of vertical thickness of 1 m, as two separate interfaces.
- A vertical plume with thickness equal to 40 m or thicker, is detectable with no interference with input frequency of 30 Hz and with 20° incident angle. A plume is visible with constructive interference with thickness of 20 m. Partly interference occurs for a plume with vertical thickness of 10 m or smaller. The reflection is stronger indicating the presence of a plume for thickness equal and greater than 3 m. For thickness 1 m, the reflection is not changing in the area where the plume is located.

- A vertical plume with thickness equal 20 m or thicker, is detectable with no interference with input frequency of 60 Hz and 20° incident angle. A plume is visible with constructive interference for vertical thickness of 10 m. For a plume with vertical thickness of 5 m or smaller, partly interference occurs. The reflection is stronger indicating the presence of a plume for thickness equal to and greater than 3 m. For thickness of 1 m, the reflection is not changing in the area where the plume is located, same as for 30 Hz.

- No vertical reflections was possible to detect with realistic PSDM filter parameters and incident an angle of 20°.

- Vertical reflections is visible for incident angle of 0°, and all PSDM filter options turned off.

References

AKI, K. & RICHARDS, P. G. 1980. *Quantitative seismology,* : W. H. Freeman & Co. pp.123.

ANDREASSEN, K. 2009. Lecture Notes for Marine Geophysics GEO-3123, University of Tromsø.

ANDREASSEN, K., NILSSEN, E. & ØDEGAARD, C. 2007. Analysis of shallow gas and fluid migration within the Plio-Pleistocene sedimentary succession of the SW Barents Sea continental margin using 3D seismic data. *Geo-Marine Letters,* 27**,** 155-171.

ARTS, R., EIKEN, O., CHADWICK, A., ZWEIGEL, P., VAN DER MEER, B. & KIRBY, G. 2004a. Seismic monitoring at the Sleipner underground CO2 storage site (North Sea). *Geological Society, London, Special Publications,* 233**,** 181-191.

ARTS, R., EIKEN, O., CHADWICK, A., ZWEIGEL, P., VAN DER MEER, L. & ZINSZNER, B. 2004b. Monitoring of CO2 injected at Sleipner using time-lapse seismic data. *Energy,* 29**,** 1383-1392.

BENTHAM, M. & KIRBY, M. 2005. Stockage du CO2 dans les aquifères salins. *Oil & Gas Science and Technology - Rev. IFP,* 60**,** 559-567.

BOAIT, F. C., WHITE, N. J., BICKLE, M. J., CHADWICK, R. A., NEUFELD, J. A. & HUPPERT, H. E. 2012. Spatial and temporal evolution of injected CO2 at the Sleipner Field, North Sea. *Journal of Geophysical Research: Solid Earth,* 117**,** B03309.

BROWN, A. R. 1999. *Interpretation of three-dimensional seismic data,* AAPG Memoir 42, Tulsa, Oklahoma, pp. 514.

BRUANT, R. G., GUSWA, A. J., CELIA, M. A. & PETERS, C. A. 2002. Safe storage of CO2 in deep saline aquifers. *Environmental Science & Technology,* 36**,** 240A-245A.

BÜNZ, S., FAVEROLA, A. & PANIERI, G. 2014. Lecture notes in GEO-3151 Seminar in Energy and Environment.

BÖHRINGER, C., RUTHERFORD, T. F. & TOL, R. S. J. 2009. THE EU 20/20/2020 targets: An overview of the EMF22 assessment. *Energy Economics,* 31, Supplement 2**,** S268-S273.

CHADWICK, A., ARTS, R., BERNSTONE, C., MAY, F., THIBEAU, S. & ZWEIGEL, P. 2008. *Best practice for the storage of CO2 in saline aquifers - observations and guidlines from the SACS and CO2STORE projects.* , Nottingham, UK. (British Geological Survey Occasional Publications, 14).

CHADWICK, A. & WILLIAMS, G. 2010. Quantitative analysis of time-lapse seismic monitoring data at the Sleipner CO2 storage operation. *The Leading Edge,* 29**,** 170-177.

CHADWICK, R. A., ARTS, R., EIKEN, O., KIRBY, G. A., LINDEBERG, E. & ZWEIGEL, P. 2004a. 4D Seismic Imaging of an Injected C02 Plume at the Sleipner Field, Central North Sea. *Geological Society, London, Memoirs,* 29**,** 311-320.

CHADWICK, R. A., ZWEIGEL, P., GREGERSEN, U., KIRBY, G. A., HOLLOWAY, S. & JOHANNESSEN, P. N. 2004b. Geological reservoir characterization of a CO2 storage site: The Utsira Sand, Sleipner, northern North Sea. *Energy,* 29**,** 1371-1381.

CMI. 2011. *Carbon Mitigation Iniative* [Online]. Author: Roberta Hotinski. Available: http://cmi.princeton.edu/wedges/.

CREWES. 2001-2005. *CREWES Reflectivity Explorer 2.1* [Online]. University if Calgary: The Consortium for Research in Elastic Wave Exploration Seismology. Available: http://www.crewes.org/ResearchLinks/ExplorerPrograms/ReflEx/REcrewes2_1.html.

DVORKIN, J., A.GUTIERREZ, M. & GRANA, D. 2014. *Seismic Reflections of Rock Properties,* United States of America, Cambrigde University Press.

GELIUS, L. J. & JOHANSEN, T. A. 2010. *GeoCLASS* [Online]. UniGEO as. Available: http://www.unigeo.no.
GHADERI, A. & LANDRØ, M. 2009. Estimation of thickness and velocity changes of injected carbon dioxide layers from prestack time-lapse seismic data. *Geophysics,* 74**,** O17-O28.
HALLAND, E. K., JOHANSEN, W. T. & RIIS, F. 2011. *CO2 Storage Atlas Norwegian North Sea*, Norwegian Petroleum Directorate.
HERMANRUD, C., ANDRESEN, T., EIKEN, O., HANSEN, H., JANBU, A., LIPPARD, J., BOLÅS, H. N., SIMMENES, T. H., TEIGE, G. M. G. & ØSTMO, S. 2009. Storage of CO2 in saline aquifers–Lessons learned from 10 years of injection into the Utsira Formation in the Sleipner area. *Energy Procedia,* 1**,** 1997-2004.
HOLLOWAY, S. 2005. Underground sequestration of carbon dioxide—a viable greenhouse gas mitigation option. *Energy,* 30**,** 2318-2333.
IPCC 2005. IPCC Special Report on Carbon Dioxide Capture and Storage. . Prepared by Working Group III of the Intergovernmental Panel on Climate Change [Metz, B., O. Davidson, H. C. de Coninck, M. Loos, and L. A. Meyer (eds.)]. Cambridge University Press, Cambridge, United Kingdom and New York, NY, USA, 442 pp.
IPCC 2007. Climate Change 2007: Mitigation. Contribution of Working Group III to the Fourth Assessment Report of the Intergovernmental Panel on Climate Change [B. Metz, O.R. Davidson, P.R. Bosch, R. Dave, L.A. Meyer (eds)], Cambridge University Press, Cambridge, United Kingdom and New York, NY, USA., XXX pp.
JOHANSEN, T. A. 2013. Lecture Notes in AG-341 Geological Constraints of CO2 Sequestration, UNIS.
KARSTENS, J. & BERNDT, C. 2015. Seismic chimneys in the Southern Viking Graben – Implications for palaeo fluid migration and overpressure evolution. *Earth and Planetary Science Letters,* 412**,** 88-100.
LECOMTE, I. 2008. Resolution and illumination analyses in PSDM: A ray-based approach. *The Leading Edge,* 27**,** 650-663.
MAVKO, G., MUKERJI, T. & DVORKIN, J. 1998. *The rock physics handbook: tools for seismic analysis in porous media*, Cambridge University Press.
MIKKELSEN, E. R. 2009. *Monitoring of CO2 sequestration at the Longyearbyen CO2 Lab by time-lapse seismic: an interdisciplinary rock physics study*, [Trondheim], E.R. Mikkelsen.
MONK, D. J. 2010. Fresnel-zone binning: Fresnel-zone shape with offset and velocity function. *Geophysics*, 75**,** T9-T14.
NORSAR 2014a. SeisRoX 3.0.1 Manual.
NORSAR. 2014b. *NORSAR Webpage* [Online]. assist2net. Available: http://www.norsar.no/seismod/Products/SeisRoX/SimPLI/SimPLI-Workflow/.
OECD/IEA 2013. Technology Roadmap: Carbon Capture and Storage, 2013. Report 2013**,** pp. 24.
PEARCE, J. M. 2006. What can we learn from natural analogues? *In:* LOMBARDI, S., ALTUNINA, L. K. & BEAUBIEN, S. E. (eds.) *Advances in the Geological Storage of Carbon Dioxide.* Springer Netherlands.
PRUESS, K. 2008. On CO2 fluid flow and heat transfer behavior in the subsurface, following leakage from a geologic storage reservoir. *Environmental Geology,* 54**,** 1677-1686.
RAFAELSEN, B. 2013. Lecture Notes in GEO-3115 Petroleum Geology.
SELLEY, R. C. 1998. *Elements of Petroleum Geology*.
SHERIFF, R. E. & GELDART, L. P. 1995. *Exploration Seismology*, Press Syndicate of the University of Cambridge.

SHIPTON, Z. K., EVANS, J. P., KIRSCHNER, D., KOLESAR, P. T., WILLIAMS, A. P. & HEATH, J. 2004. Analysis of CO2 leakage through 'low-permeability' faults from natural reservoirs in the Colorado Plateau, east-central Utah. *Geological Society, London, Special Publications,* 233**,** 43-58.

SHUEY, R. T. 1985. *A simplification of the Zoeppritz Equations,* Geophysics, 50, 609-614.

THEHIGHERLEARNING.COM. 2014. *NASA Confirms That Huge Methane Cloud In U.S. Southwest Is the Real Deal* [Online]. Available: http://thehigherlearning.com/2014/10/13/nasa-confirms-that-huge-methane-cloud-in-u-s-southwest-is-real-deal/.

Appendix A

Acoustic velocities change due to different saturation of CO_2. This appendix illustrates how to calculate these changes by using the Gassmann equation (Equation 3.9) and the constant parameters from Table A.1.

Table A.1 Parameters from the Sleipner filed used in the calculation. From (Ghaderi and Landrø, 2009).

Constants	Value
Porosity (φ)	0,37
Temperature	27 °C
Density of CO_2 (ρ_{CO_2}))	800 kg/m^3
Density of water (ρ_w))	1020 kg/m^3
Density of the matrix (ρ_m)	2650 kg/m^3
Bulk Modulus of CO_2 (K_{CO_2})	0,136 GPa
Bulk Modulus of water (K_w)	2,28 GPa
Bulk Modulus of matrix/solid (K_s)	36,9 GPa
Bulk Modulus of the dry rock (K_d)	2,56 GPa
Shear Modulus of dry rock (μ_d)	0,8569 GPa

Before applying the Gassmann Equation, we need to calculate the density of the fluid and then the effective density. Using Equation 3.4 to calculate the density of the fluid:

$$\rho_{fluid} = S_w\rho_w + (1 - S_w)\rho_{CO_2}$$

Using Equation 3.3 to calculate the density of the rock (effective density) later to be used in calculation of the acoustic velocities:

$$\rho = (1 - \varphi)\,\rho_{matrix} + \varphi\rho_{fluid}$$

Before using the Gassmann equation we also need to know all the bulk modulus. In Table A.1 we find some of them, but we need to calculate the bulk modulus of the fluid. In this case we have to fluid types and need to use Equation 3.10:

$$\frac{1}{K_f} = \frac{S_w}{K_w} + \frac{S_g}{K_g} + \frac{S_l}{K_l}$$

In this case we only have saturation of water (S_w) and gas (S_g) and can drop the liquid part. After rewriting this equation, we get:

$$K_f = \frac{1}{\frac{S_w}{K_w} + \frac{S_g}{K_g}}$$

Then we can use Equation 3.9 to calculate the effective bulk modulus:

$$K^* = \frac{Kd\,[-(1+\varphi)+\frac{\varphi Ks}{Kf}]+Ks}{\frac{\varphi Ks}{Kf}-\frac{Kd}{Ks}+(1-\varphi)}$$

The effective shear modulus can be expressed by Equation 3.11, and is as mentioned in chapter Elastic properties3.1 equal to the shear modulus of the dry rock from Table A.1:

$$\mu^* = \mu_d$$

By using the parameters in Table A.1 with the result from these equations, one can easily calculate the seismic velocities V_p and V_s using Equation 3.1 and Equation 3.2:

$$V_p = \sqrt{\frac{K + \frac{4}{3}\mu}{\rho}}$$

$$V_s = \sqrt{\frac{\mu}{\rho}}$$

The calculations in the following tables use the exact number with all possible decimals, and not the approach listed in the table.

Calculations for 0% CO_2 saturation		
Equation used:	Parameters added:	Result:
$\rho_{fluid} = S_w\rho_w + (1 - S_w)\rho_{CO_2}$	$\rho_{fluid} = 1 \cdot 1020\ kg/m^3 + 0$	$\rho_{fluid} = 1020\ kg/m^3$
$\rho = (1 - \varphi)\ \rho_{matrix} + \varphi\rho_{fluid}$	$\rho = (1 - 0{,}37) \cdot 2650\ kg/m^3 + 0{,}37 \cdot 1020\ kg/m^3$	$\rho = 2046{,}9\ kg/m^3 \approx 2047\ kg/m^3$
$K_f = \frac{1}{\frac{S_w}{K_w} + \frac{S_g}{K_g}}$	$K_f = \frac{1}{\frac{1}{2{,}28\ GPa} + 0}$	$K_f = 2{,}28\ GPa$
$K^* = \frac{Kd\ [-(1+\varphi)+\frac{\varphi Ks}{Kf}]+Ks}{\frac{\varphi Ks}{Kf}-\frac{Kd}{Ks}+(1-\varphi)}$	$K^* = \frac{2{,}56\ GPa\cdot\left[-(1+0{,}37)+\frac{0{,}37\cdot 36{,}9\ GPa}{2{,}28\ GPa}\right]+36{,}9\ GPa}{\frac{0{,}37\cdot 36{,}9\ GPa}{2{,}28\ GPa}-\frac{2{,}56\ GPa}{36{,}9\ GPa}+(1-0{,}37)}$	$K^* = 7{,}439\ GPa \approx 7{,}44\ GPa$
$\mu^* = \mu_d$	$\mu^* = 0{,}8569\ GPa$	$\mu^* = 0{,}8569\ GPa$
$V_p = \sqrt{\frac{K + \frac{4}{3}\mu}{\rho}}$	$V_p = \sqrt{\frac{7{,}44\ GPa\ + \frac{4}{3}\cdot 0{,}8569\ GPa}{2047\ kg/m^3}}$	$V_p = 2047{,}6\ m/s \approx 2048\ m/s$
$V_s = \sqrt{\frac{\mu}{\rho}}$	$V_s = \sqrt{\frac{0{,}8569\ GPa}{2047\ kg/m^3}}$	$V_s = 647\ m/s$

Calculations for 10% CO_2 saturation		
Equation used:	Parameters added:	Result:
$\rho_{fluid} = S_w\rho_w + (1 - S_w)\rho_{CO_2}$	$\rho_{fluid} = 0{,}9 \cdot 1020\frac{kg}{m^3} + (1 - 0{,}9) \cdot 800 kg/m^3$	$\rho_{fluid} = 998\ kg/m^3$
$\rho = (1 - \varphi)\ \rho_{matrix} + \varphi\rho_{fluid}$	$\rho = (1 - 0{,}37) \cdot 2650\ kg/m^3 + 0{,}37 \cdot 998\ kg/m^3$	$\rho = 2038{,}76\ kg/m^3 \approx\ 2039\ kg/m^3$
$K_f = \frac{1}{\frac{S_w}{K_w} + \frac{S_g}{K_g}}$	$K_f = \frac{1}{\frac{0{,}9}{2{,}28\ GPa} + \frac{0{,}1}{0{,}136\ GPa}}$	$K_f = 0{,}884\ GPa \approx 0{,}88\ GPa$
$K^* = \frac{Kd\ [-(1+\varphi)+\frac{\varphi Ks}{Kf}]+Ks}{\frac{\varphi Ks}{Kf}-\frac{Kd}{Ks}+(1-\varphi)}$	$K^* = \frac{2{,}56\ GPa\cdot\left[-(1+0{,}37)+\frac{0{,}37\cdot 36{,}9\ GPa}{0{,}88\ GPa}\right]+36{,}9\ GPa}{\frac{0{,}37\cdot 36{,}9\ GPa}{0{,}88\ GPa}-\frac{2{,}56\ GPa}{36{,}9\ GPa}+(1-0{,}37)}$	$K^* = 4{,}558\ GPa \approx 4{,}56\ GPa$
$\mu^* = \mu_d$	$\mu^* = 0{,}8569\ GPa$	$\mu^* = 0{,}8569\ GPa$
$V_p = \sqrt{\frac{K + \frac{4}{3}\mu}{\rho}}$	$V_p = \sqrt{\frac{4{,}56\ GPa\ + \frac{4}{3}\cdot 0{,}8569\ GPa}{2039\ kg/m^3}}$	$V_p = 1672{,}2\ m/s \approx 1672\ m/s$
$V_s = \sqrt{\frac{\mu}{\rho}}$	$V_s = \sqrt{\frac{0{,}8569\ GPa}{2039\ kg/m^3}}$	$V_s = 648\ m/s$

Calculations for 20% CO_2 saturation		
Equation used:	Parameters added:	Result:
$\rho_{fluid} = S_w\rho_w + (1 - S_w)\rho_{CO_2}$	$\rho_{fluid} = 0{,}8 \cdot 1020\frac{kg}{m^3} + (1 - 0{,}8) \cdot 800 kg/m^3$	$\rho_{fluid} = 976\ kg/m^3$
$\rho = (1 - \varphi)\ \rho_{matrix} + \varphi\rho_{fluid}$	$\rho = (1 - 0{,}37) \cdot 2650\ kg/m^3 + 0{,}37 \cdot 976\ kg/m^3$	$\rho = 2030{,}6\ kg/m^3 \approx\ 2031\ kg/m^3$
$K_f = \frac{1}{\frac{S_w}{K_w} + \frac{S_g}{K_g}}$	$K_f = \frac{1}{\frac{0{,}8}{2{,}28\ GPa} + \frac{0{,}2}{0{,}136\ GPa}}$	$K_f = 0{,}549\ GPa \approx 0{,}55\ GPa$
$K^* = \frac{Kd\ [-(1+\varphi)+\frac{\varphi Ks}{Kf}]+Ks}{\frac{\varphi Ks}{Kf}-\frac{Kd}{Ks}+(1-\varphi)}$	$K^* = \frac{2{,}56\ GPa\cdot\left[-(1+0{,}37)+\frac{0{,}37\cdot 36{,}9\ GPa}{0{,}55\ GPa}\right]+36{,}9\ GPa}{\frac{0{,}37\cdot 36{,}9\ GPa}{0{,}55\ GPa}-\frac{2{,}56\ GPa}{36{,}9\ GPa}+(1-0{,}37)}$	$K^* = 3{,}816\ GPa \approx 3{,}82\ GPa$
$\mu^* = \mu_d$	$\mu^* = 0{,}8569\ GPa$	$\mu^* = 0{,}8569\ GPa$
$V_p = \sqrt{\frac{K + \frac{4}{3}\mu}{\rho}}$	$V_p = \sqrt{\frac{3{,}82\ GPa\ + \frac{4}{3}\cdot 0{,}8569\ GPa}{2031\ kg/m^3}}$	$V_p = 1562{,}7\ m/s \approx 1563\ m/s$
$V_s = \sqrt{\frac{\mu}{\rho}}$	$V_s = \sqrt{\frac{0{,}8569\ GPa}{2031\ kg/m^3}}$	$V_s = 649{,}6\ m/s \approx 650\ m/s$

Calculations for 30% CO_2 saturation		
Equation used:	Parameters added:	Result:
$\rho_{fluid} = S_w\rho_w + (1 - S_w)\rho_{CO_2}$	$\rho_{fluid} = 0{,}7 \cdot 1020\frac{kg}{m^3} + (1 - 0{,}7) \cdot 800 kg/m^3$	$\rho_{fluid} = 954\ kg/m^3$
$\rho = (1 - \varphi)\ \rho_{matrix} + \varphi\rho_{fluid}$	$\rho = (1 - 0{,}37) \cdot 2650\ kg/m^3 + 0{,}37 \cdot 954\ kg/m^3$	$\rho = 2022{,}48\, kg/m^3 \approx\ 2022\ kg/m^3$
$K_f = \frac{1}{\frac{S_w}{K_w} + \frac{S_g}{K_g}}$	$K_f = \frac{1}{\frac{0{,}7}{2{,}28\ GPa} + \frac{0{,}3}{0{,}136\ GPa}}$	$K_f = 0{,}397\ GPa \approx 0{,}40\ GPa$
$K^* = \frac{Kd\ [-(1+\varphi)+\frac{\varphi Ks}{Kf}]+Ks}{\frac{\varphi Ks}{Kf}-\frac{Kd}{Ks}+(1-\varphi)}$	$K^* = \frac{2{,}56\ GPa\cdot\left[-(1+0{,}37)+\frac{0{,}37\cdot 36{,}9\ GPa}{0{,}40\ GPa}\right]+36{,}9\ GPa}{\frac{0{,}37\cdot 36{,}9\ GPa}{0{,}40\ GPa}-\frac{2{,}56\ GPa}{36{,}9\ GPa}+(1-0{,}37)}$	$K^* = 3{,}476\ GPa \approx 3{,}48\ GPa$
$\mu^* = \mu_d$	$\mu^* = 0{,}8569\ GPa$	$\mu^* = 0{,}8569\ GPa$
$V_p = \sqrt{\frac{K + \frac{4}{3}\mu}{\rho}}$	$V_p = \sqrt{\frac{3{,}48\ GPa\ + \frac{4}{3}\cdot 0{,}8569\ GPa}{2022\ kg/m^3}}$	$V_p = 1511{,}2\ m/s \approx 1511\ m/s$
$V_s = \sqrt{\frac{\mu}{\rho}}$	$V_s = \sqrt{\frac{0{,}8569\ GPa}{2022\ kg/m^3}}$	$V_s = 650{,}9\ m/s \approx 651\ m/s$

Calculations for 40% CO_2 saturation		
Equation used:	Parameters added:	Result:
$\rho_{fluid} = S_w\rho_w + (1 - S_w)\rho_{CO_2}$	$\rho_{fluid} = 0{,}6 \cdot 1020\frac{kg}{m^3} + (1 - 0{,}6) \cdot 800 kg/m^3$	$\rho_{fluid} = 932\ kg/m^3$
$\rho = (1 - \varphi)\ \rho_{matrix} + \varphi\rho_{fluid}$	$\rho = (1 - 0{,}37) \cdot 2650\ kg/m^3 + 0{,}37 \cdot 932\ kg/m^3$	$\rho = 2014{,}3\, kg/m^3 \approx\ 2014\ kg/m^3$
$K_f = \frac{1}{\frac{S_w}{K_w} + \frac{S_g}{K_g}}$	$K_f = \frac{1}{\frac{0{,}6}{2{,}28\ GPa} + \frac{0{,}4}{0{,}136\ GPa}}$	$K_f = 0{,}312\ GPa \approx 0{,}31\ GPa$
$K^* = \frac{Kd\ [-(1+\varphi)+\frac{\varphi Ks}{Kf}]+Ks}{\frac{\varphi Ks}{Kf}-\frac{Kd}{Ks}+(1-\varphi)}$	$K^* = \frac{2{,}56\ GPa\cdot\left[-(1+0{,}37)+\frac{0{,}37\cdot 36{,}9\ GPa}{0{,}31\ GPa}\right]+36{,}9\ GPa}{\frac{0{,}37\cdot 36{,}9\ GPa}{0{,}31\ GPa}-\frac{2{,}56\ GPa}{36{,}9\ GPa}+(1-0{,}37)}$	$K^* = 3{,}281\ GPa \approx 3{,}28\ GPa$
$\mu^* = \mu_d$	$\mu^* = 0{,}8569\ GPa$	$\mu^* = 0{,}8569\ GPa$
$V_p = \sqrt{\frac{K + \frac{4}{3}\mu}{\rho}}$	$V_p = \sqrt{\frac{3{,}28\ GPa\ + \frac{4}{3}\cdot 0{,}8569\ GPa}{2014\ kg/m^3}}$	$V_p = 1481{,}9\ m/s \approx 1482\ m/s$
$V_s = \sqrt{\frac{\mu}{\rho}}$	$V_s = \sqrt{\frac{0{,}8569\ GPa}{2014\ kg/m^3}}$	$V_s = 652{,}2\ m/s \approx 652\ m/s$

Calculations for 50% CO_2 saturation		
Equation used:	Parameters added:	Result:
$\rho_{fluid} = S_w\rho_w + (1 - S_w)\rho_{CO_2}$	$\rho_{fluid} = 0{,}5 \cdot 1020\frac{kg}{m^3} + (1 - 0{,}5) \cdot 800 kg/m^3$	$\rho_{fluid} = 910\ kg/m^3$
$\rho = (1 - \varphi)\ \rho_{matrix} + \varphi\rho_{fluid}$	$\rho = (1 - 0{,}37) \cdot 2650\ kg/m^3 + 0{,}37 \cdot 910\ kg/m^3$	$\rho = 2006{,}2\, kg/m^3 \approx\ 2006\ kg/m^3$
$K_f = \frac{1}{\frac{S_w}{K_w} + \frac{S_g}{K_g}}$	$K_f = \frac{1}{\frac{0{,}5}{2{,}28\ GPa} + \frac{0{,}5}{0{,}136\ GPa}}$	$K_f = 0{,}256\ GPa \approx 0{,}26\ GPa$
$K^* = \frac{Kd\ [-(1+\varphi)+\frac{\varphi Ks}{Kf}]+Ks}{\frac{\varphi Ks}{Kf}-\frac{Kd}{Ks}+(1-\varphi)}$	$K^* = \frac{2{,}56\ GPa\cdot\left[-(1+0{,}37)+\frac{0{,}37\cdot 36{,}9\ GPa}{0{,}26\ GPa}\right]+36{,}9\ GPa}{\frac{0{,}37\cdot 36{,}9\ GPa}{0{,}26\ GPa}-\frac{2{,}56\ GPa}{36{,}9\ GPa}+(1-0{,}37)}$	$K^* = 3{,}154\ GPa \approx 3{,}15\ GPa$
$\mu^* = \mu_d$	$\mu^* = 0{,}8569\ GPa$	$\mu^* = 0{,}8569\ GPa$
$V_p = \sqrt{\frac{K + \frac{4}{3}\mu}{\rho}}$	$V_p = \sqrt{\frac{3{,}15\ GPa\ + \frac{4}{3}\cdot 0{,}8569\ GPa}{2006\ kg/m^3}}$	$V_p = 1463{,}5/s \approx 1464\ m/s$
$V_s = \sqrt{\frac{\mu}{\rho}}$	$V_s = \sqrt{\frac{0{,}8569\ GPa}{2006\ kg/m^3}}$	$V_s = 653{,}5\ m/s \approx 654\ m/s$

Calculations for 60% CO_2 saturation		
Equation used:	Parameters added:	Result:
$\rho_{fluid} = S_w\rho_w + (1 - S_w)\rho_{CO_2}$	$\rho_{fluid} = 0{,}4 \cdot 1020\frac{kg}{m^3} + (1 - 0{,}4) \cdot 800 kg/m^3$	$\rho_{fluid} = 888\ kg/m^3$
$\rho = (1 - \varphi)\ \rho_{matrix} + \varphi\rho_{fluid}$	$\rho = (1 - 0{,}37) \cdot 2650\ kg/m^3 + 0{,}37 \cdot 888\ kg/m^3$	$\rho = 1998{,}0\ kg/m^3 \approx\ 1998\ kg/m^3$
$K_f = \frac{1}{\frac{S_w}{K_w} + \frac{S_g}{K_g}}$	$K_f = \frac{1}{\frac{0{,}4}{2{,}28\ GPa} + \frac{0{,}6}{0{,}136\ GPa}}$	$K_f = 0{,}217\ GPa \approx 0{,}22\ GPa$
$K^* = \frac{Kd\ [-(1+\varphi)+\frac{\varphi Ks}{Kf}]+Ks}{\frac{\varphi Ks}{Kf}-\frac{Kd}{Ks}+(1-\varphi)}$	$K^* = \frac{2{,}56\ GPa\cdot\left[-(1+0{,}37)+\frac{0{,}37\cdot 36{,}9\ GPa}{0{,}22\ GPa}\right]+36{,}9\ GPa}{\frac{0{,}37\cdot 36{,}9\ GPa}{0{,}22\ GPa}-\frac{2{,}56\ GPa}{36{,}9\ GPa}+(1-0{,}37)}$	$K^* = 3{,}065\ GPa \approx 3{,}07\ GPa$
$\mu^* = \mu_d$	$\mu^* = 0{,}8569\ GPa$	$\mu^* = 0{,}8569\ GPa$
$V_p = \sqrt{\frac{K + \frac{4}{3}\mu}{\rho}}$	$V_p = \sqrt{\frac{3{,}07\ GPa\ + \frac{4}{3}\cdot 0{,}8569\ GPa}{1998\ kg/m^3}}$	$V_p = 1451{,}2\ m/s \approx 1451 m/s$
$V_s = \sqrt{\frac{\mu}{\rho}}$	$V_s = \sqrt{\frac{0{,}8569\ GPa}{1998\ kg/m^3}}$	$V_s = 654{,}8\ m/s \approx 655\ m/s$

Calculations for 70% CO_2 saturation		
Equation used:	Parameters added:	Result:
$\rho_{fluid} = S_w\rho_w + (1 - S_w)\rho_{CO_2}$	$\rho_{fluid} = 0{,}3 \cdot 1020\frac{kg}{m^3} + (1 - 0{,}3) \cdot 800 kg/m^3$	$\rho_{fluid} = 866\ kg/m^3$
$\rho = (1 - \varphi)\ \rho_{matrix} + \varphi\rho_{fluid}$	$\rho = (1 - 0{,}37) \cdot 2650\ kg/m^3 + 0{,}37 \cdot 866\ kg/m^3$	$\rho = 1989{,}9\, kg/m^3 \approx\ 1990\ kg/m^3$
$K_f = \frac{1}{\frac{S_w}{K_w} + \frac{S_g}{K_g}}$	$K_f = \frac{1}{\frac{0{,}3}{2{,}28\ GPa} + \frac{0{,}7}{0{,}136\ GPa}}$	$K_f = 0{,}189\ GPa \approx 0{,}19\ GPa$
$K^* = \frac{Kd\ [-(1+\varphi)+\frac{\varphi Ks}{Kf}]+Ks}{\frac{\varphi Ks}{Kf}-\frac{Kd}{Ks}+(1-\varphi)}$	$K^* = \frac{2{,}56\ GPa\cdot\left[-(1+0{,}37)+\frac{0{,}37\cdot 36{,}9\ GPa}{0{,}19\ GPa}\right]+36{,}9\ GPa}{\frac{0{,}37\cdot 36{,}9\ GPa}{0{,}19\ GPa}-\frac{2{,}56\ GPa}{36{,}9\ GPa}+(1-0{,}37)}$	$K^* = 3{,}000\ GPa \approx 3{,}00\ GPa$
$\mu^* = \mu_d$	$\mu^* = 0{,}8569\ GPa$	$\mu^* = 0{,}8569\ GPa$
$V_p = \sqrt{\frac{K + \frac{4}{3}\mu}{\rho}}$	$V_p = \sqrt{\frac{3{,}00\ GPa\ + \frac{4}{3}\cdot 0{,}8569\ GPa}{1990\ kg/m^3}}$	$V_p = 1442{,}8\ m/s \approx 1443\ m/s$
$V_s = \sqrt{\frac{\mu}{\rho}}$	$V_s = \sqrt{\frac{0{,}8569\ GPa}{1990\ kg/m^3}}$	$V_s = 656{,}2\ m/s \approx 656\ m/s$

Calculations for 80% CO_2 saturation		
Equation used:	Parameters added:	Result:
$\rho_{fluid} = S_w\rho_w + (1 - S_w)\rho_{CO_2}$	$\rho_{fluid} = 0{,}2 \cdot 1020\frac{kg}{m^3} + (1 - 0{,}2) \cdot 800 kg/m^3$	$\rho_{fluid} = 844\ kg/m^3$
$\rho = (1 - \varphi)\ \rho_{matrix} + \varphi\rho_{fluid}$	$\rho = (1 - 0{,}37) \cdot 2650\ kg/m^3 + 0{,}37 \cdot 844\ kg/m^3$	$\rho = 1981{,}7 kg/m^3 \approx 1982\ kg/m^3$
$K_f = \frac{1}{\frac{S_w}{K_w} + \frac{S_g}{K_g}}$	$K_f = \frac{1}{\frac{0{,}2}{2{,}28\ GPa} + \frac{0{,}8}{0{,}136\ GPa}}$	$K_f = 0{,}167\ GPa \approx 0{,}17\ GPa$
$K^* = \frac{Kd\ [-(1+\varphi)+\frac{\varphi Ks}{Kf}]+Ks}{\frac{\varphi Ks}{Kf}-\frac{Kd}{Ks}+(1-\varphi)}$	$K^* = \frac{2{,}56\ GPa\cdot\left[-(1+0{,}37)+\frac{0{,}37\cdot 36{,}9\ GPa}{0{,}17\ GPa}\right]+36{,}9\ GPa}{\frac{0{,}37\cdot 36{,}9\ GPa}{0{,}17\ GPa}-\frac{2{,}56\ GPa}{36{,}9\ GPa}+(1-0{,}37)}$	$K^* = 2{,}949\ GPa \approx 2{,}95\ GPa$
$\mu^* = \mu_d$	$\mu^* = 0{,}8569\ GPa$	$\mu^* = 0{,}8569\ GPa$
$V_p = \sqrt{\frac{K + \frac{4}{3}\mu}{\rho}}$	$V_p = \sqrt{\frac{2{,}95\ GPa\ + \frac{4}{3}\cdot 0{,}8569\ GPa}{1982\ kg/m^3}}$	$V_p = 1436{,}9\ m/s \approx 1437\ m/s$
$V_s = \sqrt{\frac{\mu}{\rho}}$	$V_s = \sqrt{\frac{0{,}8569\ GPa}{1982\ kg/m^3}}$	$V_s = 657{,}5\ m/s \approx 658\ m/s$

Calculations for 90% CO_2 saturation		
Equation used:	Parameters added:	Result:
$\rho_{fluid} = S_w\rho_w + (1 - S_w)\rho_{CO_2}$	$\rho_{fluid} = 0{,}1 \cdot 1020\frac{kg}{m^3} + (1 - 0{,}1) \cdot 800 kg/m^3$	$\rho_{fluid} = 822\ kg/m^3$
$\rho = (1 - \varphi)\ \rho_{matrix} + \varphi\rho_{fluid}$	$\rho = (1 - 0{,}37) \cdot 2650\ kg/m^3 + 0{,}37 \cdot 822\ kg/m^3$	$\rho = 1973{,}6\ kg/m^3 \approx\ 1974\ kg/m^3$
$K_f = \frac{1}{\frac{S_w}{K_w} + \frac{S_g}{K_g}}$	$K_f = \frac{1}{\frac{0{,}1}{2{,}28\ GPa} + \frac{0{,}9}{0{,}136\ GPa}}$	$K_f = 0{,}150\ GPa \approx 0{,}15\ GPa$
$K^* = \frac{Kd\ [-(1+\varphi)+\frac{\varphi Ks}{Kf}]+Ks}{\frac{\varphi Ks}{Kf}-\frac{Kd}{Ks}+(1-\varphi)}$	$K^* = \frac{2{,}56\ GPa\cdot\left[-(1+0{,}37)+\frac{0{,}37\cdot 36{,}9\ GPa}{0{,}15\ GPa}\right]+36{,}9\ GPa}{\frac{0{,}37\cdot 36{,}9\ GPa}{0{,}15\ GPa}-\frac{2{,}56\ GPa}{36{,}9\ GPa}+(1-0{,}37)}$	$K^* = 2{,}909\ GPa \approx 2{,}91\ GPa$
$\mu^* = \mu_d$	$\mu^* = 0{,}8569\ GPa$	$\mu^* = 0{,}8569\ GPa$
$V_p = \sqrt{\frac{K + \frac{4}{3}\mu}{\rho}}$	$V_p = \sqrt{\frac{2{,}91\ GPa\ + \frac{4}{3}\cdot 0{,}8569\ GPa}{1974\ kg/m^3}}$	$V_p = 1432{,}8\ m/s \approx 1433\ m/s$
$V_s = \sqrt{\frac{\mu}{\rho}}$	$V_s = \sqrt{\frac{0{,}8569\ GPa}{1974\ kg/m^3}}$	$V_s = 658{,}9\ m/s \approx 659\ m/s$

Calculations for 100% CO_2 saturation		
Equation used:	Parameters added:	Result:
$\rho_{fluid} = S_w\rho_w + (1 - S_w)\rho_{CO_2}$	$\rho_{fluid} = 0 + (1 - 0) \cdot 800 kg/m^3$	$\rho_{fluid} = 800\ kg/m^3$
$\rho = (1 - \varphi)\ \rho_{matrix} + \varphi\rho_{fluid}$	$\rho = (1 - 0{,}37) \cdot 2650\ kg/m^3 + 0{,}37 \cdot 800\ kg/m^3$	$\rho = 1965{,}5\ kg/m^3 \approx 1966\ kg/m^3$
$K_f = \frac{1}{\frac{S_w}{K_w} + \frac{S_g}{K_g}}$	$K_f = \frac{1}{0 + \frac{1}{0{,}136\ GPa}}$	$K_f = 0{,}136\ GPa \approx 0{,}14\ GPa$
$K^* = \frac{Kd\ [-(1+\varphi)+\frac{\varphi Ks}{Kf}]+Ks}{\frac{\varphi Ks}{Kf}-\frac{Kd}{Ks}+(1-\varphi)}$	$K^* = \frac{2{,}56\ GPa \cdot \left[-(1+0{,}37)+\frac{0{,}37 \cdot 36{,}9\ GPa}{0{,}14\ GPa}\right]+36{,}9\ GPa}{\frac{0{,}37 \cdot 36{,}9\ GPa}{0{,}14\ GPa}-\frac{2{,}56\ GPa}{36{,}9\ GPa}+(1-0{,}37)}$	$K^* = 2{,}876\ GPa \approx 2{,}88\ GPa$
$\mu^* = \mu_d$	$\mu^* = 0{,}8569\ GPa$	$\mu^* = 0{,}8569\ GPa$
$V_p = \sqrt{\frac{K + \frac{4}{3}\mu}{\rho}}$	$V_p = \sqrt{\frac{2{,}88\ GPa + \frac{4}{3} \cdot 0{,}8569\ GPa}{1965\ kg/m^3}}$	$V_p = 1429{,}9\ m/s \approx 1430\ m/s$
$V_s = \sqrt{\frac{\mu}{\rho}}$	$V_s = \sqrt{\frac{0{,}8569\ GPa}{1965\ kg/m^3}}$	$V_s = 660{,}2\ m/s \approx 660\ m/s$

Appendix B

This appendix shortly describes scattering isochrones and how to create models in NORSAR.

Scattering isochron

Scattering isochron is the loci of points in the subsurface with the same scattering travel time. This means that the wave will use the same amount of time to travel down and up from these points. The scattering isochrons are the same as a wavefront, and will occur as circles in a homogenous model with zero offset, and as an ellipse if the distance between the source and the receiver are non-zero (Figure B.1).

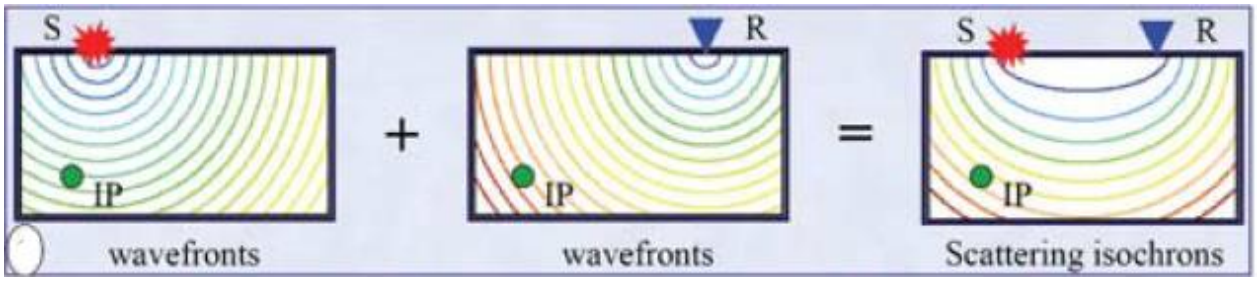

Figure B.1 Summation of the wave fronts from the source and receiver creating the scattering isochrones. Modified from (Lecomte, 2008)

How to create the background model using NORSAR 2D and NORSAR 3D

This is a summary of how I created my background model (and also a guide to create other simple models) using NORSAR 2D and 3D and how the models went from 2D to 2.5D to the final 3D model ready to use in SeisRoX. I started to create 2D models in NORSAR 2D and the first step was to create a section with an inline (parallel to the Y-axis in SeisRoX). The size in Y-direction of my geometry was found from the size of the Sleipner-Petrel-project, and is 5,85 km. I decided to use a maximum depth of 2 km in Z-direction (Figure B.2).

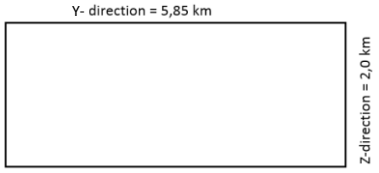

Figure B.2 2D model geometry.

The next step is to create interfaces (Figure B.3).

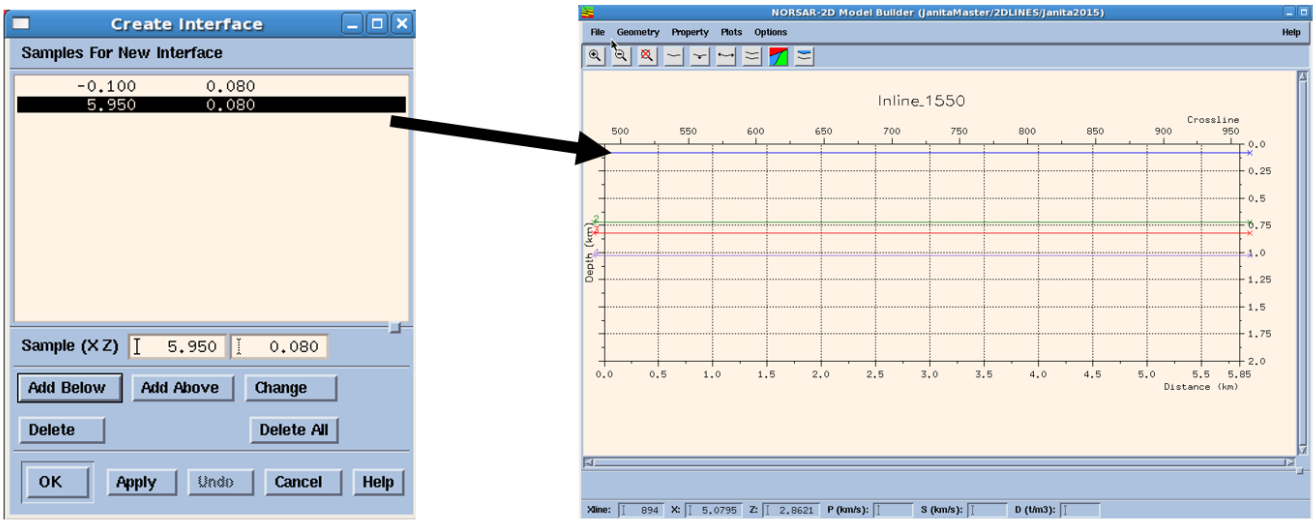

Figure B.3 The left picture shows how to create a new interface, and the corresponding example is the blue interface in the right picture.

Then I created blocks between the interfaces (Figure B.5), before I created property functions. I created constant-functions used in the Ocean-column (and CO2-plume), and vertical linear sampled functions used in the rest of the blocks (Figure B.4).

After creating all the sampled and constant functions, I assigned the values to the corresponding blocks.

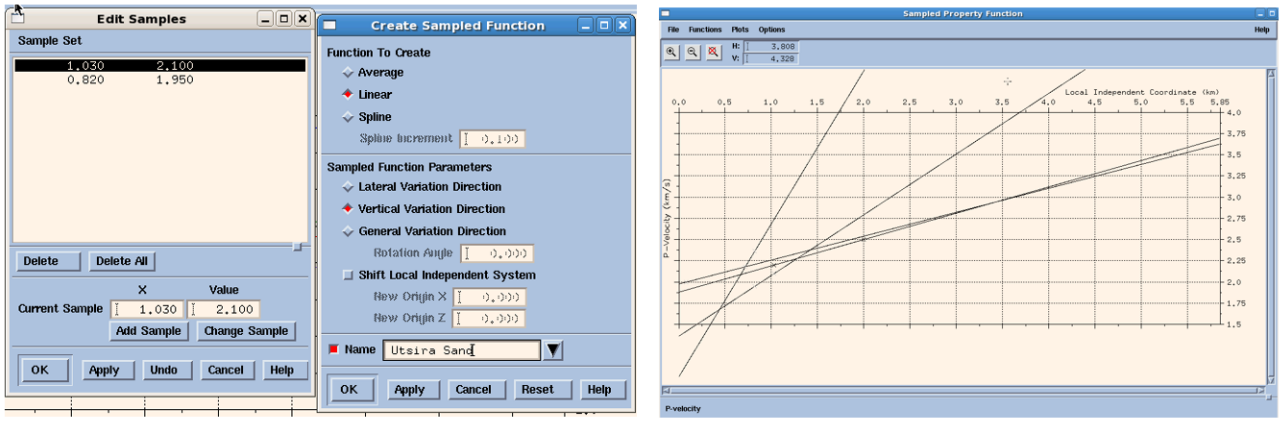

Figure B.4 From left to right, how to create a sampled property function. All the different sampled functions used in the background model are shown in the right picture.

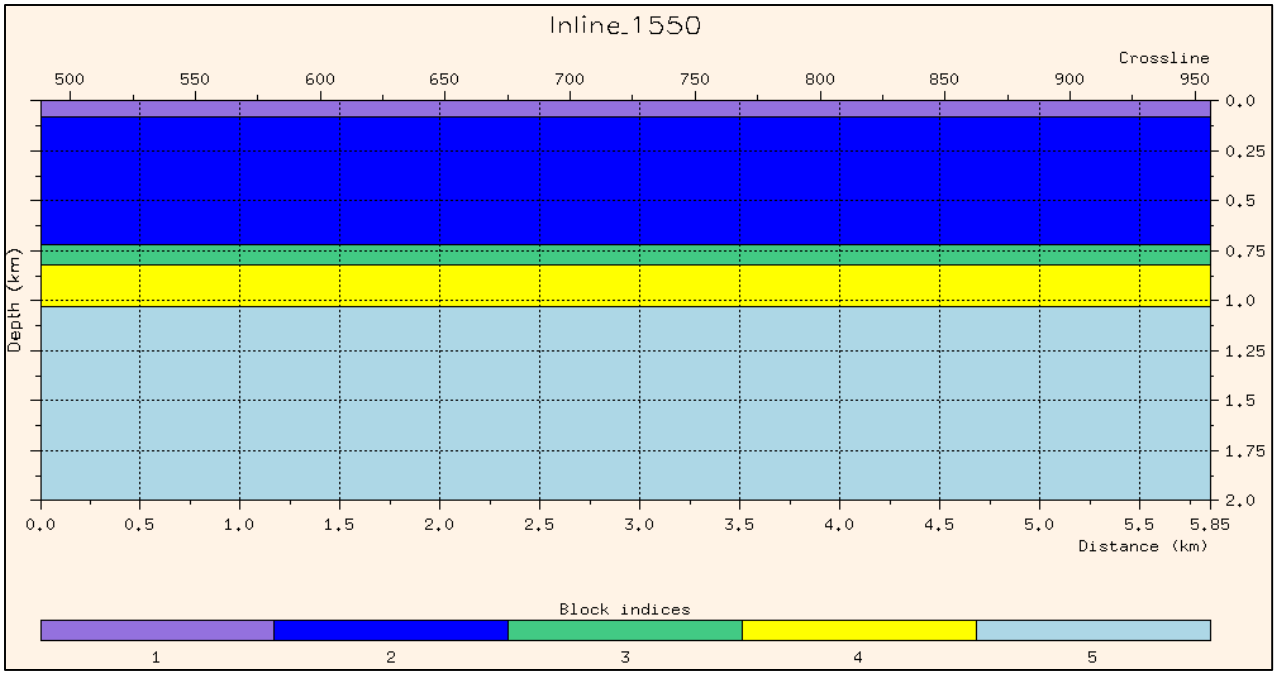

Figure B.5 2D model with blocks in the background model

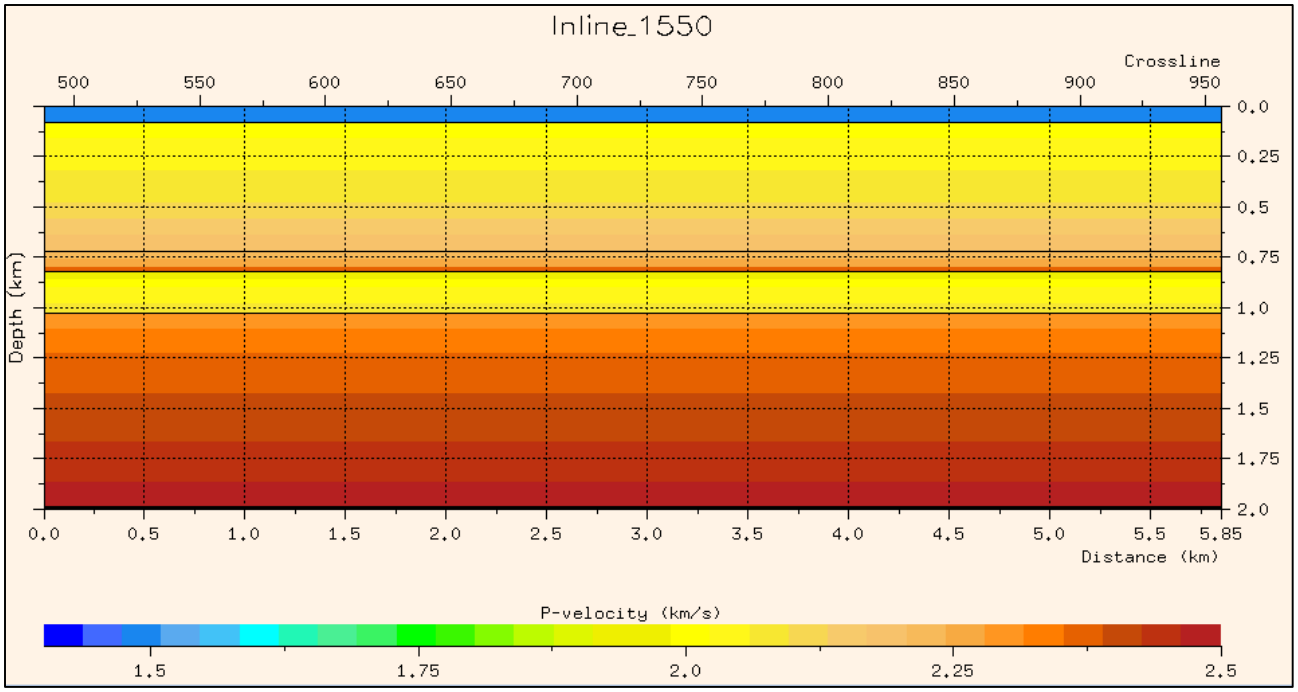

Figure B.6 The P-velocity in the background model.

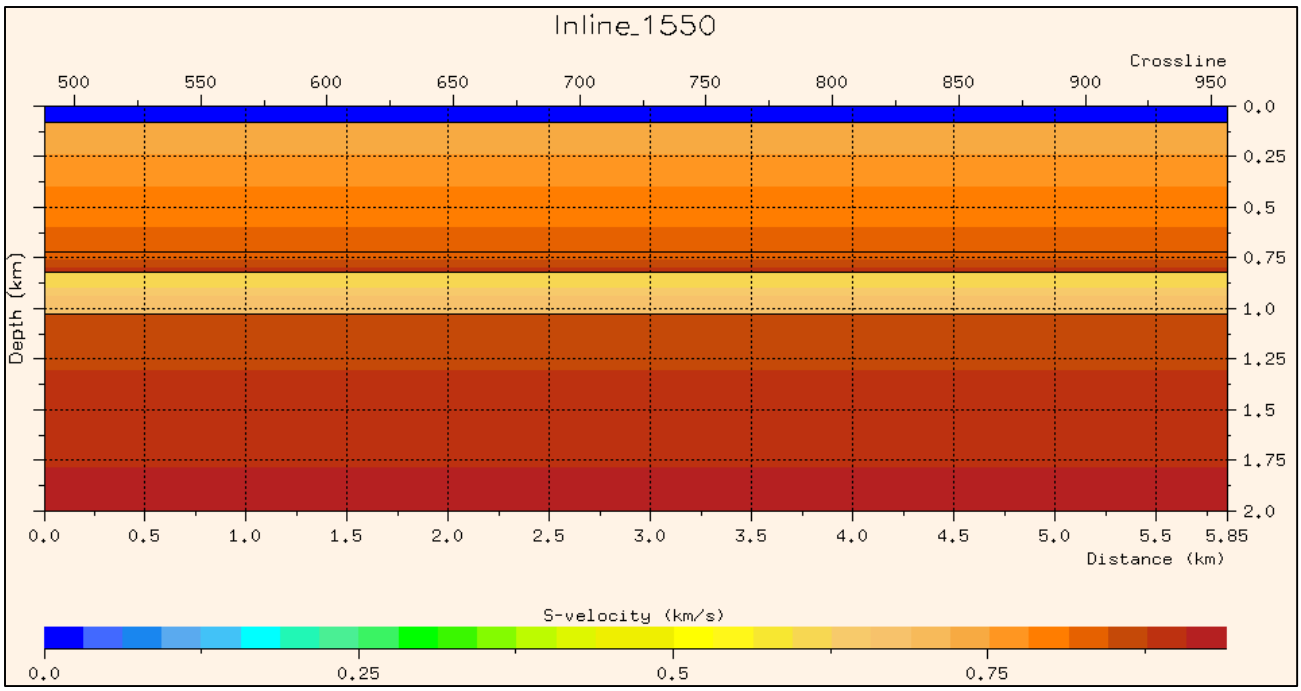

Figure B.7 The S-velocity in the background model.

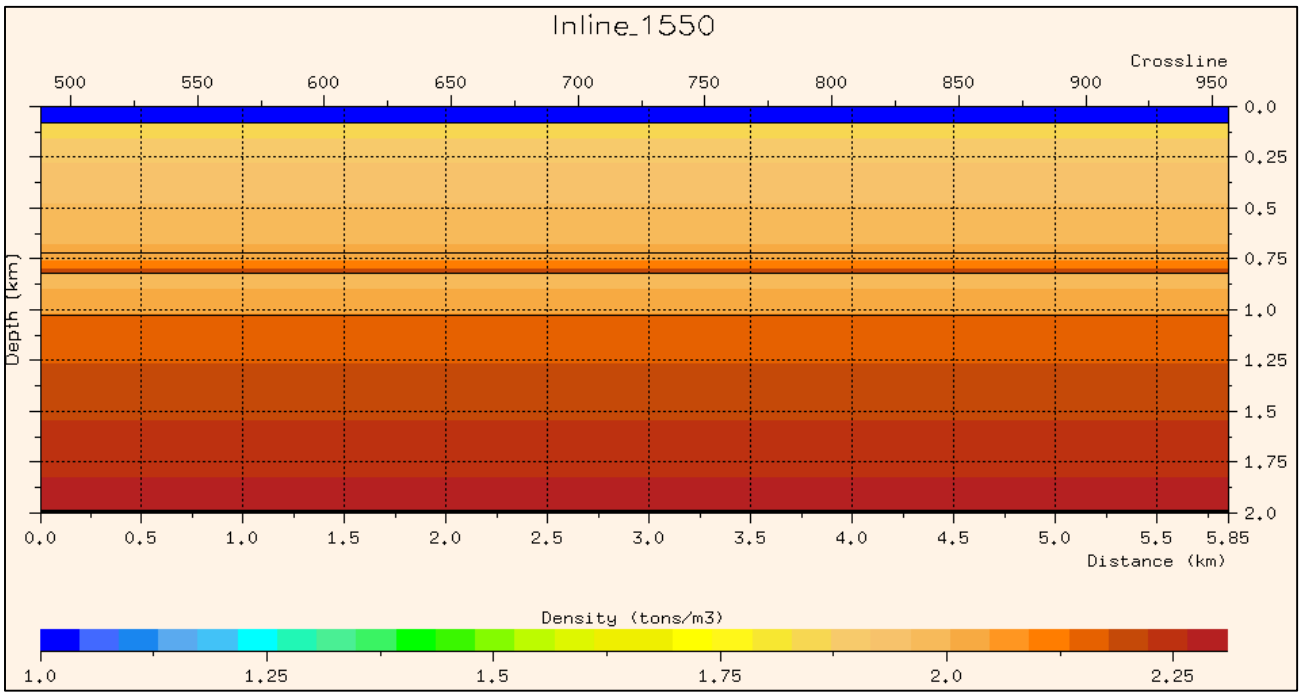

Figure B.8 The density in the background model.

When the properties are assigned in the background model, the model is saved as a SMIF-file. All previous work are done in NORSAR 2D, but the remaining part to create a complete SeisRoX model are done in NORSAR 3D.

In NORSAR 3D I open the SMIF-model created in NORSAR 2D. I create a 2,5D model by extend the horizons in Y-directions (2D was only in Y and Z-direction) (Figure B.9). When this is done, I can save the model as a SeisRox model (3D). The finished model will now appear in the SeisRox window.

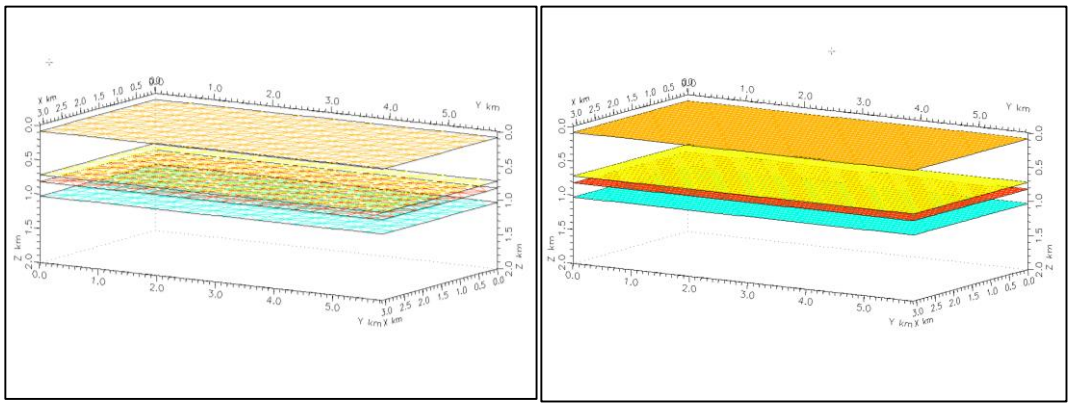

Figure B.9 Left: 2,5D background model in NORSAR 3D.Right: 3D model of the background ready to use in SeisRoX.

SeisRoX

SeisRox has two main tabs, the Objects-tab and the Workflows-tab. Under the objects-tab, we find the data used in the modeling. I can create models, survey, sub survey etc. (Figure B.10). Under the workflow-tab, I first chose which workflow I would work on, and in this thesis is it the **Local-target PSDM Simulator.** Then I insert the inputs used in the workflow; reservoir model, background model, survey, wavelet and define target area (PSDM parameters) (Figure B.10).

Summary of what I did in NORSAR 2D/3D and SeisRoX:

1. Created a new project, a common project for both NORSAR and SeisRoX
2. Created the background model and several reservoir models in NORSAR 2D
3. Assigned properties to the blocks in NORSAR 2D (Vp, Vs, RHO)
4. Exported the model as a SMIF-file from NORSAR 2D to use in NORSAR 3D
5. From the Smif-model in NORSAR 3D, created a 2.5D model
6. Exported the 2.5D model as a SeisRoX (3D) model
7. Created a survey in SeisRoX
8. Created a new SIMPLI local target reservoir workflow
9. Assigned the wavelet used in the workflow
10. Assigned the reservoir- and background-model used in the workflow
11. Assigned the PSDM parameters used in the target area

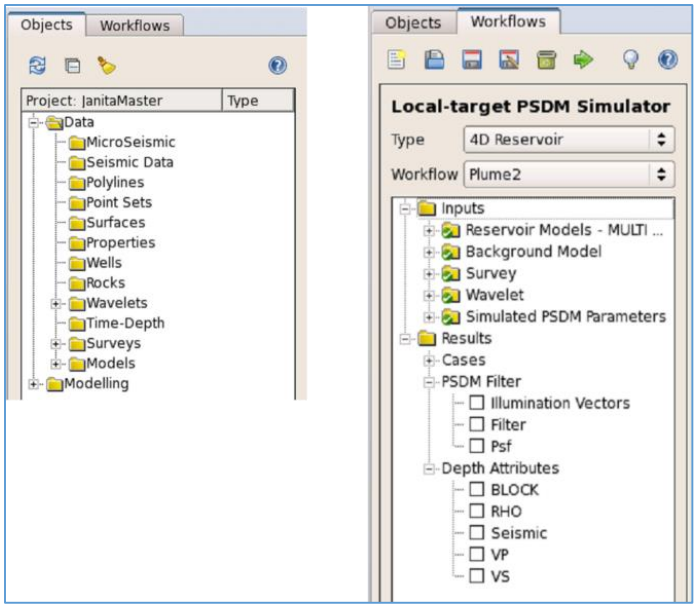

Figure B.10 Left: The Object tab. Right: The workflow tab.

Figure B.11 illustrates the window where we assign the PSDM parameters.

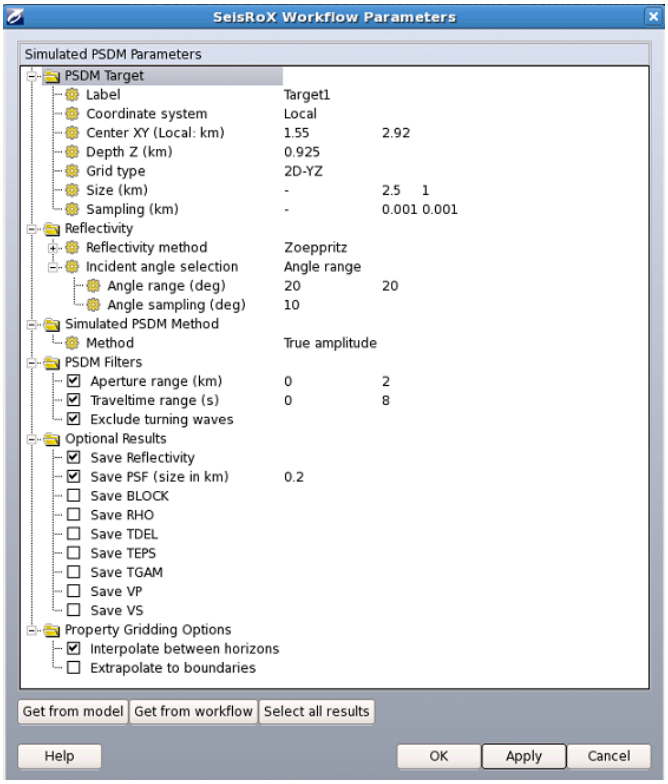

Figure B.11 Illustration of the PSDM parameters window.

Appendix C

This appendix illustrates some of the reservoir models not shown in chapter 6.3.2.1.

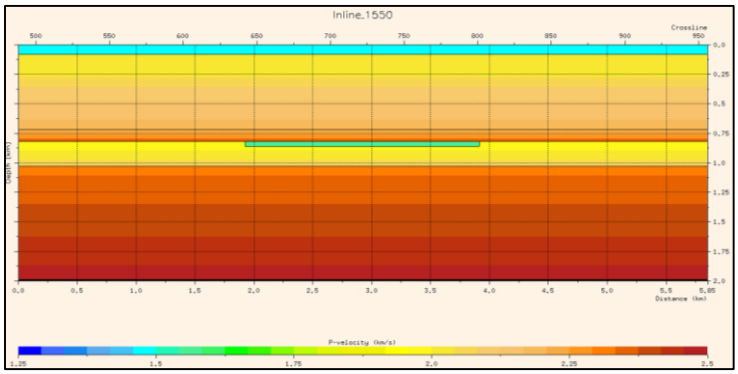

Figure C.1 Reservoir model 4 with corresponding P-velocity to 20 % CO_2 saturation. The vertical thickness of the plume is 40 m. The horizontal extent is about 2 km.

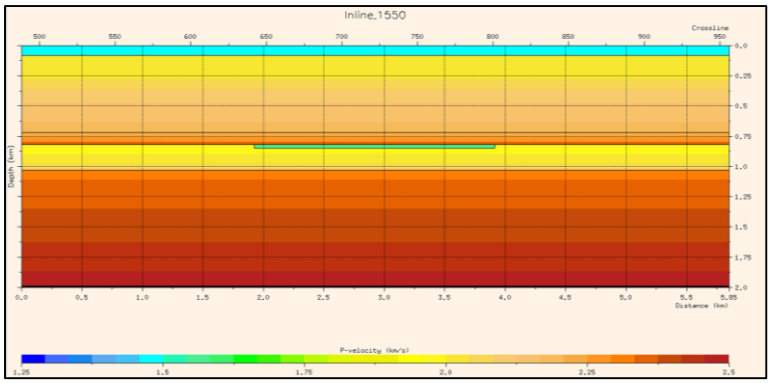

Figure C.2 Reservoir model 5, vertical thickness of 30 m. Horizontal extent of about 2 km. The model is assigned with P-velocity equal to 20 % CO_2 saturation.

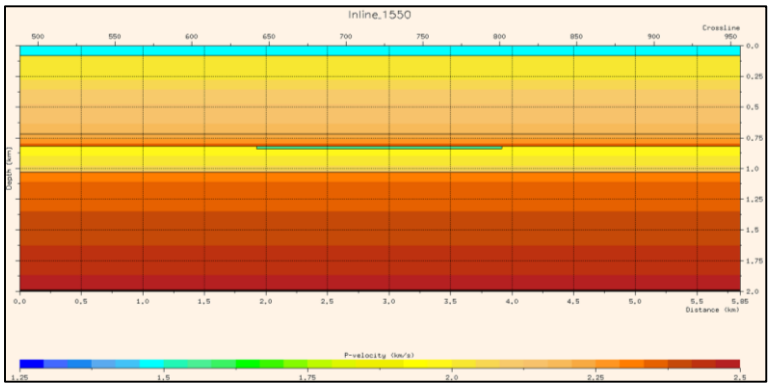

Figure C.3 Reservoir model 6 with P-velocity equals 20 % CO_2 saturation. The plume is about 2 km in horizontal extent and 20 m in vertical thickness.

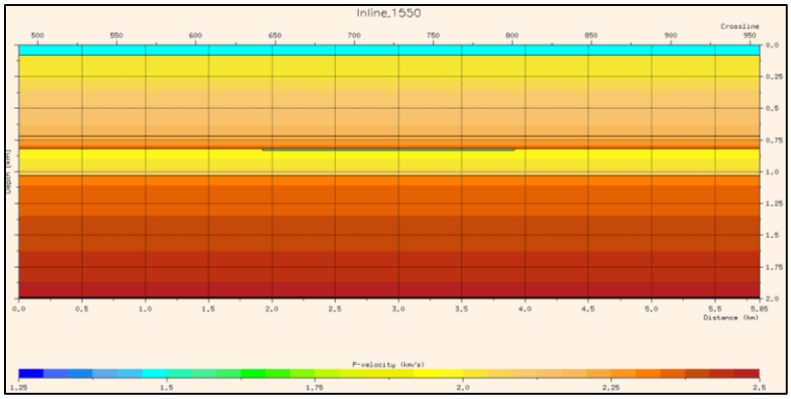

Figure C.4 Reservoir model 7 with P-velocity equals 20 % CO_2 saturation. Vertical thickness of the plume is 10 m, and horizontal extent is about 2 km.

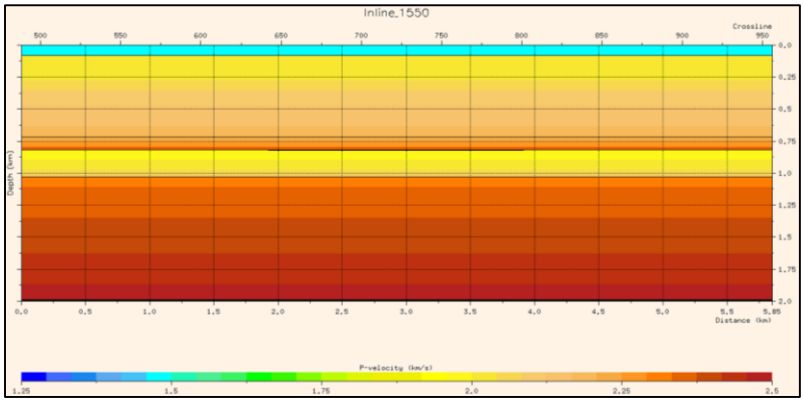

Figure C.5 Reservoir model 8 with P-velocity equals 20 % CO_2 saturation. Vertical thickness of the plume is 5 m, and horizontal extent is about 2 km.

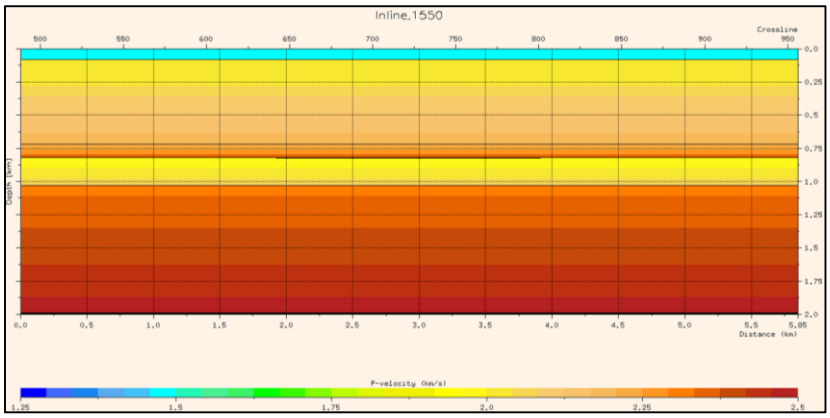

Figure C.6 Reservoir model 9 with P-velocity equals to 20% CO_2 saturation. Vertical thickness of the plume is 3 m, and horizontal extent is about 2 km.

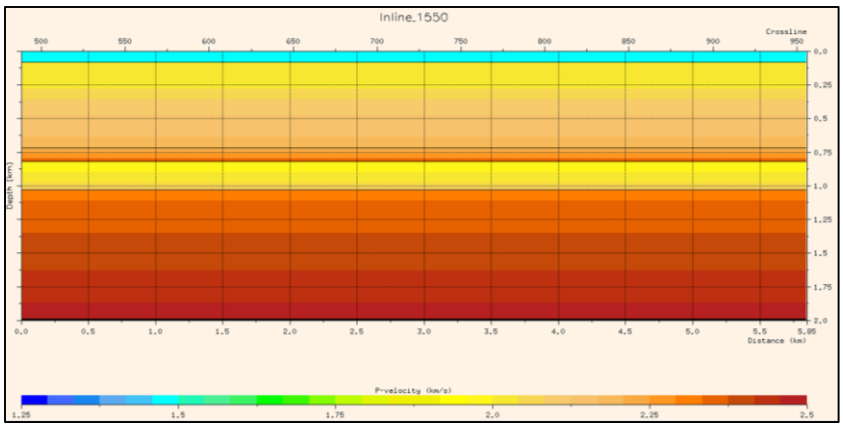

Figure C.7 Reservoir model 10 with P-velocity equals to 20% CO_2 saturation. Vertical thickness of the plume is 1 m, and horizontal extent is about 2 km.

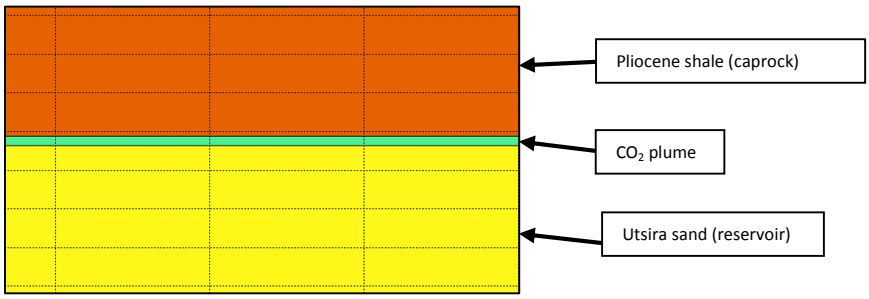

Figure C.8 Outcrop of reservoir model 10. The plume with vertical thickness of 1 m is illustrated.

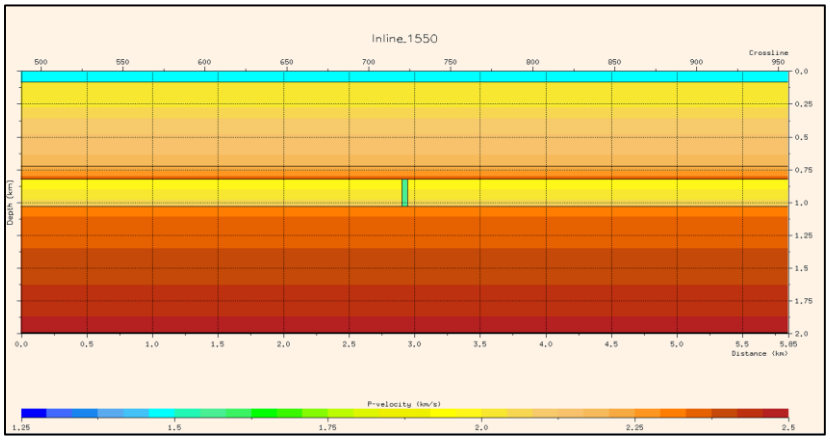

Figure C.9 Reservoir model 12 with P-velocity equal 20 % CO_2 saturation. The horizontal thickness of the plume is 40 m. The vertical extent of the plume is from the base Utsira to top Utsira, about 210 m.

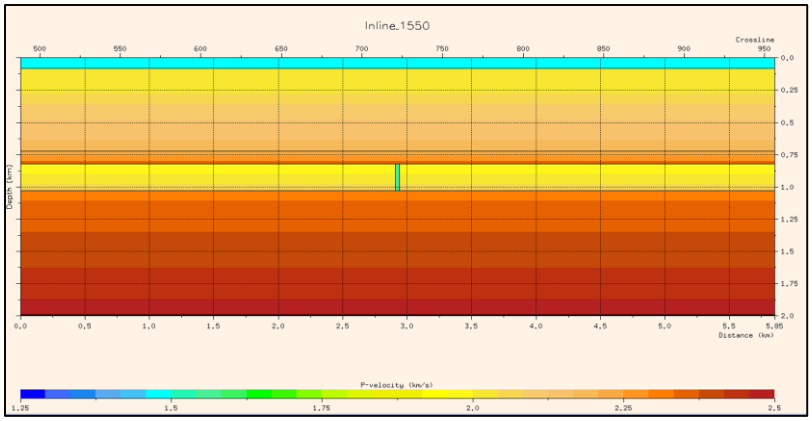

Figure C.10 Reservoir model 13 with P-velocity equal 20 % CO_2 saturation. The horizontal thickness of the plume is 30 m. The vertical extent of the plume is from the base Utsira to top Utsira, about 210 m.

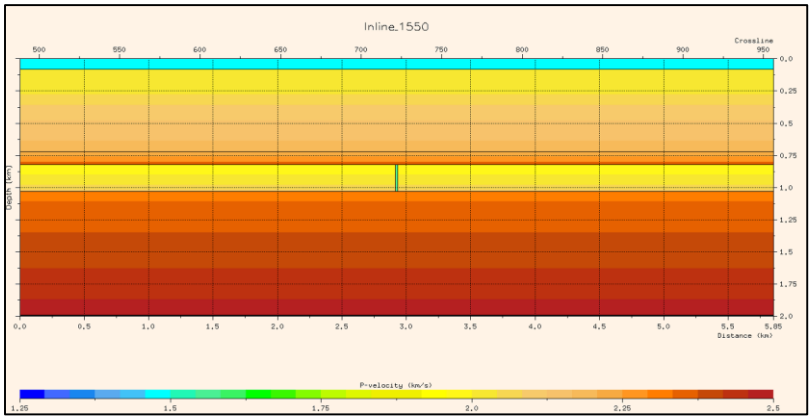

Figure C.11 Reservoir model 14 with P-velocity equal 20 % CO_2 saturation. The horizontal thickness of the plume is 20 m. The vertical extent of the plume is from the base Utsira to top Utsira, about 210 m.

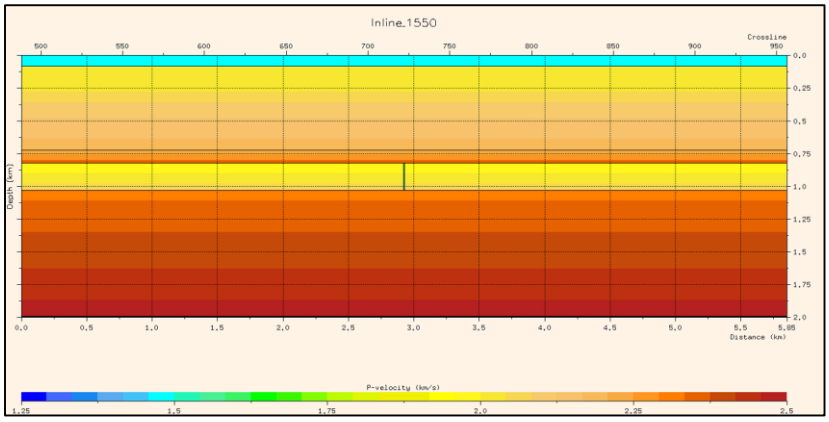

Figure C.12 Reservoir model 15 with P-velocity equal 20 % CO_2 saturation. The horizontal thickness of the plume is 10 m. The vertical extent of the plume is from the base Utsira to top Utsira, about 210 m.

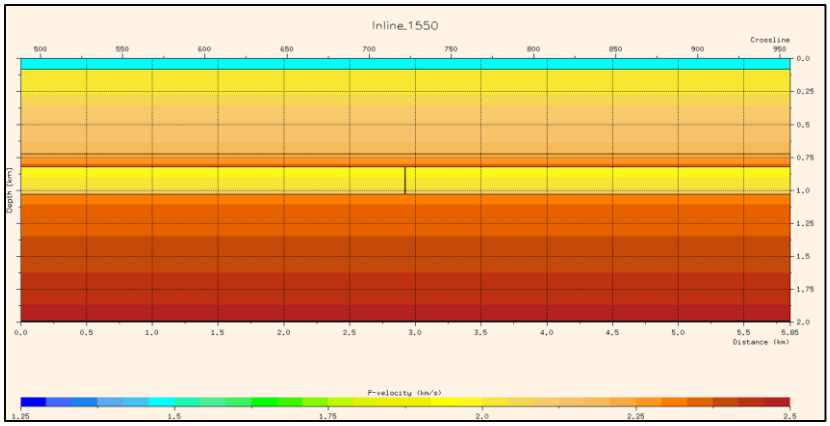

Figure C.13 Reservoir model 16 with P-velocity equal 20 % CO_2 saturation. The horizontal thickness of the plume is 5 m. The vertical extent of the plume is from the base Utsira to top Utsira, about 210 m.

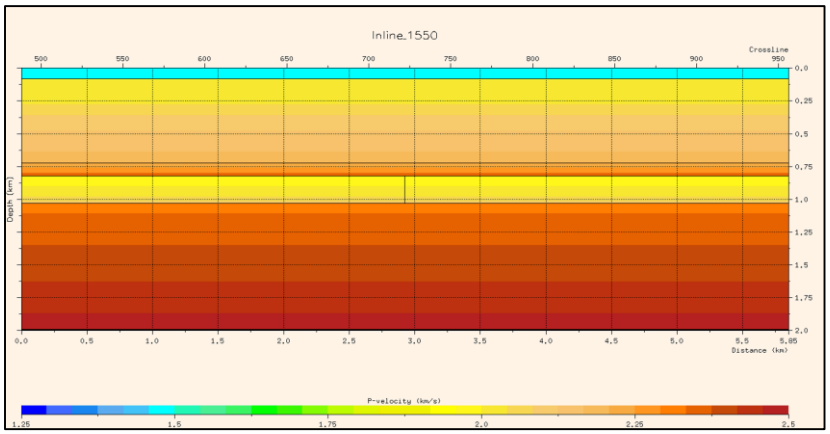

Figure C.14 Reservoir model 17 with P-velocity equal 20 % CO_2 saturation. The horizontal thickness of the plume is 3 m. The vertical extent of the plume is from the base Utsira to top Utsira, about 210 m.

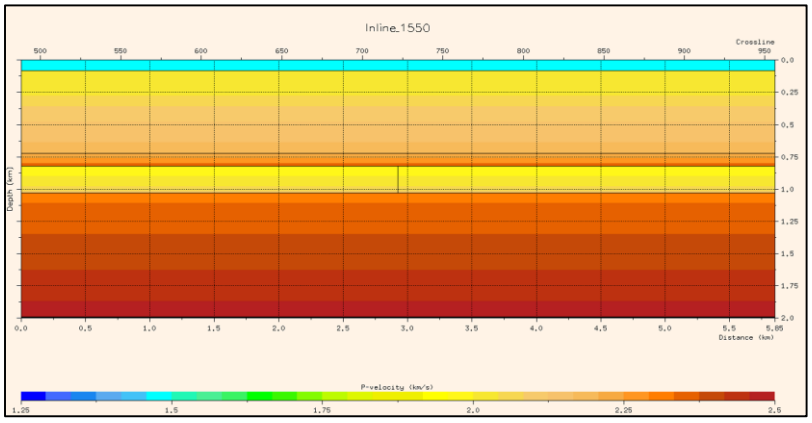

Figure C.15 Reservoir model 18 with P-velocity equal 20 % CO_2 saturation. The horizontal thickness of the plume is 1 m. The vertical extent of the plume is from the base Utsira to top Utsira, about 210 m.

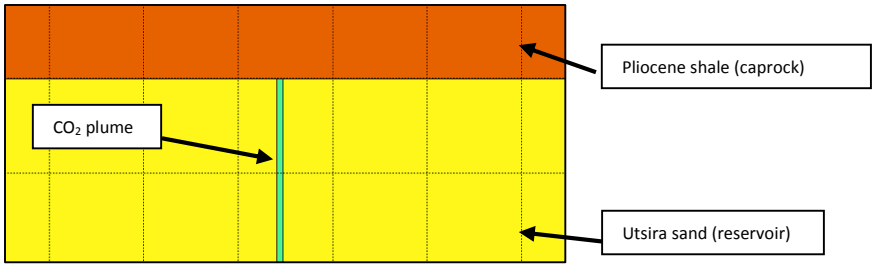

Figure C.16 Outcrop of reservoir model 18. The plume with horizontal thickness of 1 m is illustrated.